Universität Osnabrück

Dissertation

(kumulativ)

Aspects of Non-Equilibrium Behavior in Isolated Quantum Systems

zur Erlangung des Grades eines
Doktors der Naturwissenschaften (Dr. rer. nat.)

dem Fachbereich Physik der Universität Osnabrück
vorgelegt von

Robin Heveling

Osnabrück, August 2022

Betreuender Professor & 1. Gutachter: Prof. Dr. Jochen Gemmer
2. Gutachter: Prof. Dr. Robin Steinigeweg

"It's the questions we can't answer that teach us the most."

- Kvothe in *The Wise Man's Fear*

Constituent Parts

Publications

This cumulative dissertation is based on the publications [P1] - [P6].

[P1] Robin Heveling, Lars Knipschild, and Jochen Gemmer
"Compelling bounds on equilibration times - the issue with Fermi's golden rule"
Journal of Physics A: Mathematical and Theoretical **53**, 375303 (2020)
DOI: 10.1088/1751-8121/ab9e2b

[P2] Robin Heveling, Lars Knipschild, and Jochen Gemmer
"Comment on 'Equilibration Time Scales of Physically Relevant Observables' "
Physical Review X **10**, 028001 (2020)
DOI: 10.1103/PhysRevX.10.028001

[P3] Robin Heveling, Lars Knipschild, and Jochen Gemmer
"Modeling the Impact of Hamiltonian Perturbations on Expectation Value Dynamics"
Zeitschrift für Naturforschung A **75**, 5 (2020)
DOI: 10.1515/zna-2020-0034

[P4] Robin Heveling, Jiaozi Wang, Robin Steinigeweg, and Jochen Gemmer
"Integral fluctuation theorem and generalized Clausius inequality for microcanonical and pure states"
Physical Review E **105**, 064112 (2022)
DOI: 10.1103/PhysRevE.105.064112

[P5] Robin Heveling, Jiaozi Wang, and Jochen Gemmer
"Numerically probing the universal operator growth hypothesis"
Physical Review E **106**, 014152 (2022)
DOI: 10.1103/PhysRevE.106.014152

[P6] Robin Heveling, Jiaozi Wang, Christian Bartsch, and Jochen Gemmer
"Stability of exponentially damped oscillations under perturbations of the Mori-Chain"
Journal of Physics Communications **6**, 085009 (2022)
DOI: 10.1088/2399-6528/ac863b

Publication [P7] will not be discussed in detail in this dissertation.

[P7] Robin Heveling, Johannes Richter, and Jürgen Schnack
"Thermal density matrix renormalization group for highly frustrated quantum spin chains: A user perspective"
Journal of Magnetism and Magnetic Materials **487**, 165327 (2019)
DOI: 10.1016/j.jmmm.2019.165327

Scientific Outreach

Some results of this dissertation have been presented at various meetings and workshops.

Talks

- *"Integral fluctuation theorem for microcanonical and pure states"*
  Research Unit FOR 2692 PhD Meeting
  May 2021, Osnabrück

- *"Impact of perturbations on expectation value dynamics"*
  International FOR 2692 Workshop: "Fundamental Aspects of Statistical Mechanics and the Emergence of Thermodynamics in Non-Equilibrium Systems"
  September 2020, Jülich

- *"Equilibration times in finite quantum systems"*
  Research Unit FOR 2692 PhD Meeting
  July 2019, Bielefeld

- *"Bounds on equilibration times in finite quantum systems"*
  Spring Meeting of the German Physical Society
  April 2019, Regensburg

- *"Density Matrix Renormalization Group at Finite Temperatures"*
  Mini-Workshop
  Oktober 2018, Bielefeld

Posters

- *"Impact of perturbations on expectation value dynamics"*
  International FOR 2692 Workshop: "Fundamental Aspects of Statistical Mechanics and the Emergence of Thermodynamics in Non-Equilibrium Systems"
  September 2019, Delmenhorst

Aspects of Non-Equilibrium Behavior in Isolated Quantum Systems

Robin Heveling
Fachbereich Physik, Universität Osnabrück, Barbarastr. 7, D-49076 Osnabrück, Germany

Based on the publications [P1–P6], the cumulative dissertation at hand addresses quite diverse aspects of non-equilibrium behavior in isolated quantum systems. The works presented in publications [P1, P2] concern the issue of finding generally valid upper bounds on equilibration times, which ensure the eventual occurrence of equilibration in isolated quantum systems. Recently, a particularly compelling bound for physically relevant observables has been proposed. Said bound is examined analytically as well as numerically. It is found that the bound fails to give meaningful results in a number of standard physical scenarios. Continuing, publication [P4] examines a particular integral fluctuation theorem (IFT) for the total entropy production of a small system coupled to a substantially larger but finite bath. While said IFT is known to hold for canonical states, it is shown to be valid for microcanonical and even pure energy eigenstates as well by invoking the physically natural conditions of "stiffness" and "smoothness" of transition probabilities. The validity of the IFT and the existence of stiffness and smoothness are numerically investigated for various lattice models. Furthermore, this dissertation puts emphasis on the issue of the route to equilibrium, i.e., to explain the omnipresence of certain relaxation dynamics in nature, while other, more exotic relaxation patterns are practically never observed, even though they are *a priori* not disfavored by the microscopic laws of motion. Regarding this question, the existence of stability in a larger class of dynamics consisting of exponentially damped oscillations is corroborated in publication [P6]. In the same vein, existing theories on the ubiquity of certain dynamics are numerically scrutinized in publication [P3]. Finally, in publication [P5], the recently proposed "universal operator growth hypothesis", which characterizes the complexity growth of operators during unitary time evolution, is numerically probed for various spin-based systems in the thermodynamic limit. The hypothesis is found to be valid within the limits of the numerical approach.

CONTENTS

I. Introduction

The interplay of many microscopic constituents can give rise to surprisingly regular behavior on the macroscopic scale. For instance, a ball consistently traces a parabola when thrown, even though the individual atoms of ball and air act in an uncontrollable, chaotic manner. Another example is the mixing of two liquids. While the boundary between the liquids distorts in an evermore intricate pattern, the situation on the macroscopic scale becomes conceivably simple. Eventually, an equilibrium is reached and all initial imbalances of temperature, pressure, concentration, etc. have disappeared. This phenomenon occurs despite the microscopic dynamics never coming to a halt.

The frameworks of *statistical mechanics* and *thermodynamics* are tremendously successful at "glossing over the details" and characterizing equilibrium states of macroscopic systems with only a handful of parameters. However, away from equilibrium, generally valid laws are hard to come by. Notable exceptions and pillars of non-equilibrium statistical physics are *linear response theory* (LRT) [7] and *fluctuation theorems* (FTs) [8].

The former concerns systems weakly perturbed by an external force. The response of these displaced systems is routinely found in terms of *autocorrelation functions* evaluated exactly at equilibrium. The latter mentioned FTs relate the entropy production of processes, which may take the system arbitrarily far away from equilibrium, to properties of the equilibrated system in a quantitative manner. Therefore, LRT and FTs suggest that information about the equilibrium state is subtly encoded in the behavior of a system driven out of equilibrium.

Relating back to the above example of two mixing liquids, it is puzzling how an equilibrium state can be reliably reached in the first place. The laws that govern the motion on the microscopic scale do not inherently prefer the direction towards equilibrium. Nevertheless, as soon as the liquids are mixed, they will not separate again. This apparent emergence of macroscopic *irreversibility* from microscopic *reversibility*[1] is, to this day, not understood in a satisfying manner.

More precisely, the *second law of thermodynamics*, which comprises irreversibility in the sense that entropy tends to maximize, has not yet been rigorously derived from the microscopic equations of motion, e.g., the Schrödinger equation. The following section I A gives a short description of this emergent arrow of time.

[1] In the 1960s it was found that processes involving the weak nuclear force can break time reversal symmetry [9]. However, these processes are quite exotic and far too weak to possibly explain the apparent direction of time in everyday life.

These general issues of *equilibration* and *thermalization* in isolated quantum systems have experienced renewed interest in the last decades, leading to a sort of "revival" of the field of (non-equilibrium) statistical mechanics. First and foremost, this revival is driven by tremendous progress on the experimental side. Nearly isolated quantum systems, e.g., ultracold atoms trapped in optical lattices [10–14], can be controlled with unprecedented accuracy in the lab. Further, on the theoretical side, much headway has been made by the discovery of the *eigenstate thermalization hypothesis* [15, 16] and *quantum typicality* [17, 18]. These advancements are accompanied by developments of sophisticated numerical techniques and broad availability of powerful computational resources.

Recently, the specifics of the *route to equilibrium* have gathered much attention as well [19–21]. That is to say, if a system reaches equilibrium, it commonly does so in familiar patterns. For instance, exponential decays are ubiquitous in nature [22, 23]. Then again, other, more exotic relaxation dynamics -like recurrence dynamics- are not disfavored by the microscopic laws of motion from the outset. However, no observation has been made in which a (sufficiently large) system, after it has already spend some time in equilibrium, becomes spontaneously imbalanced and has to restart the relaxation process. This issue of the omnipresence of some dynamics over others can be tackled by means of stability arguments, which find common relaxation patterns to be more stable against perturbations.

Next follows a short story (descriptive and non-historic) of the arrow of time, after which the scope of this thesis is presented in Sec. I B.

A. The Arrow of Time

The end of the nineteenth century was a pleasant time for physicists. Particles had a definite position and momentum, and their collective dynamical evolution could in principle be worked out via the laws of classical mechanics. Further, Maxwell's equations accurately described electromagnetic phenomena.

There were just a few theoretical kinks that needed to be ironed out, for instance, the spectrum of a black-body, which unfortunately radiated infinite energy. In 1901, Max Planck proposed that light transfers its energy in indivisible chunks -light quanta- and employed this idea to successfully explain the black-body spectrum [24]. This success is viewed by many as the inception of quantum mechanics. Over the course of time, the list of observations that could not be reconciled with classical physics grew longer and the demand for a novel framework of physics became more and more evident. Today, the theory of quantum mechanics is one of the most successful scientific theories and an inevitable part of modern physics.

While, more than a century later, physicists struggle with questions of quantum gravity, dark matter and inconsistencies in the standard model, a long-known yet unsolved issue within quantum mechanics has regained attention in the last decades. This issue is the emergence of an *Arrow of Time* from the underlying time-symmetric quantum theory.

Here, "time-symmetric" refers to the fact that the fundamental laws of nature, e.g., the Schrödinger equation, are invariant under *time reversal*. That is to say that, on a basic level, every process that is allowed to happen forwards in time also has a non-zero probability to happen backwards.

A pendulum that swings in one direction can swing in the other direction. An atom may emit a photon at the cost of sending one of its electrons to an energetically lower orbital, or the atom may absorb a photon, lifting one of its electrons to a state of higher energy.

However, this principle does not seem to consistently extent to our experience in the macroscopic world. As an example, consider a high-board diver attempting to jump into the water. After leaving the platform, the diver's potential gravitational energy is converted to kinetic energy, which is then promptly transferred to the water after impact. The kinetic energy of the water quickly dissipates to smaller and smaller length scales, after which it can be safely described as heat energy. Now imagine the time-reversed process. The diver is peacefully swimming in the water when suddenly a huge number of surrounding water molecules conspire to transfer their kinetic energy to the diver, who is then spontaneously catapulted into the air. It is safe to assume that something like this never happened and will never happen.

Of course, such a scenario does not need to involve gravity. A classic example, which must not go unmentioned in this thesis, is a hot cup of coffee. Over the course of time, the coffee cools down until it has reached the temperature of the surrounding air. A spontaneously reheating coffee would be nice, but is, unfortunately, unheard of.

This phenomenon, the emergence of an arrow of time from underlying time-symmetric theories, poses one of the biggest unsolved problems in modern physics.

B. Scope of this Thesis

The cumulative dissertation at hand is based on the publications [P1–P6]. These works touch on quite diverse issues in the field of (non-equilibrium) quantum statistical mechanics and (non-equilibrium) quantum thermodynamics. Hence, the relatively broad and encompassing title *"Aspects of Non-Equilibrium Behavior in Isolated Quantum Systems"*.

The present text is structured as follows. Section II provides the theoretical background on which the publications [P1–P6] rely. To begin, in Sec. II A 2, the general issue of thermalization in isolated quantum systems is discussed, since this topic underlies most publications in some manner. Thereafter, fundamental results on fluctuation theorems are reviewed in Sec. II B, directly relating to Pub. [P4]. Next, in Sec. II C, the framework of the recursion method is introduced, which lays the groundwork for Pubs. [P5], [P6] and partially [P3]. Finally, a brief discussion on employed models and numerical methods is included in Sec. II D.

Section III constitutes the guide to the publications [P1–P6]. Each of the guide's sections corresponds to a respective paper, with the only exception of Pubs. [P1] and [P2], which share a section due to their similarity.

Finally, section IV summarizes the results of this dissertation and gives some prospects for possible future research.

Despite best efforts for self-containedness, the present text is not meant as a stand-alone. The presentation of the publications [P1–P6] in section III is naturally shortened and leaves out some important details. Therefore, this thesis should be understood as a mere supporting text to the publications, which are attached at the end.

In the main body of this thesis, many influential works in the fields of quantum statistical mechanics are referenced. This list of citations is necessarily incomplete and not meant to be exhaustive. Further important references can be found in the publications [P1–P6].

II. Theoretical Background

This section provides the theoretical background on which the publications [P1–P6] rely. To begin, in Sec. II A, the general issue of thermalization in isolated quantum systems is discussed. Thereafter, fundamental results on fluctuation theorems are reviewed in Sec. II B directly relating to Pub. [P4]. Next, in Sec. II C, the framework of the recursion method is introduced, which lays the groundwork for Pubs. [P5], [P6] and partially [P3]. Finally, Sec. II D constitutes a brief introduction to employed computational methods.

A. Thermalization in Isolated Quantum Systems

This section addresses aspects of thermalization in isolated quantum systems. For starters, basic principles of quantum mechanics and statistical physics are briefly recalled in Sec. II A 1. Thereafter, definitions and notions of equilibration and thermalization are introduced in Sec. II A 2. Lastly, in Secs. II A 3 and II A 4, the Eigenstate Thermalization Hypothesis and the concept of quantum typicality, two fundamental mechanisms enabling thermalization, are respectively presented and discussed.

1. Quantum Statistical Mechanics

The purpose of this section is to recall basic principles of quantum mechanics and statistical physics. This brief review is naturally far from exhaustive and there is a particular focus on concepts and scenarios that are actually relevant to the publications presented later on. All following statements, unless further indicated, can be found in standard textbooks on the matter.

At the heart of every mathematical description of a quantum system stands a Hilbert space $\mathscr{H}$, a complex vector space equipped with an inner product $\langle \cdot | \cdot \rangle$. In the following, the Hilbert space is assumed to be of finite dimension, although the results presented in this dissertation are not necessarily restricted to this case. In quantum mechanics, all information about the state of a system is encoded in the so-called wave function $|\psi\rangle \in \mathscr{H}$. Physical observables, such as position, momentum, spin, etc. are modeled by Hermitian operators $\mathcal{A} : \mathscr{H} \to \mathscr{H}$ acting on the Hilbert space[2]. Eigenvalues a_n and eigenstates $|a_n\rangle$ of $\mathcal{A}$ are defined by the eigenvalue equation $\mathcal{A}|a_n\rangle = a_n|a_n\rangle$. Since $\mathcal{A}$ is Hermitian, i.e., $\mathcal{A} = \mathcal{A}^\dagger$, all eigenvalues a_n are real and the eigenstates $|a_n\rangle$ can be chosen as an orthonormal basis of the Hilbert space.

[2] Throughout this thesis, there will be no strict distinction between the operator $\mathcal{A}$ and the observable it is representing.

The possible outcomes of a measurement are the eigenvalues a_n of the measured observable $\mathcal{A}$. The theory of quantum mechanics is inherently probabilistic. There is generally no way to determine a measurement outcome with certainty, it is merely possible to ascribe probabilities p_n to the measurement outcomes a_n. These probabilities are given by the absolute squares of the overlap between the current state of the system and the corresponding eigenstates, i.e.,

$$p_n = \sum_{i=1}^{g_n} |\langle a_n^i | \psi \rangle|^2 \,, \tag{1}$$

where the sum takes a possible g_n-fold degeneracy into account. Right after the measurement process, the wave function $|\psi\rangle$ is instantaneously projected into the eigensubspace associated with the measured eigenvalue, i.e.,

$$|\psi\rangle \to \frac{\Pi_n |\psi\rangle}{\sqrt{\langle \psi | \Pi_n | \psi \rangle}} \,, \quad \text{where} \quad \Pi_n = \sum_{i=1}^{g_n} |a_n^i\rangle\langle a_n^i| \,. \tag{2}$$

Arguably the most important operator in quantum mechanics is the Hamiltonian $\mathcal{H}$. It is the quantum mechanical counterpart to the classical Hamilton function and generator of time translations. The time evolution of a quantum system is governed by the time-dependent Schrödinger equation

$$\mathrm{i}\hbar \frac{\partial}{\partial t} |\psi(t)\rangle = \mathcal{H}(t) |\psi(t)\rangle \,. \tag{3}$$

For now, the Hamiltonian is assumed to be time-independent, i.e., $\mathcal{H}(t) = \mathcal{H}$ (this restriction is dropped again in Sec. II B). Further, the reduced Planck's constant is set to unity ($\hbar = 1$). Given some initial state $|\psi(0)\rangle$, the Schrödinger equation is formally solved by

$$|\psi(t)\rangle = e^{-\mathrm{i}\mathcal{H}t} |\psi(0)\rangle = \mathcal{U}(t) |\psi(0)\rangle \,. \tag{4}$$

The newly introduced symbol $\mathcal{U}$ denotes the time evolution operator. Since the Hamiltonian $\mathcal{H}$ is Hermitian, the time evolution operator $\mathcal{U}$ is unitary, i.e., $\mathcal{U}\mathcal{U}^\dagger = 1$. The fact that time evolution in quantum mechanics is unitary has some far-reaching consequences regarding the issue of equilibration (cf. Sec. II A 2).

For one thing, the time evolution never comes to a rest, the system keeps evolving even if an apparent equilibrium is reached. For another, the evolving state will eventually get arbitrarily close to the initial state again[3].

[3] In the sense that for all $\epsilon > 0$ there exists a time $T > 0$ such that $|| \, |\psi(T)\rangle - |\psi(0)\rangle \, || < \epsilon$, where $|| \cdot ||$ denotes the norm induced by the inner product. These events of close proximity are called Poincaré recurrences [25].

In contrast to the measurement process, unitary time evolution is completely deterministic.
The eigenvalue equation of the Hamiltonian $\mathcal{H}$ is referred to as the time-independent Schrödinger equation.

$$\mathcal{H}|\psi\rangle = E|\psi\rangle \tag{5}$$

Its solution yields eigenvalues E_n and eigenstates $|n\rangle$, whereby the formal solution to the time-dependent Schrödinger equation takes the form

$$|\psi(t)\rangle = \sum_n c_n e^{-\mathrm{i}E_n t}|n\rangle \tag{6}$$

with complex coefficients $c_n = \langle n|\psi(0)\rangle$.
Oftentimes the expected outcome of a measurement is of interest. The expectation value of a measurement of some observable $\mathcal{A}$ with respect to some normalized state $|\psi\rangle$ is given by

$$\langle\mathcal{A}\rangle_\psi = \langle\psi|\mathcal{A}|\psi\rangle\,. \tag{7}$$

In general, the expectation value is dependent on time, plugging Eq. (6) into Eq. (7) yields

$$\langle\mathcal{A}\rangle_{\psi(t)} = \sum_{m,n} c_m^\star c_n e^{\mathrm{i}(E_m - E_n)t}\mathcal{A}_{mn}\,, \tag{8}$$

where $\mathcal{A}_{mn} = \langle m|\mathcal{A}|n\rangle$ denote the matrix elements of the operator $\mathcal{A}$ in the eigenbasis of the Hamiltonian. In the Heisenberg picture of motion the time dependence is shifted from the states to the observables, which evolve according to $\mathcal{A}(t) = \mathcal{U}^\dagger(t)\mathcal{A}\mathcal{U}(t)$.
At the time when the theory of quantum mechanics was still eagerly developed, (classical) statistical physics had already established itself as a mature research field. Needless to say that proven concepts of classical statistical physics were soon tested within the novel framework of quantum mechanics. Thus, the field of quantum statistical mechanics emerged, whose fundamental principles are subject of the second part of this section.
Macroscopic objects consist of an enormous number of particles, e.g., $N = 10^{23}$. *In principle*, the behavior of the object and its constituent parts is perfectly well described by the Schrödinger equation. However, keeping track of all microscopic degrees of freedom is practically impossible[4]. Luckily, in most scenarios the knowledge of what every single particle is doing is neither relevant nor necessary. Only emergent macroscopic properties like temperature, magnetization, pressure, etc. are of interest.

[4] It does not help that in quantum mechanics the microscopic degrees of freedom are exponential in the particle number, yielding unfathomable $10^{10^{23}}$ degrees of freedom.

The framework of quantum statistical mechanics provides powerful tools that allow to calculate macroscopic, experimentally accessible observables under a few key assumptions.
One central idea in statistical mechanics is to consider statistical ensembles, i.e., many identical copies of a given system. Each copy is situated in the microstate $|\psi_\alpha\rangle$ and weighs in with a probability w_α.
Mathematically, a statistical ensemble is represented by a density operator

$$\rho = \sum_\alpha w_\alpha|\psi_\alpha\rangle\langle\psi_\alpha|\,, \tag{9}$$

which is a positive-semidefinite Hermitian operator of unit trace, i.e., $\mathrm{Tr}[\rho] = 1$. A measure of how many microstates are involved in the mixture ρ is given by the *purity*

$$\gamma = \mathrm{Tr}[\rho^2]\,. \tag{10}$$

A density operator represents a pure state if $\gamma = 1$, in this case $\rho = |\psi\rangle\langle\psi|$ for some $|\psi\rangle$, and a mixed state if $\gamma < 1$. Maximum mixedness is achieved for $\gamma = 1/d$, where d is the Hilbert-space dimension.
The time evolution of a density operator is governed by the von Neumann equation

$$\mathrm{i}\frac{\partial}{\partial t}\rho(t) = [\mathcal{H}, \rho(t)]\,. \tag{11}$$

For a pure state this reduces to the Schrödinger equation [Eq. (3)]. A formal solution for the time-dependent density operator is given by

$$\rho(t) = \mathcal{U}(t)\rho(0)\mathcal{U}^\dagger(t)\,, \tag{12}$$

where again the time-evolution operator occurs. Time-dependent expectation values with respect to a mixed state are calculated via

$$\langle\mathcal{A}\rangle_{\rho(t)} = \mathrm{Tr}[\rho(t)\mathcal{A}]\,, \tag{13}$$

which again reduces to Eq. (7) for a pure state.
The introduction of mixed states further allows to assign states to subsystems of larger, composite systems. Conceptually dividing a given system into subsystems "A" and "B", the reduced density operator ρ_A of subsystem "A" can be obtained from the state ρ of the whole system by "tracing out" subsystem "B", i.e.,

$$\rho_\mathrm{A} = \mathrm{Tr}_\mathrm{B}[\rho]\,. \tag{14}$$

In general, ρ_A is a mixed state, even if ρ is pure. This is the case if entanglement exists between the two subsystems, i.e., ρ can not be written as a product state $\rho_\mathrm{A} \otimes \rho_\mathrm{B}$.

The *von Neumann entropy* (a similar measure as purity) of a mixed state is defined by

$$\mathcal{S}_{\mathrm{vN}}(\rho) = -k_{\mathrm{B}}\mathrm{Tr}[\rho\log\rho]\,, \tag{15}$$

where k_{B} denotes Boltzmann's constant, which will be set to unity in the following ($k_{\mathrm{B}} = 1$). The von Neumann entropy is an informational form of entropy and measures the amount of information (or lack thereof) contained in the state ρ. For a pure state it vanishes, since it is known for certain in which state the system is situated. Importantly, the von Neumann entropy is invariant under unitary transformations, i.e., it is a conserved quantity. This observation has fueled (and still fuels) the search for alternative definitions of entropy, which should ideally increase over the course of time. Due to the subadditivity of $\mathcal{S}_{\mathrm{vN}}$, i.e., $\mathcal{S}_{\mathrm{vN}}(\rho) \leq \mathcal{S}_{\mathrm{vN}}(\rho_{\mathrm{A}}) + \mathcal{S}_{\mathrm{vN}}(\rho_{\mathrm{B}})$, the von Neumann entropy of subsystems is allowed to increase over time.
Of particular importance are statistical ensembles that describe systems at equilibrium, so-called *thermodynamic ensembles*. To determine which microstates partake in these ensembles, further assumptions are needed. The *principle of maximum entropy* states that an equilibrium ensemble should maximize the entropy while still respecting the conditions imposed on the system.
In 1957, Jaynes pointed out that there is a correspondence between entropy and information, such that the maximum entropy state is also the state that requires the least amount of information to describe [26, 27]. Thus, the above principle is also known as *Jaynes' principle* and it can be viewed as an application of Occam's razor. The two most prominent thermodynamic ensembles are introduced in the following.
The *microcanonical ensemble* describes an isolated system with fixed energy $\mathcal{E}$ at equilibrium. Included in the ensemble are all energy eigenstates within an energy shell $\mathcal{I} = [\mathcal{E} - \Delta/2, \mathcal{E} + \Delta/2]$ of width Δ centered around the energy $\mathcal{E}$, i.e.,

$$\rho_{\mathrm{mc}} = \frac{1}{\Omega_{\mathcal{I}}} \sum_{n:E_n\in\mathcal{I}} |n\rangle\langle n|\,. \tag{16}$$

For most purposes, the width of the energy shell Δ should be small compared to the width of the whole spectrum, but large compared to the average level spacing. The symbol $\Omega_{\mathcal{I}}$ denotes the number of energy eigenstates in the energy interval. Microcanonical expectation values[5] of observables are then given by

$$\langle\mathcal{A}\rangle_{\rho_{\mathrm{mc}}} = \mathrm{Tr}[\rho_{\mathrm{mc}}\mathcal{A}]\,. \tag{17}$$

[5] Throughout this thesis, different notations for this expectation value occur, which are $\langle\mathcal{A}\rangle_{\rho_{\mathrm{mc}}}$, $\langle\mathcal{A}\rangle_{\mathrm{mc}}$ and $\mathcal{A}_{\mathrm{mc}}$.

The von Neumann entropy of the microcanonical ensemble conveniently coincides with the Boltzmann entropy, i.e., $\mathcal{S}_{\mathrm{vN}}(\rho_{\mathrm{mc}}) = \log\Omega_{\mathcal{I}}$.
The second prominent ensemble is the *canonical ensemble*, which describes a system weakly coupled to a larger heat bath at temperature $T = 1/\beta$. The density operator that maximizes the von Neumann entropy given a fixed mean energy reads

$$\rho_{\mathrm{can}} = \frac{1}{\mathcal{Z}_\beta}\sum_n e^{-\beta E_n}\,|n\rangle\langle n|\,, \tag{18}$$

with the canonical partition function $\mathcal{Z}_\beta = \mathrm{Tr}[e^{-\beta\mathcal{H}}]$. In the thermodynamic limit, i.e., in the limit of infinite systems, the canonical distribution becomes sharply peaked and expectation values of observables generally coincide with predictions by the microcanonical ensemble[6] at energy $\mathcal{E} = \mathrm{Tr}[\rho_{\mathrm{can}}\mathcal{H}]$. To calculate expectation values for large systems, this *equivalence of ensembles* can be exploited to choose a thermodynamic ensemble that is easy to work with.

2. Equilibration and Thermalization

While the rules of statistical mechanics presented in the last section accurately describe equilibrated systems, the term equilibrium has not yet been further elaborated on. Following an intuitive notion, an *equilibrium state* is characterized by stationary dynamics, i.e., expectation values of observables no longer drastically change over time and only mildly fluctuate around some equilibrium value. This practical definition requires a (subjective) choice of an "acceptable" range δA of deviations, e.g., one percent of the difference between initial and equilibrium value. Further notions of equilibration include, e.g., *equilibration on average* [28] or *equilibration of subsystems* [29–31].
In view of the aforementioned Poincaré recurrences, a system can not remain in equilibrium indefinitely. Therefore, one might argue that "true" equilibration can not occur in isolated quantum systems. The time scales at which these recurrences happen, however, are so large that calling them "astronomical" would not do justice. Even for moderately sized systems consisting only of a handful of particles, the recurrence times easily exceed

[6] Although temperature is *a priori* defined only in the canonical case, there are ways to assign a temperature to microcanonical and even pure states. For instance, as described above, given an energy $\mathcal{E}$ of a microcanonical or pure state, the corresponding inverse temperature is given by the specific β for which $\mathcal{E} = \mathrm{Tr}[e^{-\beta\mathcal{H}}\mathcal{H}]/\mathcal{Z}_\beta$. Another possibility, which is employed in some publications, is via the density of states, i.e., $\beta = \partial\log\Omega(E)/\partial E|_{E=\mathcal{E}}$.

the age of the universe. Thus, recurrence events are of no relevance to the practical issues of equilibration negotiated here.

The temporal average over a time interval $[0, \tau]$ of a time-dependent expectation value is given by

$$\overline{\mathcal{A}}_\tau = \frac{1}{\tau}\int_0^\tau \langle \mathcal{A}(t)\rangle \,\mathrm{d}t\,. \tag{19}$$

Of particular interest is the *long-time average*[7]

$$\overline{\mathcal{A}} = \lim_{\tau\to\infty} \overline{\mathcal{A}}_\tau\,, \tag{20}$$

which can be explicitly calculated. To this end, the expression for the time-dependent expectation value of a pure state[8] in Eq. (8) is conveniently split into a diagonal and an off-diagonal part, i.e.,

$$\begin{aligned}\langle \mathcal{A}(t)\rangle &= \langle\psi(t)|\mathcal{A}|\psi(t)\rangle \\ &= \sum_n |c_n|^2 \mathcal{A}_{nn} + \sum_{m\neq n} c_m^\star c_n e^{\mathrm{i}(E_m-E_n)t}\mathcal{A}_{mn}\,.\end{aligned} \tag{21}$$

Plugging Eq. (21) into Eq. (20), the off-diagonal terms dephase and average to zero under the non-resonance condition[9]. The diagonal term remains and the long-time average evaluates to

$$\overline{\mathcal{A}} = \sum_n |c_n|^2 \mathcal{A}_{nn}\,. \tag{22}$$

This expression still features the initial state in the form of the coefficients c_n. Intuitively, the equilibrium value should, however, be independent of the specific initial state, such that the system has lost all memory once equilibrium is reached. The two subsequent sections II A 3 and II A 4 offer mechanisms that solve this issue and lead to *initial state independence* [34].

The long-time average $\overline{\mathcal{A}}$ can be interpreted as the expectation value with respect to a *diagonal ensemble* defined by $\rho_{\mathrm{de}} = \sum_n |c_n|^2 |n\rangle\langle n|$.

Note that the value $\overline{\mathcal{A}}$ always exists, even if the expectation value does not remain close to it. Therefore, a properly equilibrated observable should further feature only small deviations from $\overline{\mathcal{A}}$.

These deviations can be quantified by the long-time average of the temporal fluctuations[10], which is given by

$$\begin{aligned}\sigma^2_{\mathcal{A}} &= \lim_{\tau\to\infty}\frac{1}{\tau}\int_0^\tau [\langle\mathcal{A}(t)\rangle - \overline{\mathcal{A}}]^2\,\mathrm{d}t \\ &= \sum_{m\neq n} |c_m|^2|c_n|^2|\mathcal{A}_{mn}|^2\,.\end{aligned} \tag{23}$$

The second line follows by plugging in Eq. (21) and again assuming non-degenerate energy gaps. Thus, it is evident from Eq. (23) that fluctuations are to some extent controlled by the off-diagonal elements.

In systems with many degrees of freedom, equilibration (in some sense) can be shown to occur quite generically [36–38]. In fact, preparing setups that do not equilibrate seem to demand a lot of fine-tuning [39].

Mathematical relations that ensure equilibration are frequently cast in the form of inequalities of the type

$$\mu[T_{\delta A}] \leq f[\mathcal{H}, \mathcal{A}, \rho]\,. \tag{24}$$

Here, $\mu[\,\cdot\,]$ denotes some measure of the time $T_{\delta A}$ spend "away" from equilibrium, i.e., the amount of time at which $|\langle\mathcal{A}(t)\rangle - \overline{\mathcal{A}}| \geq \delta A$. The function $f[\,\cdot\,]$ on the right-hand side of Eq. (24) denotes some general, possibly quite involved function of the Hamiltonian $\mathcal{H}$, observable $\mathcal{A}$ and initial state ρ.

The logical question that arises next is whether the long-time equilibrium state agrees with predictions by statistical mechanics. As mentioned, initial non-equilibrium conditions will persist in the dephased state ρ_{de} since the ρ_{nn} are conserved quantities.

Nevertheless, the long-time average value $\overline{\mathcal{A}}$ should coincide with the thermal value, e.g., $\mathcal{A}_{\mathrm{mc}}$ in the microcanonical case. If this is indeed the case, the system is said to have undergone *thermalization* and

$$\overline{\mathcal{A}} \simeq \mathcal{A}_{\mathrm{mc}}\,. \tag{25}$$

The two following sections discuss sufficient conditions under which thermalization eventually occurs.

---

[7] It is assumed that limits of this type are well-defined.

[8] For simplicity, the following considerations are laid out for pure states. However, they generalize to mixed states in a straightforward manner by replacing $|c_n|^2 \to \rho_{nn}$ and $c_m^\star c_n \to \rho_{mn}$.

[9] Which states that $E_n - E_m = E_k - E_l$ if and only if $n = k$ and $m = l$ [32, 33].

[10] The temporal fluctuations concern the deviation of $\langle\mathcal{A}(t)\rangle$ from $\overline{\mathcal{A}}$ and are distinct from "quantum fluctuations", which concern the deviation of measurement outcomes from $\overline{\mathcal{A}}$ [35].
For comparison, the long-time average of quantum fluctuations reads

$$\lim_{\tau\to\infty}\frac{1}{\tau}\int_0^\tau \langle[\mathcal{A}(t) - \overline{\mathcal{A}}]^2\rangle\,\mathrm{d}t\,.$$

3. Eigenstate Thermalization Hypothesis

The *Eigenstate Thermalization Hypothesis* (ETH) outlines a fundamental mechanism that ensures eventual thermalization of isolated quantum systems [15, 16]. For instance, the ETH reconciles the apparent discrepancy between the microcanonical [Eq. (17)] and the long-time average expectation value [Eq. (22)] discussed at the end of Sec. II A 2.

One central idea of the hypothesis is that the expectation values $\langle n|\mathcal{A}|n\rangle$ of local, few-body observables with respect to energy eigenstates of generic, non-integrable Hamiltonians coincide with the thermal equilibrium value $\mathcal{A}_{\mathrm{mc}}$ at that energy[11].

Srednicki proposed a formulation of the ETH, which can be motivated by random-matrix theory [40], that is an ansatz for the matrix representation of an observable in the energy eigenbasis [35], i.e.,

$$\mathcal{A}_{mn} = A(\epsilon)\delta_{mn} + \Omega(\epsilon)^{-\frac{1}{2}} f_A(\epsilon,\omega) r_{mn}\,, \tag{26}$$

with $\epsilon = (E_m + E_n)/2$ and $\omega = E_m - E_n$. Crucially, A and f_A are smooth functions of their arguments and $A(\epsilon)$ coincides with the microcanonical expectation value at energy ϵ. The r_{mn} can be thought of as random[12] numbers (only constrained to $r_{mn} = r^\star_{nm}$) drawn from a Gaussian distribution with zero mean and unit variance. Finally, $\Omega(\epsilon)$ denotes the density of states at energy ϵ. This ansatz incorporates the aforementioned idea of thermal eigenstates, but also has further consequences, which will be briefly discussed in the following.

Starting from Eq. (22) and assuming the ETH to be valid, an initial (pure) state with a relatively sharp energy distribution around an energy $\mathcal{E}$ yields the long-time average expectation value

$$\overline{\mathcal{A}} = \sum_n |c_n|^2 \mathcal{A}_{nn} \approx A(\mathcal{E}) \sum_n |c_n|^2 = A(\mathcal{E})\,. \tag{27}$$

Here, the diagonal elements $\mathcal{A}_{nn}$ only change negligibly over the populated energy range and were thus approximated by $A(\mathcal{E})$, which is per ETH ansatz more or less independent of n. Continuing, the microcanonical expectation value reads

$$\mathcal{A}_{\mathrm{mc}} = \frac{1}{\Omega_{\mathcal{I}}} \sum_{n:E_n\in\mathcal{I}} \mathcal{A}_{nn} \approx \frac{A(\mathcal{E})}{\Omega_{\mathcal{I}}} \sum_{n:E_n\in\mathcal{I}} 1 = A(\mathcal{E})\,, \tag{28}$$

where the same approximation was employed. Thus, $\overline{\mathcal{A}} \simeq \mathcal{A}_{\mathrm{mc}}$ and both expectation values coincide.

This finding is often referred to as the *diagonal ETH*, since only properties of $A(\epsilon)$ were utilized.

While the diagonal ETH ensures matching long-time and microcanonical mean values, in thermal equilibrium the time-dependent expectation value should further only fluctuate mildly. As is evident from Eq. (23), the off-diagonal elements $\mathcal{A}_{mn}$ need to be small in order for $\sigma^2_{\mathcal{A}}$ to be small. Plugging the ETH ansatz [Eq. (26)] into the expression for the long-time average of the temporal fluctuations [Eq. (23)] yields

$$\begin{aligned}\sigma^2_{\mathcal{A}} &= \sum_{m\neq n} |c_m|^2 |c_n|^2 |\mathcal{A}_{mn}|^2 \\ &\leq \max_{m\neq n} |\mathcal{A}_{mn}|^2 \propto \Omega(\mathcal{E})^{-1}\,.\end{aligned} \tag{29}$$

At the inequality sign, the off-diagonal elements were bounded by their maximum and normalization of the state was used. The final relation reveals that the temporal fluctuations are inversely proportional to the density of states at energy $\mathcal{E}$. Since $\Omega(\mathcal{E})$ is routinely exponentially large in system size [42], the fluctuations in turn become exponentially small in system size and expectation values indeed stay close to their respective equilibrium values. This finding, together with the essentially random off-diagonal elements, is commonly referred to as the *off-diagonal ETH*.

To summarize, the off-diagonal ETH implies equilibration on average, while (in addition) the diagonal ETH implies thermalization on average. Thus, the full ETH (diagonal + off-diagonal) is a sufficient condition for thermalization on average in isolated quantum systems (assuming suitable initial states).

There exists a multitude of variations of the ETH, which either slightly weaken or strengthen certain assumptions or statements. For instance, the *rigged ETH* [19] is a strengthened version of the ETH in which the the envelope function $f_A(\epsilon,\omega)$ is additionally assumed to be (approximately) independent of the mean energy ϵ, i.e., $f_A(\epsilon,\omega) \approx f_A(\omega)$, at least within the populated energy interval.

To date, a rigorous "proof" of the ETH's validity based on physically plausible conditions is still lacking. However, it is generally believed that the ETH holds for "physical" observables (local and few-body) and generic, non-integrable Hamiltonians [40]. On the one hand, this belief stems from various numerical investigations of quantum lattice models, in which the ETH is explicitly checked by computing corresponding matrix elements [43–48]. On the other hand, there exist heuristic arguments in favor of the general validity of the ETH [16, 33, 40].

The daunting task of understanding under which conditions the ETH holds naturally extends to characterizing scenarios in which it breaks down.

---

[11] This means that energy eigenstates are "typical", cf. Sec. II A 4.

[12] Recently, investigations into the existence of correlations between matrix elements of physical observables have gathered much attention [41].

The two most prominent classes of systems in this category are integrable[13] systems and certain types of disordered systems.

Systems of the first class are commonly characterized by an extensive number of local conservation laws [49, 57]. Consequently, integrable systems usually fail to thermalize to standard statistical ensembles such as the microcanonical ensemble. Rather, they have been found to reach steady states matching predictions by the *generalized Gibbs ensemble* [58], which is the ensemble obtained by taking into account additional conserved quantities when applying the principle of maximum entropy.

The second class consists of systems with (sufficiently strong) disorder, leading to *many-body localization* (MBL) [59–62]. Systems exhibiting MBL routinely feature suppressed transport properties, inhibiting the spread of information through the systems. As a consequence, many-body localized systems fail to act as their own heat bath and thermalization does not occur. A transition between a MBL- and an ETH-phase may occur by tuning the disorder strength [63].

While none of the publications [P1–P6] take the ETH into the main focus, the hypothesis turns up in Pubs. [P1, P2] as part of analytical arguments regarding bounds on equilibration times. Further, the close relation between the rigged ETH and the (yet to be introduced) properties of "stiffness" and "smoothness" of transition probabilities is discussed in Pub. [P4].

4. Quantum Typicality

The Schrödinger equation (or von Neumann equation for that matter) entail no mechanism that changes the purity or mixedness of a state. Consequently, the purity $\gamma = \mathrm{Tr}[\rho^2]$ is a conserved quantity and it is impossible for a pure initial state $\rho(0) = |\psi(0)\rangle\langle\psi(0)|$ to unitarily evolve into an equilibrium ensemble like ρ_{mc}. However, a quantum state itself is not measurable. Rather, direct measurements or expectation values of observables are of physical relevance.

The concept of *quantum typicality* states that, under certain conditions, pure states can behave similarly to entire statistical ensembles and yield basically the same expectation values [17, 18, 64, 65]. In particular, the vast majority of pure states ("typical" states) give rise to expectation values close to the thermal equilibrium value. In other words, non-equilibrium pure states are mathematically rare.

Pure states evolving in time are thus exceedingly likely to evolve into typical states signaling apparent equilibration. Further, the state is likely to remain in the giant "bubble" of typical states, even though the dynamics never come to a halt.

To demonstrate that a random state is likely to be typical, it needs to be specified what is meant by drawing a random state from the Hilbert space. With respect to some arbitrary orthonormal basis $\{|\xi_k\rangle\}$, any pure state can be written as $|\phi\rangle = \sum_k c_k|\xi_k\rangle$ with complex coefficients c_k. It can be shown that drawing the real and imaginary parts of c_k from a Gaussian distribution with zero mean and variance $1/2$ corresponds to a uniform distribution on a complex sphere [66] (almost sphere, but variance of norms is small, see below). The resulting distribution of pure states is invariant under unitary transformations, i.e., $|\phi\rangle$ and $|\phi'\rangle = \mathcal{U}|\phi\rangle$ are equally likely ($\mathcal{U}$ is an arbitrary unitary operator). The state $|\phi\rangle$ is said to be drawn according to the unitary invariant *Haar-measure* and is called a *Haar-random* state (hereafter just referred to as a random state).

Starting from the ensemble of random states $|\phi\rangle$, a new ensemble can be constructed with states

$$|\psi\rangle = \sum_k c_k \mathcal{R}|\xi_k\rangle\,, \tag{30}$$

where $\mathcal{R}$ is some Hermitian, non-negative operator. A state $|\psi\rangle$ from this ensemble is likely to yield similar expectation values as the statistical ensemble $\rho = \mathcal{R}\mathcal{R}^\dagger$ [67], provided the following conditions are met. First, the state ρ should be sufficiently mixed such that $\gamma = \mathrm{Tr}[\rho^2] \ll 1$. Second, the spectral width of the pertinent observable $\mathcal{A}$ should not significantly change under upscaling of the system (as is the case for, e.g., local operators and adequately defined sums thereof). Note that $\mathcal{R}$ can be chosen such that $\mathrm{Tr}[\rho] = 1$.

Let the average over the random state ensemble from Eq. (30) be denoted by $\mathbb{E}[\,\cdot\,]$. The ensemble average of the (unnormalized) expectation value of some observable $\mathcal{A}$ then evaluates to

$$\mathbb{E}[\langle\psi|\mathcal{A}|\psi\rangle] = \sum_{i,j} \mathbb{E}[c_i^\star c_j]\langle\xi_i|\mathcal{R}^\dagger\mathcal{A}\mathcal{R}|\xi_j\rangle = \mathrm{Tr}[\rho\mathcal{A}]\,, \tag{31}$$

where $\mathbb{E}[c_i^\star c_j] = \delta_{ij}$ was used [65, 67, 68]. Indeed, the ensemble average coincides with the expectation value of $\mathcal{A}$ with respect to ρ. Abbreviating $\mathcal{A}' = \mathcal{R}^\dagger\mathcal{A}\mathcal{R}$, the ensemble average of the squared expectation value is given by [65, 67, 68]

$$\begin{aligned}\mathbb{E}[\langle\psi|\mathcal{A}|\psi\rangle^2] &= \sum_{i,j,k,l} \mathbb{E}[c_i^\star c_j c_k^\star c_l]\langle\xi_i|\mathcal{A}'|\xi_j\rangle\langle\xi_k|\mathcal{A}'|\xi_l\rangle \\ &= \mathrm{Tr}[(\rho\mathcal{A})^2] + \mathrm{Tr}[\rho\mathcal{A}]^2\,,\end{aligned} \tag{32}$$

[13] The issue of integrability in quantum mechanics is much discussed topic in itself [28, 49]. Common definitions are based on the Bethe ansatz [50–52], energy level statistics [53–55] or the existence of an integrable classical limit [56].

where $\mathbb{E}[c_i^\star c_j c_k^\star c_l] = \delta_{ij}\delta_{kl} + \delta_{il}\delta_{jk}$ was used[14]. The resulting ensemble variance can then be bounded as

$$\begin{aligned} \mathrm{var}(\mathcal{A}) &= \mathbb{E}[\langle\psi|\mathcal{A}|\psi\rangle^2] - \mathbb{E}[\langle\psi|\mathcal{A}|\psi\rangle]^2 \\ &= \mathrm{Tr}[(\rho\mathcal{A})^2] \leq \mathrm{Tr}[\rho^2\mathcal{A}^2] \leq \gamma||\mathcal{A}||^2\,, \end{aligned} \tag{33}$$

where at the first inequality sign, the Cauchy-Schwarz inequality with respect to the Frobenius inner product $(\mathcal{A}|\mathcal{B}) = \mathrm{Tr}[\mathcal{A}^\dagger\mathcal{B}]$ was employed. At the second inequality sign, the trace was carried out in the eigenbasis $\{|a_j\rangle\}$ of the observable and the squares of the eigenvalues a_j^2 were bounded from above by the square of the largest absolute eigenvalue $||\mathcal{A}||^2$. Since, per assumption, $||\mathcal{A}||$ only changes mildly under upscaling and $\gamma \ll 1$, the variance is quite small. Introducing the *effective dimension* $d_{\mathrm{eff}} = \gamma^{-1}$, the standard deviation thus scales as $\propto 1/\sqrt{d_{\mathrm{eff}}}$. Consequently, the vast majority of states from the ensemble in Eq. (30) indeed yield expectation values close to $\langle\mathcal{A}\rangle_\rho$.

Choosing $\mathcal{A}$ as the unit operator ($\mathcal{A} = 1$), it immediately follows that $\mathbb{E}[\langle\psi|\psi\rangle] = 1$ and further that $\mathbb{E}[(\langle\psi|\psi\rangle - 1)^2] = \mathrm{Tr}[\rho^2] \ll 1$.

Setting $\mathcal{R} = 1/\sqrt{d}$ yields $\mathbb{E}[\langle\psi|\mathcal{A}|\psi\rangle] = \mathrm{Tr}[\mathcal{A}]/d$ and $\mathrm{var}(\mathcal{A}) = \mathrm{Tr}[\mathcal{A}^2]/d^2 \leq ||\mathcal{A}||^2/d$. Here, the identity operator can be defined on the whole Hilbert space or on a subspace specified by some constraint, e.g., a microcanonical energy shell. In this case, a random state $|\psi\rangle$ yields the microcanonical expectation value with high probability.

Relating this result back to Sec. II A 3, the diagonal ETH basically states that energy eigenstates are typical. However, it is important to note that the ETH and typicality are two distinct concepts. While the ETH is expected to hold for local, few-body observables in non-integrable systems [40], typicality only relies on a sufficiently large Hilbert space and also works when the ETH is violated.

A further application of the typicality concept is *canonical typicality* [17, 69, 70], which reveals that the vast majority of pure states of an isolated compound system yield reduced density operators of small subsystems (by tracing out the larger part of the system) that are practically indistinguishable from the canonical ensemble on the considered subsystem (relating respective energy and temperature as described in footnote 6).

Yet another remarkable result is *dynamical typicality* [66, 71–73], which extends the above considerations to time-dependent expectation values. As mentioned in Sec. II A 1, in the Heisenberg picture of motion the observable $\mathcal{A}(t)$ evolves in time, while the state ρ does not. Due to unitarity, the spectrum of $\mathcal{A}$ remains unchanged, especially $||\mathcal{A}||$, such that the above upper bound on the ensemble variance still holds. From Eq. (31) and replacing $\mathcal{A} \to \mathcal{A}(t)$, it follows that the overwhelming majority of pure states from the ensemble in Eq. (30) feature time-dependent expectation values similar to the time-dependent expectation value with respect to the mixed state ρ.

In Pubs. [P1–P6], the concept of typicality reappears in several places. In particular, dynamical typicality was employed in Pubs. [P1, P3] to drastically reduce the computational cost of the simulations (cf. Sec. II D 2).

B. Fluctuation Theorems

The *second law of thermodynamics* determines in which direction thermodynamic processes are allowed to happen and in which they are not. It can be stated as

$$\mathrm{d}S \geq \frac{\delta Q}{T}\,. \tag{34}$$

Here, δ denotes an imperfect differential, since heat Q, just like work W, is path-dependent and thus no function of state. For a system that exchanges no heat with its surrounding, Eq. (34) becomes $\mathrm{d}S \geq 0$. Thus, in isolated systems the entropy can only increase. Equality holds if the process is reversible.

There are various equivalent formulations of the second law, one of which goes back to Clausius (1854) [74]: *"Heat can never pass from a colder to a warmer body without some other change, connected therewith, occurring at the same time."*[15] In this sense, the second law introduces a kind of irreversibility, which is absent in the microscopic laws of motion.

The second law firmly holds for processes involving macroscopic objects. However, going to smaller and smaller systems, it becomes apparent that the second law is merely of statistical nature. There may be exceedingly rare but possible processes in which the entropy does indeed decrease [75]. These deviations are not random, but themselves obey rigid rules, which are often summarized under the name of fluctuation theorems [8, 75–81]. Fluctuation theorems formulate and to some extent generalize the second law.

This section provides the theoretical background for publication [P4]. To begin, in Sec. II B 1, the general strategy to derive integral and detailed fluctuation theorems is presented. Said strategy is exemplarily applied to the case of an isolated, driven system in Sec. II B 2. Finally, Sec. II B 3 introduces the fluctuation theorem central to Pub. [P4], which concerns the entropy production of a system-bath setup.

[14] This relation neglects the case $i = j = k = l$, which, however, is of order d^{-1} and therefore negligible when $d \gg 1$ [65].

[15] Original quote is in german.

1. Integral and Detailed Fluctuation Theorems

This section introduces *two-point measurement statistics* and presents a strategy to derive generally valid fluctuation theorems for various scenarios. The considerations laid out in the following as well as in Sec. II B 2 closely follow Ref. [8].

Consider an isolated, possibly driven quantum system, i.e., the Hamiltonian may depend on time. In this case, the time-evolution operator reads

$$\mathcal{U}(t) = \exp_+\left[-\mathrm{i} \int_0^t \mathcal{H}(t')\,\mathrm{d}t' \right], \tag{35}$$

where the "+"-subscript denotes proper time-ordering. Further, the observable may be time dependent (in the Schrödinger picture), e.g., due to an external driving. Consequently, eigenvalues and eigenstates of the observable may depend on time as well, i.e., $\mathcal{A}(t)|a_t\rangle = a_t|a_t\rangle$. The initial state is denoted by ρ_0.

One of the central quantities to construct fluctuation theorems is the *joint probability* to measure the eigenvalue a_0 at time $t = 0$ and the eigenvalue a_t at some later time t, after the system has undergone unitary time evolution. This probability is given by

$$\begin{aligned} P(a_t, a_0) &= \mathrm{Tr}[\Pi_{a_t}\mathcal{U}\,\Pi_{a_0}\rho_0\Pi_{a_0}\mathcal{U}^\dagger\Pi_{a_t}] \\ &= R(a_t, a_0)\langle a_0|\rho_0|a_0\rangle\,. \end{aligned} \tag{36}$$

Here, $\Pi_{a_t} = |a_t\rangle\langle a_t|$ denotes the projector into the eigensubspace[16] associated with the eigenvalue a_t. It is straightforward to show that $\sum_{a_t,a_0} P(a_t, a_0) = 1$ by employing the general properties $\Pi_{a_t}^2 = \Pi_{a_t}$ and $\sum_{a_t} \Pi_{a_t} = 1$ of projection operators.

In Eq. (36), the *transition probability* to go from the state $|a_0\rangle$ at $t = 0$ to the state $|a_t\rangle$ at time t reads

$$R(a_t, a_0) = |\langle a_t|\mathcal{U}|a_0\rangle|^2\,. \tag{37}$$

The joint probability can be used to define a new expectation value[17] $\langle\!\langle\cdot\rangle\!\rangle$, which denotes an average with respect to differences in projective measurement outcomes at the initial time $t = 0$ and some final time t. For any quantity $q(a_t, a_0)$, this expectation value is defined as

$$\langle\!\langle q\rangle\!\rangle = \sum_{a_t,a_0} P(a_t, a_0)q(a_t, a_0)\,. \tag{38}$$

In analogy to Eq. (36), a corresponding *time-reversed joint probability* is given by

$$\begin{aligned} P^{\mathrm{tr}}(a_0, a_t) &= \mathrm{Tr}[\Pi_{a_0}\mathcal{U}^\dagger\Pi_{a_t}\rho_0^{\mathrm{tr}}\Pi_{a_t}\mathcal{U}\,\Pi_{a_0}] \\ &= R(a_t, a_0)\langle a_t|\rho_0^{\mathrm{tr}}|a_t\rangle\,. \end{aligned} \tag{39}$$

Here, the initial state ρ_0^{tr} simply evolves backwards in time under $\mathcal{U}^\dagger$. Proceeding from the joint probabilities in Eqs. (36) and (39), the quantity

$$s(a_t, a_0) = \log\frac{P(a_t, a_0)}{P^{\mathrm{tr}}(a_0, a_t)} = \log\frac{\langle a_0|\rho_0|a_0\rangle}{\langle a_t|\rho_0^{\mathrm{tr}}|a_t\rangle} \tag{40}$$

can be defined. Constructing $e^{-s(a_t,a_0)}$ from Eq. (40), an *integral fluctuation theorem* (IFT) of the form

$$\langle\!\langle e^{-s}\rangle\!\rangle = \sum_{a_t,a_0} P(a_t, a_0)e^{-s(a_t,a_0)} = 1 \tag{41}$$

immediately follows from the normalization of the time-reversed joint probabilities $P^{\mathrm{tr}}(a_0, a_t)$.

Exploiting the Jensen inequality $e^{\langle\!\langle x\rangle\!\rangle} \leq \langle\!\langle e^x\rangle\!\rangle$, Eq. (41) yields $\langle\!\langle s\rangle\!\rangle \geq 0$, which resembles the second law of thermodynamics and hints at a close relation between the quantity $s(a_t, a_0)$ and thermodynamic entropy.

Defining a *probability distribution* for continuous s via

$$p(s) = \sum_{a_t,a_0} P(a_t, a_0)\delta(s - s(a_t, a_0)) \tag{42}$$

and a corresponding distribution $p^{\mathrm{tr}}(s)$ for the backwards process, a *detailed fluctuation theorem* can be derived [8], reading

$$\frac{p(s)}{p^{\mathrm{tr}}(-s)} = e^s\,. \tag{43}$$

Thus far, the fluctuation theorems in Eqs. (41) and (43) are completely general without any further restrictions. They are also useless since $s(a_t, a_0)$ and $\langle\!\langle\cdot\rangle\!\rangle$ are basically defined to ensure their validity.

Fluctuation theorems with physical meaning only arise from Eqs. (41) and (43), when $s(a_t, a_0)$ can be exclusively expressed in terms of physical, measurable quantities, i.e., eigenvalues of $\mathcal{A}(0)$ and $\mathcal{A}(t)$. Therefore, suitable $\mathcal{A}(t), \rho_0$ and ρ_0^{tr} need to be found, for which such useful fluctuation theorems emerge. The arguably most prominent yet simple example of a fluctuation theorem is presented in the next section.

---

[16] For simplicity, it is assumed that the eigenvalues a_t are non-degenerate. In the case of degeneracy, additional indices i, j can be introduced to differentiate states with the same a_t.

[17] Not to be confused with the quantum mechanical expectation value $\langle\cdot\rangle$ defined in Eq. (7).

2. Jarzynski Equation and Crooks Relation

This section derives detailed and integral work fluctuation theorems for isolated, driven quantum systems as special cases of the recipe presented in the last section. To set the stage, consider a system described by the Hamiltonian $\mathcal{H}(0)$ in the canonical state $\rho_0 = e^{-\beta\mathcal{H}(0)}/\mathcal{Z}_\beta(0)$ resulting from contact with a heat bath at inverse temperature β. At $t = 0$, the reservoir is removed and the energy is measured for the first time, i.e., $\mathcal{A}(t) = \mathcal{H}(t)$ and $a_0 = E_0$. After the measurement, the system evolves unitarily in time under the time-dependent Hamiltonian $\mathcal{H}(t)$. The second energy measurement is taken at some later time t, i.e., $a_t = E_t$. In the backwards process, the system is initially in the canonical state with respect to $\mathcal{H}(t)$, i.e., $\rho_0^{\mathrm{tr}} = e^{-\beta\mathcal{H}(t)}/\mathcal{Z}_\beta(t)$. The energy is measured at some time t. Then, the state is evolved backwards in time after which the energy is measured again at $t = 0$.
According to Eq. (40), the quantity s evaluates to

$$s(E_t, E_0) = \beta[(E_t - E_0) - \Delta F] \tag{44}$$

simply by plugging in energy eigenstates and respective initial states. Here, $\Delta F = F(t) - F(0)$ denotes the difference in free energy $F(t) = -\beta^{-1}\log\mathcal{Z}_\beta(t)$ between both canonical equilibrium states. Indeed, s only depends on physically measurable quantities.
Since the system is isolated, all changes in energy $E_t - E_0$ can be attributed to work w done on the system by the driving, i.e.,

$$w = E_t - E_0\,. \tag{45}$$

In reference to Eq. (41), the *Jarzynski equation* [76] reads

$$\langle\!\langle e^{-\beta w}\rangle\!\rangle = e^{-\beta\Delta F}\,. \tag{46}$$

Due to Jensen's inequality it follows that

$$\langle\!\langle w\rangle\!\rangle \geq \Delta F\,, \tag{47}$$

which is a common formulation of the second law of thermodynamics when work can be done on/by the system. The expectation value $\langle\!\langle w\rangle\!\rangle$ can also be expressed in terms of standard quantum mechanical expectation values, i.e.,

$$\langle\!\langle w\rangle\!\rangle = \langle\mathcal{H}(t)\rangle_{\rho(t)} - \langle\mathcal{H}(0)\rangle_{\rho(0)}\,. \tag{48}$$

The corresponding detailed fluctuation theorem, called *Crooks relation* [78], is given by

$$\frac{p(w)}{p^{\mathrm{tr}}(-w)} = e^{\beta(w-\Delta F)}\,. \tag{49}$$

3. IFT for Entropy Production in a System-Bath Compound

This section derives the integral fluctuation theorem relevant to Pub. [P4] and discusses a generalizing formulation to arbitrary initial states.
Consider a system-bath setup with Hamiltonian

$$\mathcal{H} = \mathcal{H}_{\mathrm{sys}} + \mathcal{H}_{\mathrm{bath}} + \mathcal{H}_{\mathrm{int}}\,, \tag{50}$$

where $\mathcal{H}_{\mathrm{sys}}$ is the system Hamiltonian and $\mathcal{H}_{\mathrm{bath}}$ is the bath Hamiltonian. System and bath are allowed to interact via an interaction term $\mathcal{H}_{\mathrm{int}}$. The eigenstates of the system and bath are denoted by $|k\rangle$ and $|b\rangle$, respectively. Bath energy eigenvalues are denoted by $\varepsilon^b_{\mathrm{bath}}$. The composite system is initialized in a product state

$$\rho_0 = \rho_{\mathrm{sys}}(0) \otimes e^{-\beta\mathcal{H}_{\mathrm{bath}}}/\mathcal{Z}_\beta \tag{51}$$

of some initial system state $\rho_{\mathrm{sys}}(0)$ and a canonical bath state with $\mathcal{Z}_\beta = \mathrm{Tr}[e^{-\beta\mathcal{H}_{\mathrm{bath}}}]$. The reference state ρ_0^{tr} for the backwards process simply replaces $\rho_{\mathrm{sys}}(0)$ by $\rho_{\mathrm{sys}}(t)$. The observable under consideration is an "entropy-production operator" given by[18]

$$\sigma(t) = -\log\rho_{\mathrm{sys}}(t) + \beta\mathcal{H}_{\mathrm{bath}}\,, \tag{52}$$

which is explicitly time dependent due to the first term. Eigenvalues of the entropy-production operator read

$$\sigma^{j,a}(t) = -\log P^j_{\mathrm{sys}}(t) + \beta\varepsilon^a_{\mathrm{bath}}\,, \tag{53}$$

where $P^j_{\mathrm{sys}}(t)$ are the eigenvalues of $\rho_{\mathrm{sys}}(t)$. Corresponding eigenstates are denoted by $|\sigma^{j,a}(t)\rangle$.
Now that all quantities that enter Eq. (40) have been introduced, said equation yields

$$s(ja, kb) = -\log\frac{P^j_{\mathrm{fin}}}{P^k_{\mathrm{ini}}} + \beta(\varepsilon^a_{\mathrm{bath}} - \varepsilon^b_{\mathrm{bath}})\,, \tag{54}$$

where the short-hand notation $P^k_{\mathrm{ini}} = P^k_{\mathrm{sys}}(0)$ and $P^j_{\mathrm{fin}} = P^j_{\mathrm{sys}}(t)$ was used. As required, s is expressed only in terms of eigenvalues of $\sigma(t)$.
Continuing, s is exponentiated, i.e.,

$$e^{-s(ja,kb)} = \frac{P^j_{\mathrm{fin}}}{P^k_{\mathrm{ini}}}e^{-\beta(\varepsilon^a_{\mathrm{bath}} - \varepsilon^b_{\mathrm{bath}})}\,. \tag{55}$$

Further, the joint probability [Eq. (36)] reads

$$P(ja, kb) = R(ja, kb)P^k_{\mathrm{ini}}e^{-\beta\varepsilon^b_{\mathrm{bath}}}/\mathcal{Z}_\beta\,. \tag{56}$$

[18] In case of further conserved quantities, the second term should be modified accordingly. For instance, $\beta(\mathcal{H}_{\mathrm{bath}} - \mu\mathcal{N}_{\mathrm{bath}})$ when particle number is conserved. Here, μ is the chemical potential.

The resulting IFT then holds by construction, i.e.,

$$\begin{aligned}\langle\langle e^{-s}\rangle\rangle &= \sum_{j,a,k,b} P(ja,kb)e^{-s(ja,kb)} \\ &= \sum_{j,a,k,b} R(ja,kb)P^k_{\mathrm{ini}}\frac{e^{-\beta\varepsilon^b_{\mathrm{bath}}}}{\mathcal{Z}_\beta}\frac{P^j_{\mathrm{fin}}}{P^k_{\mathrm{ini}}}e^{-\beta(\varepsilon^a_{\mathrm{bath}}-\varepsilon^b_{\mathrm{bath}})} \\ &= \sum_{j,a,k,b} R(ja,kb)P^j_{\mathrm{fin}}\frac{e^{-\beta\varepsilon^a_{\mathrm{bath}}}}{\mathcal{Z}_\beta} \\ &= \sum_{j,a} P^j_{\mathrm{fin}}\frac{e^{-\beta\varepsilon^a_{\mathrm{bath}}}}{\mathcal{Z}_\beta} = 1\,.\end{aligned} \tag{57}$$

Here, the double stochasticity of the transition probabilities was utilized, i.e., $\sum_{k,b} R(jk,ab) = 1$, as well as the normalization of respective states in the last step. Hence, an IFT for the entropy production of a system-bath compound has been shown to hold for canonical bath states. Employing the Jensen inequality yields

$$\begin{aligned}\langle\langle s\rangle\rangle &= \langle\sigma(t)\rangle_{\rho(t)} - \langle\sigma(0)\rangle_{\rho(0)} \\ &= \Delta S_{\mathrm{sys}} + \beta\Delta U_{\mathrm{bath}} \geq 0\,.\end{aligned} \tag{58}$$

Here, ΔS_{sys} is the change in von Neumann entropy of the system and ΔU_{bath} accounts for entropy change in the bath due to heat transfer. This equation corresponds to a generalized Clausius inequality.

A naturally arising question is whether an IFT can be derived that also holds for microcanonical (or even pure) bath states. Naively executing the presented strategy with states $\rho_0 = \rho_{\mathrm{sys}}(0)\otimes\rho_{\mathrm{mc}}$ and, e.g., $\rho_0^{\mathrm{tr}} = \rho_{\mathrm{sys}}(t)\otimes\rho_{\mathrm{mc}}$ yields a (trivially) valid relation. However, this relation would not be useful since logarithms of microcanonical occupation probabilities occur, which can not be directly measured (in contrast to the canonical case, in which eigenvalues of $\mathcal{H}_{\mathrm{bath}}$ appear).

At this point, a slight change in perspective proves helpful. Instead of starting from ρ_0 and ρ_0^{tr} and following the above recipe, begin by considering some physical quantity $s_{\mathrm{ph}}(a_t,a_0)$ of interest resembling entropy. An expression for $\langle\langle e^{-s_{\mathrm{ph}}}\rangle\rangle$ is obtained via Eq. (38), i.e.,

$$\langle\langle e^{-s_{\mathrm{ph}}}\rangle\rangle = \sum_{a_t,a_0}\langle a_0|\rho_0|a_0\rangle R(a_t,a_0)\,e^{-s_{\mathrm{ph}}(a_t,a_0)}\,. \tag{59}$$

For an attempt at a microcanonical version of Eq. (57), choose s_{ph} as in Eq. (54) and an initial state $\rho_0 = \rho_{\mathrm{sys}}(0)\otimes\rho_{\mathrm{mc}}$. Now, if a suitable ρ_0^{tr} could be found such that $s_{\mathrm{ph}}(a_t,a_0) = s(a_t,a_0)$ [cf. Eq. (40)], one is in business since in this case automatically $\langle\langle e^{-s_{\mathrm{ph}}}\rangle\rangle = 1$. If no such ρ_0^{tr} can be found, the quantity $\langle\langle e^{-s_{\mathrm{ph}}}\rangle\rangle$ may still be close to unity and, thus, an IFT may still approximately hold due to other mechanisms. Publication [P4] identifies the properties stiffness and smoothness of $R(a_t,a_0)$ as such potential mechanisms.

C. Recursion Method Framework

This section introduces the framework of the *recursion method* [82, 83] mainly employed in Pubs. [P5, P6]. In particular, Sec. II C 1 presents the Lanczos algorithm in Liouville space. Thereafter, in Sec. II C 2, further central quantities are defined and their relation among each other is discussed. Finally, the universal operator growth hypothesis as brought forth in Ref. [84] is presented in Sec. II C 3.

1. Operator Growth in Liouville Space

A pair of Hamiltonian $\mathcal{H}$ and observable[19] $\mathcal{O}$ give rise to a corresponding *autocorrelation function*[20]

$$C(t) = \mathrm{Tr}[\mathcal{O}(t)\mathcal{O}]\,, \tag{60}$$

where the observable evolves in time according to the Heisenberg equation

$$\frac{\mathrm{d}}{\mathrm{d}t}\mathcal{O}(t) = \mathrm{i}\mathcal{L}\mathcal{O}(t)\,. \tag{61}$$

The superoperator $\mathcal{L}$ acting on the observable as $\mathcal{L}\mathcal{O} \equiv [\mathcal{H},\mathcal{O}]$ is called the *Liouvillian*. Just as wave functions evolve under the Hamiltonian, operators evolve under the Liouvillian, i.e., $\mathcal{O}(t) = e^{\mathrm{i}\mathcal{L}t}\mathcal{O}$.

For the following considerations, it is convenient to work directly in the Hilbert space of operators, the *Liouville space*, and denote its elements $\mathcal{O}$ as states $|\mathcal{O})$. The Liouville space is equipped with an infinite-temperature inner product $(\mathcal{O}_1|\mathcal{O}_2) = \mathrm{Tr}[\mathcal{O}_1^\dagger\mathcal{O}_2]$, which induces a norm via $||\mathcal{O}|| = \sqrt{(\mathcal{O}|\mathcal{O})}$. In this manner, the autocorrelation function may be written as $C(t) = (\mathcal{O}|e^{\mathrm{i}\mathcal{L}t}|\mathcal{O})$.

For now, the Liouville space is assumed to be of finite dimension d. This restriction is dropped in Pub. [P5], where infinite systems are considered.

For the purpose of characterizing operator growth, choosing the so-called *Krylov basis* as a basis of the Liouville space is advantageous. The Krylov basis is constructed by considering the observable $\mathcal{O}$ as an initial "seed" and repeatedly applying $\mathcal{L}$. Every newly generated state is orthogonalized with respect to the set of already existing states using a Gram-Schmidt procedure. This process, also referred to as the *Lanczos algorithm*, is detailed in the following [84].

---

[19] To keep notation consistent with Pubs. [P5, P6], the observable is now denoted by $\mathcal{O}$ instead of $\mathcal{A}$.

[20] The autocorrelation function is usually normalized such that $C(0) = 1$.

To begin, consider the normalized initial state $|\mathcal{O}_0) = |\mathcal{O})$, i.e., $(\mathcal{O}|\mathcal{O}) = 1$, and set $b_1 = ||\mathcal{L}\mathcal{O}_0||$ as well as $|\mathcal{O}_1) = \mathcal{L}|\mathcal{O}_0)/b_1$. Then iteratively compute

$$\begin{aligned} |\mathcal{Q}_n) &= \mathcal{L}|\mathcal{O}_{n-1}) - b_{n-1}|\mathcal{O}_{n-2})\,, \\ b_n &= ||\mathcal{Q}_n||\,, \\ |\mathcal{O}_n) &= |\mathcal{Q}_n)/b_n\,. \end{aligned} \tag{62}$$

The representation of the Liouvillian with respect to the Krylov basis is tridiagonal[21], i.e.,

$$L_{mn} = (\mathcal{O}_m|\mathcal{L}|\mathcal{O}_n) = \begin{pmatrix} 0 & b_1 & 0 & \dots \\ b_1 & 0 & b_2 & \\ 0 & b_2 & 0 & \ddots \\ \vdots & & \ddots & \ddots \end{pmatrix}_{mn}\,, \tag{63}$$

where the *Lanczos coefficients* b_n are real, positive numbers output by the algorithm. They can be interpreted as hopping amplitudes in a tight-binding model. In this manner, many physical problems, like the calculation of autocorrelation functions, can be reduced to a one-dimensional (finite or semi-infinite) chain, which is referred to as the *"Mori-chain"* in the title of Pub. [P6].
The coefficients b_n can be used to characterize the complexity growth of operators and as a signature of quantum chaos [84–90].
Rewriting the Heisenberg equation of motion in the Krylov basis yields

$$\partial_t \varphi_n = b_n \varphi_{n-1} - b_{n+1}\varphi_{n+1}\,, \tag{64}$$

where $\varphi_n(t) \equiv \mathrm{i}^{-n}(\mathcal{O}_n|\mathcal{O}(t))$. The initial condition is given by $\varphi_n(0) = \delta_{n0}$ and $\varphi_{-1} \equiv 0$.
The above Eq. (64) takes the form of a discrete Schrödinger equation and can be numerically solved by familiar means of, e.g., exact diagonalization or iterative schemes, cf. Sec. II D 2. The autocorrelation function coincides with the amplitude on the first site, i.e., $C(t) = \varphi_0(t)$.

2. Memory-Kernel, Spectral Function and Moments

Central quantities that appear in Pubs. [P3, P5, P6] besides the autocorrelation function $C(t)$ and the Lanczos coefficients b_n, are the (first) memory-kernel $K(t)$, the spectral function $\Phi(\omega)$ and the moments μ_{2n}. This section introduces the latter three and examines some relations between all five quantities.

[21] With zeros on the diagonal since $\mathcal{O}_0$ is Hermitian.

To start, a few remarks on the relation between the already introduced $C(t)$ and b_n are in order. There exists a (non-linear) one-to-one map between the Lanczos coefficients b_n and the autocorrelation function $C(t)$. Thus, a set of b_n's uniquely determines $C(t)$ and vice versa. However, the correspondence can be quite subtle, i.e., there may be fairly similar dynamics with vastly different Lanczos coefficients. On the other side, similar Lanczos coefficients may lead to quite different dynamics. The autocorrelation function $C(t)$ is obtained from the b_n by solving Eq. (64) with $\varphi_n(0) = \delta_{n0}$ as described above. The other way around, given some $C(t)$, it is possible to reverse-engineer the b_n from $C(t)$ to some extent, see appendix of Pub. [P6].
The *spectral function* $\Phi(\omega)$ is introduced as the Fourier transform of $C(t)$, i.e.,

$$\Phi(\omega) = \int_{-\infty}^{\infty} e^{-\mathrm{i}\omega t}\, C(t)\,\mathrm{d}t\,. \tag{65}$$

The *moments* μ_{2n} of the autocorrelation function are defined by

$$\mu_{2n} = \frac{\mathrm{d}^{2n}}{\mathrm{d}t^{2n}} C(t)\Big|_{t=0} \tag{66}$$

or, respectively, in terms of the spectral function

$$\mu_{2n} = \int \omega^{2n}\, \Phi(\omega)\,\mathrm{d}\omega\,. \tag{67}$$

Since $C(t)$ is an even function, all odd moments necessarily vanish. The information contained in the moments μ_{2n} is identical to the information conveyed by the Lanczos coefficients b_n. The two quantities can be converted into each other as follows.
From moments to Lanczos coefficients:
To calculate the Lanczos coefficients b_n from a given set of moments μ_{2n}, first define $c_n = \mu_{2n}/\mu_0$. Then, compute determinants of certain matrices constructed from the normalized moments c_n, i.e., $B_n = \det(c_{i+j})_{0\le i,j\le n-1}$ where $n \ge 2$ and $B_0 = B_1 = 1$ as well as $C_n = \det(c_{i+j+1})_{0\le i,j\le n-1}$, where $n \ge 1$ and $C_0 = 1$. The Lanczos coefficients are obtained as fractions of these determinants, i.e.,

$$b_{2n}^2 = \frac{B_{n+1}C_{n-1}}{B_n C_n}\,, \quad b_{2n-1}^2 = \frac{B_{n-1}C_n}{B_n C_{n-1}}\,. \tag{68}$$

From Lanczos coefficients to moments:
Take the representation L of the Liouvillian $\mathcal{L}$ in the Krylov space spanned by the vectors generated by the Lanczos algorithm, cf. Eq. (63). The moments μ_{2n} can be easily read off as the upper-left element of even powers $2n$ of the matrix L, i.e.,

$$\mu_{2n} = (L^{2n})_{00}\,. \tag{69}$$

The quantities $C(t)$, $\Phi(\omega)$ and μ_{2n} all depend linearly on one another, whereas the respective relations to b_n are highly non-linear.
Next, the concept of a *memory-kernel* is introduced, which appears in Pub. [P3]. Given some reference dynamics $C(t)$, its memory-kernel $K(t)$ is implicitly defined by the integro-differential equation

$$\frac{\mathrm{d}}{\mathrm{d}t}C(t) = -\int_0^t K(t-t')C(t')\,\mathrm{d}t' \,. \tag{70}$$

The map between $C(t)$ and $K(t)$ is bijective. Hence, it is possible to calculate the (unique) memory-kernel $K(t)$ solely from the function $C(t)$ and, vice versa, the function $C(t)$ can be calculated given the memory-kernel $K(t)$ and some initial value $C(0)$. Loosely speaking, the memory-kernel captures in which manner a system remembers its history.
Iterating the above equation by considering the memory-kernel of the "first" memory-kernel $K(t)$ and so on, yields a sequence of memory-kernels $\mathcal{K}_n$ connected by a set of coupled Volterra equations, i.e.,

$$\frac{\mathrm{d}}{\mathrm{d}t}\mathcal{K}_n(t) = -\int_0^t \mathcal{K}_{n+1}(t-t')\mathcal{K}_n(t')\,\mathrm{d}t' \,. \tag{71}$$

Here, $n = 0, 1, 2, ...$, $\mathcal{K}_0(t) \equiv C(t)$ and $\mathcal{K}_1(t) \equiv K(t)$. Taking the Laplace transform[22] of Eq. (71) yields

$$\Phi_n(s) = \frac{\mathcal{K}_n(0)}{s + \Phi_{n+1}(s)} \,, \tag{72}$$

where

$$\Phi_n(s) = \int_0^\infty e^{-st}\mathcal{K}_n(t)\,\mathrm{d}t \tag{73}$$

denotes the Laplace transform of $\mathcal{K}_n(t)$ and s is a complex argument.
An alternative way to obtain the n-th memory-kernel is by erasing the first n columns and rows of the Liouvillian matrix in Eq. (63). The resulting matrix represents the operator $\mathcal{L}_n$ (by definition of $\mathcal{L}_n$).
It can be shown that the n-th memory-kernel is proportional to the autocorrelation function of $\mathcal{O}_n$ evolving under $\mathcal{L}_n$. In particular,

$$\mathcal{K}_n(t) = b_n^2(\mathcal{O}_n|e^{\mathrm{i}\mathcal{L}_n t}|\mathcal{O}_n) \,, \tag{74}$$

which entails that $\mathcal{K}_n(0) = b_n^2$, since $|\mathcal{O}_n)$ is normalized.

[22] Expressions for Laplace transforms of derivatives and convolutions can be found in respective tables.

Expanding Eq. (72) and setting $s = \mathrm{i}\omega$ yields

$$\Phi_0(\mathrm{i}\omega) = \cfrac{1}{\mathrm{i}\omega + \cfrac{b_1^2}{\mathrm{i}\omega + \cfrac{b_2^2}{\mathrm{i}\omega + ...}}} \,. \tag{75}$$

This continued fraction terminates at b_d^2 for finite, d-dimensional systems. The expression in Eq. (75) is related to the spectral function via

$$\Phi(\omega) = 2\mathrm{Re}[\Phi_0(\mathrm{i}\omega)] \,. \tag{76}$$

It can be shown that the spectral function takes the functional form

$$\Phi(\omega) \propto [P_d(\omega^2)]^{-1} \,, \tag{77}$$

where $P_d(\omega^2)$ denotes an even polynomial of order ω^{2d}.

3. Operator Growth Hypothesis

This section presents the *universal operator growth hypothesis* as brought forth in Ref. [84].
The hypothesis concerns the asymptotic behavior of the Lanczos coefficients b_n. It basically states that in generic, non-integrable systems the Lanczos coefficients of local, few-body observables grow asymptotically linear, i.e., above some n the growth is given by

$$b_n \sim \alpha n + \gamma + o(1) \,, \tag{78}$$

where $\alpha > 0$ and γ are real constants and $o(g_n)$ denotes some real sequence f_n with $\lim_{n\to\infty} |f_n/g_n| = 0$.
In the special case of a one-dimensional system, the asymptotic growth is sublinear due to an additional logarithmic correction i.e.,

$$b_n \sim A\,\frac{n}{\ln n} + o(n/\ln n) \,, \tag{79}$$

where $A > 0$ is a real constant. The above equations entail that the b_n can never grow faster than linear, e.g., quadratically or exponentially.
These bounds on fastest possible, asymptotic growth ultimately originate from a powerful statement on the behavior of the spectral function $\Phi(\omega)$ for large ω.
The spectral function usually features non-vanishing high-frequency tails for generic many-body systems.
By means of geometric arguments, these tails can be rigorously bounded by an exponential function such that

$$\Phi(\omega) \leq K e^{-\kappa|\omega|} \tag{80}$$

for some adequately chosen constant $K > 0$ and decay constant $\kappa > 0$, which is related to the geometry of the system [91].

It can be shown that spectral functions actually featuring exponentially decaying tails give rise to asymptotically linear growth in the Lanczos coefficients [92, 93]. Therefore, the operator growth hypothesis is equivalent to an exponentially decaying spectral function and basically states that the Lanczos coefficients should grow as fast as "permitted by the geometry". Rigorous lower bounds exist as well [94].
The operator growth hypothesis has been probed in several works, testing its validity numerically [95, 96] as well as analytically [84]. Publication [P5] adds to this list by numerically checking the hypothesis for systems in the thermodynamic limit. Further, the numerical experiments in Pub. [P6] assume the validity of the hypothesis.

D. Numerical Experiments

Experiments are an indispensable mechanism to confirm or reject physical theories and arguably constitute the backbone of all of science.
In the last decades, the field of quantum statistical mechanics has experienced a sort of renaissance, not last due to tremendous progress on the experimental side. In particular, experiments probing essentially isolated quantum systems have seen rapid advancements. Ultracold atoms, for instance, can be controlled with unprecedented accuracy [10–14, 97–101], enabling observations of, e.g., quantum phase transitions, Bose-Einstein condensation and quantum magnetism.
The publications [P1, P3–P6] feature *numerical experiments*, i.e., simulations of quantum systems on a computer. One major advantage of numerical simulations is the full control over all microscopic degrees of freedom. For example, systems can be easily prepared in an energy eigenstate.
This section provides the background to the numerical simulations presented in Pubs. [P1, P3–P6]. In Sec. II D 1, basic spin models are introduced, which are heavily featured in the publications. Numerical methods, e.g., to solve the Schrödinger equation, are discussed in Sec. II D 2.

1. Quantum Spin Models

Interacting quantum spins on lattices are arguably one of the simplest examples of many-body quantum systems. It is (at least conceptually) relatively straightforward to simulate these spin systems on a computer. Despite their seeming simplicity, spin systems are rich in complexity and decades worth of research have been conducted. This research includes, for instance, physical questions of transport and relaxation [102], modeling of magnetic molecules [103, 104] as well as issues of purely mathematical nature [105].

Publications [P1, P3–P6] feature spin systems in some form as numerical testbeds for proposed theories. Thus, the basics of quantum spin and most commonly encountered models are discussed in the following.
For starters, a single spin of spin quantum numbers s is considered. This (non-negative) number s can either be integer or half-integer, classifying the particle carrying the spin as either a fermion or a boson. The spin of the particle is mathematically represented by operators $\vec{s} = (s^x, s^y, s^z)$. Importantly, the components do not commute and instead satisfy the commutation relation

$$[s^i, s^j] = \mathrm{i}\,\varepsilon_{ijk} s^k\,, \tag{81}$$

where ε_{ijk} is the antisymmetric Levi-Civita symbol and $i, j, k \in \{x, y, z\}$ [sum over k included in Eq. (81)].
This relation resembles the commutation relation of angular momentum, hinting at the close connection between the two quantities. As a consequence, spin is sometimes referred to as the intrinsic angular momentum of a particle.
Since the spatial components of the spin operator do not commute, a single direction, usually the z-direction, is chosen as an axis of reference. Then, a basis of the Hilbert space of a single spin is spanned by the eigenstates $|s, m_s\rangle$ of the s^z-operator. The magnetic quantum number $m_s \in \{-s, -s+1, ..., s-1, s\}$ attains values from $-s$ to s in unit steps. Thus, the Hilbert-space dimension is $d = 2s + 1$. Since $[\vec{s}^{\,2}, s^z] = 0$, the basis states are also eigenstates of the total spin.

$$\vec{s}^{\,2}|s, m_s\rangle = s(s+1)|s, m_s\rangle \tag{82}$$
$$s^z|s, m_s\rangle = m_s|s, m_s\rangle \tag{83}$$

Raising and lowering operators can be introduced as $s^\pm = s^x \pm \mathrm{i}s^y$. They act on basis states as follows: $s^\pm|s, m_s\rangle = \sqrt{s(s+1) - m_s(m_s \pm 1)}|s, m_s \pm 1\rangle$.
Thus far, only a single spin has been considered. The next step is to allow multiple spins, arranged on L lattice sites, that may interact with one another. The mathematical structure that is used to describe quantum systems of many particles is the product Hilbert space

$$\mathscr{H} = \bigotimes_{\ell=1}^{L} \mathscr{H}_\ell\,. \tag{84}$$

The dimension of the product Hilbert space equals the product of the local dimensions, i.e.,

$$\dim \mathscr{H} = \prod_{\ell=1}^{L} \dim \mathscr{H}_\ell\,. \tag{85}$$

If all spins have the some spin quantum number s, simply $\dim \mathscr{H} = (2s+1)^L = d^L$.

A natural basis of the product Hilbert space is inherited from the local bases. The so-called *Ising basis* (or product basis) is given by $\{|m\rangle\} \equiv \{|m_1 m_2 ... m_L\rangle\}$.
The local spin operators are "inflated" to the whole Hilbert space, e.g., an operator on site ℓ reads

$$s_\ell^{x,y,z} = ... \otimes 1 \otimes \underbrace{s^{x,y,z}}_{\ell-\text{th site}} \otimes 1 \otimes ... \,, \tag{86}$$

where 1 denotes the identity and the one-particle operator $s^{x,y,z}$ acts on site ℓ. Operators acting on different sites naturally commute.
In the following, common models of interacting spins are presented. The Hamiltonian of the *Heisenberg model* [106] (also called *XXZ model*) is given by

$$\begin{aligned} \mathcal{H}_{\text{XXZ}} &= \sum_{\ell,\ell'} J_{\ell\ell'} [s_\ell^x s_{\ell'}^x + s_\ell^y s_{\ell'}^y + \Delta s_\ell^z s_{\ell'}^z] \\ &= \sum_{\ell,\ell'} J_{\ell\ell'} [(s_\ell^+ s_{\ell'}^- + s_\ell^- s_{\ell'}^+)/2 + \Delta s_\ell^z s_{\ell'}^z] \,. \end{aligned} \tag{87}$$

Here, the lattice geometry is expressed via the interaction matrix $J_{\ell\ell'}$. Geometries featured in the publications are simple chains, ladders and also a wheel-like structure. The interaction can be either ferromagnetic or antiferromagnetic, depending on the sign of $J_{\ell\ell'}$. In these cases, two coupled spins in the ground state either align or anti-align. This may lead to complicated *frustration effects* when spins can not simultaneously meet the demands of all their neighbors [107, 108].
The Heisenberg Hamiltonian can be rewritten with raising and lowering operators, see second line in Eq. (87). In this form, it can be seen that the first $xxyy$-term effectively transports magnetization through the system. This term is sometimes referred to as the "kinetic term". Consequently, the second zz-term is sometimes called the "potential term".
The *anisotropy* Δ distinguishes the z-direction. Spin transport in the Heisenberg chain is generally believed to be diffusive for $\Delta > 1$ and ballistic for $\Delta < 1$ [102].
The Heisenberg model possesses certain symmetries. For instance, the total magnetization $s^z = \sum_\ell s_\ell^z$ in z-direction is a conserved quantity since $[\mathcal{H}, s^z] = 0$. For $\Delta = 1$, the model additionally possesses SU(2)-symmetry and the total spin $\vec{s} = \sum_\ell \vec{s}_\ell$ is conserved as well, i.e., $[\mathcal{H}, \vec{s}^{\,2}] = 0$. Depending on the lattice geometry, further symmetries may exist, e.g., translational invariance or point group symmetries. These symmetries can be exploited to solve the Schrödinger equation more easily, see Sec. II D 2.

A further model featured in the publications is the *Ising model* [109], whose Hamiltonian reads

$$\mathcal{H}_{\text{Ising}} = \sum_{\ell,\ell'} J_{\ell\ell'} s_\ell^x s_{\ell'}^x + h_\ell s_\ell^z \,. \tag{88}$$

The local *Zeeman terms* $h_\ell s_\ell^z$ take interaction with a magnetic field into account.
Everything discussed thus far holds true for any spin quantum number s. However, the systems featured in the publications all have $s = 1/2$, which constitutes the "most quantum" case[23], since a measurement of, e.g., the z-component can only yield two results, either "spin-up" or "spin-down". Further, $s = 1/2$ corresponds to the smallest local dimension $d = 2$ and is thus easier to manage than larger values of s.
For the spin quantum number $s = 1/2$, the spin operators represented in the natural basis $|1/2, 1/2\rangle \equiv |\uparrow\rangle$, $|1/2, -1/2\rangle \equiv |\downarrow\rangle$ are related to the Pauli matrices via $s^{x,y,z} = \sigma^{x,y,z}/2$ where

$$\sigma^x = \begin{pmatrix} 0 & 1 \\ 1 & 0 \end{pmatrix} , \; \sigma^y = \begin{pmatrix} 0 & -\mathrm{i} \\ \mathrm{i} & 0 \end{pmatrix} , \; \sigma^z = \begin{pmatrix} 1 & 0 \\ 0 & -1 \end{pmatrix} . \tag{89}$$

Depending on the model, spin-1/2 systems can be mapped to either *free* or *interacting fermions* via a Jordan-Wigner transformation [110]. Further, a description as *hard-core bosons* appears in Pub. [P4].

2. Numerical Methods

The landscape of numerical techniques to tackle many-body quantum systems is vast. This section discusses a selection of methods, including and particularly focusing on those which were employed to obtain the numerical results presented in the publications [P1, P3–P6].
To work with states and operators on a computer, they need to be represented as matrices and vectors, respectively. Components of the Hamiltonian matrix are given by $H_{\sigma\sigma'} = \langle\sigma|\mathcal{H}|\sigma'\rangle$ and components of the state vector by $\psi_\sigma = \langle\sigma|\psi\rangle$, both with respect to some basis $\{|\sigma\rangle\}$. In many scenarios, the aforementioned Ising basis constitutes a convenient working basis.
Maybe the most straightforward way to numerically handle many-body quantum systems is the method of *exact diagonalization* (ED). Within this approach, the time-independent Schrödinger equation [cf. Eq. (5)] is solved directly by computing the eigenstates $|n\rangle$ and corresponding eigenvalues E_n of the Hamiltonian matrix, i.e.,

$$\mathcal{H}\,|n\rangle = E_n\,|n\rangle \,. \tag{90}$$

[23] The classical limit is obtained by taking $s \to \infty$, $\hbar \to 0$ while keeping $\hbar\sqrt{s(s+1)}$ constant.

Both $|n\rangle$ and E_n are independent of the chosen working basis. In practice, the diagonalization routine itself is implemented from standard linear algebra packages like, e.g., LAPACK.

With the knowledge of all energy eigenvalues and eigenstates, dynamical and thermodynamic quantities [cf. Sec. II A 1] can be calculated exactly - the dynamics, in principle, even for arbitrarily long times.

One major drawback of ED is that its applicability is restricted to comparatively small systems. The reasons for this are twofold. On the one hand, standard diagonalization routines have a quite demanding computational complexity of $\mathcal{O}(d^3)$, where d total dimension. On the other hand, even before that and more severe, storing the matrix in memory can be challenging. Thus, the method of ED is only practically feasible for matrices up to a dimension of about $10^5 \times 10^5$. For instance, 18 spins 1/2 ($d \approx 2 \cdot 10^5$) require about 500 GB of memory if no symmetries are used. Therefore, ED is oftentimes employed when the exact knowledge of eigenvalues and eigenstates is of absolute necessity, or when going to larger systems brings no further benefit. The publications [P4] and [P6] employ ED.

For systems beyond the range of ED, the time-dependent Schrödinger equation can be tackled by a variety of approximate numerical techniques, which commonly rely on finding an approximation $\mathcal{U}'(\delta t)$ to the time evolution operator $\mathcal{U}(\delta t) = e^{-\mathrm{i}\mathcal{H}\delta t}$. The approximate solution is then obtained by iteratively propagating the state in time, i.e.,

$$|\psi(t+\delta t)\rangle \approx \mathcal{U}'(\delta t)|\psi(t)\rangle\,. \tag{91}$$

Here, δt denotes the time step, which should be chosen sufficiently small to maintain a certain degree of accuracy, but still large enough to reach the desired endpoint of the simulation in an acceptable amount of time. Some widely popular methods that follow this strategy are, e.g., Runge-Kutta expansions [111, 112], Suzuki-Trotter decompositions [113, 114] or Krylov-space techniques [115].

The method that is most heavily employed in the publications presented later on is based on Chebyshev polynomials [116–118]. Therefore, this approach is discussed in more detail in the following.

An arbitrary but well-behaved function $f(x)$ can be expanded into a polynomial series $f(x) = \sum_{n=0}^{\infty} \alpha_n P_n(x)$, which is always possible if the polynomials $P_n(x)$ fulfill some orthogonality relation. All types of (orthogonal) polynomials can, in principle, be used for such an expansion. However, it turns out that in many scenarios (including the one at hand) a certain set of polynomials is best suited [119]. These are the Chebyshev polynomials of the first kind denoted by $T_n(x)$ [120].

All properties of Chebyshev polynomials listed in the following can be found in Ref. [121]. The Chebyshev polynomials are orthogonal with respect to the weighted scalar product

$$\langle T_n, T_m\rangle = \int_{-1}^{1} \frac{T_m(x)T_n(x)}{\pi\sqrt{1-x^2}}\,\mathrm{d}x = \delta_{mn} w_n \tag{92}$$

with $w_n = (\delta_{n0}+1)/2$. A recursive relation that comes in handy later is given by

$$T_n(x) = 2xT_{n-1}(x) - T_{n-2}(x) \tag{93}$$

with $T_0(x) = 1$ and $T_1(x) = x$. A closed expression also exists, i.e., $T_n(x) = \cos(n \arccos x)$. A function $f(x)$ expanded into Chebyshev polynomials reads

$$f(x) = c_0 + 2\sum_{n=1}^{\infty} c_n T_n(x)\,, \tag{94}$$

where $c_n = \langle T_n, f\rangle$. For the case at hand, not a real-valued function needs to be expanded, but a complex-valued matrix exponential. This is done by rescaling the spectrum of the Hamiltonian to the interval $[-1, 1]$. Let $E_{\max}$ and $E_{\min}$ denote the extremal eigenvalues of $\mathcal{H}$. Define $a = (E_{\max} - E_{\min})/(2-\epsilon)$ and $b = (E_{\max} + E_{\min})/2$ and set $\mathcal{H}' = (\mathcal{H} - b)/a$. Extremal eigenvalues can be obtained without full exact diagonalization via, e.g, the Lanczos algorithm [122]. The parameter ϵ is a small safety parameter that ensures that the rescaled spectrum lies well within the interval $[-1, 1]$. The expansion of the time-evolution operator is then given by

$$e^{-\mathrm{i}\mathcal{H}\delta t} = e^{-\mathrm{i}b\delta t}\big[c_0(a\delta t) + \sum_{n=1}^{\infty} c_n(a\delta t)T_n(\mathcal{H}')\big] \tag{95}$$

with coefficients

$$c_n(a\delta t) = \int_{-1}^{1} \frac{T_n(x)e^{-\mathrm{i}ax\delta t}}{\pi\sqrt{1-x^2}}\,\mathrm{d}x = (-\mathrm{i})^n \mathcal{J}_n(a\delta t)\,, \tag{96}$$

where $\mathcal{J}_n$ denote Bessel functions of the first kind. Since the coefficients c_n only depend on the time step δt, but not on time itself, they only have to be computed once. Applying Eq. (95) to a state boils down to calculating $T_n(\mathcal{H}')|\psi\rangle$ for various n, which can be done recursively using Eq. (93). Terminating the sum in Eq. (95) at $M-1$ gives the M-th order Chebyshev approximation of the time-evolution operator.

In most pure-state propagation schemes, the central operation is the application of the Hamiltonian to a state. This corresponds to matrix-vector-multiplications, which can be heavily parallelized.

However, as mentioned above, even storing the matrix in memory can be a bottleneck and push larger systems out of reach[24].
In practice, it is possible to circumvent this problem of limited memory to a certain degree. Since it is known how the spin operators act on basis states, the action of the Hamiltonian $\mathcal{H}$ on some state $|\psi\rangle$ can be directly implemented[25] without storing $\mathcal{H}_{\sigma\sigma'}$ in memory.
As an example, consider the Heisenberg Hamiltonian in Eq. (87) for a two-site spin-1/2 system. The kinetic term swaps respective components of the state vector (or gives zero), whereas the zz-coupling term simply yields additional factors in the components of $|\psi\rangle$, i.e.,

$$\begin{aligned} s_1^z s_2^z |m_1 m_2\rangle &= m_1 m_2 |m_1 m_2\rangle \\ 2(s_1^x s_2^x + s_1^y s_2^y)|m_1 m_2\rangle &= (1-\delta_{m_1 m_2})|m_2 m_1\rangle \end{aligned} \tag{97}$$

In this manner, there is no need to store the Hamiltonian matrix at all and the matrix elements (or contributions thereto) are calculated "on the fly". This massively reduces the memory usage as only a handful of vectors need to be stored.
Thus far, only time evolution of pure states was discussed. However, it is sometimes desirable to likewise evolve a mixed state ρ in time. An example relevant to this thesis may be that ρ is a product state of an excited system state $|\uparrow\rangle_{\text{sys}}$ and mixed bath state ρ_{bath}.
To this end, the in Sec. II A 4 presented concept of dynamical typicality comes in handy. Exploiting typicality, the full statistical ensemble ρ can be replaced by a pure state that yields more or less the same time-dependent expectation value with an induced error $\epsilon \propto 1/\sqrt{d_{\text{eff}}}$. In this manner, efficient time-evolution schemes for pure states can be practically employed for mixed states as well.
To further increase performance, symmetries possessed by the system may be exploited to effectively reduce the dimension of the problem. For instance, the Heisenberg model conserves magnetization and eigenstates can be labeled with the good quantum number S^z. Representing the Hamiltonian in a symmetry-adapted basis leads to a block-diagonal matrix structure [123].
In this manner, only the individual blocks need to be diagonalized (or used for propagation in time), which greatly reduces numerical effort. Further commonly occurring symmetries include conservation of total spin [SU(2)-symmetry], translational invariance or other point-group symmetries depending on the geometry.

To complete the picture on time evolution, some additional numerical methods are briefly mentioned that conceptually go beyond merely approximating the time-evolution operator.
The numerical linked-cluster expansion (NLCE) [124, 125], for instance, allows to calculate some quantities in the thermodynamic limit up to some time[26].
Even more involved methods compress the information in the state itself, like the density matrix renormalization group (DMRG), which is routinely formulated in terms of matrix product states (MPS) [126, 127].
To end this section, the numerical details for the computation of the Lanczos coefficients b_n are discussed. The Lanczos algorithm that yields the b_n corresponding to some $C(t)$ has been presented in Sec. II C 1.
In practice, a suitable basis of the Liouville space is needed. A convenient choice is the set of Pauli strings $\{|\mathcal{P}\rangle\}$, i.e., $\mathcal{P} = \otimes_\ell \mathcal{P}_\ell$ with $\mathcal{P}_\ell \in \{1_\ell, \sigma_\ell^x, \sigma_\ell^y, \sigma_\ell^z\}$. The commutation relation of the Pauli matrices $\sigma^a\sigma^b = \delta_{ab}1 + \mathrm{i}\epsilon_{abc}\sigma^c$ [sum over c included, also cf. Eq. (81)] ensures that the Pauli strings are orthonormal, i.e., $(\mathcal{P}|\mathcal{P}') = \delta_{\mathcal{P}\mathcal{P}'}$. Thus, any operator may be written as $|\mathcal{O}) = \sum_\alpha c_\alpha |\mathcal{P}_\alpha)$.
The commutator of two operators then boils down to the commutator of Pauli strings, which evaluates to $[\mathcal{P}, \mathcal{P}'] = (1-(-1)^{\chi(\mathcal{P},\mathcal{P}')})\mathcal{P}\mathcal{P}'$, where $\chi(\mathcal{P},\mathcal{P}')$ counts the number of sites on which $\mathcal{P}_\ell \neq \mathcal{P}'_\ell$ when both $\mathcal{P}_\ell$, $\mathcal{P}'_\ell$ are not the identity 1_ℓ [96].
A representation of a finite[27] Pauli string that reduces computational cost is given by [128]

$$\mathcal{P} = \mathrm{i}^\delta (-1)^\epsilon (\sigma_1^z)^{v_1} (\sigma_1^x)^{w_1} \otimes \ldots \otimes (\sigma_n^z)^{v_n} (\sigma_n^x)^{w_n} . \tag{98}$$

The newly introduced parameters are binary, i.e., $\delta, \epsilon, v_k, w_k \in \{0,1\}$, such that a Pauli string of length n can be represented by two binary vectors v, w and two binary digits δ, ϵ. Commutators and other operations can then be simplified and broken down to this binary level as well [84, 128]. In this manner, the Lanczos algorithm can be efficiently implemented.

[24] Hamiltonian matrices of spin-based systems often exhibit some sparseness, which, however, only pushes the limits of practicality to some extent.
[25] With this knowledge, the matrix representation is computed in the first place.
[26] NLCE in itself is not a method for time evolution. It relies on other time-evolution schemes, e.g., the ones presented above.
[27] The implementation based on Pauli strings and binary numbers can be generalized to infinite systems by exploiting translational invariance [84].

III. Guide to Publications

This section gives an overview of the work that has been published in Pubs. [P1–P6]. Each of the following sections corresponds to a respective paper, with the only exception of Pubs. [P1] and [P2], which share a section due to their similarity.
The mathematical notation largely coincides with the notation in the theoretical background section. When inconsistencies are unavoidable, the notation from the publications is preferred.
Publications [P1], [P2] and [P3] rely mostly on theoretical concepts outlined in Sec. II A. Publication [P4] concerns a particular fluctuation theorem and thus directly relates to Sec. II B. Publications [P5] and [P6] are formulated in the framework of the recursion method and make use of concepts introduced in Sec. II C. All publications, except Pub. [P2], in some form employ numerical methods presented in Sec. II D.
The following sections are structured as follows. First, some context and motivation for the presented work is given. Thereafter, the main results are laid out and explained in a necessarily shortened manner. Citations relating to other works are kept to a minimum here. For details, additional results and further references the reader is always referred to the respective publication.

[P1]. Compelling Bounds on Equilibration Times - the Issue with Fermi's Golden Rule (including [P2])

While general results in the form of Eq. (24) oftenly ensure the occurrence of equilibration in the very long run under relatively mild conditions concerning the Hamiltonian, observable and initial state, they hardly entail any relevant information on the "true" equilibration time T_{eq}, which is usually much shorter. That is to say, the times at which these results establish equilibration are "unrealistically long" compared to the times at which stationary dynamics have evidently already set in. This shortcoming is partly due to the reliance on as few assumptions as possible in order to obtain results that are as generally applicable as possible. Thus, fine-tuned, "pathological" setups that exhaust the unsatisfactorily large bounds are inevitably included.
Consequently, improved bounds on equilibration times based on additional, physically plausible conditions that capture the actual, physical state of affairs are much sought after. Such a bound (based on additional conditions on all $\mathcal{H}, \mathcal{A}$ and ρ) has been suggested by García-Pintos et al. in Ref. [129] [hereafter referred to as the "García-Pintos bound" (GPB)].
The paper *"Compelling Bounds on Equilibration Times – the Issue with Fermi's Golden Rule"* [P1] numerically probes the GPB and finds that it is not applicable/useful in the limit of weak interactions (at least) for the specific setup at hand, which shares some features with standard solid-state systems like periodicity and locality. Unrelated to the GPB, the presented numerics shed some light on the breakdown of standard quantum master equations in the "superweak" coupling limit, which occurs for finite-sized baths.
The *"Comment on 'Equilibration Time Scales of Physically Relevant Observables'"* [P2] presents two standard scenarios and one concrete, spin-based example (all entailing slow, exponential dynamics) in which the GPB is analytically shown to not be applicable.
Both publications begin with a brief recapitulation of the main results of Ref. [129]. In short, the GPB is an explicit expression for a point in time denoted by T_{eq}, at which for all $T \gg T_{\mathrm{eq}}$ it holds that $\overline{D}_T \ll 1$, where $D(t) \propto [\langle \mathcal{A}(t) \rangle - \overline{\mathcal{A}}]^2$, i.e.,

$$T_{\mathrm{eq}} = \frac{\pi a ||\mathcal{A}||^{1/2} Q^{5/2}}{\sqrt{\partial_t^2 \langle \mathcal{A}(t) \rangle|_{t=0}}} \,. \tag{99}$$

Here, $||\mathcal{A}||$ denotes the largest absolute eigenvalue and a, Q are defined below. Evidently, the GPB links T_{eq} to the initial "curvature" of the expectation value dynamics $\partial_t^2 \langle \mathcal{A}(t) \rangle|_{t=0}$. An actual, concrete bound on the equilibration time only arises from Eq. (99) if the numerator can be shown to be in an adequate sense small or at least bounded. This is a pivotal feature on which the "predictive power" of the GPB hinges. The crucial quantities in the numerator are a and Q, which are both quite involved functions of $\mathcal{H}, \mathcal{A}$ and ρ. Concretely, they depend on the probability distribution

$$p_{jk} \begin{cases} \propto |\rho_{jk} \mathcal{A}_{jk}| \,, & \text{for } E_j \neq E_k \\ = 0 \,, & \text{for } E_j = E_k \end{cases} \tag{100}$$

with $\sum_{j,k} p_{jk} = 1$. Here, energy eigenvalues E_j, E_k correspond to energy eigenstates $|j\rangle, |k\rangle$ and matrix elements are abbreviated as $\rho_{jk} = \langle j|\rho|k\rangle$ and $\mathcal{A}_{jk} = \langle j|\mathcal{A}(0)|k\rangle$. For practicality, the probability distribution p_{jk} is "coarse-grained" into a histogram $w(G)$, where G denotes the energy gap. The quantities a and Q that eventually enter the GPB are now defined as

$$a = w_{\max} \sigma_G \,, \quad Q = \sum_{j,k: E_j \neq E_k} \frac{|\rho_{jk} \mathcal{A}_{jk}|}{||\mathcal{A}||} \,, \tag{101}$$

where $w_{\max}$ is the maximum of $w(G)$ and σ_G the standard deviation. As it is practically impossible to calculate a from its definition for many-body quantum systems, the authors of Ref. [129] instead resort to an assumption. They argue that $a \sim 1$ may be expected for $w(G)$ that are "unimodal", which means that $w(G)$ essentially consists of one central elevation like a Gaussian or a box distribution, etc.

For the first standard scenario in which the numerator in Eq. (99) diverges, consider the expectation value of an observable $\mathcal{A}$ that is conserved with respect to an unperturbed Hamiltonian, i.e., $[\mathcal{H}_0, \mathcal{A}] = 0$. A weak, symmetry-breaking perturbation $\lambda\mathcal{V}$ commonly[28] leads to slow, (mono-)exponential dynamics, i.e.,

$$\langle \mathcal{A}(t) \rangle = [\langle \mathcal{A}(0) \rangle - \overline{\mathcal{A}}] e^{-t/\tau_{\mathrm{rel}}} + \overline{\mathcal{A}}\,, \tag{102}$$

where $\tau_{\mathrm{rel}} = r\lambda^{-2}$ and r is a real, positive number that depends on $\mathcal{H}_0$ and $\mathcal{V}$. Replacing the time derivatives in the denominator of Eq. (99) by a commutator $\mathrm{i}[\mathcal{H}, \cdot\,]$ with $\mathcal{H} = \mathcal{H}_0 + \lambda\mathcal{V}$ and exploiting the well-justified assumption $T_{\mathrm{eq}} \geq \tau_{\mathrm{rel}}$ yields a lower bound on the numerator in Eq. (99), i.e.,

$$\pi a ||\mathcal{A}||^{1/2} Q^{5/2} \geq r \frac{\sqrt{c_1\lambda + c_2\lambda^2}}{\lambda^2}\,. \tag{103}$$

The r.h.s. clearly diverges in the limit of weak interactions $\lambda \to 0$. Consequently, either a or Q (or both) in the numerator diverge as well.

Exponential dynamics also commonly occur when slow Fourier modes in sufficiently large systems are considered. In this case, a similar lower bound on the numerator is derived, which diverges in the limit of small wave numbers $k \to 0$. This is the second standard scenario presented in Pub. [P2] and will not be laid out in detail here.

The final takeaway of Pub. [P2] is that it is probably the quantity a that diverges and not Q. This conclusion is drawn by considering a concrete, physical example, which is nonetheless simple enough to allow for analytical analysis. Thus, the assumption $a \sim 1$ by the authors of Ref. [129] is likely to be unjustified in many physically common scenarios, even if $w(G)$ is unimodal.

The above results are substantiated by the numerical analysis presented in Pub. [P1], in which a particular system-bath setup is investigated. The system consists only of a single spin, whose interaction with the bath is controlled by the interaction strength λ. The system's magnetization in z-direction, initially polarized, is monitored over the course of time. For a visual representation of the Hamiltonian and specifics on Hamiltonian, observable and initial states see Pub. [P1].

The time-dependent expectation value of the system's magnetization in z-direction is displayed in Fig. 1 for three interaction strengths.

In accordance with open quantum system theory, these results suggest to distinguish three cases.

i. Non-Markovian regime: for strong coupling (e.g. $\lambda = 1.0$) the magnetization quickly decays to the equilibrium value $\langle S^z_{\mathrm{sys}} \rangle_{\mathrm{mc}}$ in a non-exponential way. The description of these dynamics requires the incorporation of memory effects in some way. While this is a very active field in open quantum theory, it is not investigated any further in Pub. [P1].

ii. Markovian regime: for weak coupling (e.g. $\lambda = 0.1$) there is a mono-exponential decay to the thermal equilibrium. This exponential decay is in full accordance with Fermi's golden rule (FGR). A large number of systems in areas ranging from quantum optics to condensed matter fall into this regime [23, 133].

iii. Superweak coupling regime: for very weak coupling (e.g. $\lambda = 0.01$) the magnetization does not decay to the thermal equilibrium value at all, it rather gets stuck at a value closer to the initial value, which indicates the breakdown of FGR. This value depends on the interaction strength and on the bath size. In accordance with standard open quantum system theory, below results indicate that this regime only exists for finite baths.

Next, Pub. [P1] systematically investigates the relation between the long-time value $\overline{S^z_{\mathrm{sys}}}$, the interaction strength λ and the bath size N. It is found that the critical interaction strength $\lambda_{\mathrm{crit}}(N)$, below which the dynamics gets stuck, is exponentially small in the bath size. Hence, this effect quickly becomes undetectable for larger baths.

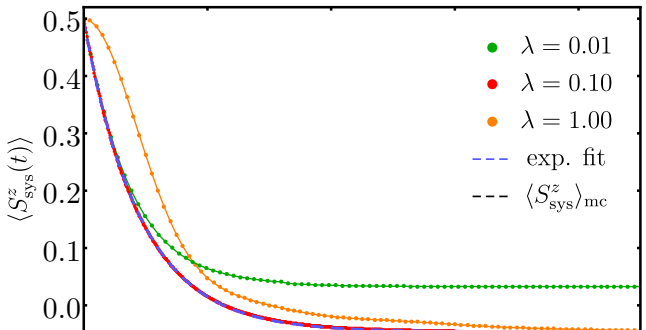

Figure 1. Decay of the magnetization for $N = 25$. For strong coupling (e.g. $\lambda = 1.0$) the magnetization decays quickly and non-exponentially to the thermal expectation value. Note that the time axis is scaled with λ^2. For weak coupling (e.g. $\lambda = 0.1$) the magnetization decays exponentially toward the thermal equilibrium value. For very weak coupling (e.g. $\lambda = 0.01$) the magnetization gets stuck at a non-thermal long-time average value.

[28] Provided that $\mathcal{H}_0$ has a sufficiently wide and dense spectrum. Many well-understood approaches, such as Fermi's golden rule, Weisskopf-Wigner theory and projection operator techniques (Nakajima- Zwanzig, Mori, etc.), arrive at such exponential decay dynamics [22, 23, 130–132] for standard, non-equilibrium situations.

Coming back to the numerical assessment of the GPB, a lower bound of the numerator in Eq. (99) is calculated explicitly for the setup at hand. To this end, the relaxation time τ_{rel} and the curvature term in the denominator are determined for the respective dynamics. It is found that the numerator grows at least up to values of ca. 55 already for $N = 25$ and interactions within the range of numerical accessibility. Moreover, the data do not indicate any "nearby" upper bound of the numerator at 55, which is at odds with a conclusive application of the GPB.

[P3]. Modeling the Impact of Hamiltonian Perturbations on Expectation Value Dynamics

There is an abundance of evidence that some relaxation dynamics are much more common in nature than others. For example, slow exponential dynamics commonly arise whenever a system interacts weakly with an environment or whenever long-wavelength Fourier components of spatial densities of conserved quantities are considered. In contrast, "strange" relaxation dynamics, like recurrence dynamics[29], are seldom if ever observed. Recently, there have been attempts to trace this dominance back to a certain stability of the prevalent dynamics versus generic Hamiltonian perturbations. In particular, three theories have been brought forth in Refs. [134], [135] and [20], respectively, which suggest that a majority of the numerous, permissible Hamiltonian perturbations entail more or less the same type of alteration to the decay dynamics. The theories are hereafter referred to as "theory [134], [135], [20]".
The paper *"Modeling the Impact of Hamiltonian Perturbations on Expectation Value Dynamics"* [P3] applies the three theories to a particular spin-based setup. To begin, the gist of the three theories is briefly presented for self-containedness. Their respective conditions are named and scrutinized with regard to the scenario at hand. Lastly, the results are evaluated and the accuracy of each theory is assessed. Satisfying agreement is found in the weak perturbation regime only for theory [20].
In short, the theories [134, 135] work with ensembles of perturbations and predict that a "typical" perturbation will lead to an (exponential) damping[30] of the unperturbed dynamics $a(t)$, i.e.,

$$\tilde{a}(t) = e^{-\gamma t} a(t) \tag{104}$$

for some γ depending on microscopic properties.

[29] This refers to "early" recurrences after the system has already equilibrated and not to Poincaré recurrences.
[30] Since the slope of autocorrelation functions vanishes at $t = 0$, the dynamics can not truly be exponentially damped.

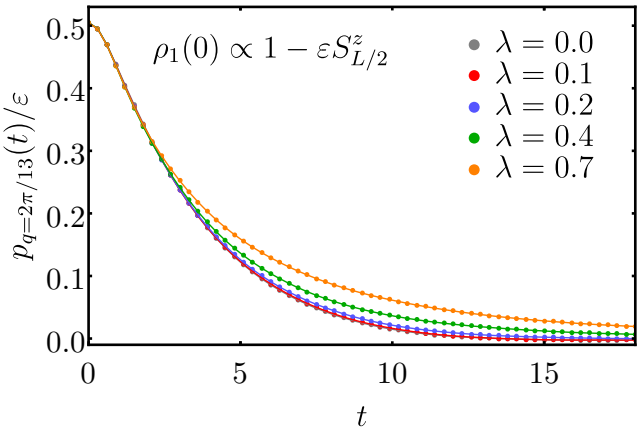

Figure 2. The time dependence of the slowest mode of a magnetization wave with $q = 2\pi/13$ is depicted for various perturbation strengths for the initial state $\rho_1(0)$. For small perturbations the unperturbed dynamic ($\lambda = 0.0$, grey curve) remains basically unchanged. For stronger perturbations there is a noticeable slowdown of the decay.

For details, the reader is referred to the publications themselves. The mechanics of theory [20] will be laid out in more detail, since it exclusively provides viable results (for the case at hand) and utilizes the concept of the memory-kernel introduced in Sec. II C 2.
Contrary to the other two theories, in theory [20] the dynamics itself is not directly damped, rather the perturbation leads to an exponential damping of the (first) memory-kernel. Thus, the perturbed dynamics $\tilde{a}(t)$ are obtained from the unperturbed dynamics $a(t)$ via

$$a(t) \to K(t) \to \tilde{K}(t) \to \tilde{a}(t)\,, \tag{105}$$

where $\tilde{K}(t) = e^{-\gamma\tau} K(t)$. Here, γ is a free fit parameter and the integro-differential Eq. (70) gives the relation between dynamics and memory-kernel.
For the below defined spin systems, this is merely an heuristic approach[31]. For other scenarios, the memory-kernel ansatz has been rigorously proven to hold [136]. Further, numerical evidence for its validity exists beyond what can be rigorously established [20, 137].
To probe the three theories, a spin ladder described by the Hamiltonian $\mathcal{H}_0$ is considered, with additional $s^z s^z$-couplings as a perturbation $\mathcal{V}$ on the diagonals. The total Hamiltonian then reads $\mathcal{H} = \mathcal{H}_0 + \lambda\mathcal{V}$, where λ is the perturbation strength. The observable $\mathcal{A}$ is chosen as the slowest Fourier mode of the magnetization along the legs of the ladder. The two initial states $\rho_{1,2}$

[31] The fact that $[\mathcal{V}, \mathcal{A}] = 0$ for the below defined systems makes a successful applications of the memory-kernel ansatz more probable, see Pub. [P3] for details.

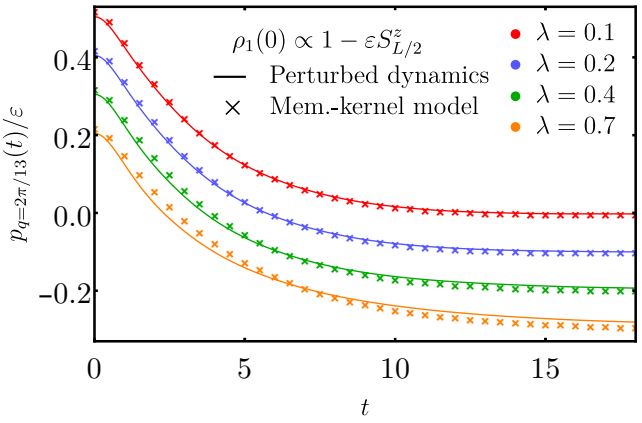

Figure 3. Solid lines represent the perturbed dynamics from Fig. 2, vertically shifted in steps of -0.1. Crosses indicate the data obtained from the memory-kernel ansatz.

are at finite and infinite temperature, respectively, and feature a single polarized "spin-up" rung. For a visual representation and specifics on Hamiltonian, observable and initial states see Pub. [P3].

Numerically solving the time-dependent Schrödinger equation with methods presented in Sec. II D 2, it is found that the magnetization spreads (more or less diffusively) throughout the ladder. Consequently, the expectation value of the observable decays more or less exponentially. The dynamics for various perturbations strengths are displayed in Fig. 2 for the infinite-temperature initial state ρ_1.

While the specific conditions for the applicability of theory [134] and [135] are quite difficult to check in detail, it is argued in Pub. [P3] that the setup at hand should yield at least somewhat reasonable results. However, the perturbed dynamics decay slower than the unperturbed one, which is visible in Fig. 2. Since theories [134] and [135] predict a damping of the dynamics, see Eq. (104), they fail to capture the perturbed dynamics even qualitatively since a damping leads to faster decaying dynamics.

These findings suggest that the perturbation $\mathcal{V}$ is indeed one of the mathematically untypical members of the ensemble considered in theory [134]. However, even though $\mathcal{V}$ is untypical with respect to an ensemble of random matrices, it is a physically simple perturbation consisting of standard spin-spin interactions.

The additional failure of theory [135] only leaves theory [20] as a possible candidate to describe the observed behavior. The prediction by the memory-kernel model is depicted in Fig. 3 for the infinite-temperature initial state ρ_1. For weak perturbations ($\lambda = 0.1, 0.2$) the memory-kernel model seems to capture the modified dynamics quite well. For stronger perturbations ($\lambda = 0.4, 0.7$) there are some noticeable deviations. That being said, it comes as no surprise that the memory-kernel model loses potency in the strong perturbation regime, as it was originally conceived to describe the alteration of dynamics due to weak perturbations.

[P4]. Integral Fluctuation Theorem and Generalized Clausius Inequality for Microcanonical and Pure States

An integral fluctuation theorem (IFT) for the entropy production of a system-bath setup has been derived in Sec. II B 3. Further, its (exact) validity has been demonstrated for canonical bath states. While the IFT itself is more encompassing, its most prominent consequence is a generalized Clausius inequality, cf. Eq. (58), which is sometimes viewed as one possibility to express the second law of thermodynamics [138].

Given the significance of the generalized Clausius inequality, it is remarkable that, so far, the validity of the respective IFT has been proven only in full generality for canonical states, but not for microcanonical or pure states [8, 139]. It is worth mentioning that for far-from-equilibrium statements like fluctuation theorems, results from the canonical ensemble do not straightforwardly carry over to, e.g., the microcanonical ensemble simply by the equivalence of ensembles [140–142].

The paper *"Integral Fluctuation Theorem and Generalized Clausius Inequality for Microcanonical and Pure States"* [P4] establishes the validity of the above IFT for microcanonical and pure states under two conditions, which are referred to as "stiffness" and "smoothness" of transition probabilities. The validity of the IFT and the existence of stiffness and smoothness are numerically investigated for various lattice models.

Recall that the IFT in question [cf. Eq. (59)] reads[32]

$$\langle\!\langle e^{-\Delta\sigma} \rangle\!\rangle = \sum_{j,k,a,b} P^j_{\text{fin}} W^b_{\text{ini}}\, e^{-\beta(\varepsilon^a_{\text{bath}} - \varepsilon^b_{\text{bath}})} \times R(jk,ab) = 1\,. \tag{106}$$

which holds exactly for canonical bath states, as shown in Sec. II B 3. The question that Pub. [P4] aims to answer is under which conditions Eq. (106) holds true when W^b_{ini} corresponds to a microcanonical or even a pure state.

To tackle this issue, a "coarse-grained" IFT quantity is derived as an intermediate step, which reads

[32] The quantity s is now denoted by $\Delta\sigma$.

$$\langle\!\langle e^{-\Delta\sigma}\rangle\!\rangle_{\text{c.g.}} = \sum_{j,k,A,B} P^j_{\text{fin}} W^B_{\text{ini}} e^{-\beta\delta(A-B)} \times \overline{R}(jk,AB)\,. \tag{107}$$

Since the system comprises only a few energy levels, e.g., a single spin, just the energy of the bath is divided into bins of finite size. In short, capitalized letters now indicate energy ranges $E^B_{\text{bath}} = [(B-1/2)\delta, (B+1/2)\delta]$ and δ is the bin size of the graining. Further details of the coarse-graining process, like the construction of average transition probabilities[33] $\overline{R}(jk,AB)$ between energy ranges in the bath or interpretation of the coarse-grained IFT quantity are laid out in Pub. [P4].
Continuing, the central properties of stiffness and smoothness are introduced.
A transition probability to go from some initial energy interval E^B_{bath} to a final energy interval E^A_{bath} is called *stiff* (for given j,k) if

$$\overline{R}(jk,AB) = \overline{R}(jk,A-B)\,, \tag{108}$$

i.e., the probability to transition from the initial energy interval E^B_{bath} to a state within the final energy interval E^A_{bath} is only a function of the difference in energies.
A set of transition probabilities $R(jk,Ab)$ from an initial state $|k,b\rangle$ to a final energy interval E^A_{bath} is called *smooth* (for given j,k), if

$$r(jk,Ab) = R(jk,Ab) - \overline{R}(jk,AB) \approx 0 \tag{109}$$

for all $b \in B$, i.e., all transition probabilities to go from a state with initial energy $\varepsilon^b_{\text{bath}}$ within the initial interval E^B_{bath} to the final energy interval E^A_{bath} are close to the average value of transition probabilities within that initial energy interval.
The paper continues to rigorously show that the assumption of stiffness leads to the validity of the coarse-grained IFT for $W^B_{\text{ini}} = \delta_{B,B_0}$, i.e.,

$$\langle\!\langle e^{-\Delta\sigma}\rangle\!\rangle_{\text{c.g.}} = 1\,. \tag{110}$$

Furthermore, the assumption of smoothness yields

$$\langle\!\langle e^{-\Delta\sigma}\rangle\!\rangle \overset{r\to 0}{\longrightarrow} \langle\!\langle e^{-\Delta\sigma}\rangle\!\rangle_{\text{c.g.}}\,. \tag{111}$$

Hence, the validity of the microscopic IFT even and especially for initial energy eigenstates, may be inferred from the validity of the coarse-grained IFT, if Eq. (109) applies sufficiently well. These are the two main analytical results of the paper.

[33] Denoted by an overbar, but not to be confused with the notation for a temporal average used earlier.

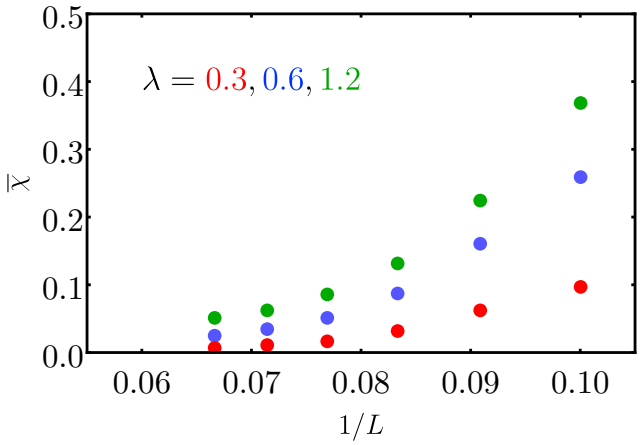

Figure 4. Bath-size dependence of the stiffness quantifier $\overline{\chi}$ for the Ising model at $t = 4$ for various interaction strengths. For all λ, the quantifier decreases with increasing bath size, indicating perfect stiffness in the limit of infinitely large baths, i.e., $L \to \infty$.

In App. C of Pub. [P4], the connection of stiffness to the rigged ETH is discussed. Further, it is argued that stiffness may be the rule rather than the exception.
The natural question that arises next is whether stiffness and smoothness are present in physical systems. To this end, three models are investigated numerically - an Ising model with defects, a hard-core boson model and an integrable Heisenberg chain. Some selected results for the Ising model are displayed in the following.
In order to measure to what extent stiffness and smoothness are present, two quantifiers $\overline{\chi}$ and $\overline{\varphi}$ are introduced. Both quantifiers tend to zero if the respective assumptions (stiffness and smoothness) indeed apply. For definitions of quantifiers as well as details on Hamiltonians and initial states see Pub. [P4].
The stiffness quantifier $\overline{\chi}$ is plotted over the inverse bath size in Fig. 4. There is a clear decrease of $\overline{\chi}$ with L for all λ. Moreover, the figure suggests that stiffness becomes perfectly fulfilled and thus the coarse-grained IFT exactly valid in the thermodynamic limit. This finding is accompanied by the (approximate) validity of the coarse-grained IFT, which is not displayed here.
The smoothness quantifier $\overline{\varphi}$ is logarithmically plotted in Fig. 5 as a function of bath size L. It appears to decrease exponentially with L for all λ. Thus, perfect smoothness in the sense of Eq. (109) may be expected in the thermodynamic limit. To numerically check the pure state IFT [Eq. (106)], Fig. 6 displays the average (also denoted by an overbar) over the absolute deviations from unity for 100 individual pure states around some energy $\mathcal{E}$. A small average of the absolute deviations signals a good agreement with the microscopic IFT for the majority of the individual initial states.

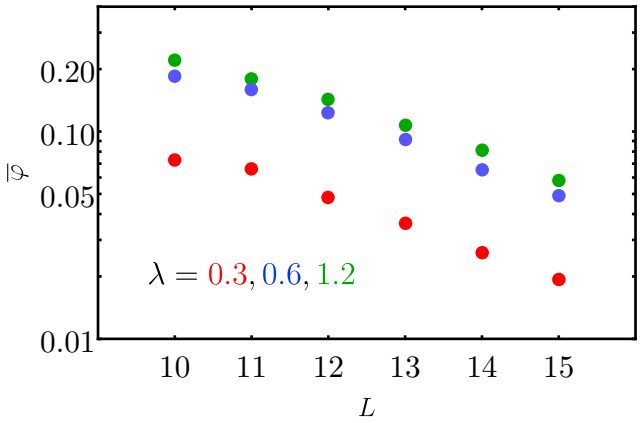

Figure 5. Bath-size dependence of the smoothness quantifier $\overline{\varphi}$ for the Ising model for various interaction strengths λ at $t = 4$. For all λ, the quantifier decreases (approximately exponentially) with increasing bath size, indicating perfect smoothness in the limit of infinitely large baths, i.e., $L \to \infty$.

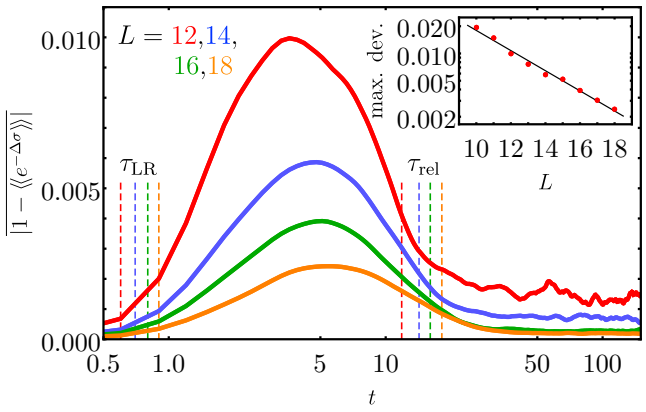

Figure 6. Average "violations" of the microscopic IFT [Eq. (106)] plotted over time t for the Ising model for a simultaneous scaling of interaction strength λ and bath size L as described in Pub. [P4]. This scaling is chosen to keep open a gap between the Lieb-Robinson time τ_{LR} and the relaxation time τ_{rel} (respective dashed vertical lines), even in the limit of large baths. Inset: Maximum average violation of the microscopic IFT logarithmically plotted over bath size. The average violation decreases exponentially with bath size L, indicating the increasing validity of the microscopic IFT even within the temporal gap.

For each system size, the deviations exhibit a clear maximum at intermediate times. These maxima may be related to the build-up and drop-off of correlations between system and bath [143, 144]. However, already for relatively small system sizes, the maximum deviation is rather small, e.g., approximately one percent for $L = 12$. But more importantly, the maximum of the deviations decreases exponentially with increasing bath size, as especially the inset of Fig. 6 shows. Thus, the microscopic IFT for pure states is found to be fulfilled to very good accuracy already for mesoscopic-sized baths at all times. This result furthermore confirms the expectations induced by Figs. 4 and 5.

At this point, alternative approaches [139, 145, 146] to the IFT should be mentioned, which are based on Lieb-Robinson times, typicality and the ETH. With these tools, the IFT can be proved for pure states in case of infinitely large baths as well as for extremely large baths paired with intermediate interaction strengths between system and bath. However, there is a significant, physically relevant set of combinations of bath sizes and interaction strengths for which these approaches are unsuitable [147]. These scenarios that are not covered feature a lack of overlap between the Lieb-Robinson time and the relaxation time (within this gap, the validity of the IFT for pure states can not be established by these approaches). Nevertheless, Fig. 6 demonstrates that also within the temporal gap (which remains open as the bath grows) the IFT is fulfilled to very good accuracy. Since the result based on stiffness and smoothness makes no reference to any time scales, the findings of Pub. [P4] go conceptually beyond Refs. [139, 145, 146].

The publication presents more numerical results for a hard-core boson model and an integrable Heisenberg chain. While the outcomes in the boson model are similar to the ones presented above, the integrable model is found to violate the microscopic IFT to a larger extent, i.e., deviations are on the order of ten percent. An analysis of stiffness and smoothness quantifiers suggests that it is indeed the violation of smoothness (and not stiffness) that causes these deviations.

[P5]. Numerically Probing the Universal Operator Growth Hypothesis

As stated in Sec. II A 4, the idea of "typicality of states" is that an overwhelming majority of pure states (at some energy) give rise to corresponding thermal expectation values. Thus, it is quite likely that over the course of time a pure state eventually ends up in the giant "bubble" of typical states.

In the Heisenberg picture formulation of quantum mechanics, not the states are time dependent, but the observables themselves. Hence, it may be somewhat expected to find a similar notion of "typicality of observables", going from initially simple, few-particle operators to more complex, generic operators.

The paper "*Numerically Probing the Universal Operator Growth Hypothesis*" [P5], no surprise, numerically probes the "universal operator growth hypothesis" proposed in Ref. [84] and discussed in Sec. II C 3. Besides numerical verification, Pub. [P5] derives a particular upper bound $\mathcal{B}_n$ on the Lanczos coefficients b_n and compares it to the actual growth in physical, spin-based models.

Said bound is derived from geometric arguments involving the locality of the Hamiltonian as well as the lattice configuration. These arguments are easiest applied by considering the moments μ_{2n} of the autocorrelation function, which can be written as

$$\mu_{2n} = ||\mathcal{L}^n \mathcal{O}||^2 \,. \tag{112}$$

Here, $\mathcal{O}$ is a local operator with $||\mathcal{O}|| = 1$ and $\mathcal{H} = \sum_\ell h_\ell$ a local Hamiltonian, or, respectively, $\mathcal{L} = \sum_k \ell_k$ a local Liouvillian with terms $\ell_k = [h_k, \cdot\,]$. In the following, the inequality $||\ell \mathcal{A}|| \leq \mathcal{E}\, ||\mathcal{A}||$ is repeatedly used, where $\mathcal{E}$ denotes the maximum eigenvalue of ℓ. Equality holds if the operator $\mathcal{A}$ is an eigenoperator of the local Liouvillian corresponding to the largest eigenvalue (all $\ell_k = \ell$ are assumed to be of the same type). Additionally exploiting the triangle inequality, the moments can be bounded as

$$\mu_{2n} = ||\mathcal{L}^n \mathcal{O}||^2 \leq \mathcal{E}^{2n} N_{\text{sum}}^2(n) \,. \tag{113}$$

Here, N_{sum} is a geometric term that counts the number of "trivially non-vanishing" terms in the sum $\mathcal{L}^n = \sum_{x_1,\ldots,x_n} \ell_{x_1} \ldots \ell_{x_n}$. This number typically grows quite fast with n and can be exactly determined for simple geometries [148].

The above bound on the moments is sharp, meaning first, no sequence of physical moments μ_{2n} can possibly grow faster and, importantly, second, this bound could *in principle* be achieved (as opposed to, e.g., two times the bound). This is the case if and only if all involved inequalities are satisfied as equalities[34].

The fastest growing moments, i.e., moments equal to the r.h.s. of Eq. (113), can be translated to corresponding coefficients $\mathcal{B}_n$ as described in Sec. II C 2, which will be interpreted as a sort of "global uniform" upper bound on the b_n, meaning that it is impossible to further increase the value of one specific coefficient "by hand", without simultaneously decreasing the value of another one (or several other ones). For more details on determining N_{sum} and the interpretation of $\mathcal{B}_n$ the reader is referred to Pub. [P5].

[34] Publication [P5] makes no statement about the existence of such a fine-tuned pair of $\mathcal{H}$ and $\mathcal{A}$.

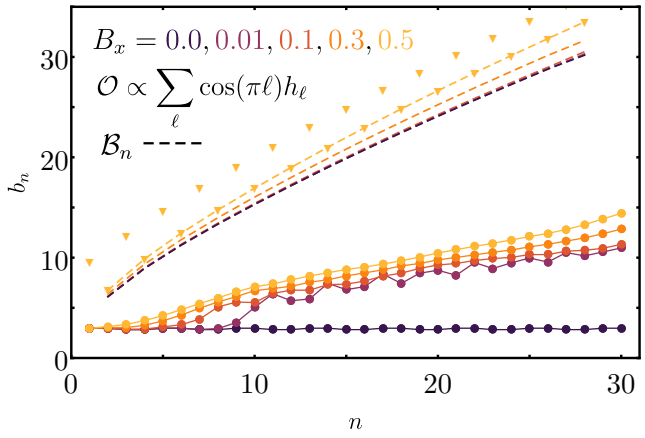

Figure 7. Lanczos coefficients b_n of the transverse Ising model for the fast mode of an energy wave. The integrability-breaking magnetic field attains values from $B_x = 0.0$ to $B_x = 0.5$. The transition from a free model to a non-integrable model is evident. The coefficients $\mathcal{B}_n$ are explicitly depicted for the case $B_x = 0.5$ as yellow triangles. Dashed lines indicate the "lower branches" of the corresponding $\mathcal{B}_n$. To avoid clutter, only the dashed lines are depicted as a guide to the eye for other values of B_x. The coefficients $\mathcal{B}_n$ are larger than the physical b_n by a factor of about two.

The publication continues by introducing the investigated models, i.e., 1d and 2d Ising models as well as 1d Heisenberg models. Respective Hamiltonians take the form $\mathcal{H} = \mathcal{H}_0 + \lambda \mathcal{V}$, where $\mathcal{H}_0$ is an integrable part and $\lambda \mathcal{V}$ breaks the integrability via, e.g., an additional magnetic field in the Ising models, or long-range interactions in the Heisenberg models. Observables are, for instance, Fourier modes of energy waves with support throughout the whole (infinite) system, or local operators supported only on a single site. For specifics on Hamiltonians and observables, see Pub. [P5].

A frequently observed growth pattern of the Lanczos coefficients is depicted in Fig. 7 for a fast Fourier mode of an energy wave in the Ising model. Without an integrability-breaking term, i.e., $B_x = 0$, the Lanczos coefficients seem to be more or less constant. In this case, the system can be mapped to free fermions via a Jordan-Wigner transformation [110].

As soon as a small perturbation that breaks the integrability is introduced, e.g., $B_x = 0.01$, the Lanczos coefficients begin to grow. The distinction between the free case and non-integrable cases is clearly visible.

The growth for larger values of B_x already looks quite linear. The slight curvature also hints at a possible logarithmic correction due to the system's one-dimensionality.

The data presented in Fig. 7 support the operator growth hypothesis and similar results have been found for other observables in Pub. [P5] and Refs. [84, 96].

Additionally, Pub. [P5] numerically shows that a 2d Ising model yields strictly linear growth (without a logarithmic correction), which is also in favor of the hypothesis. In contrast, linear growth could not be clearly identified in the Heisenberg model. Not least, this may be due to a limited availability of numerical data for larger n.
The second main result of Pub. [P5] concerns the derived bound $\mathcal{B}_n$, which is also depicted in Fig. 7 as dashed lines. It can be seen that the bound is larger than the physical coefficients by about a factor of two. Given the excessive usage of inequalities in its derivation, it is not surprising that the bound is not tightly achieved.
The reason for the consideration of this bound in the first place is that in Ref. [84], a similar, much looser bound has been derived, which has been shown to correspond to an asymptotically linear, upper bound on the b_n. Since the "optimized" bound in Eq. (113) is not tightly achieved, the much looser bound from Ref. [84] is even less tight. However, the growth observed in, e.g., Fig. 7, seems to nonetheless be consistent with the hypothesis. Thus, Pub. [P5] corroborates the sentiment that the "fastest possible growth" is to be understood with respect to the "functional form" of the growth, rather than the concrete, numerical values. Along this line of thinking, modified coefficients $\tilde{\mathcal{B}}_n$ obtained from a rescaled "effective" energy scale $\tilde{\mathcal{E}}$ in Eq. (113) could capture the correct asymptotic behavior, giving a prospect for possible future research.

[P6]. Stability of Exponentially Damped Oscillations under Perturbations of the Mori-Chain

While concepts like the ETH and quantum typicality hint at fundamental mechanisms ensuring eventual equilibration, they are not concerned in which manner this equilibrium is reached. It is an empirical fact that some relaxation dynamics, e.g., exponential decays, occur much more often in nature than others, e.g., recurrence dynamics. Recently, there have been attempts to trace this dominance back to a certain stability of the prevalent dynamics versus generic Hamiltonian perturbations [20].
The paper *"Stability of Exponentially Damped Oscillations under Perturbations of the Mori-Chain"* [P6] tackles this issue from yet another angle, namely in the framework of the recursion method (cf. Sec. II C). Numerical experiments are performed, which suggest the existence of stability in a larger class of relaxation dynamics consisting of exponentially damped oscillations (including exponential decays as oscillations with zero frequency).
To set the stage, the general strategy to probe the stability of classes of dynamics is laid out. To this end, two correlation functions $C_A(t)$ and $C_B(t)$ are chosen, whose respective stability will be assessed and compared. In the first investigation of Pub. [P6], $C_A(t)$ is an exponential decay and $C_B(t)$ a Gaussian decay.
Publication [P6] goes into much detail how corresponding Lanczos coefficients b_n^A and b_n^B can be found, that do not only reproduce the dynamics, but additionally satisfy further physically plausible conditions, which are:
i. Compliance with the operator growth hypothesis [84].
ii. Similarity of relaxation time scales.
iii. Specific magnitude requirements.
The considered perturbation is designed on the level of Lanczos coefficients b_n, which are slightly altered according to $\tilde{b}_n = b_n + \lambda v_n$. Here, λ is the perturbation strength and v_n is given by

$$v_n = \sum_{k=1}^{N_\mathrm{f}} x_k \cos(2\pi nk/d) + y_k \sin(2\pi nk/d)\,, \qquad (114)$$

where the x_k, y_k are real, random numbers from a Gaussian distribution with zero mean and unit variance. They are normalized as $\sum_k x_k^2 + y_k^2 = 1$.
The sum in Eq. (114) is capped at a number N_f. This corresponds to excluding higher frequencies, which induces a minimal correlation length in the coefficients $\tilde{b}_n$. This is necessary to avoid localization effects, which occur when k's larger than $N_\mathrm{f} \approx d/3$ are included (d is the dimension of the Liouville space).
The stability is assessed by measuring to what extent the perturbed dynamics still falls into the original class of functions to which the unperturbed dynamics belonged. To this end, the perturbed dynamics is fitted with a function that also describes the unperturbed dynamics. The quality of such a fit $f(t)$ is assessed by calculating "how far off" it is from the given perturbed dynamics. Concretely, a measure of the "error" ϵ is defined by the expression

$$\epsilon = \sqrt{\frac{1}{N_\mathrm{eq}} \sum_{n=0}^{N_\mathrm{eq}} (\tilde{C}(t_n) - f(t_n))^2}\,, \qquad (115)$$

where $\tilde{C}$ denotes the perturbed dynamics and N_eq corresponds to the time at which equilibrium is reached.
A similar quantifier σ is introduced to measure how strongly the unperturbed dynamics are altered due to the perturbation in the first place. This concludes the short version of the overall strategy.
Publication [P6] continues to apply said strategy to two cases. The first case compares the stability of exponential decays to that of Gaussian decays. The second case concerns two kinds of damped oscillations, the first with an exponential damping factor, the second with a Gaussian damping factor. The results of the first case are presented in the following.

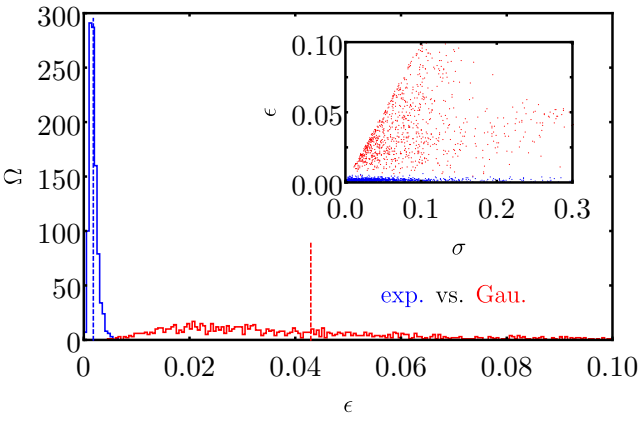

Figure 8. Histogram of the fit quality measure ϵ with a bin size of $5 \cdot 10^{-4}$. Dashed lines indicate respective mean values. The stability of the exponential decay is evident. In contrast, the Gaussian decay does not seem to be stable, as the deviations ϵ become quite large. Inset: scatter plot of all points (σ_i, ϵ_i). Both dynamics are equally affected by the perturbation.

Turning on the perturbation ($\lambda = 0.5$), the altered dynamics are fitted by exponential and Gaussian decays, respectively. While the publication displays figures of unperturbed coefficients and dynamics as well as examples of perturbed cases, here, for conciseness, only the most important data are depicted.
A histogram of all deviations ϵ (obtained from $N = 1000$ repetitions) of the fits from the respective perturbed dynamics is displayed in Fig. 8. There is a clear division between the exponential cases (blue) and the Gaussian cases (red), i.e., the mean deviation in the exponential case is about twenty times smaller than in the Gaussian case (dashed lines in Fig. 8).
The inset takes the second quantifier σ into account in order to exclude the possibility that exponential decays are generally less affected by the constructed perturbation than the Gaussian decays. Since this is evidently not the case, it is concluded that exponential decays are indeed stable with respect to perturbations [as in Eq. (114)]. In contrast, Gaussian decays seem to be quite unstable.
Publication [P6] proceeds to the second investigation, a comparison between the two above-mentioned kinds of damped oscillations. Exponentially damped oscillations are found to be stable. In contrast, oscillations damped by a Gaussian factor are found to be more unstable. However, the distinction is not as striking as in the case presented above.
The dynamics that Pub. [P6] has found to be stable are ubiquitous in nature. For example, slow exponential dynamics may commonly arise whenever a system interacts weakly with an environment or whenever long-wavelength Fourier components of spatial densities of conserved quantities are considered. Further, exponentially damped oscillations are routinely observed in the context of open quantum systems [22, 23]. They arise whenever a small system featuring oscillating observables is weakly coupled to an environment, which causes the oscillation to be exponentially damped.
To obtain the final result of the paper, the restriction on N_f is lifted, such that the perturbation modifies the b_n in a completely random, uncorrelated matter. As hinted at above, localization effects similar to Anderson localization [149] emerge, which yield uncommon, "pathological" dynamics. This finding could be of interest in the context of the works on "typicality of perturbations" [134, 150, 151], as it presents a criterion to identify "untypical" perturbations.

IV. Summary and Conclusion

The dissertation at hand discussed the works presented in the publications [P1–P6], in which quite diverse aspects of non-equilibrium behavior in isolated quantum systems have been addressed.
The first two publications [P1, P2] have examined a compelling bound on equilibration times. While said bound is mathematically sound, it has been (numerically and analytically) shown to be inapplicable to many standard scenarios featuring slow, exponential relaxation dynamics.
Publication [P3] has numerically scrutinized three theories modeling the effect of perturbations on expectation value dynamics. For the specific spin-based setup, only one theory has been shown to yield good results for weak perturbations.
A major part of this dissertation concerned fluctuation theorems. Publication [P4] has investigated a particular integral fluctuation theorem (IFT) for the entropy production of a system-bath setup. Said IFT has been analytically shown to hold for microcanonical and pure bath states under the assumption that the transition probabilities satisfy the conditions of stiffness and smoothness. The validity of the IFT and the existence of stiffness and smoothness have been numerically investigated for various lattice models. In the investigated non-integrable systems, the IFT becomes more and more fulfilled the larger the bath gets. Fittingly, stiffness and smoothness also become more and more fulfilled with growing bath sizes. In the integrable case, the IFT is violated to some extent for pure bath states, which is traced back to the absence of sufficient smoothness. These findings demonstrate the significance of stiffness and smoothness, thus, possible prospects for future research could be to examine the origins of their (non-) validity more closely.

Continuing, publication [P5] has numerically examined the recently proposed "universal operator growth hypothesis" for various spin-based systems in the thermodynamic limit. The hypothesis has been shown to be valid within the limits of the numerical approach. Further, the specific growth pattern has been found to be consistent with an "optimized" upper bound, hinting at a possible direction of future research.
Finally, publication [P6] has addressed the issue of stability of relaxation dynamics in the framework of the recursion method. A larger class of functions consisting of exponentially damped oscillations has been numerically found to be stable against certain perturbations on the level of Lanczos coefficients. This finding subtly hints at the possibility that exponentially damped oscillations constitute sort of fundamental "building blocks" of relaxation dynamics. This notion is part of a set of ideas that has been affectionately named "the weak model" and it will be interesting to see what future research comes out of it.

[P1] R. Heveling, L. Knipschild, and J. Gemmer, Journal of Physics A: Mathematical and Theoretical **53**, 375303 (2020).
[P2] R. Heveling, L. Knipschild, and J. Gemmer, Phys. Rev. X **10**, 028001 (2020).
[P3] R. Heveling, L. Knipschild, and J. Gemmer, Zeitschrift für Naturforschung A **75**, 475 (2020).
[P4] R. Heveling, J. Wang, R. Steinigeweg, and J. Gemmer, Phys. Rev. E **105**, 064112 (2022).
[P5] R. Heveling, J. Wang, and J. Gemmer, Phys. Rev. E **106**, 014152 (2022).
[P6] R. Heveling, J. Wang, C. Bartsch, and J. Gemmer, Journal of Physics Communications **6**, 085009 (2022).
[7] N. H. Ryogo Kubo, Morikazu Toda, *Statistical Physics II* (Springer Berlin Heidelberg, 1991).
[8] M. Esposito, U. Harbola, and S. Mukamel, Rev. Mod. Phys. **81**, 1665 (2009).
[9] C. S. Wu, E. Ambler, R. W. Hayward, D. D. Hoppes, and R. P. Hudson, Phys. Rev. **105**, 1413 (1957).
[10] M. Greiner, O. Mandel, T. Esslinger, T. W. Hänsch, and I. Bloch, Nature **415**, 39 (2002).
[11] O. Mandel, M. Greiner, A. Widera, T. Rom, T. W. Hänsch, and I. Bloch, Nature **425**, 937 (2003).
[12] T. Kinoshita, T. Wenger, and D. S. Weiss, Nature **440**, 900 (2006).
[13] I. Bloch, J. Dalibard, and W. Zwerger, Rev. Mod. Phys. **80**, 885 (2008).
[14] T. Langen, R. Geiger, and J. Schmiedmayer, Annual Review of Condensed Matter Physics **6**, 201 (2015).
[15] M. Srednicki, Phys. Rev. E **50**, 888 (1994).
[16] J. M. Deutsch, Phys. Rev. A **43**, 2046 (1991).
[17] S. Goldstein, J. L. Lebowitz, R. Tumulka, and N. Zanghì, Phys. Rev. Lett. **96**, 050403 (2006).
[18] S. Lloyd, arXiv:1307.0378 (2013).
[19] J. Richter, J. Gemmer, and R. Steinigeweg, Phys. Rev. E **99**, 050104 (2019).
[20] L. Knipschild and J. Gemmer, Phys. Rev. E **98**, 062103 (2018).
[21] L. Knipschild and J. Gemmer, Phys. Rev. E **101**, 062205 (2020).
[22] M. O. Scully and M. S. Zubairy, *Quantum Optics* (Cambridge University Press, 1997).
[23] H.-P. Breuer and F. Petruccione, *The Theory of Open Quantum Systems* (Oxford University Press, 2006).
[24] M. Planck, Annalen der Physik **309**, 553 (1901).
[25] H. Poincaré, Acta Mathematica **13**, 1 (1890).
[26] E. T. Jaynes, Phys. Rev. **106**, 620 (1957).
[27] E. T. Jaynes, Phys. Rev. **108**, 171 (1957).
[28] C. Gogolin and J. Eisert, Reports on Progress in Physics **79**, 056001 (2016).
[29] N. Linden, S. Popescu, A. J. Short, and A. Winter, Phys. Rev. E **79**, 061103 (2009).
[30] T. Farrelly, F. G. S. L. Brandão, and M. Cramer, Phys. Rev. Lett. **118**, 140601 (2017).
[31] N. Linden, S. Popescu, A. J. Short, and A. Winter, New Journal of Physics **12**, 055021 (2010).
[32] J. von Neuman and E. Wigner, Physikalische Zeitschrift **57**, 467 (1929).
[33] H. Tasaki, Phys. Rev. Lett. **80**, 1373 (1998).
[34] A. Khodja, D. Schmidtke, and J. Gemmer, Phys. Rev. E **93**, 042101 (2016).
[35] M. Srednicki, Journal of Physics A: Mathematical and General **32**, 1163 (1999).
[36] P. Reimann and M. Kastner, New Journal of Physics **14**, 043020 (2012).
[37] A. J. Short and T. C. Farrelly, New Journal of Physics **14**, 013063 (2012).
[38] A. J. Short, New Journal of Physics **13**, 053009 (2011).
[39] R. Gallego, H. Wilming, J. Eisert, and C. Gogolin, Phys. Rev. A **98**, 022135 (2018).
[40] L. D'Alessio, Y. Kafri, A. Polkovnikov, and M. Rigol, Advances in Physics **65**, 239 (2016).
[41] J. Wang, M. H. Lamann, J. Richter, R. Steinigeweg, A. Dymarsky, and J. Gemmer, Phys. Rev. Lett. **128**, 180601 (2022).
[42] L. D. Landau and E. M. Lifshitz, *Statistical Physics,* (Butterworth-Heinemann Ltd, 1980).
[43] M. Rigol, V. Dunjko, and M. Olshanii, Nature **452**, 854 (2008).
[44] R. Steinigeweg, J. Herbrych, and P. Prelovšek, Phys. Rev. E **87**, 012118 (2013).
[45] R. Mondaini and M. Rigol, Phys. Rev. E **96**, 012157 (2017).
[46] H. Kim, T. N. Ikeda, and D. A. Huse, Phys. Rev. E **90**, 052105 (2014).
[47] G. Biroli, C. Kollath, and A. M. Läuchli, Phys. Rev. Lett. **105**, 250401 (2010).
[48] R. Steinigeweg, A. Khodja, H. Niemeyer, C. Gogolin, and J. Gemmer, Phys. Rev. Lett. **112**, 130403 (2014).
[49] J.-S. Caux and J. Mossel, Journal of Statistical Mechanics: Theory and Experiment **2011**, P02023 (2011).

[50] B. Sutherland, *Beautiful Models* (World Scientific, 2004).
[51] W. Beugeling, R. Moessner, and M. Haque, Phys. Rev. E **89**, 042112 (2014).
[52] T. N. Ikeda, Y. Watanabe, and M. Ueda, Phys. Rev. E **87**, 012125 (2013).
[53] A. Pal and D. A. Huse, Phys. Rev. B **82**, 174411 (2010).
[54] B. V. Fine, T. A. Elsayed, C. M. Kropf, and A. S. de Wijn, Phys. Rev. E **89**, 012923 (2014).
[55] R. V. Jensen and R. Shankar, Phys. Rev. Lett. **54**, 1879 (1985).
[56] M. Castagnino and O. Lombardi, Chaos, Solitons and Fractals **28**, 879 (2006).
[57] S. Weigert, Physica D: Nonlinear Phenomena **56**, 107 (1992).
[58] M. Rigol, V. Dunjko, V. Yurovsky, and M. Olshanii, Phys. Rev. Lett. **98**, 050405 (2007).
[59] R. Nandkishore and D. A. Huse, Annual Review of Condensed Matter Physics **6**, 15 (2015).
[60] D. A. Abanin and Z. Papić, Annalen der Physik **529**, 1700169 (2017).
[61] D. A. Huse, R. Nandkishore, and V. Oganesyan, Phys. Rev. B **90**, 174202 (2014).
[62] M. Serbyn, Z. Papić, and D. A. Abanin, Phys. Rev. Lett. **111**, 127201 (2013).
[63] D. J. Luitz, N. Laflorencie, and F. Alet, Phys. Rev. B **91**, 081103 (2015).
[64] P. Reimann, Phys. Rev. Lett. **99**, 160404 (2007).
[65] J. Gemmer, M. Michel, and G. Mahler, *Quantum Thermodynamics* (Springer Berlin Heidelberg, 2009).
[66] C. Bartsch and J. Gemmer, Phys. Rev. Lett. **102**, 110403 (2009).
[67] P. Reimann and J. Gemmer, Physica A: Statistical Mechanics and its Applications **552**, 121840 (2020).
[68] P. W. Brouwer and C. W. J. Beenakker, Journal of Mathematical Physics **37**, 4904 (1996).
[69] S. Popescu, A. J. Short, and A. Winter, Nature Physics **2**, 754 (2006).
[70] J. Gemmer and G. Mahler, The European Physical Journal B - Condensed Matter and Complex Systems **31**, 249 (2003).
[71] R. Steinigeweg, J. Gemmer, and W. Brenig, Phys. Rev. Lett. **112**, 120601 (2014).
[72] B. N. Balz, J. Richter, J. Gemmer, R. Steinigeweg, and P. Reimann, *Dynamical Typicality for Initial States with a Preset Measurement Statistics of Several Commuting Observables* (Springer International Publishing, 2018).
[73] P. Reimann, Phys. Rev. E **97**, 062129 (2018).
[74] R. Clausius, Annalen der Physik **169**, 481 (1854).
[75] C. Jarzynski, Annu. Rev. Condens. Matter Phys. **2**, 329 (2011).
[76] C. Jarzynski, Phys. Rev. Lett. **78**, 2690 (1997).
[77] C. Jarzynski, J. Stat. Phys. **98**, 77 (2000).
[78] G. E. Crooks, Phys. Rev. E **60**, 2721 (1999).
[79] M. Campisi, P. Hänggi, and P. Talkner, Rev. Mod. Phys. **83**, 771 (2011).
[80] S. An, J.-N. Zhang, M. Um, D. Lv, Y. Lu, J. Zhang, Z.-Q. Yin, H. T. Quan, and K. Kim, Nat. Phys. **11**, 193 (2015).
[81] T. P. Xiong, L. L. Yan, F. Zhou, K. Rehan, D. F. Liang, L. Chen, W. L. Yang, Z. H. Ma, M. Feng, and V. Vedral, Phys. Rev. Lett. **120**, 010601 (2018).
[82] V. Viswanath and G. Müller, *The Recursion Method: Applications to Many-Body Dynamics* (Springer, New York, 2008).
[83] D. Mattis, *How to Reduce Practically Any Problem to One Dimension* (Springer Berlin Heidelberg, 1981).
[84] D. Parker, X. Cao, A. Avdoshkin, T. Scaffidi, and E. Altman, Phys. Rev. X **9**, 041017 (2019).
[85] C. W. von Keyserlingk, T. Rakovszky, F. Pollmann, and S. L. Sondhi, Phys. Rev. X **8**, 021013 (2018).
[86] A. Nahum, S. Vijay, and J. Haah, Phys. Rev. X **8**, 021014 (2018).
[87] T. Rakovszky, F. Pollmann, and C. W. von Keyserlingk, Phys. Rev. X **8**, 031058 (2018).
[88] V. Khemani, A. Vishwanath, and D. A. Huse, Phys. Rev. X **8**, 031057 (2018).
[89] S. Gopalakrishnan, D. A. Huse, V. Khemani, and R. Vasseur, Phys. Rev. B **98**, 220303 (2018).
[90] A. Chan, A. De Luca, and J. T. Chalker, Phys. Rev. X **8**, 041019 (2018).
[91] D. Abanin, W. De Roeck, and F. Huveneers, Phys. Rev. Lett. **115**, 256803 (2015).
[92] D. S. Lubinsky, Acta Applicandae Mathematica **33**, 121 (1993).
[93] A. Magnus, *Asymptotic Behaviour of Continued Fraction Coefficients Related to Singularities of the Weight Function* (Springer Berlin Heidelberg, 1987).
[94] X. Cao, Journal of Physics A: Mathematical and Theoretical **54**, 144001 (2021).
[95] A. Dymarsky and M. Smolkin, Phys. Rev. D **104**, L081702 (2021).
[96] J. D. Noh, Phys. Rev. E **104**, 034112 (2021).
[97] S. Trotzky, Y.-A. Chen, A. Flesch, I. P. McCulloch, U. Schollwöck, J. Eisert, and I. Bloch, Nat. Phys. **8**, 325 (2012).
[98] A. M. Kaufman, M. E. Tai, A. Lukin, M. Rispoli, R. Schittko, P. M. Preiss, and M. Greiner, Science **353**, 794 (2016).
[99] C. Gross and I. Bloch, Science **357**, 995 (2017).
[100] M. F. Parsons, F. Huber, A. Mazurenko, C. S. Chiu, W. Setiawan, K. Wooley-Brown, S. Blatt, and M. Greiner, Phys. Rev. Lett. **114**, 213002 (2015).
[101] D. Ohl de Mello, D. Schäffner, J. Werkmann, T. Preuschoff, L. Kohfahl, M. Schlosser, and G. Birkl, Phys. Rev. Lett. **122**, 203601 (2019).
[102] B. Bertini, F. Heidrich-Meisner, C. Karrasch, T. Prosen, R. Steinigeweg, and M. Žnidarič, Rev. Mod. Phys. **93**, 025003 (2021).
[103] J. Schnack, Contemporary Physics **60**, 127 (2019).
[104] J. Schnack, *Molecular magnetism* (Springer Berlin Heidelberg, 2004).
[105] R. Steinigeweg and H.-J. Schmidt, Mathematical Physics, Analysis and Geometry **12**, 19 (2009).
[106] W. Heisenberg, Zeitschrift für Physik **49**, 619 (1928).
[107] J. Vannimenus and G. Toulouse, Journal of Physics C: Solid State Physics **10**, L537 (1977).
[108] J. Schnack, Comptes Rendus Chimie **10**, 15 (2007).
[109] E. Ising, Zeitschrift für Physik **31**, 253 (1925).

[110] P. Jordan and E. Wigner, Zeitschrift für Physik **47** (1928).
[111] C. Runge, Mathematische Annalen **46**, 167 (1895).
[112] T. A. Elsayed and B. V. Fine, Phys. Rev. Lett. **110**, 070404 (2013).
[113] P. de Vries and H. De Raedt, Phys. Rev. B **47**, 7929 (1993).
[114] D. W. Berry, G. Ahokas, R. Cleve, and B. C. Sanders, Communications in Mathematical Physics **270**, 359 (2007).
[115] A. Nauts and R. E. Wyatt, Phys. Rev. Lett. **51**, 2238 (1983).
[116] H. Tal-Ezer and R. Kosloff, The Journal of Chemical Physics **81**, 3967 (1984).
[117] R. Kosloff, Annual Review of Physical Chemistry **45**, 145 (1994).
[118] V. V. Dobrovitski and H. A. De Raedt, Phys. Rev. E **67**, 056702 (2003).
[119] T. J. Rivlin, *The Chebyshev Polynomials* (John Wiley and Sons Inc., 1974).
[120] P. L. Chebyshev, Acta Mathematica **7**, 539–586 (1854).
[121] J. Mason and D. Handscomb, *Chebyshev Polynomials* (Chapman and Hall, 2002).
[122] C. Lanczos, Journal of Research of the National Bureau of Standards **45**, 255 (1950).
[123] R. Schnalle and J. Schnack, International Reviews in Physical Chemistry **29**, 403 (2010).
[124] M. Rigol, T. Bryant, and R. R. P. Singh, Phys. Rev. Lett. **97**, 187202 (2006).
[125] B. Tang, E. Khatami, and M. Rigol, Computer Physics Communications **184**, 557 (2013).
[126] U. Schollwöck, Annals of Physics **326**, 96 (2011).
[127] S. Paeckel, T. Köhler, A. Swoboda, S. R. Manmana, U. Schollwöck, and C. Hubig, Annals of Physics **411**, 167998 (2019).
[128] J. Dehaene and B. De Moor, Phys. Rev. A **68**, 042318 (2003).
[129] L. P. García-Pintos, N. Linden, A. S. L. Malabarba, A. J. Short, and A. Winter, Phys. Rev. X **7**, 031027 (2017).
[130] L. V. Hove, Physica **23**, 441 (1957).
[131] C. Bartsch, R. Steinigeweg, and J. Gemmer, Phys. Rev. E **77**, 011119 (2008).
[132] E. Joos, H. D. Zeh, C. Kiefer, D. J. W. Giulini, J. Kupsch, and I. O. Stamatescu, *Decoherence and the Appearance of a Classical World in Quantum Theory* (Springer Berlin Heidelberg, 2003).
[133] U. Weiss, *Quantum Dissipative Systems* (World Scientific, 2012).
[134] L. Dabelow and P. Reimann, Phys. Rev. Lett. **124**, 120602 (2020).
[135] J. Richter, F. Jin, L. Knipschild, H. De Raedt, K. Michielsen, J. Gemmer, and R. Steinigeweg, Phys. Rev. E **101**, 062133 (2020).
[136] L. Knipschild and J. Gemmer, Phys. Rev. A **99**, 012118 (2019).
[137] J. Richter et. al, Phys. Rev. B **99**, 144422 (2019).
[138] R. Clausius, *The Mechanical Theory of Heat,* (London: Taylor and Francis, 1867).
[139] E. Iyoda, K. Kaneko, and T. Sagawa, Phys. Rev. Lett. **119**, 100601 (2017).
[140] P. Talkner, P. Hänggi, and M. Morillo, Phys. Rev. E **77**, 051131 (2008).
[141] P. Talkner, M. Morillo, J. Yi, and P. Hänggi, New Journal of Physics **15**, 095001 (2013).
[142] B. Cleuren, C. Van den Broeck, and R. Kawai, Phys. Rev. Lett. **96**, 050601 (2006).
[143] S. Cusumano, V. Cavina, M. Keck, A. De Pasquale, and V. Giovannetti, Phys. Rev. A **98**, 032119 (2018).
[144] K. Ptaszyński and M. Esposito, Phys. Rev. Lett. **122**, 150603 (2019).
[145] E. Iyoda, K. Kaneko, and T. Sagawa, Phys. Rev. E **105**, 044106 (2022).
[146] K. Kaneko, E. Iyoda, and T. Sagawa, Phys. Rev. E **96**, 062148 (2017).
[147] J. Gemmer, L. Knipschild, and R. Steinigeweg, arXiv:1712.02128 (2017).
[148] A. Avdoshkin and A. Dymarsky, Phys. Rev. Research **2**, 043234 (2020).
[149] P. W. Anderson, Phys. Rev. **109**, 1492 (1958).
[150] L. Dabelow, P. Vorndamme, and P. Reimann, Phys. Rev. Research **2**, 033210 (2020).
[151] L. Dabelow and P. Reimann, Journal of Statistical Mechanics: Theory and Experiment **2021**, 013106 (2021).

Acknowledgments

This work would not exist in its current form without the help, support and encouragement of many co-authors, colleagues and friends. It is my pleasure to acknowledge and thank all these people who impacted the outcome of this dissertation in a positive way.

First and foremost, I feel truly grateful to my supervisor Jochen Gemmer. Thank you for almost daily discussions in which I benefitted very much from your great physical insight, for countless entertaining coffee breaks and for helping me route through the academic and scientific world. Your guidance left nothing to be desired and I can say that from our collaboration I will take more with me than just knowledge about physics.

Further, I would like to extend my gratitude to Robin Steinigeweg for many interesting discussions on and off physics, for his openness to answer questions at any time as well as for agreeing to write the second report on this thesis.

I would also like to thank Prof. Dr. Joachim Wollschläger and Dr. Stefan Korte for agreeing to be part of the PhD committee.

Thanks is due to my predecessor and former office mate Lars Knipschild, who really helped me ease into my PhD. Thank you for always making time to answer my numerous questions of varying cleverness.

I give thanks to my current office mate Jiaozi Wang, who will already have computed the numerical data before you even know that you needed it. Thank you for many enjoyable discussions on chess and the state of the chinese national football team. All the best for your further academic career!

Much gratitude is owed to Tjark Heitmann, who was there from the very beginning. Thank you for making this journey with me, starting in Bielefeld and going as far as Norway. Your LaTeX wizardry is much appreciated.

I would like to extent thanks to Dennis Schubert, who arrived in Osnabrück at the same time as Tjark and myself. Thank you for the time we spent together and I hope you have some exceptional experiences on your world tour!

I am also grateful to my further (former) colleagues Jonas Richter, Mats Lamann and Christian Bartsch as well as all members of the research unit FOR2692, especially Jürgen Schnack for piquing my interest in non-equilibrium quantum mechanics and for establishing the connection to Osnabrück.

I would like to express my deep gratitude to my parents and my brother, on whom I know I can always rely. Thank you so much for your continued support throughout all these years!

Lastly, I am ever so grateful to my lovely Nadine for being understanding when my mind was preoccupied, reminding me what is important (besides physics) and simply always being there for me.

Preprint of Publication [P1]

Robin Heveling, Lars Knipschild, and Jochen Gemmer
"Compelling bounds on equilibration times - the issue with Fermi's golden rule"
Journal of Physics A: Mathematical and Theoretical **53**, 375303 (2020)
DOI: 10.1088/1751-8121/ab9e2b

Compelling Bounds on Equilibration Times - the Issue with Fermi's Golden Rule

Robin Heveling,* Lars Knipschild,† and Jochen Gemmer‡
Department of Physics, University of Osnabrück, D-49069 Osnabrück, Germany

Putting a general, physically relevant upper bound on equilibration times in closed quantum systems is a recently much pursued endeavor. In PRX, 7, 031027 (2017) García-Pintos et al. suggest such a bound. We point out that the general assumptions which allow for an actual estimation of this bound are violated in cases in which Fermi's Golden Rule and related open quantum system theories apply. To probe the range of applicability of Fermi's Golden Rule for systems of the type addressed in the above work, we numerically solve the corresponding Schrödinger equation for some finite spin systems comprising up to 25 spins. These calculations shed light on the breakdown of standard quantum master equations in the "superweak" coupling limit, which occurs for finite sized baths.

I. INTRODUCTION

The last decades have seen a major progress in the field of equilibration in closed quantum systems [1]. Concepts like typicality [2–4] and the eigenstate thermalization hypothesis [5, 6] have been brought forth. Furthermore, it has been established that for an initial state ρ populating many energy levels, expectation values $\langle A(t)\rangle$ will generically be very close to their temporal averages for most times within the interval to which the average refers ("equilibration on average"). While the conditions for this statement to be true are rather mild concerning the observable A and the Hamiltonian H [7–9], the respective time interval may be very large. For specific observables it may, e.g., scale with the dimension of the relevant Hilbert space [10, 11]. Moreover, concrete examples are known in which the corresponding equilibration times for physically relevant observables scale as $T_{\mathrm{eq}} \propto N^{\alpha}$, $\alpha \geq 1/2$, where N is the size of the system. This result has been found for systems featuring long range [12] as well as short range interactions [13], albeit for a somewhat different definitions of equilibration times. In fact, already for mesoscopic many-body systems with standard interaction strengths, the required equilibration interval may be on the order of the age of the universe [12]. Thus, although the above statements in some sense establish equilibration under moderate conditions in the very long run, it is unclear whether or not this equilibration will ever occur in a physically relevant period of time. Hence, the question of an upper bound on this relaxation timescale has recently been much discussed. Since it is always possible to find mathematically well defined, permissible initial states that fully exhaust the above, unsatisfactorily large time interval, most contributions focus on additional, physically plausible conditions. These conditions, which are intended to capture the actual, physical state of affairs, may be imposed on the initial state, the observable, the structure of the system, or combinations thereof [14–19]. In the present paper we primarily discuss results from Ref. [20]. The latter rests on assumptions on all of the above.

This paper is organized as follows: In Sect. II we briefly present a main result from Ref. [20]. Furthermore, we elaborate on the lack of predictive power of this result in cases in which Fermi's Golden Rule applies. In Sect. III we explain some models, each of which comprises a single spin in a magnetic field interacting with a (finite) bath, consisting of spins itself. We initialize the system in a standard system-bath product state and numerically solve the Schrödinger equation, monitoring the system's spin component parallel to the magnetic field. These data unveil the regime of validity of Fermi's Golden Rule with respect to the crucial system parameters. Sect. IV discusses the scaling of the critical interaction strength at which open system predictions start to become unreliable. In Sect. V the implications of the numerical findings from Sect. III on the assumptions and statements from Ref. [20] are named and explained. Eventually, we sum up and conclude in Sect. VI.

II. GARCÍA-PINTOS BOUND AND FERMI'S GOLDEN RULE

To begin with, we state the main result of Ref. [20] (hereafter called the García-Pintos bound (GPB)) in a comprehensive form. The GPB addresses an equilibration time T_{eq}. To further specify T_{eq} we introduce some notation. Let ρ be the initial state of the system. Furthermore, let $A(t)$ denote an observable A in the Heisenberg picture and $\langle A(t)\rangle := \mathrm{Tr}\{A(t)\rho\}$ its time dependent expectation value. Because the closed system dynamics is unitary (and the system is finite), $\langle A(t)\rangle$ has a well de-

* rheveling@uos.de
† lknipschild@uos.de
‡ jgemmer@uos.de

fined "infinite time average" $\overline{\langle A\rangle} =: \langle A\rangle_{\rm eq}$, which is routinely considered as the equilibrium value of A in case the observable A equilibrates at all [9]. Now, consider a deviation $D(t)$ of the actual expectation value from its equilibrium, i.e., $D(t) := (\langle A(t)\rangle - \langle A\rangle_{\rm eq})^2/4||A||^2$, where $||A||$ is the largest absolute eigenvalue of A. Moreover, consider an average of $D(t)$ over the time interval $[0,T]$ denoted by $\overline{D}_T$. The condition that defines $T_{\rm eq}$ is that $\overline{D}_T \ll 1$ must hold for $T \gg T_{\rm eq}$ (for non-equilibrating systems such a $T_{\rm eq}$ may not exist [9]). The GPB is an explicit expression for such a $T_{\rm eq}$ (see Eq. (4)), based on $\rho, A(0)$ and H, where H is the Hamiltonian of the system. As the GPB involves somewhat refined functions of the above three operators, we need to specify these before stating the GPB explicitly. A central role is taken by the probability distribution p_{jk}, which is defined as

$$\begin{aligned} p_{jk} \propto |\rho_{jk}A_{kj}| \quad &\text{for} \quad E_j - E_k \neq 0\,, \\ p_{jk} = 0 \quad &\text{for} \quad E_j - E_k = 0\,, \quad \sum_{j,k} p_{jk} = 1\,, \end{aligned} \tag{1}$$

where E_j, E_k are energy eigenvalues corresponding to energy eigenstates $|j\rangle, |k\rangle$. Furthermore, matrix elements are abbreviated as $\rho_{jk} := \langle j|\rho|k\rangle, A_{jk} := \langle j|A(0)|k\rangle$. While the GPB is not limited to this case, here, we focus on the p_{jk} that may be described in terms of a probability density function $w(G)$. All examples we present below conform with such a description and it is plausible that this applies to many generic many-body scenarios. Prior to defining $w(G)$, we define $w(G,\epsilon)$ as

$$w(G,\epsilon) := \frac{1}{\epsilon}\sum_{j,k} \Theta\Big(\frac{\epsilon}{2} - |E_j - E_k - G|\Big)\, p_{jk}\,, \tag{2}$$

where Θ is the Heaviside function. This definition is the standard construction of a histogram in which the p_{jk} are sorted according to their respective energy differences $E_j - E_k$. It is now assumed that there exists a range of (small but not too small) ϵ such that $w(G,\epsilon)$ is essentially independent of variations of ϵ within this range. The $w(G,\epsilon)$ from this "independence regime" are simply abbreviated as $w(G)$. Let the standard deviation of $w(G)$ be denoted by σ_G. Additionally, let $w_{\rm max}$ denote the maximum of $w(G)$. The quantities a and Q that eventually enter the GPB are now defined as

$$a := w_{\rm max}\sigma_G\,, \quad Q := \sum_{i,j:E_i\neq E_j} \frac{|\rho_{ij}A_{ji}|}{||A||}\,. \tag{3}$$

We can now state the GPB:

$$T_{\rm eq} = \frac{\pi a||A||^{1/2}Q^{5/2}}{\sqrt{|{\rm Tr}([[\rho,H],H]A)|}} = \frac{\pi a||A||^{1/2}Q^{5/2}}{\sqrt{|\frac{{\rm d}^2}{{\rm d}t^2}\langle A(t)\rangle\big|_{t=0}|}}\,. \tag{4}$$

Obviously, the GPB links $T_{\rm eq}$ to the initial "curvature" of the observable dynamics $\partial_t^2\langle A(t)\rangle|_{t=0}$ (which is practically accessible, cf. Fig. 7). An actual, concrete bound on the equilibration time by means of $T_{\rm eq}$, however, only arises from Eq. (4) if the numerator can be shown to be in an adequate sense small or at least bounded. This is a pivotal feature on which the "predictive power" of the GPB hinges. The crucial quantities in the numerator are a and Q. As it is practically impossible to calculate a from its definition for many-body quantum systems, García-Pintos et al. instead offer an assumption.

They argue that $a \sim 1$ may be expected for $w(G)$ that are "unimodal". Unimodal means that $w(G)$ essentially consists of one central elevation like a Gaussian or a box distribution, etc. Indeed, a is invariant with respect to a rescaling as $w(G) \to sw(sG)$, as it would result from rescaling the Hamiltonian as $H \to sH$ (here s is some real, positive number). García-Pintos et al. also offer various upper bounds on Q for different situations.

In the remainder of this section, we explain in which sense the conclusiveness of the GPB is in conflict with Fermi's Golden Rule (FGR). Let us stress that this conflict does not concern the validity or correctness of Eq. (4) as such, the latter is undisputed. It only concerns the assumptions on a and Q, which are required to find an actual value or estimate for $T_{\rm eq}$. (Note that there is some evidence (cf. Sect. V) that specifically the assumption on a is violated, rather than the assumption on Q). Consider a Hamiltonian consisting of an unperturbed part H_0 and a perturbation $H_{\rm int}$.

$$H = H_0 + \lambda H_{\rm int} \tag{5}$$

Furthermore, consider an observable A, which is conserved under H_0, i.e. $[A, H_0] = 0$. If H_0 has a sufficiently wide and dense spectrum and λ is small, FGR may apply under well investigated conditions [21–23]. The applicability of the FGR approach yields, in the simplest case, a monoexponential decay, i.e.

$$\langle A(t)\rangle = (\langle A(0)\rangle - \langle A\rangle_{\rm eq})e^{-t/\tau_{\rm rel}} + \langle A\rangle_{\rm eq}\,, \tag{6}$$

where $\tau_{\rm rel} := r\lambda^{-2}$ and r is a real, positive number that depends on H_0 and $H_{\rm int}$. More refined approaches, such as the Weisskopf-Wigner theory or open quantum system approaches, also arrive at such exponential decay dynamics [24, 25]. In the relevant case $\partial_t\langle A(t)\rangle|_{t=0} = 0$, obviously Eq. (6) cannot apply at $t = 0$. In this case Eq. (6) is meant to apply after a short "Zeno time" $\tau_{\rm zeno}$ that is often very short compared to the relaxation time $\tau_{\rm rel}$ [23]. (Note, however, that the denominator of Eq. (4) addresses a time below the Zeno time, if the latter is nonzero). We now aim to find the principal dependence of quantities in Eq. (4) on the interaction strength λ. While the definition of $T_{\rm eq}$ as given at the beginning of the present Sect. does not fix the relation of $\tau_{\rm rel}$ and $T_{\rm eq}$

rigorously, for exponential decays it appears plausible to require at least

$$T_{\mathrm{eq}} \geq \tau_{\mathrm{rel}}\,. \tag{7}$$

For the denominator of Eq. (4) we find with Eq. (5)

$$\sqrt{\left|\frac{\mathrm{d}^2}{\mathrm{d}t^2}\langle A(t)\rangle\big|_{t=0}\right|} = \sqrt{|c_1\lambda + c_2\lambda^2|}\,, \tag{8}$$

where $c_1 = \mathrm{Tr}([H_{\mathrm{int}}, A][\rho, H_0])$, $c_2 = \mathrm{Tr}([H_{\mathrm{int}}, A][\rho, H_{\mathrm{int}}])$. Plugging Eqs. (6, 7, 8) into Eq. (4) yields

$$\pi a ||A||^{1/2} Q^{5/2} \geq r\frac{\sqrt{|c_1\lambda + c_2\lambda^2|}}{\lambda^2} \tag{9}$$

for the numerator of Eq. (4). Obviously, the numerator of Eq. (4) diverges in the limit of weak interactions, i.e. $\lambda \to 0$. The latter holds even if $c_1 = 0$. This contradicts the central assumption behind the GPB as outlined below Eq. (4). Hence, the validity of FGR in the weak coupling limit and a conclusive applicability of the GPB are mutually exclusive. This is the first main result of the present paper. Note that, in the above scenario, the exponential decay is due to some small "conservation breaking" part of the Hamiltonian. However, exponential decay also often occurs without some part of the Hamiltonian being particularly small, e.g., slow Fourier modes in sufficiently large systems. Although the practical success of FGR is beyond any doubt, the theoretical applicability of FGR rests on various assumptions on the system in question, so does the applicability of standard open system methods. In order to learn about the applicability of either the GPB or FGR from considering examples, we analyze some spin systems in the following Sect. III by numerically solving the respective Schrödinger equations. This analysis is comparable to numerical investigations performed in Ref. [20]. However, other than García-Pintos et al. we analyze the weak coupling limit and consider system sizes that are too large to allow for numerically exact diagonalization of the respective Hamiltonians.

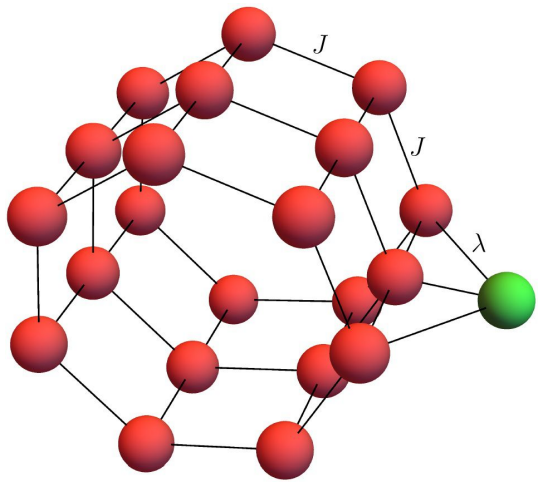

Figure 1. Single system spin (green) and spin-bath (red) interact with strength λ. Solid black lines indicate isotropic Heisenberg interactions.

III. NUMERICAL SPIN-BASED EXPERIMENTS PROBING EQUILIBRATION TIMES

While we analyze a number of concretely specified models below, it is important to note that these models just represent some generic instances of the system-bath scenarios which are routinely considered in open quantum system theory. The (non-integrable) baths share some properties with standard solid state systems, like periodicity and locality (in this respect they differ from the otherwise comparable models from Refs. [26–28]). Other than that, the details of our modeling are not peculiar at all. We varied details of the bath Hamiltonians in piecemeal fashion and found all below results unaltered (cf. App. C). Our archetypal model is an isotropic spin-1/2 Heisenberg system, consisting of a single system spin coupled to a bath. The bath is rectangularly shaped with $3 \times L$ spins and features periodic boundary conditions in the longitudinal direction resulting in a wheel-like structure (cf. Fig. 1). Thus, the total number of spins is given by $N = 3L + 1$. The single system spin is subject to an external magnetic field in the z-direction and interacts with three neighboring bath spins in the transverse direction. This model is non-integrable in the sense of the Bethe-Ansatz.
The bath Hamiltonian reads

$$\begin{aligned} H_{\mathrm{bath}} = J\sum_{r=1}^{3}\sum_{i=1}^{L}\left(S^x_{i,r}S^x_{i+1,r} + S^y_{i,r}S^y_{i+1,r} + S^z_{i,r}S^z_{i+1,r}\right) \\ + J\sum_{i=1}^{L}\left(S^x_{i,1}S^x_{i,2} + S^y_{i,1}S^y_{i,2} + S^z_{i,1}S^z_{i,2}\right) \\ + J\sum_{i=1}^{L}\left(S^x_{i,2}S^x_{i,3} + S^y_{i,2}S^y_{i,3} + S^z_{i,2}S^z_{i,3}\right), \end{aligned} \tag{10}$$

where $S^{x,y,z}_{i,r}$ are spin-1/2 operators at site (i, r) and $L + 1 \equiv 1$. The exchange coupling constant J as well as $\hbar$ are set to unity. The Hamiltonian of the system is given by

$$H_{\mathrm{sys}} = BS^z_{\mathrm{sys}}\,, \tag{11}$$

where $S^{x,y,z}_{\mathrm{sys}}$ denote the spin-1/2 operators of the additional system spin and $B = 0.5$.

The interaction between bath and system is described by the Hamiltonian

$$H_{\text{int}} = \Big[\big(S^x_{1,1} + S^x_{1,2} + S^x_{1,3}\big) S^x_{\text{sys}} + \big(S^y_{1,1} + S^y_{1,2} + S^y_{1,3}\big) S^y_{\text{sys}} + \big(S^z_{1,1} + S^z_{1,2} + S^z_{1,3}\big) S^z_{\text{sys}} \Big] \tag{12}$$

and contributes with a factor λ to the total Hamiltonian

$$H = H_{\text{sys}} + H_{\text{bath}} + \lambda H_{\text{int}} \,. \tag{13}$$

The considered initial states are product states of a system state $\pi_\uparrow$ and a bath state $\pi_{E,\delta}$. This corresponds to a situation where system and bath are initially uncorrelated and then brought into contact via H_{int} at $t = 0$. The system state is a projector onto the S^z_{sys}-eigenstate corresponding to spin-up. The bath state $\pi_{E,\delta}$ is a projector onto a (small) energy window of width δ centered around a mean energy E.

$$\rho = \frac{\pi_\uparrow \otimes \pi_{E,\delta}}{\text{Tr}\{\pi_\uparrow \otimes \pi_{E,\delta}\}} \tag{14}$$

Concretely, we fix the width of the energy window $\delta = 0.1$, which is very small compared to the scale of the full energy spectrum of the bath. Given the size of the systems, it comprises nevertheless a very large number of energy eigenstates. To keep track of finite size effects, we increment the baths circumference L in steps of size one, thus adding three spins to the bath in each step. An inverse temperature β is defined as $\partial_E \log \Omega(E)$, where $\Omega(E)$ is the density of states of the bath at energy E. This "microcanonical" definition of temperature is also employed in Ref. [20]. For comparability of different bath sizes we aim at keeping β fixed while incrementing the bath size. As H_{bath} is local, the bath energy is expected to scale linearly with the bath size. Hence, we choose a scaling of the initial bath energy as $E \approx -0.15(N-1)$, which corresponds to choosing $\beta \approx 0.4$. Given these specifications of the Hamiltonian and the initial state, we numerically solve the corresponding Schrödinger equation and monitor the expectation value of the z-component of the magnetization of the system-spin, i.e. $\langle S^z_{\text{sys}}(t)\rangle$. Some results are displayed in Fig. 2 for a schematic overview. In accord with open quantum system theory, these results suggest to distinguish three cases.

i. *non-Markovian regime*: For strong coupling (e.g. $\lambda = 1.0$) the magnetization quickly decays to the equilibrium value, i.e. $\langle S^z_{\text{sys}}\rangle_{\text{mc}}$, in a nonexponential way. The description of these dynamics requires the incorporation of memory effects in some way. While this is a very active field in open quantum theory, we do not investigate this regime any further in the present paper.

ii. *Markovian regime*: For weak coupling (e.g. $\lambda = 0.1$) there is a monoexponential decay to the thermal equilibrium. This exponential decay is in full accord with FGR. A large number of systems ranging from quantum optics to condensed matter fall into this regime [25, 29]. It also largely coincides with the field of quantum semigroups and the Lindblad approach.

iii. *superweak coupling regime*: For very weak coupling (e.g. $\lambda = 0.01$) the magnetization does not decay to the thermal equilibrium value at all, it rather gets stuck at

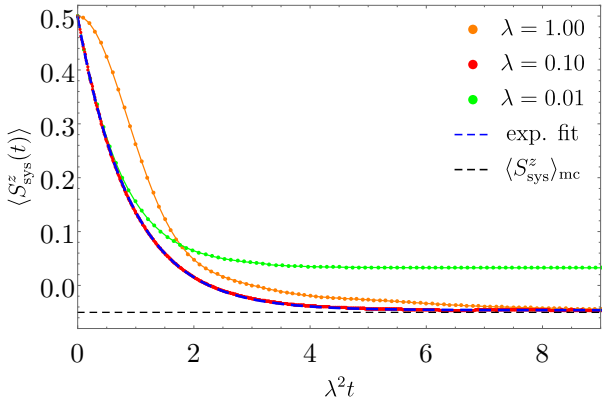

Figure 2. Decay of the magnetization for $N = 25$. For strong coupling (e.g. $\lambda = 1.0$) the magnetization decays quickly and nonexponentially to the thermal expectation value. Note that the time axis is scaled with λ^2. For weak coupling (e.g. $\lambda = 0.1$) the magnetization decays exponentially towards the thermal equilibrium value. For very weak coupling (e.g. $\lambda = 0.01$) the magnetization gets stuck at a non-thermal longtime average value.

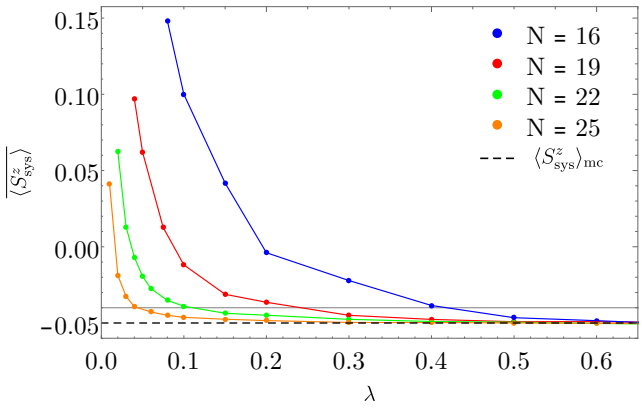

Figure 3. Longtime average value of the magnetization plotted over the interaction strength λ for various bath sizes. For sufficiently strong coupling the system thermalizes for all bath sizes. For sufficiently weak coupling the magnetization gets stuck for all bath sizes.

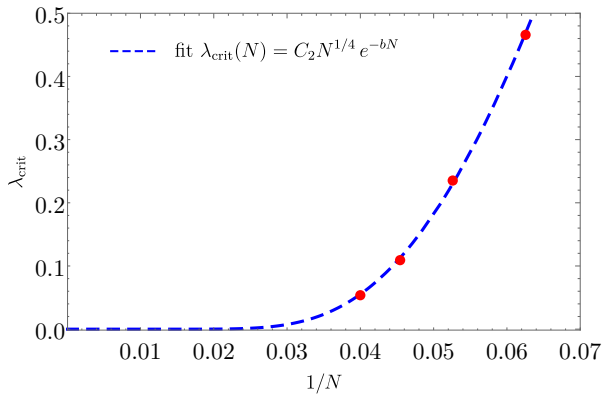

Figure 4. Critical interaction strength plotted over inverse system size. The data is fitted as $\lambda_{\rm crit}(N) = C_2 N^{1/4} \exp^{-bN}$ with fit parameters $C_2 = 12.7$ and $b = 0.25$. The principal form of this fit is motivated in Sect. IV.

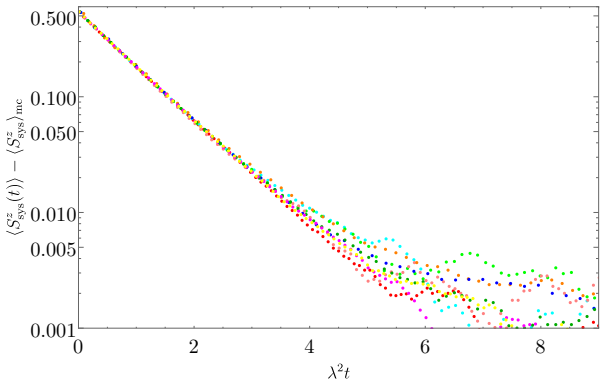

Figure 5. Various exponential decays from the Markovian regime logarithmically plotted. Depicted are 9 curves; for $N = 22$ ($N = 25$) the curves for $\lambda = 0.2, 0.15, 0.1$ ($\lambda = 0.3, 0.2, 0.15, 0.1, 0.08, 0.06$) are shown. For short times the collapse is evident, at $t \sim 5$ quantum fluctuations become more prominent.

a value closer to the initial value, which indicates the breakdown of FGR. This value depends on the interaction strength and on the bath size. In accord with standard open quantum system theory, our below results indicate that this regime only exists for finite baths. We are not aware of any systematic approach to this regime in the literature to date. As the conflict between the GPB and FGR arises in the limit of weak interactions, cf. Eq. (9), we are primarily interested in the transition from the Markovian to the superweak regime. A prime indicator of superweak dynamics is, as mentioned, that $\langle S^z_{\rm sys}(t)\rangle$ no longer decays down to the microcanonical expectation value $\langle S^z_{\rm sys}\rangle_{\rm mc} = -0.05$ as it does in the non-Markovian and the Markovian regime. Fig. 3 shows the longtime average value of the magnetization plotted over the interaction strength λ for various bath sizes. For sufficiently strong coupling the magnetization decays to the thermal equilibrium value for all bath sizes. For each bath size there exists a critical interaction strength $\lambda_{\rm crit}$, below which the magnetization gets stuck at a non-thermal longtime average value, thus signaling the transition from the Markovian to the superweak regime. This critical interaction strength $\lambda_{\rm crit}$ decreases with bath size. We chose $\overline{\langle S^z_{\rm sys}\rangle} = -0.04$ (horizontal grey line) to define $\lambda_{\rm crit}$. This choice is quite arbitrary, but it turns out that the below scaling of $\lambda_{\rm crit}$ is rather insensitive to the exact positioning of this threshold, as long as it is sufficiently close to the thermal equilibrium value. This finding is corroborated in App. D, where the scaling of the fit parameters C_2 and b with the critical threshold value of $\overline{\langle S^z_{\rm sys}\rangle}$ is shown. Obviously, one expects $\overline{\langle S^z_{\rm sys}\rangle} \to 0.5$ as $\lambda \to 0$. Fig. 4 displays the critical interaction strength plotted over the inverse system size. It strongly suggests that $\lambda_{\rm crit} \to 0$ very quickly with increasing bath size N. Hence, for all mesoscopic to macroscopic systems, and even more so in the thermodynamic limit, the transition to the superweak regime practically never occurs, such that behavior other than Markovian can hardly be expected even for physically very weak interactions. While this finding is another main result of the quantitative analysis at hand, it qualitatively hardly comes as a surprise in a larger context, given the practical success of Markovian quantum master equations. However, to elaborate on this result somewhat further, we present a theory that captures the data in Fig. 4 rather accurately in Sect. IV. Next we confirm the validity of FGR in the Markovian regime and discuss relaxation/equilibration times in all regimes. The motivation for the latter is twofold: On the one hand equilibration times enter the GPB (cf. Eq. (4)), on the other hand the scaling of equilibration times with the interaction strength may serve as a additional, quantitative indicator for the validity of FGR. Fig. 5 displays the observable dynamics $\langle S^z_{\rm sys}(t)\rangle$ for all 11 interaction strengths and bath sizes from the Markovian regime, which is lower bounded by $\lambda_{\rm crit}$ as determined from Fig. 4 and upper bounded by $\lambda_{\text{non-Mark}} \approx 0.3$ for all N. Note the the time axis is scaled with the squared interaction strength such that a collapse of the data onto one decaying exponential indicates the accordance with Eq. (6) and hence FGR. This collapse is evident.

In Fig. 6 the relaxation time $\tau_{\rm rel}$ is plotted over λ^{-2}. Here $\tau_{\rm rel}$ is the time at which the magnetization has decayed to $1/e$ of its original value relative to the equilibrium value (cf. Eq. (6)). In the Markovian regime, i.e. for $\lambda^{-2}_{\text{non-Mark}} \leq \lambda^{-2} \leq \lambda^{-2}_{\rm crit}$, the relaxation time scales as $\tau_{\rm rel} \sim \lambda^{-2}$, as predicted by FGR, which also confirms the applicability of FGR in the Markovian regime. At very small λ, i.e. in the superweak coupling regime, $\tau_{\rm rel}$

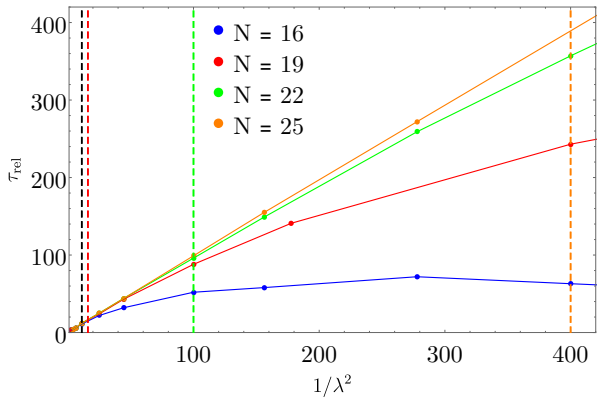

Figure 6. Relaxation time plotted over the inverse interaction strength squared for various bath sizes. Left of the vertical dashed black line lies the non-Markovian regime. Between the vertical dashed black line and the vertical dashed colored lines lies the respective Markovian regime, i.e, the vertical dashed colored lines indicate the corresponding $\lambda_{\rm crit}^{-2}$'s. For $N = 16$ the Markovian regime does not exist. Within the respective Markovian regimes $\tau_{\rm rel} \approx 0.95\lambda^{-2}$ holds for all system sizes in accord with FGR.

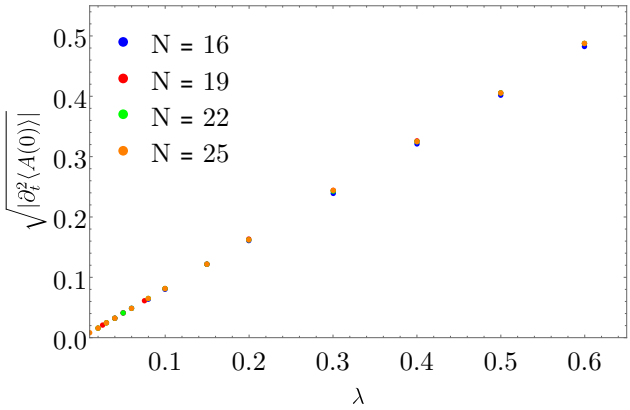

Figure 7. Square root of the initial curvature of the observable dynamics at $t = 0$ plotted over the interaction strength. The data indicate that this quantity is independent of the system size in all regimes of the interaction strength.

first increases more slowly with increasing λ^{-2} and likely eventually even decreases to zero. From the data displayed in Fig. 6 this behavior is, however, qualitatively only visible for $N = 16$ due to numerical limitations at extremely small λ. Eventually, we directly numerically probe the connection between short time and long time dynamics suggested in Eq. (4). To this end we compute the "initial curvatures" $\sqrt{|\partial_t^2\langle A(t)\rangle|_{t=0}|}$ for various interaction strengths and systems sizes. The result is displayed in Fig. 7. As expected from Eq. (8), and in full accord with a corresponding statement in Ref. [20], the square root of the initial curvature scales linearly with λ and is practically independent of the system size. We are now set to assess the crucial numerator from Eq. (4) numerically. From Eqs. (4, 7) follows

$$\pi a ||A||^{1/2} Q^{5/2} = T_{\rm eq} \sqrt{\left|\frac{{\rm d}^2}{{\rm d}t^2}\langle A(t)\rangle\big|_{t=0}\right|} \geq \tau_{\rm rel} \sqrt{\left|\frac{{\rm d}^2}{{\rm d}t^2}\langle A(t)\rangle\big|_{t=0}\right|}. \tag{15}$$

The lower bound to the numerator is displayed in Fig. 8. Recall that for a conclusive application of the GPB this numerator must be appropriately upper bounded. Correspondingly, Ref. [20] offers estimates for both a and Q. While $a \sim 1$ is simply traced back to the unimodality of w, the discussion on the order of magnitude of Q is quite involved. However, in the case of weak interactions, a microcanonical initial bath state comprising a large number of energy eigenstates, and an exponentially growing density of states in the bath (with an exponent β which is not too large), Q may also be expected to be of order unity, according to Ref. [20]. All these conditions apply to the models at hand. However, quite in contrast we find that the numerator grows at least up to values of ca. 55 already for $N = 25$ and interactions within the range of our numerical accessibility. Moreover, the data do not indicate any "nearby" upper bound of the numerator at 55. This is at odds with a conclusive application of the GPB and another main result of the present paper. Large numerators must occur, as outlined in Sect. II, for large systems in the Markovian regime on the verge to the superweak regime.

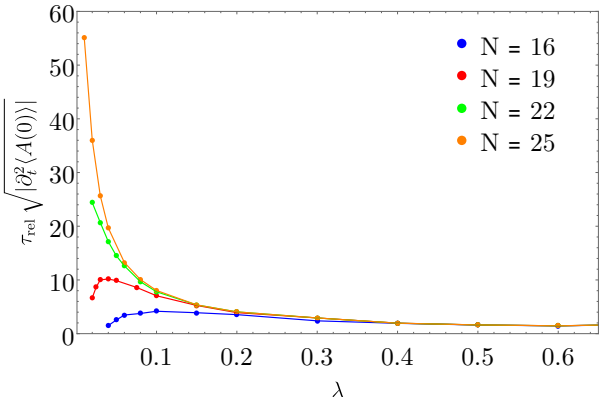

Figure 8. Numerator of Eq. (4), i.e, the central quantity of the GPB plotted over the interaction strength. The numerator reaches values substantially larger than unity. The increase of the numerator with decreasing λ extends into the superweak regime.

Although Fig. 8 indicates that in the outer mathematical limit (which may be considered to be physically less relevant) $\lambda \to 0$, the numerator may eventually be of order unity, its growth appears to continue substantially into the superweak regime. While we are unable to verify this directly, it appears plausible that the unbound growth of the numerator is due to an unbound growth of a, while $Q \sim 1$ may very well hold. We argue for this plausibility in Sect. V.

We sum up this section as follows: In a potentially wide regime of interaction strengths, which is lower bounded by λ_{crit}, FGR is found to apply as suggested by standard open quantum system theory in the Markovian regime. The lower bound appears to decrease rapidly with system size N (cf. also Sect. IV), making it practically irrelevant for mesoscopic and macroscopic systems. This relates to the GPR inasmuch as the validity of FGR implies the breakdown of the practical applicability of the GPB at sufficiently weak interactions. We numerically confirmed the occurrence of this breakdown directly for a system comprising $N = 25$ spins.

IV. GENERAL SCALING OF λ_{crit} WITH TOTAL SYSTEM SIZE

While the results on λ_{crit} in Fig. 4 are model dependent, a similar scaling may be expected whenever H_{int} complies with the eigenstate thermalization hypothesis. This claim is substantiated in the following. The starting point is the assumption that within the superweak regime, the overlap of the eigenstates of the uncoupled system $|n, \mathrm{sys} + \mathrm{bath}\rangle$ and those of the full system $|n, \mathrm{sys} + \mathrm{bath} + \mathrm{int}\rangle$ is relatively large, i.e.

$$|\langle n, \mathrm{sys} + \mathrm{bath} | n, \mathrm{sys} + \mathrm{bath} + \mathrm{int}\rangle| \approx 1 \,. \tag{16}$$

A strong indication for this to occur, arises from the leading order contributions to a perturbative correction to the eigenstates being small. This condition may, according to textbook level perturbation theory, be approximated as

$$\lambda^2 \sum_{m \neq n} \frac{|\langle m, \mathrm{s} + \mathrm{b} | H_{\mathrm{int}} | n, \mathrm{s} + \mathrm{b}\rangle|^2}{((m-n)\frac{1}{\Omega(N,\beta)})^2} \ll 1 \,, \tag{17}$$

where $\Omega(N, \beta)$ is the density of states of a system comprising N spins (or other similar subsystems) at the energy that corresponds to the inverse temperature β. In Eq. (17) it is assumed that the level spacing within the relevant energy regime may be approximated as being constant. In this case the "mean" level spacing is given by $1/\Omega(N, \beta)$. Following the eigenstate thermalization hypothesis ansatz [30] we furthermore assume that there exists a typical value for the absolute squares of the matrix elements of the coupling operator, which varies with the energies E_n, E_m only on energy scales much larger than the one relevant here. Furthermore, the eigenstate thermalization hypothesis suggests a specific scaling of these matrix elements with the density of states. Following the eigenstate thermalization hypothesis we thus assume

$$|\langle m, \mathrm{sys} + \mathrm{bath} | H_{\mathrm{int}} | n, \mathrm{sys} + \mathrm{bath}\rangle|^2 \approx \frac{C_1}{\Omega(N, \beta)} \,, \tag{18}$$

where C_1 is some real constant.

Exploiting this, Eq. (17) turns into

$$\lambda^2 C_1 \Omega(N, \beta) \sum_{k \neq 0} \frac{1}{k^2} \ll 1 \,. \tag{19}$$

As the sum assumes the finite value $\pi^2/3$, we conclude

$$\lambda_{\mathrm{crit}} = \frac{C_2}{\sqrt{\Omega(N, \beta)}} \tag{20}$$

for the scaling of λ_{crit}, where C_2 is a constant whose concrete value depends on $H_{\mathrm{sys}}, H_{\mathrm{bath}}$ and H_{int}. Now we turn to an estimate for $\Omega(N, \beta)$. For a sufficiently large Heisenberg spin system (or any other system consisting of N similar, similarly and locally interacting subsystems) it is reasonable to assume that the density of states is Gaussian with mean zero and variance proportional to the particle number N.

$$\Omega(N, E) \sim \frac{2^N}{\sqrt{N}} e^{-E^2/\alpha N} \tag{21}$$

Using $\beta = \partial_E \log \Omega$ leads to

$$\Omega(N, \beta) \sim \frac{1}{\sqrt{N}} e^{(\log 2 - 0.25\alpha\beta^2)N} \,. \tag{22}$$

Inserting this into Eq. (20) and fitting for C_2 and α yields the dashed line in Fig. 4, which matches the data quite well. This remarkable agreement in turn backs up the argumentation which lead to Eq. (20). As the density of states is routinely expected to scale exponentially in system size, Eq. (20) indicates that λ_{crit} will generally be exponentially small in the system size and thus the superweak regime will practically never be observed.

V. GARCÍA-PINTOS BOUND AND EXPONENTIALLY DECAYING OBSERVABLES

As explained in Sect. II the applicability of the GPB hinges on the two parameters a and Q, both of which should be of order unity to establish a meaningful relation between the short time dynamics and the equilibration time in the sense of the GPB. However, for some of the numerical examples considered in

Sect. III, at least one of the parameters must be substantially larger than unity. While we are unable to perform a direct numerical check for large system sizes, we strongly suspect that $a \sim 1$ is violated at weak interactions even though the corresponding $w(G)$ (cf. Sect. II) is strictly unimodal. In the remainder of the present section we explain and back up this claim.

Consider the mathematically simple case of an infinite-temperature bath in the initial state $\rho = (S^z_{\mathrm{sys}} + 1_{\mathrm{sys}}/2) \otimes 1_{\mathrm{bath}}/d_{\mathrm{bath}}$. This state yields

$$\langle S^z_{\mathrm{sys}}(t)\rangle = \mathrm{Tr}\{S^z_{\mathrm{sys}}(t)\rho\} = \mathrm{Tr}\{S^z_{\mathrm{sys}}(t)S^z_{\mathrm{sys}}\} \tag{23}$$

for the dynamics of the observable $\langle S^z_{\mathrm{sys}}(t)\rangle$, which may be rewritten as

$$\langle S^z_{\mathrm{sys}}(t)\rangle = \sum_{j,k} |\langle j|S^z_{\mathrm{sys}}|k\rangle|^2 e^{\mathrm{i}(E_j - E_k)t}\,. \tag{24}$$

Now, consider the distribution p_{jk} as defined in Eq. (1) for this initial state of observable $A = S^z_{\mathrm{sys}}$.

$$p_{jk} \propto |\langle j|S^z_{\mathrm{sys}}|k\rangle^2| = |\langle j|S^z_{\mathrm{sys}}|k\rangle|^2 \quad \text{for} \quad j \neq k \tag{25}$$

For non-integrable systems in the sense of a Bethe ansatz, the eigenstate thermalization hypothesis may be expected to hold, yielding $|\langle j|S^z_{\mathrm{sys}}|j\rangle|^2 \approx 0$. Exploiting this case, the insertion of Eq. (25) into Eq. (24) yields

$$\langle S^z_{\mathrm{sys}}(t)\rangle \propto \sum_{j,k} p_{jk} e^{\mathrm{i}(E_j - E_k)t}\,. \tag{26}$$

To the extend that p_{jk} may indeed be replaced by a smooth probability density as discussed around Eq. (2), Eq. (26) may be rewritten as

$$\langle S^z_{\mathrm{sys}}(t)\rangle \propto \int w(G) e^{\mathrm{i}Gt}\mathrm{d}G\,. \tag{27}$$

Thus, for the present scenario, $w(G)$ is essentially the Fourier transform of the observable dynamics $\langle S^z_{\mathrm{sys}}(t)\rangle$. Based on the numerical findings displayed, e.g., in Fig. 2 it appears plausible that $\langle S^z_{\mathrm{sys}}(t)\rangle$ will be an exponential decay for infinite temperature initial states as well. Therefore, $w(G)$ will be Lorentzian. While a Lorentzian distribution is clearly unimodal with one well-behaved maximum, its variance diverges. Consequently a, as defined in Eq. (3), diverges as well. Thus, in contrast to the assumptions in Ref. [20], $a \sim 1$ does not hold. This is the last main result of the present paper. Of course σ_G cannot really diverge in any system featuring a finite energy spectrum. However, the finiteness of the spectrum essentially causes a cut-off of the tails of the Lorentzian at some frequency. This cut-off actually renders the standard deviation σ_G finite. Nonetheless, this standard deviation does not reasonably reflect the width of $w(G)$. It will be much larger than other measures of the width such as the full-width-at-half-maximum, etc. Some attention should also be paid to the question whether or not the GPB scales with the size of the environment. (Earlier works presented upper bounds that explicitly depend on the size of the environment, which is often seen as a drawback [10, 11]). While the GPB does not explicitly dependent on the size of the environment, the latter may enter via the parameter a. For any (weak) interaction strength λ there exists a system size $N(\lambda_{\mathrm{crit}})$ above which FGR applies. Above that size the GPB is independent of N. Below or at $N(\lambda_{\mathrm{crit}})$, however, the numerator in Eq. (4) may depend on N rather strongly. For arbitrarily small λ this $N(\lambda_{\mathrm{crit}})$ may become arbitrarily large. Thus, in the class of models discussed in the paper at hand, one can always find instances for which the GPB depends on system size even for very large systems, i.e. $N \gg 1$.

VI. SUMMARY AND CONCLUSION

In the paper at hand we conceptually and numerically analyzed an upper bound on equilibration times presented in a recent paper by García-Pintos et al. To this end, we investigated a standard system-bath setup by monitoring the system's magnetization for various bath sizes and interaction strengths. This numerical investigation is based on the solution of the time dependent Schrödinger equation for the full system, including the bath. We identified a Markovian regime of interaction strengths λ in which Fermi's Golden Rule holds, i.e., the system thermalizes in an exponential way and the equilibration time scales as λ^{-2}. This relates to the García-Pintos bound inasmuch as the validity of Fermi's Golden Rule and the usefulness of the García-Pintos bound are analytically shown to be mutually exclusive at sufficiently small λ. At extremely small λ, we indeed find a "superweak" regime in which Fermi's Golden rule does not apply. This regime (in principle) exists for finite baths and is reached below some λ_{crit} which is shown to scale inversely exponentially in the bath size, suggesting that the superweak regime practically ceases to exist when considering moderately large systems. However, in the superweak regime the García-Pintos bound may eventually regain applicability, although its non-applicability is found to extend also into the superweak regime.

Acknowledgments: Stimulating discussion with R. Steinigeweg and J. Richter are gratefully acknowledged. We also thank L. P. García-Pintos and A. M. Alhambra for interesting discussions, as well as A. J. Short for a comment on an early version of this paper. This work was supported by the Deutsche Forschungsgemeinschaft (DFG) within the Research Unit FOR 2692 under Grant No. 397107022.

APPENDIX

Details of our numerical implementation will be discussed in this appendix. We make use of the concept of typicality (cf. App. A) and use a time evolution algorithm (real and imaginary) based on Chebyshev polynomials (cf. App. B). Since the full Hamiltonian conserves magnetization, we perform the procedure outlined below in each magnetization subspace. The dynamics in the full Hilbert space are obtained by piecing together the contributions of each magnetization subspace weighted with their respective binomial weight. Note that the main hindrance to our calculations is not the exponentially large Hilbert space dimension, but rather the extremely long times that have to be reached in real time for small interaction strengths. In App. C a result for randomized bath couplings is shown.

A. Typicality

As mentioned in Sect. III, the initial state is a product state of a microcanonical bath state and a projected spin-up system state. Since the numerical integration of the von-Neumann equation can be cumbersome, we make use of the concept of typicality, which states that a single "typical" pure state can have the same thermodynamic properties as the full statistical ensemble [31]. Not only is it more memory efficient to work with pure states, the availability of efficient time evolution algorithms for pure states, e.g. Runge-Kutta or Chebyshev polynomials, constitutes a major advantage. To find such a typical state, a pure state $|\phi\rangle$ is drawn at random from the Hilbert space according to the unitary invariant Haar measure.

$$|\phi\rangle = \sum_i c_i |i\rangle \tag{A1}$$

Real and imaginary part of the complex coefficients c_i are drawn from a Gaussian distribution with mean zero and unit variance and the set $\{|i\rangle\}$ is an arbitrary basis of the Hilbert space, e.g., the Ising basis. Consider the new normalized state

$$|\psi\rangle = \frac{\sqrt{\rho}\,|\phi\rangle}{\sqrt{\langle\phi|\rho|\phi\rangle}}\,. \tag{A2}$$

It can be shown [32] that for the overwhelmingly majority of random states $|\phi\rangle$, the pure state $|\psi\rangle$ exhibits effectively the the same thermodynamic behavior as the mixed state ρ, i.e.,

$$\langle A(t)\rangle = \mathrm{Tr}\{\rho A(t)\} = \langle\psi|A(t)|\psi\rangle + \varepsilon\,. \tag{A3}$$

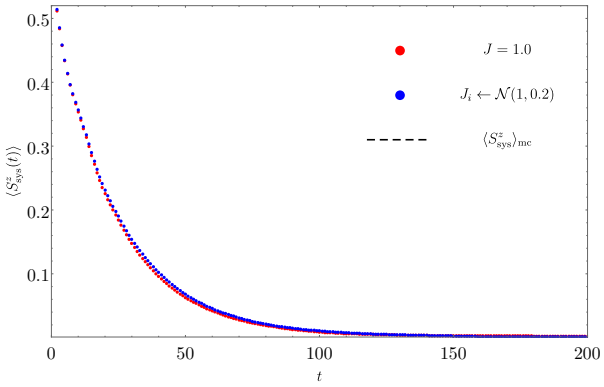

Figure 9. Comparison between setups with couplings set to unity and randomly drawn couplings. There is no apparent difference.

Importantly, the induced error $\varepsilon = \varepsilon(|\psi\rangle)$ has mean zero, i.e., $\bar{\varepsilon} = 0$, and a standard deviation that scales inversely proportional to the square root of the effective Hilbert space dimension, i.e., $\sigma(\varepsilon) \propto 1/\sqrt{d_{\mathrm{eff}}}$ [33]. The effective dimension $d_{\mathrm{eff}} = 1/\mathrm{Tr}\{\rho^2\}$ is a measure of how many pure states contribute to the mixture ρ.
In the paper at hand the initial state ρ (cf. Eq. (14)) is a projection operator. Therefore, it is permissible to drop the square root in the numerator in Eq. (A2). Now the projectors $\pi_\uparrow \otimes 1$ and $1 \otimes \pi_{E,\delta}$ need to be applied to the state $|\phi\rangle$, which is an element of the product Hilbert space. As we are working in the Ising basis, the action of $\pi_\uparrow \otimes 1$ on $|\phi\rangle$ is easily implemented by setting corresponding components of the state vector to zero. Since it is unfeasible to diagonalize the full many-body Hamiltonian, we replace the bath projector by a Gaussian filter which suppresses contributions of energy eigenstates far away from the desired energy E, resulting in a narrowly populated energy window of width (variance) δ.

$$\pi_{E,\delta} \approx \exp\left(\frac{-(H_{\mathrm{bath}} - E)^2}{2\delta}\right) \tag{A4}$$

The Gaussian filter is applied with a Chebyshev algorithm (cf. App. B). Lastly, the resulting wave function is normalized to obtain the state $|\psi\rangle$ as in Eq. (A2). In this scenario the effective dimension d_{eff} is essentially the number of states in the energy window. Increasing the size of the system, while keeping δ fixed, results in an exponentially growing effective dimension d_{eff} and therefore in a negligible typicality error for moderately sized systems.

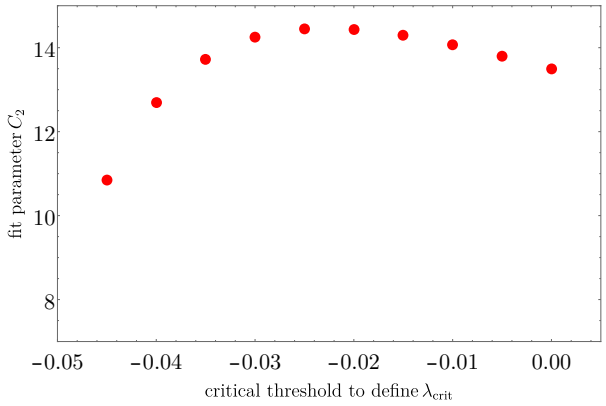

Figure 10. Scaling of the fit parameter C_2 with the choice of the critical threshold.

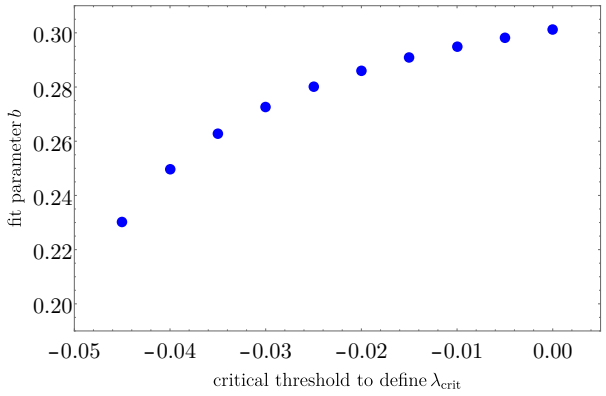

Figure 11. Scaling of the fit parameter b with the choice of the critical threshold.

B. Chebyshev polynomials

A Chebyshev type algorithm is employed in order to evolve a pure state in real and imaginary time [34, 35]. Say it is desirable to approximate a scalar function $f(x)$ in the interval $[-1, 1]$ by a polynomial expansion, i.e.

$$f(x) \approx \sum_n d_n P_n(x)\,, \tag{B1}$$

with coefficients d_n and polynomials P_n of order n. The unique set of polynomials that minimizes the maximum error in this interval is called Chebyshev polynomials of the first kind. They are denoted by $T_n(x)$ and can be written down recursively as

$$T_n(x) = 2xT_{n-1}(x) - T_{n-2}(x) \tag{B2}$$

with $T_0(x) = 1$ and $T_1(x) = x$. They are orthogonal with respect to the weighted scalar product

$$\langle T_n|T_m\rangle = \int_{-1}^{1} \frac{T_n(x)T_m(x)}{\pi\sqrt{1-x^2}}\,\mathrm{d}x = \delta_{nm}D_n \tag{B3}$$

with $D_n = 1$ and $D_{n>0} = 1/2$. In order to approximate the time evolution operator, the bandwidth of the Hamiltonian has to be rescaled accordingly. Defining $\omega = (E_{\max} - E_{\min})/2$ and $\chi = (E_{\max} + E_{\min})/2$, where $E_{\max}$ ($E_{\min}$) is the maximal (minimal) energy eigenvalue, the rescaled Hamiltonian is obtained by $\tilde{H} = (H - \chi)/\omega$. In practice a small safety parameter is chosen that ensures that the rescaled spectrum lies well within $[-1, 1]$.
Now we get

$$e^{-\mathrm{i}H\Delta t} = e^{-\mathrm{i}\chi\Delta t}\left[d_0(\omega\Delta t) + 2\sum_{n\geq 1} d_n(\omega\Delta t)T_n(\tilde{H})\right] \tag{B4}$$

with complex coefficients

$$d_n(\omega\Delta t) = \int_{-1}^{1} \frac{T_n(x)e^{-\mathrm{i}x\omega\Delta t}}{\pi\sqrt{1-x^2}}\mathrm{d}x = (-\mathrm{i})^n J_n(\omega\Delta t), \tag{B5}$$

where J_n denotes the n-th order Bessel function of the first kind. Since the coefficients only depend on the time step, but not on time itself, they only have to calculated once. Applying Eq. (B4) to a state $|\psi(t)\rangle$ boils down to calculating $T_n(\tilde{H})|\psi(t)\rangle$ for various n, which can be done iteratively using Eq. (B2). Terminating the sum in Eq. (B4) at an upper bound M gives the M-th order Chebyshev approximation of the time evolution operator. The required order for convergence depends on the particular problem. For our biggest system with $N = 25$ spins we had to go up to order 40.

C. Validity of numerical results for a larger class of systems

While the investigated model class may seem peculiar, it has just been chosen as one generic representative of the whole of condensed matter type systems. To exclude that overall results are just due to any unintentional, subtle conserved quantities, etc., we redid parts of our numerical analysis with randomized bath couplings, drawn from a Gaussian distribution with mean zero and standard deviation 0.2. One result is displayed in Fig. 9 for $N = 25$ and $\lambda = 0.2$. One readily verifies that the curves coincide nicely. This hints at the generic nature of our model class.

D. Scaling of fit parameters with choice of critical threshold

The choice of $\overline{\langle S^z_{\rm sys}\rangle} = -0.04$ to define $\lambda_{\rm crit}$ is rather arbitrary. However, the above two figures show that the fit parameters C_2 and b are quite insensitive to the exact positioning of this threshold, as long as it is sufficiently close to the thermal equilibrium value. Furthermore, the principled form of the curve in Fig. 4 is quite robust to small variations of the fit parameters.

[1] C. Gogolin and J. Eisert, Reports on Progress in Physics **79**, 056001 (2016).
[2] S. Goldstein, J. L. Lebowitz, R. Tumulka, and N. Zanghì, Phys. Rev. Lett. **96**, 050403 (2006).
[3] P. Reimann, Phys. Rev. Lett. **99**, 160404 (2007).
[4] S. Lloyd, arXiv:1307.0378v1 (1988).
[5] M. Srednicki, Phys. Rev. E **50**, 888 (1994).
[6] J. M. Deutsch, Phys. Rev. A **43**, 2046 (1991).
[7] P. Reimann, Phys. Rev. Lett. **101**, 190403 (2008).
[8] N. Linden, S. Popescu, A. J. Short, and A. Winter, Phys. Rev. E **79**, 061103 (2009).
[9] A. J. Short and T. C. Farrelly, New Journal of Physics **14**, 013063 (2012).
[10] S. Goldstein, T. Hara, and H. Tasaki, Phys. Rev. Lett. **111**, 140401 (2013).
[11] A. S. L. Malabarba, L. P. García-Pintos, N. Linden, T. C. Farrelly, and A. J. Short, Phys. Rev. E **90**, 012121 (2014).
[12] M. Kastner, Phys. Rev. Lett. **106**, 130601 (2011).
[13] M. Schiulaz, E. J. Torres-Herrera, and L. F. Santos, Phys. Rev. B **99**, 174313 (2019).
[14] M. Cramer, C. M. Dawson, J. Eisert, and T. J. Osborne, Phys. Rev. Lett. **100**, 030602 (2008).
[15] M. Diez, N. Chancellor, S. Haas, L. C. Venuti, and P. Zanardi, Phys. Rev. A **82**, 032113 (2010).
[16] Vinayak and M. Žnidarič, Journal of Physics A: Mathematical and Theoretical **45**, 125204 (2012).
[17] E. J. Torres-Herrera and L. F. Santos, Phys. Rev. A **89**, 043620 (2014).
[18] T. R. de Oliveira, C. Charalambous, D. Jonathan, M. Lewenstein, and A. Riera, New Journal of Physics **20**, 033032 (2018).
[19] A. Dymarsky, Phys. Rev. B **99**, 224302 (2019).
[20] L. P. García-Pintos, N. Linden, A. S. L. Malabarba, A. J. Short, and A. Winter, Phys. Rev. X **7**, 031027 (2017).
[21] L. V. Hove, Physica **23**, 441 (1957).
[22] C. Bartsch, R. Steinigeweg, and J. Gemmer, Phys. Rev. E **77**, 011119 (2008).
[23] E. Joos, H. D. Zeh, C. Kiefer, D. J. W. Giulini, J. Kupsch, and I. O. Stamatescu, *Decoherence and the Appearance of a Classical World in Quantum Theory*, Physics and Astronomy Online Library (Springer, 2003).
[24] M. O. Scully and M. S. Zubairy, *Quantum Optics* (Cambridge University Press, 1997).
[25] H.-P. Breuer and F. Petruccione, *The Theory of Open Quantum Systems* (2006).
[26] P. Zhao, H. De Raedt, S. Miyashita, F. Jin, and K. Michielsen, Phys. Rev. E **94**, 022126 (2016).
[27] J. Lages, V. V. Dobrovitski, M. I. Katsnelson, H. A. De Raedt, and B. N. Harmon, Phys. Rev. E **72**, 026225 (2005).
[28] M. Esposito and P. Gaspard, Phys. Rev. E **68**, 066113 (2003).
[29] U. Weiss, *Quantum Dissipative Systems*, 4th ed. (World Scientific, 2012).
[30] M. Srednicki, Journal of Physics A: Mathematical and General **32**, 1163 (1999).
[31] B. N. Balz, J. Richter, J. Gemmer, R. Steinigeweg, and P. Reimann, "Dynamical typicality for initial states with a preset measurement statistics of several commuting observables," in *Thermodynamics in the Quantum Regime: Fundamental Aspects and New Directions* (Springer International Publishing, Cham, 2018) pp. 413–433.
[32] P. Reimann and J. Gemmer, Physica **A**, 121840 (2019).
[33] P. Reimann, Phys. Rev. E **97**, 062129 (2018).
[34] H. Tal-Ezer and R. Kosloff, The Journal of Chemical Physics **81**, 3967 (1984).
[35] H. D. Raedt and K. Michielsen, *Computational Methods for Simulating Quantum Computers* (American Scientific Publisher, 2004).

Preprint of Publication [P2]

Robin Heveling, Lars Knipschild, and Jochen Gemmer
"Comment on 'Equilibration Time Scales of Physically Relevant Observables' "
Physical Review X **10**, 028001 (2020)
DOI: 10.1103/PhysRevX.10.028001

Comment on "Equilibration Time Scales of Physically Relevant Observables"

Robin Heveling,* Lars Knipschild,† and Jochen Gemmer‡
Department of Physics, University of Osnabrück, D-49069 Osnabrück, Germany

Putting a generally valid upper bound to equilibration times of physically relevant observables is a much pursued endeavor. Recently such a bound has been suggested by Garcia-Pintos et al. While the mathematical correctness of the bound as such is undisputed, its concrete calculation requires the knowledge of certain quantities, which Garcia-Pintos et al. assess by means of assumptions. We show that, e.g., in standard cases of slow, exponential equilibration (at least) one of these assumptions is not valid. This demonstration highlights the difficulty to judge the validity of the above assumptions without further information, which are in general not attainable.

I. ADDRESSED RESULT FROM PRX, 7, 031027 (2017) AND DEFINITION OF $w(G)$

For selfcontainedness, we (re-)state the main result of Ref. [1] (hereafter called the García-Pintos bound (GPB)) in a comprehensive form. (It should be quick read-through for readers familiar with this result.) Furthermore, we define the function $w(G)$, cf. Eq. (2), which is directly calculated from the probability distribution denoted by p_{jk} in Ref. [1].

The GPB addresses an equilibration time T_{eq}. To further specify T_{eq} we introduce some notation. Let ρ be the initial state of the system. Let furthermore $A(t)$ denote an observable A in the Heisenberg picture and $\langle A(t)\rangle := \mathrm{Tr}\{A(t)\rho\}$ its time-dependent expectation value. Due to the closed system dynamics being unitary (and the system being finite), $\langle A(t)\rangle$ has a well-defined "infinite-time average" $\overline{\langle A\rangle} := \langle A\rangle_{\mathrm{eq}}$, which is routinely considered as the equilibrium value of A in case the observable A equilibrates at all [2]. Consider now a deviation $D(t)$ of the actual expectation value from its equilibrium, i.e. $D(t) := (\langle A(t)\rangle - \langle A\rangle_{\mathrm{eq}})^2/4||A||^2$, where $||A||$ is the largest absolute eigenvalue of A. Consider furthermore an average of $D(t)$ over the time interval $[0,T]$ denoted by $\overline{D}_T$. The condition that defines T_{eq} is that $\overline{D}_T \ll 1$ must hold for $T \gg T_{\mathrm{eq}}$ (for non-equilibrating systems such a T_{eq} may not exist [2]). The GPB is an explicit expression for such a T_{eq} (see Eq. (4)) based on $\rho, A(0)$ and the Hamiltonian of the system H. As the GPB involves somewhat refined functions of the above three operators, we need to specify these before stating the GPB explicitly. A central role is taken by the probability distribution p_{jk}, which is defined as

$$p_{jk} \propto |\rho_{jk}A_{kj}| \text{ for } E_j - E_k \neq 0\,, \qquad (1)$$
$$p_{jk} = 0 \text{ for } E_j - E_k = 0, \quad \sum_{j,k} p_{jk} = 1\,,$$

where E_j, E_k are energy eigenvalues corresponding to energy eigenstates $|j\rangle, |k\rangle$. Furthermore, matrix elements are abbreviated as $\rho_{jk} := \langle j|\rho|k\rangle$, $A_{jk} := \langle j|A(0)|k\rangle$. While the GPB is not limited to this case, we focus here on p_{jk} which allow for a description in terms of a probability density function $w(G)$. The examples we present below conform with such a description and it is plausible that this applies to generic many-body scenarios. Prior to defining $w(G)$, we define $w(G,\epsilon)$ as

$$w(G,\epsilon) := \frac{1}{\epsilon}\sum_{j,k}\Theta\Big(\frac{\epsilon}{2} - |E_j - E_k - G|\Big)\,p_{jk}\,, \qquad (2)$$

where Θ is the Heaviside function. This is the standard construction of a histogram in which the p_{jk} are sorted according to their respective energy gaps $E_j - E_k$. It is now assumed that there exists a range of (small but not too small) ϵ such that $w(G,\epsilon)$ is essentially independent of variations of ϵ within this range. The $w(G,\epsilon)$ from this "independence regime" are simply abbreviated as $w(G)$. Let the standard deviation of $w(G)$ be denoted by σ_G. (In Ref. [1] σ_G denotes the standard deviation of $w(G,0)$, however, here we focus on situations where this difference is negligible.) Let furthermore $w_{\max}$ denote the maximum of $w(G)$. The quantities a and Q that eventually enter the GPB are now defined as

$$a := w_{\max}\sigma_G\,, \qquad Q := \sum_{i,j:E_i\neq E_j}\frac{|\rho_{ij}A_{ji}|}{||A||}\,. \qquad (3)$$

We are now set to state the GPB:

$$T_{\mathrm{eq}} = \frac{\pi a||A||^{1/2}Q^{5/2}}{\sqrt{|\mathrm{Tr}\{[[\rho,H],H]A\}|}} = \frac{\pi a||A||^{1/2}Q^{5/2}}{\sqrt{|\frac{\mathrm{d}^2}{\mathrm{d}t^2}\langle A(t)\rangle\big|_{t=0}|}}\,. \qquad (4)$$

* rheveling@uos.de
† lknipschild@uos.de
‡ jgemmer@uos.de

II. THE GENERAL PROBLEM OF UPPER BOUNDING a, Q IN THE CASE OF SLOW EXPONENTIAL DECAY DYNAMICS

Obviously, the GPB links $T_{\rm eq}$ to the initial "curvature" of the observable dynamics $\partial_t^2\langle A(t)\rangle|_{t=0}$ (which is often practically computable, simply from its form in the denominator in the middle of the double equation in Eq. (4)). An actual, concrete value or upper bound for $T_{\rm eq}$, however, may only be computed from Eq. (4) if also the numerator can be be computed or upper bounded. Let us stress that this (rather obvious) statement is pivotal for the argument in the Comment at hand. The three main results, which are formulated further below, attain there significance only in connection with this statement. The crucial quantities in the numerator are a and Q. As it is practically impossible to calculate a from its definition for many-body quantum systems, García-Pintos et al. instead resort to an assumption concerning a. They argue that $a \sim 1$ may be expected for $w(G)$ that are "unimodal". Unimodal means that $w(G)$ essentially consists of one central elevation like a Gaussian or a box distribution, etc. Indeed, a is invariant with respect to a rescaling $w(G) \to sw(sG)$, as it would result from rescaling the Hamiltonian as $H \to sH$ (here s is some real, positive number). García-Pintos et al. also offer various upper bounds on Q for different situations.

In contrast to the argument in Ref. [1], we show in the following that the assumption of any two fixed upper bounds on a and Q is necessarily violated for generic, sufficiently slow, exponential decays of $\langle A(t)\rangle$. To this end, two standard scenarios of slow dynamics are analyzed below. In Sect. III we also provide a concrete spin-based example (along the lines of Scenario 1) in which a is found to diverge while the bound on Q from Ref. [1] applies. This occurs even though $w(G)$ is unimodal.

Scenario 1*: Dynamics of quantities that are conserved except for a weak perturbation to the Hamiltonian*

Consider first an Hamiltonian consisting of an unperturbed part H_0 and a perturbation $\lambda H_{\rm int}$.

$$H = H_0 + \lambda H_{\rm int} \tag{5}$$

Consider furthermore an observable A, which is conserved under H_0, i.e. $[A, H_0] = 0$. If H_0 has a sufficiently wide and dense spectrum and λ is small, exponential decay, in the simplest case monoexponential decay, occurs, i.e.

$$\langle A(t)\rangle = (\langle A(0)\rangle - \langle A\rangle_{\rm eq})e^{-t/\tau_{\rm rel}} + \langle A\rangle_{\rm eq}\,, \tag{6}$$

where $\tau_{\rm rel} := r\lambda^{-2}$ and r is a real, finite, positive number which depends on the details of the setup. Many well understood approaches, such as the Weisskopf-Wigner theory, projection operator techniques (Nakajima-Zwanzig, Mori, etc.) arrive at such exponential decay dynamics [3–7] for standard, physical, nonequilibrium situations. A bold numerical demonstration for the emergence of dynamics in accord with Eq. (6) in closed quantum systems is given in Ref. [8]. For even more evidence see Refs. [9, 10]. If $\partial_t\langle A(t)\rangle|_{t=0} = 0$, obviously Eq. (6) cannot apply at $t = 0$. In this case Eq. (6) is meant to apply after a short "Zeno time" $\tau_{\rm zeno}$, which is usually exceedingly short compared to the relaxation time $\tau_{\rm rel}$ [4, 7]. Note, however, that the denominator of Eq. (4) necessarily addresses a time below the Zeno time, namely $t = 0$. We now aim at finding the principal dependence of quantities in Eq. (4) on the interaction strength λ. From the definition of $T_{\rm eq}$ given at the beginning of Sect. I it follows that

$$T_{\rm eq} \geq \tau_{\rm rel}\,. \tag{7}$$

For the denominator of Eq. (4) we find with Eq. (5)

$$\sqrt{\left|\frac{\mathrm{d}^2}{\mathrm{d}t^2}\langle A(t)\rangle\big|_{t=0}\right|} = \sqrt{|c_1\lambda + c_2\lambda^2|}\,, \tag{8}$$

where $c_1 = \mathrm{Tr}\{[H_{\rm int}, A][\rho, H_0]\}, c_2 = \mathrm{Tr}\{[H_{\rm int}, A][\rho, H_{\rm int}]\}$. While initial states ρ such that $c_2 = 0$ are possible, they are not generic, rather they are very rare (untypical) for a given, nonvanishing $\langle A(0)\rangle$ [11]. Plugging Eqs. (6, 7, 8) into Eq. (4) yields

$$\pi a||A||^{1/2}Q^{5/2} \geq r\frac{\sqrt{|c_1\lambda + c_2\lambda^2|}}{\lambda^2} \tag{9}$$

for the numerator of Eq. (4). Obviously, the numerator of Eq. (4) diverges in the limit of weak interactions, i.e. $\lambda \to 0$. The latter holds even if $c_1 = 0$. The divergence of the numerator of Eq. (4) necessarily implies the divergence of a or Q or both. Thus, no concrete, finite $T_{\rm eq}$ may be computed from Eq. (4) in this case. This is the first main result of the present Comment.

Scenario 2*: Dynamics of long wavelength Fourier-components of spatial densities of conserved quantities*

In the above Scenario 1 the exponential decay is due to some "conservation breaking" part of the Hamiltonian being small. However, exponential decay also often occurs without some part of the Hamiltonian being particularly small. Consider, e.g., a spatially more or less homogeneous system in which some quantity Z (like energy, particles, magnetization, etc.) is totally conserved. Nevertheless, the spatial density of this quantity $p(x, t)$ may undergo some time evolution. If this evolution complies with a diffusion equation, a Fourier component of this density, e.g. $\langle A_k(t)\rangle = \langle\int \cos(kx)p(x, t)\mathrm{d}x\rangle$, will decay exponentially, i.e.,

$$\langle A_k(t)\rangle = \langle A_k(0)\rangle e^{-\kappa k^2 t}\,, \tag{10}$$

where κ is the nonnegative, finite diffusion coefficient. However, just like in Scenario 1, we additionally need to find $\partial_t^2\langle A_k(t)\rangle|_{t=0}$ in order to find the scaling of a and Q with k. While the following consideration in principle applies to all spatial dynamics of conserved quantities, we here resort to a specific example for clarity. We consider the XXZ-chain of length N with periodic boundary conditions ($N+1\equiv 1$) and anisotropy Δ described by the Hamiltonian

$$H_{\mathrm{XXZ}} = \sum_{j=1}^{N}(S_j^x S_{j+1}^x + S_j^y S_{j+1}^y + \Delta S_j^z S_{j+1}^z)\,. \tag{11}$$

The total magnetization of the system, i.e. $Z=\sum_i S_i^z$, is conserved. The Fourier components of the spatial distribution of the magnetization are

$$A_k = \frac{1}{\sqrt{N}}\sum_{i=1}^{N}\cos(ki)S_i^z\,, \tag{12}$$

where $k = 2\pi m/N$ are the discrete wave numbers and $m = 0, 1, ..., N-1$. The scaling in N guarantees the convergence of the variances of the spectra of the A_k to finite values of order unity at large N. (This may be inferred from considering the corresponding Hilbert-Schmidt norms.) Calculating the second temporal derivatives of the A_k yields

$$\begin{aligned}-[H_{\mathrm{XXZ}},[H_{\mathrm{XXZ}},A_k]] = \\ 2(\cos(k)-1)(A_k+B_k) - \sin(k)C_k\,,\end{aligned} \tag{13}$$

where

$$\begin{aligned}B_k &= \frac{2}{\sqrt{N}}\sum_{j=1}^{N}\cos(kj)(S_{j-1}^x S_j^z S_{j+1}^x + S_{j-1}^y S_j^z S_{j+1}^y)\\ &\quad - \frac{\Delta}{\sqrt{N}}\sum_{j=1}^{N}\cos(kj)(S_{j-1}^z S_j^x S_{j+1}^x - S_{j-1}^x S_j^x S_{j+1}^z\\ &\qquad + S_{j-1}^z S_j^y S_{j+1}^y - S_{j-1}^y S_j^y S_{j+1}^z)\,,\\ C_k &= -\frac{2\Delta}{\sqrt{N}}\sum_{j=1}^{N}\sin(kj)(S_{j-1}^z S_j^x S_{j+1}^x - S_{j-1}^x S_j^x S_{j+1}^z\\ &\qquad + S_{j-1}^z S_j^y S_{j+1}^y - S_{j-1}^y S_j^y S_{j+1}^z)\,.\end{aligned} \tag{14}$$

For small k this may be approximated as

$$[H_{\mathrm{XXZ}},[H_{\mathrm{XXZ}},A_k]] \approx k^2(A_k+B_k) + k\,C_k\,. \tag{15}$$

Note that the variances of the spectra of B_k and C_k are all of order unity for any k, just like the spectra of the A_k. Relying on the small k approximation yields

$$\sqrt{\left|\frac{\mathrm{d}^2}{\mathrm{d}t^2}\langle C_k(t)\rangle\big|_{t=0}\right|} = \sqrt{c_3 k + c_4 k^2}\,, \tag{16}$$

where $c_3 = \mathrm{Tr}\{C_k\rho\}$ and $c_4 = \langle A_k(0)\rangle + \mathrm{Tr}\{B_k\rho\}$. While initial states ρ resulting in $\mathrm{Tr}\{B_k\rho\} = -\langle A_k(0)\rangle$ are mathematically possible, they are not generic or typical at all. Instead, typical values are $\mathrm{Tr}\{B_k\rho\}\approx 0$, even and especially for a given $\langle A_k(0)\rangle$ [11]. Thus, exploiting Eq. (16) yields in general, by the same line of argumentation employed before in Scenario 1 (cf. Eqs. (7, 8, 9))

$$\pi a||C_k||^{1/2}Q^{5/2} \geq \kappa\,\frac{\sqrt{|c_3 k + c_4 k^2\,,|}}{k^2} \tag{17}$$

where the r.h.s. diverges in the limit $k\to 0$, analogous to Eq. (9). Again, this divergence occurs even for $c_3 = 0$. Thus, no concrete, finite T_{eq} may be computed from Eq. (4) in this limiting case, either . This is the second main result of the present Comment. We want to emphasize the following. The XXZ-chain exhibits, depending on (nonsmall) Δ and ρ, various sorts of transport behavior, such as diffusive, ballistic, possibly superdiffusive, with the inclusion of some disorder possibly subdiffusive, etc [12, 13]. The constants a and Q cannot be simultaneously finite in the long wavelength limit ($k\to 0, N\to\infty$) if the transport is diffusive. They may be finite if the transport is, e.g., ballistic. Thus, telling whether or not a and Q are both finite is as hard as telling whether transport is ballistic or diffusive. The latter is, however, a long standing and only partially answered research question for the XXZ-chain [12].

III. CONCRETE, PHYSICAL EXAMPLE ENTAILING $a \nsim 1$

Here we present a concrete, physical example, which is nevertheless simple enough to allow for analytical analysis. This analysis unveils that, in this particular instance, indeed a diverges while the bound on Q as provided in Ref. [1] applies. The exemplary setup consists of a single spin (hereafter called the "system") subject to a magnetic field of strength B along the z-direction, weakly coupled to a large (but finite) environmental system (hereafter called the "bath"). Thus, the unperturbed Hamiltonian is given by $H_0 = BS_{\mathrm{sys}}^z + H_{\mathrm{bath}}$ and the coupling interactions by λH_{int}. The observable of choice is the magnetization in the z-direction of the system spin, i.e. $A = S_{\mathrm{sys}}^z$. For a numerical analysis of such an example see Ref. [8]. We consider the simple case of a product initial state, where the system is maximally aligned with the magnetic field

and the bath is in an infinite-temperature state, i.e. $\rho = (S^z_{\rm sys} + 1_{\rm sys}/2) \otimes 1_{\rm bath}/d_{\rm bath}$. According to Ref. [1], Sect. V, Eq. (29), this entails $Q \leq 2$. Furthermore, we obtain

$$\langle S^z_{\rm sys}(t)\rangle = {\rm Tr}\{S^z_{\rm sys}(t)\rho\} = {\rm Tr}\{S^z_{\rm sys}(t)S^z_{\rm sys}\} \tag{18}$$

for the dynamics of the observable $\langle S^z_{\rm sys}(t)\rangle$, which may be rewritten as

$$\langle S^z_{\rm sys}(t)\rangle = \sum_{j,k} |\langle j|S^z_{\rm sys}|k\rangle|^2 e^{{\rm i}(E_j - E_k)t}\,. \tag{19}$$

Now consider the distribution p_{jk} as defined in Eq. (1) for the given setting.

$$p_{jk} \propto |\langle j|S^z_{\rm sys}|k\rangle^2| = |\langle j|S^z_{\rm sys}|k\rangle|^2 \quad \text{for} \quad j \neq k \tag{20}$$

For nonintegrable systems the eigenstate thermalization hypothesis is expected to hold, yielding $|\langle j|S^z_{\rm sys}|j\rangle|^2 \approx 0$. Exploiting this, the insertion of Eq. (20) into Eq. (19) yields

$$\langle S^z_{\rm sys}(t)\rangle \propto \sum_{j,k} p_{jk} e^{{\rm i}(E_j - E_k)t}\,. \tag{21}$$

To the extend to which p_{jk} may indeed be replaced by a smooth probability density as discussed around Eq. (2), Eq. (21) may be rewritten as

$$\langle S^z_{\rm sys}(t)\rangle \propto \int w(G) e^{{\rm i}Gt} {\rm d}G\,. \tag{22}$$

Thus, for the present example, $w(G)$ is essentially the Fourier transform of the observable dynamics $\langle S^z_{\rm sys}(t)\rangle$. If the expectation value $\langle S^z_{\rm sys}(t)\rangle$ would decay strictly exponentially, i.e., if Eq. (6) would strictly apply, $w(G)$ would be strictly Lorentzian. While a Lorentzian distribution is clearly unimodal with one well-behaved maximum, its variance diverges. Consequently, a, as defined in Eq. (3), would diverge as well. This is the third main result of the Comment at hand. A strict mathematical divergence of a is only hindered by the small deviations of the true dynamics in a finite system from Eq. (6). These deviations are captured by the aforementioned Zeno time. As well known, Zeno times may become arbitrarily small in systems with arbitrarily broad energy spectra [4]. Thus, a may indeed become arbitrarily large, i.e. $a \nsim 1$. In very many standard scenarios rather large a may be expected if the coupling is sufficiently weak and the baths are large. For a numerical illustration of this statement see [8].

ACKNOWLEDGMENTS

Stimulating discussions with R. Steinigeweg and J. Richter are gratefully acknowledged. We also thank L. P. García-Pintos and A. M. Alhambra for interesting discussions, as well as A. J. Short for a comment on an early version of this paper. This work was supported by the Deutsche Forschungsgemeinschaft (DFG) within the Research Unit FOR 2692 under Grant No. 397107022.

[1] L. P. García-Pintos, N. Linden, A. S. L. Malabarba, A. J. Short, and A. Winter, Phys. Rev. X **7**, 031027 (2017).
[2] A. J. Short and T. C. Farrelly, New Journal of Physics **14**, 013063 (2012).
[3] M. O. Scully and M. S. Zubairy, *Quantum Optics* (1997).
[4] H.-P. Breuer and F. Petruccione, *The Theory of Open Quantum Systems* (2006).
[5] L. V. Hove, Physica **23**, 441 (1957).
[6] C. Bartsch, R. Steinigeweg, and J. Gemmer, Phys. Rev. E **77**, 011119 (2008).
[7] E. Joos, H. D. Zeh, C. Kiefer, D. J. W. Giulini, J. Kupsch, and I. O. Stamatescu, *Decoherence and the Appearance of a Classical World in Quantum Theory* (2003).
[8] R. Heveling, L. Knipschild, and J. Gemmer, Journal of Physics A: Mathematical and Theoretical **53**, 375303 (2020).
[9] K. Mallayya, M. Rigol, and W. De Roeck, Phys. Rev. X **9**, 021027 (2019).
[10] K. Mallayya and M. Rigol, Phys. Rev. Lett. **123**, 240603 (2019).
[11] P. Reimann and J. Gemmer, Physica A: Statistical Mechanics and its Applications , 121840 (2019).
[12] M. Ljubotina, M. Znidaric, and T. Prosen, Nature Communications **8** (2017).
[13] R. Steinigeweg and W. Brenig, Phys. Rev. Lett. **107**, 250602 (2011).

Preprint of Publication [P3]

Robin Heveling, Lars Knipschild, and Jochen Gemmer
"Modeling the Impact of Hamiltonian Perturbations on Expectation Value Dynamics"
Zeitschrift für Naturforschung A **75**, 5 (2020)
DOI: 10.1515/zna-2020-0034

Modeling the Impact of Hamiltonian Perturbations on Expectation Value Dynamics

Robin Heveling,* Lars Knipschild,† and Jochen Gemmer‡
Department of Physics, University of Osnabrück, D-49069 Osnabrück, Germany

Evidently, some relaxation dynamics, e.g. exponential decays, are much more common in nature than others. Recently there have been attempts to explain this observation on the basis of "typicality of perturbations" with respect to their impact on expectation value dynamics. These theories suggest that a majority of the very numerous, possible Hamiltonian perturbations entail more or less the same type of alteration of the decay dynamics. Thus, in this paper, we study how the approach towards equilibrium in closed quantum systems is altered due to weak perturbations. To this end, we perform numerical experiments on a particular, exemplary spin system. We compare our numerical data to predictions from three particular theories. We find satisfying agreement in the weak perturbation regime for one of these approaches.

I. INTRODUCTION

The issue of the apparent emergence of irreversible dynamics from the underlying theory of quantum mechanics still lacks an entirely satisfying answer [1]. While concepts like the "eigenstate thermalization hypothesis" [2, 3] or "typicality" [4–6] hint at fundamental mechanisms ensuring eventual equilibration, they are not concerned in which manner this equilibrium is reached. It is an empirical fact that some relaxation dynamics, e.g. exponential decays, occur much more often in nature that others, e.g. recurrence dynamics. There are efforts to attribute this dominance to a certain sturdiness of some dynamics against a large class of small alterations of the Hamiltonian [7]. In general, it is of course impossible to predict how the unperturbed dynamics will change due to an arbitrary perturbation. However, theories aiming at capturing the typical impact of generic perturbations have recently been suggested.

In the following three such theories that predict the altered dynamics due to weak, generic perturbations are very briefly presented. Notably, Refs. [7–9] are concerned with describing the modified dynamics under certain assumptions, cf. also Sect. V.

In Ref. [8] the authors consider an entire ensemble of "realistic" Hamiltonian perturbations, i.e. the ensemble members are sparse and possibly banded in the eigenbasis of the unperturbed Hamiltonian. The authors analytically calculate the ensemble average of time-dependent expectation values and argue firstly that the ensemble variance is small and secondly that thus a perturbation of actual interest is likely a "typical" member of the ensemble. The authors eventually arrive at the result that the unperturbed dynamics will likely be exponentially damped with a damping factor scaling quadratically with the perturbation strength.

A similar random matrix approach is taken in Ref. [9]. In this paper, the authors base their argument on projection operator techniques. Again, the ensemble of perturbations that are essentially random matrices in the eigenbasis of the unperturbed Hamiltonian leads to an exponential damping of the unperturbed dynamics at sufficiently long times, with a damping constant scaling quadratically with the perturbation strength. Routinely, the specific projection operator technique ("time convolutionless" [10]) yields a time-dependent damping factor, which ensures that the slope of the time-dependent expectation value at $t = 0$ remains unchanged by the perturbation.

Lastly, the authors of Ref. [7], other than the authors of Ref. [8, 9], focus on the matrix structure of the perturbation in the eigenbasis of the observable rather than in the eigenbasis of the unperturbed Hamiltonian. In this paper, the modified dynamics is not necessarily obtained by a direct damping, but rather by an exponential damping of the memory-kernel. As the predictions of this scheme are somewhat involved, we specifically outline them below in Sect. II.

This paper is structured as follows. Firstly, in Sect. II we give a short introduction to the memory-kernel ansatz employed in Ref. [7]. The numerical setup is described in Sect. III. In Sect. IV the numerical results from the solution of the Schrödinger equation are presented and discussed. Sect. V scrutinizes the possible application of the above three theories (Refs. [7–9]) to the obtained numerical results and the accuracy of the respective predictions. We conclude in Sect. VI.

* rheveling@uos.de
† lknipschild@uos.de
‡ jgemmer@uos.de

II. MEMORY-KERNEL ANSATZ

To outline the memory-kernel ansatz we first need to introduce the general description of dynamics by means of integro-differential equations of the Nakajima-Zwanzig type [11]. Consider some (reasonably well-behaved) time-dependent function $a(t)$, e.g. the expectation value of an unitarily evolving observable. There exists a map between $a(t)$ and its so-called memory-kernel $K(\tau)$, implicitly defined by the integro-differential equation

$$\frac{\mathrm{d}a(t)}{\mathrm{d}t} = -\int_0^t K(t-t')a(t')\,\mathrm{d}t' = -(K * a\,)(t)\,. \quad (1)$$

This map is bijective, i.e., it is possible to calculate the memory-kernel $K(\tau)$ solely from the function $a(t)$ and, vice versa, it is possible to calculate the function $a(t)$, given the memory-kernel $K(\tau)$ and some initial value $a(0)$. Loosely speaking, the memory-kernel describes how a system remembers its history. Ref. [7] now suggests that the generic impact of a certain class of perturbations is best captured by describing its effect on the respective memory-kernel. If the perturbation V is narrow-banded in the eigenbasis of the observable A, i.e. $[V, A] \approx 0$, then the memory-kernel $K(\tau)$ corresponding to the unperturbed dynamics will be exponentially damped as

$$\tilde{K}(\tau) = \exp(-\gamma\tau)K(\tau)\,. \quad (2)$$

To obtain the modified dynamics, we proceed as follows: from $a(t)$ we calculate the memory-kernel $K(\tau)$ and damp it according to Eq. (2). Plugging $\tilde{K}(\tau)$ back into Eq. (1) and solving for $\tilde{a}(t)$ yields the modified dynamics. In this procedure γ is a free fit parameter.

$$a(t) \to K(\tau) \to \tilde{K}(\tau) \to \tilde{a}(t) \quad (3)$$

Note that, in the context of the below (cf. Sect. III) defined spin ladders, this is an heuristic approach. However, for other scenarios, this memory-kernel ansatz is proven to hold [12]. These scenarios feature systems for which the eigenstate thermalization hypothesis (ETH) [3] applies to some observable A. The role of the perturbation is taken by an environment, which induces pure dephasing in the eigenbasis of A. The memory-kernel ansatz then applies to the expectation value of A. The rationale behind using the memory-kernel ansatz in the context of, e.g., isolated spin ladders, is that a generic perturbation V with $[V, A] \approx 0$ may have an effect comparable to the above dephasing. Moreover, the applicability of the memory-kernel ansatz to closed systems has been numerically demonstrated for some concrete but rather abstract examples in Ref. [7]. It has also been found to yield surprisingly accurate results for systems similar to the ones discussed below [13].

III. SETUP

We consider a periodic spin-1/2 ladder described by the (unperturbed) Hamiltonian

$$H_0 = H_\parallel + H_\perp\,, \quad (4)$$

with the chain Hamiltonian

$$H_\parallel = J_\parallel \sum_{k=1}^{2}\sum_{l=1}^{L} \vec{S}_{l,k}\cdot\vec{S}_{l+1,k} \quad (5)$$

and the rung Hamiltonian

$$H_\perp = J_\perp \sum_{l=1}^{L} \vec{S}_{l,1}\cdot\vec{S}_{l,2}\,, \quad (6)$$

where $\vec{S}_{l,k} = (S^x_{l,k}, S^y_{l,k}, S^z_{l,k})$ are spin-1/2 operators on lattice site (l,k) and $L+1 \equiv 1$. The interaction strength along the legs (rungs) is denoted by $J_\parallel$ ($J_\perp$) and set to unity. Additional diagonal bonds act as a perturbation V, the parameter λ indicates the perturbation strength. This results in the total Hamiltonian

$$H = H_0 + \lambda V\,,$$

which is displayed in Fig. 1. The observables of interest are the magnetizations on each rung, which are given by

$$S^z_l = S^z_{l,1} + S^z_{l,2}\,, \quad (7)$$

and the respective Fourier modes

$$S^z_q = \sum_{l=1}^{L} \cos[q(l - L/2)]S^z_l\,, \quad (8)$$

with discrete momenta $q = 2\pi k/L$ with $k = 0, 1, \ldots, L-1$. We numerically solve the Schrödinger equation and study the dynamics of the time-dependent expectation values $p_l(t) = \langle S^z_l(t)\rangle$ of the magnetization profile along the ladder as well as time-dependent expectation val-

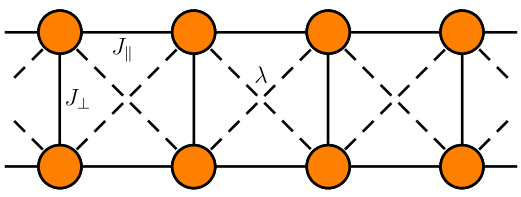

Figure 1. Orange circles mark spin sites, solid black lines mark Heisenberg interaction. Dashed diagonal lines indicate the perturbation.

ues $p_q(t) = \langle S^z_q(t)\rangle$ of the Fourier modes, especially the slowest mode with $q = 2\pi/L$. In order to be able to clearly discriminate between predictions from the memory-kernel ansatz and the other two theories, we choose a perturbation with a specific, yet physically common property named below. This perturbation on the diagonals of the ladder only consists of S^zS^z-terms.

$$V = \sum_{l=1}^{L} \left(S^z_{l,1}S^z_{l+1,2} + S^z_{l,2}S^z_{l+1,1}\right) \tag{9}$$

In this manner, the observables of interest do commute with the perturbation, i.e. $[V, S^z_q] = 0$. In other words, the perturbation V is diagonal in the eigenbasis of the observable.

We consider two types of initial states. The first initial state is given by

$$\rho_1(0) \propto 1 - \varepsilon\, S^z_{L/2}\,, \tag{10}$$

where ε is a small, positive, real number. This state can be regarded as the high temperature, strong magnetic field limit ($\beta \to 0$ while $\beta B = \varepsilon$) of the Gibbs state

$$\rho_2(0) \propto \exp[-\beta(H + BS^z_{L/2})]\,, \tag{11}$$

which is the second initial state of interest.

IV. NUMERICAL RESULTS ON THE PERTURBED DYNAMICS

We now present our numerical results. We prepare a spin ladder with $L = 13$ rungs (i.e. $N = 26$ spins) in the initial states mentioned above, which both feature a sharp magnetization peak in the middle of the ladder. During the real time evolution the magnetization will spread throughout the ladder diffusively [13], which can be seen in Fig. 2.

From Eq. (8) we obtain the Fourier modes of the broadening process. We choose to investigate the slowest mode with $q = 2\pi/13$ in depth since it is closest to an exponential decay. In Fig. 3 the slowest mode is depicted for different perturbation strengths for the first initial state $\rho_1(0)$. The unperturbed dynamic (red curve, $\lambda = 0.0$) remains basically unaltered by weak perturbations. Cranking up the perturbation strength (to $\lambda = 0.4$ or $\lambda = 0.7$) leads to a noticeable deviation and the equilibration process is much slower than in the weakly perturbed case.

The same qualitative behavior remains when going to finite temperature $\beta = 0.1$ and finite magnetic field $B = 5.0$.

In this case, the initial value $p_q(0)$ depends on the perturbation strength λ since the total Hamiltonian is part of the initial state $\rho_2(0)$, cf. Eq. (11). To be able

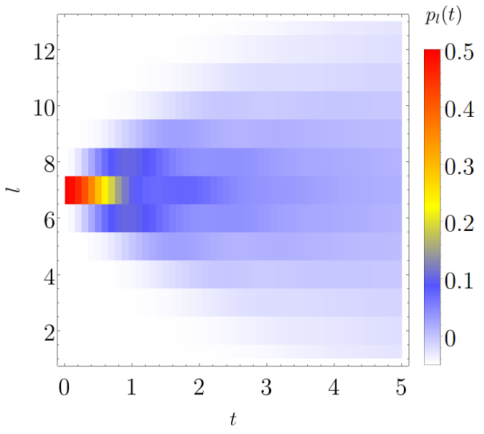

Figure 2. Broadening of the magnetization profile of a spin ladder with $L = 13$ rungs prepared in the initial state $\rho_1(0)$.

to compare the dynamics for various λ, the curves are scaled such that they all start at the same initial value of the unperturbed dynamic. The results are depicted in Fig. 4. For weak perturbations the deviation from the unperturbed dynamic is again small, although now clearly visible. For stronger perturbations the dynamics equilibrate again more slowly, however, the discrepancy to the unperturbed dynamic is more severe compared to the first initial state $\rho_1(0)$ in Fig. 3. A rough estimate indicates that at inverse temperature $\beta = 0.1$ the mean energy is down-shifted by approximately half a standard deviation of the full energy spectrum of the system with respect to the infinite temperature case ($\beta = 0$). Thus, $\beta = 0.1$ is noticeable far away from infinite temperature while still not exhibiting low temperature phenomena.

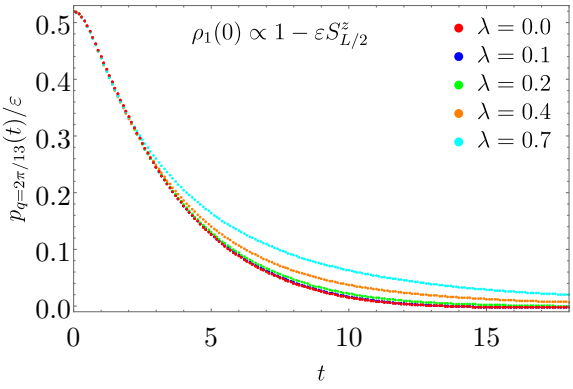

Figure 3. The time-dependence of the slowest mode with $q = 2\pi/13$ is depicted for various perturbation strengths for the initial state $\rho_1(0)$. For small perturbations the unperturbed dynamic ($\lambda = 0.0$, red curve) remains basically unchanged. For stronger perturbations there is a noticeable deviation.

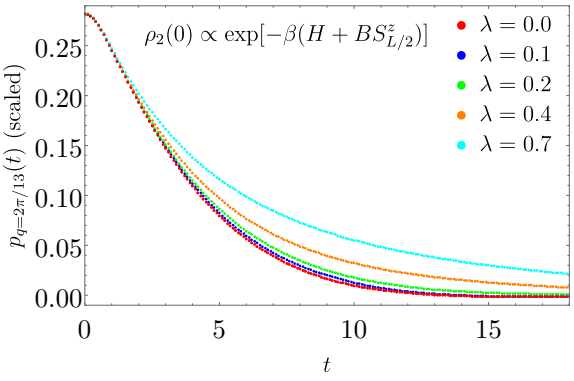

Figure 4. The time-dependence of the slowest mode with $q = 2\pi/13$ is depicted for various perturbation strengths for a Gibbsian initial state $\rho_2(0)$ with $\beta = 0.1$ and $B = 5.0$. Similar behavior as for the first initial state can be observed.

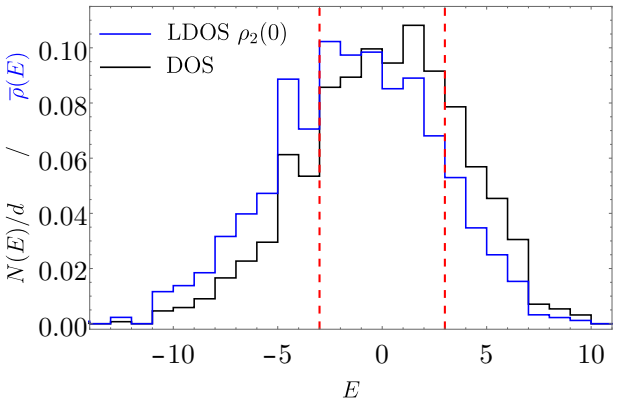

Figure 5. Density of states (black) for $N = 12$ spins. The quantity $N(E)$ is the number of energy eigenstates in a particular bin of size one, $d = 4096$ is the Hilbert space dimension. The interval of approximately constant DOS is marked from $E = -3 \ldots 3$ by red lines. A histogram of the local density of states (LDOS), i.e. the probability to find the system at a certain energy, is shown in blue. The quantity $\bar{\rho}(E)$ indicates the weight in a given bin. The LDOS of $\rho_1(0)$ is exactly identical to the DOS (black) and not shown again.

V. MODELLING THE PERTURBED DYNAMICS

Is it possible to describe the observed behavior to some extend by any the three theories mentioned in the introduction? Before we present a somewhat bold, simple comparison of the predictions from said modeling schemes with the actual perturbed dynamics, we briefly comment on the agreement of our setup (cf. Sect. III) with the preconditions of the respective theories.

The theory advocated in Ref. [8] relies on a constant density of energy eigenstates (DOS) within the energy interval occupied by the initial state $\rho(0)$ with respect to the unperturbed Hamiltonian H_0. First of all it should be noted that it is rather hard to check whether or not this criterion applies in standard situations with larger systems. However, a histogram corresponding to the DOS of H_0 for a "small" system with $N = 12$ spins is depicted in Fig. 5. The red dashed vertical lines are intended to mark the regime of more or less constant DOS (of course this choice is rather arbitrary). The initial state $\rho_1(0)$ populates the full spectrum with equal weight, i.e. 57% of the weight falls into the interval of approximately constant DOS. Likewise, although populating more low-lying energy eigenstates, a large portion (54%) of the weight of the initial state $\rho_2(0)$ still falls into the interval of approximately constant DOS, cf. Fig. 5.

The assessment of this finding is twofold: On the one hand, "natural" initial states like $\rho_1(0)$ and $\rho_2(0)$ do not necessarily live entirely in an energy window of strictly constant DOS. On the other hand, Fig. 5 indicates that the states $\rho_1(0)$ and $\rho_2(0)$ are not completely off such a description. One may thus be inclined to expect at least qualitatively reasonable results from an application of the theory presented in Ref. [8]. Concerning perturbations V, the approach in Ref. [8] strictly speaking makes no restrictions, except for "smallness". But the result from Ref. [8] is of statistical nature: To the overwhelming majority of the ensemble of matrices V that is generated by drawing matrix elements in the eigenbasis of H_0 independently at random (according to some probability distribution, which may give rise to some sparseness) the prediction of Ref. [8] (exponential damping) applies. While any V may be viewed as an instance of this set, not all V are equally likely. Again, judging the "typicality" of some concrete V is hard. However, for a qualitative evaluation of the typicality of the perturbation V at hand with respect to the above ensemble, a color-scaled plot of V in the energy eigenbasis of H_0 for $N = 12$ is depicted in Fig. 6. The red lines correspond to the energy regime marked in Fig. 5. Obviously, there is some sparseness, about 2% of all elements differ from zero. Other than that the assessment of this finding is also twofold: On the one hand, some structure is visible in Fig. 6. On the other hand, this structure is not sufficient to clearly identify V as particularly untypical. Hence, again, one may be inclined to expect at least qualitatively reasonable results from an application of the theory presented in Ref. [8]. The theory advocated in Ref. [9] relies on projection operator techniques [10] and thus has, in principle, no formal applicability limit. However, as projection operator techniques result in perturbative expansions, concrete predictions going beyond leading order are very hard to obtain [14]. Even the accurate computation of the leading order requires the knowledge of the detailed form of the ma-

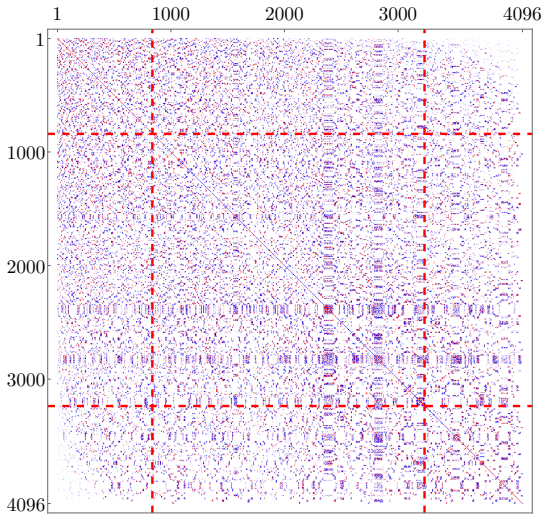

Figure 6. Matrix plot of the perturbation V in the eigenbasis of the unperturbed Hamiltonian H_0. Red lines mark the interval of approximately constant DOS, cf. Fig. 5.

trix depicted in Fig. 6 has to be taken into account. The simple guess of an exponential damping at sufficiently long times only results under preconditions that are rather similar to the ones on which the approach from Ref. [8] is based. The conditions under which the dynamics is well captured by a leading order description are technically hard to define and even harder to check. However, there are indications that the sparseness of the matrix depicted in Fig. 6 threatens the correctness of a leading order calculation [15].

The approach advocated in Ref. [7] is heuristic and primarily based on some numerical evidence, thus no formal preconditions may be formulated so far, cf. Sect. II. However, the numerical examples in Ref. [7] to which this scheme applies do feature unperturbed Hamiltonians with constant DOS, weak perturbations (small λ) and initial states of the type $\rho_1(0)$. Furthermore the V's in the examples in Ref. [7] are matrices whose elements, in the eigenbasis of the observable, are independently drawn at random according to some probability distribution. As already mentioned in Sect. II, in contrast to Refs. [8, 9], the approach in Ref. [7] takes the structure of V in the eigenbasis of the observable (here S^z_q) rather than of H_0 into account. Only if the latter approximately commute, i.e. $[V, A] \approx 0$, the prediction computed as described in Sect. II applies. For our setup we indeed have $[V, A] = 0$, cf. Sect. III.

We now embark on the announced bold comparison of the perturbed dynamics with the predictions from the three theories.

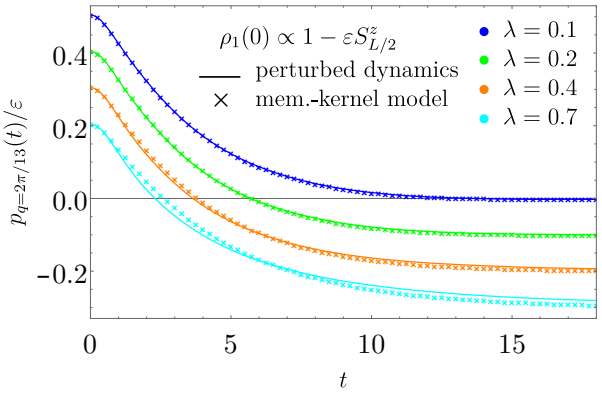

Figure 7. Slowest mode with $q = 2\pi/13$ of the infinite-temperature initial state $\rho_1(0)$ depicted for various perturbation strengths. Solid lines represent the original data from Fig. 3, vertically shifted in steps of -0.1 for better visibility. Crosses indicate the data obtained from an exponentially damped memory-kernel.

Firstly, note that for both initial states the perturbed curves lie above the unperturbed one, i.e. the stronger the perturbation the slower the relaxation occurs. Thus, theories predicting a damping of the unperturbed dynamics are not a viable option in this case. Without any further quantitative analysis this already renders the predictions from Ref. [8] and Ref. [9] qualitatively unsuitable. Moreover, it can be shown (at least for the first initial state) that all curves must feature zero slope at $t = 0$. An exponential damping (with a constant damping factor) would always change the slope at $t = 0$ to a non-zero value. A time-dependent damping factor $\Gamma(t)$ with $\Gamma(0) = 0$ (as employed in Ref. [9]) at least preserves the zero slope at $t = 0$.

These findings suggest that the perturbation V is indeed one of the mathematically untypical members of the ensemble considered in Ref. [8], even though the matrix visualization in Fig. 6 does not necessarily indicate this. However, even though V is untypical with respect to an ensemble of random matrices, it is a physically simple, common perturbation consisting of standard spin-spin interactions. The failure of the scheme presented in Ref. [9] indicates that the V at hand does not allow for a leading order truncation of the projective scheme employed therein, not even for small λ. This leaves the memory-kernel model from Ref. [7] as a the only feasible theory to describe the observed behavior.

In the following, to test the approach from Ref. [7], we apply the memory-kernel ansatz to the two unperturbed dynamics (red curves in Fig. 3 and Fig. 4). The damping constant γ from Eq. (2) functions as a fit parameter and is optimized such that the L^2-error of the two curves in question (perturbed dynamics and memory-kernel prediction) is minimized.

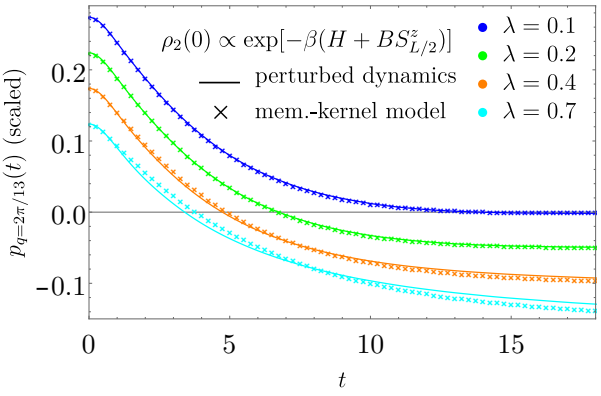

Figure 8. Slowest mode with $q = 2\pi/13$ of the Gibbsian initial state $\rho_2(0)$ with $\beta = 0.1$ and $B = 5.0$ depicted for various perturbation strengths. Solid lines represent the original data from Fig. 4, vertically shifted in steps of -0.05 for better visibility. Crosses indicate the data obtained from an exponentially damped memory-kernel.

For the infinite-temperature initial state $\rho_1(0)$ the results are depicted in Fig. 7, for the Gibbsian initial state $\rho_2(0)$ in Fig. 8. Each curve is vertically shifted to avoid clutter. For the infinite-temperature initial state $\rho_1(0)$ and weak perturbations ($\lambda = 0.1$ and $\lambda = 0.2$) the memory-kernel model seems to perfectly capture the modified dynamics. For stronger perturbations ($\lambda = 0.4$ and $\lambda = 0.7$) there are deviations visible, e.g. for short times ($t \sim 2$) the memory-kernel prediction for $\lambda = 0.7$ overshoots the perturbed dynamic while for longer times $t \gtrsim 10$ it undershoots. For the Gibbsian initial state $\rho_2(0)$ the qualitative behavior remains the same as for the first initial state. For weak perturbations the memory-kernel ansatz captures the modifications due to the perturbation extremely well. For stronger perturbations there are again more noticeable deviations. However, it comes as no surprise that the memory-kernel model looses potency in the strong perturbation regime, since it was originally conceived to describe the alteration of dynamics due to weak perturbations.

VI. SUMMARY AND CONCLUSION

In the paper at hand we numerically analyzed the applicability of three theories predicting the generic impact of Hamiltonian perturbations on expectation value dynamics to a Heisenberg spin ladder. To this end, we numerically calculated the time-dependent spatial distribution of the magnetization along the ladder for various perturbation strengths. We focused on a particular perturbation that commutes with the observable, e.g. the considered perturbation V consisting of S^zS^z-couplings on the ladder diagonals commutes with the observed spatial magnetization distribution. We consider both, infinite and finite temperatures. Two out of three scrutinized theories feature in principle well defined conditions for their applicability [8, 9], a third one is rather heuristic [7]. One of the theories with well defined conditions [8] only predicts the overwhelmingly likely behavior with respect to a hypothetical, large, "random matrix ensemble" of in principle possible perturbations V. Only the heuristic theory takes the the commutativity of the observable and the perturbation as a specifically relevant structural feature into account. It turns out to be hard to judge *a priori* whether or not the concrete spin ladder example falls into the realm of applicability of the two theories with well defined conditions. However, direct comparison of the theoretical predictions with the numerically computed results clearly shows that both theories fail even qualitatively. This suggests that, while the the considered V is very common from a physical point of view, it must be very rare and exotic with respect to the above random matrix ensemble. Only the heuristic theory was found to yield good results for weak perturbations (and acceptable results for strong perturbations). This indicates that the commutator of V with the observable is a specifically relevant structural feature that should be taken into account. A survey of the three theories for perturbations V that do not commute with the observable is left for further research.

Acknowledgments:
We thank P. Reimann and L. Dabelow for fruitful discussions on this subject. This work was supported by the Deutsche Forschungsgemeinschaft (DFG) within the Research Unit FOR 2692 under Grant No. 397107022.

[1] C. Gogolin and J. Eisert, Reports on Progress in Physics **79**, 056001 (2016).
[2] J. M. Deutsch, Phys. Rev. A **43**, 2046 (1991).
[3] M. Srednicki, Phys. Rev. E **50**, 888 (1994).
[4] S. Lloyd, arXiv:1307.0378v1 (1988).
[5] S. Goldstein, J. L. Lebowitz, R. Tumulka, and N. Zanghì, Phys. Rev. Lett. **96**, 050403 (2006).
[6] P. Reimann, Phys. Rev. Lett. **99**, 160404 (2007).
[7] L. Knipschild and J. Gemmer, Phys. Rev. E **98**, 062103 (2018).

[8] L. Dabelow and P. Reimann, Phys. Rev. Lett. **124**, 120602 (2020).
[9] J. Richter, F. Jin, L. Knipschild, H. De Raedt, K. Michielsen, J. Gemmer, and R. Steinigeweg, Phys. Rev. E **101**, 062133 (2020).
[10] H.-P. Breuer and F. Petruccione, *The Theory of Open Quantum Systems* (2006).
[11] R. Kubo, M. Toda, N. Saito, and N. Hashitsume, *Statistical Physics II: Nonequilibrium Statistical Mechanics* (1985).
[12] L. Knipschild and J. Gemmer, Phys. Rev. A **99**, 012118 (2019).
[13] J. Richter et. al, Phys. Rev. B **99**, 144422 (2019).
[14] R. Steinigeweg and T. Prosen, Phys. Rev. E **87**, 050103 (2013).
[15] C. Bartsch, R. Steinigeweg, and J. Gemmer, Phys. Rev. E **77**, 011119 (2008).

Preprint of Publication [P4]

Robin Heveling, Jiaozi Wang, Robin Steinigeweg, and Jochen Gemmer
"Integral fluctuation theorem and generalized Clausius inequality for microcanonical and pure states"
Physical Review E **105**, 064112 (2022)
DOI: 10.1103/PhysRevE.105.064112

Integral Fluctuation Theorem and Generalized Clausius Inequality for Microcanonical and Pure States

Robin Heveling,* Jiaozi Wang,† Robin Steinigeweg,‡ and Jochen Gemmer§
Department of Physics, University of Osnabrück, D-49076 Osnabrück, Germany

Fluctuation theorems are cornerstones of modern statistical mechanics and their standard derivations routinely rely on the crucial assumption of a canonical equilibrium state. Yet, rigorous derivations of certain fluctuation theorems for microcanonical states and pure energy eigenstates in isolated quantum systems are still lacking and constitute a major challenge to theory. In this work, we tackle this challenge and present such a derivation of an integral fluctuation theorem (IFT) by invoking two central and physically natural conditions, i.e., the so-called "stiffness" and "smoothness" of transition probabilities. Our analytical arguments are additionally substantiated by numerical simulations for archetypal many-body quantum systems, including integrable as well as nonintegrable models of interacting spins and hard-core bosons on a lattice. These simulations strongly suggest that "stiffness" and "smoothness" are indeed of vital importance for the validity of the IFT for microcanonical and pure states. Our work contrasts with recent approaches to the IFT based on Lieb-Robinson speeds and the eigenstate thermalization hypothesis.

I. INTRODUCTION

The question of how irreversible thermodynamics can emerge from the underlying theory of quantum mechanics has regained interest in the last decades [1]. On the theoretical side concepts like the eigenstate thermalization hypothesis [2–6] and quantum typicality [7–9] have been developed. Furthermore, rapid advancements on the experimental side in recent years enable the observation of thermalization in isolated quantum systems, e.g., in experiments on ultra-cold atoms [10–14].

At the heart of these issues is the second law of thermodynamics, which states that in isolated systems the total entropy can only increase. However, the second law is merely of statistical nature, i.e., there may be exceedingly rare but possible processes (which occur more often as systems become smaller) in which the entropy does indeed decrease [15]. These deviations are not random, but obey themselves rigid rules, which are often summarized under the name of fluctuation theorems [15–22]. Fluctuation theorems formulate and to some extent generalize the second law of thermodynamics by relating the entropy production of processes, which may take the system arbitrarily far away from equilibrium, to properties of the equilibrated system in a quantitative manner. Just as for the second law, the underlying mechanisms which render these theorems valid or invalid are still under discussion.

In this work, we consider an integral fluctuation theorem (IFT) for the total entropy production of a small quantum system coupled to a substantially larger but finite bath. While the IFT itself [Eq. (9)] is more encompassing, its most prominent consequence reads

$$S_{\mathrm{sys}}(t_1) + \frac{\langle H_{\mathrm{bath}}(t_1)\rangle}{T} \geq S_{\mathrm{sys}}(t_0) + \frac{\langle H_{\mathrm{bath}}(t_0)\rangle}{T}\,, \quad (1)$$

for $t_1 \geq t_0$. Here, S_{sys} is the von Neumann entropy of the system, the mean energy of the the bath is denoted by $\langle H_{\mathrm{bath}}\rangle$ and T is the microcanonical bath temperature. Eq. (1) corresponds to the generalized inequality of Clausius, which is sometimes viewed as one possibility to express the second law of thermodynamics [23].

Given the significance of the generalized Clausius inequality, it is remarkable that, so far, the validity of the respective IFT has only been proven in full generality for canonical initial states of the (closed) full system, but not for microcanonical or pure states [19, 24]. It is worth mentioning that for far-from-equilibrium statements like fluctuation theorems, results from the canonical ensemble do not straightforwardly carry over to, e.g., the microcanonical ensemble directly by the equivalence of ensembles. This may be inferred from, e.g., the existence of recent works, which aim at establishing alternative fluctuation relations for microcanonical conditions [25–27].

Recently, pioneering steps to bridge this gap, i.e., to establish the validity of the IFT also for (pure) initial states with a sharp bath energy, have been put forth [24, 28, 29]. These approaches rely on finite Lieb-Robinson speeds, typicality and the eigenstate thermalization hypothesis. They prove the IFT for infinite baths and also for extremely large baths paired with intermediate interaction strengths between system and bath. However, there is a significant, physically relevant set of combinations of bath sizes and interactions strengths for which these approaches [24, 28, 29] are unsuitable [30].

* rheveling@uos.de
† jiaowang@uos.de
‡ rsteinig@uos.de
§ jgemmer@uos.de

Nevertheless, also for these combinations the IFT is numerically found to hold (see Figs. 7, 9).

Related to the paper at hand, but conceptually different, are the works in Refs. [25, 26]. While these works also aim at establishing Crooks-Type fluctuation theorems for microcanonical conditions, the employed notion of entropy is different from the definition of entropy production used in [24, 28, 29] and the paper at hand, cf. Eq. (4). The former is not amenable for a direct connection to the generalized Clausius inequality. Furthermore, the former holds more or less by virtue of the laws of quantum mechanics, whereas the validity of the IFT based on the latter depends on the features of the specific physical system.

With the paper at hand, we aim to establish the validity of the IFT as in [24, 28, 29] for a wider range of systems, also covering a substantial portion of cases for which the mentioned approaches fail. To this end, we rely on entirely different concepts. We employ natural assumptions on transition probabilities, which we call "stiffness" and "smoothness". In essence, stiffness states that transition probabilities are largely independent of the specific initial energy and only depend on the difference between initial and final energy. Furthermore, smoothness states that individual transition probabilities are close to the average transition probability in some respective energy interval. The existence of stiffness and smoothness and their importance for validity the Jarzynski relation has already been numerically demonstrated [31, 32].

The paper at hand is organized as follows: In Sec. II A, the original, "microscopic" IFT and a "coarse-grained" version of it are presented. In Sec. II B, we introduce the notion of stiffness and show that the validity of the coarse-grained IFT follows from the assumption of stiffness. Next, in Sec. II C, we introduce the notion of smoothness and show that the validity of the microscopic IFT follows from the (additional) assumption of smoothness. In Sec. III, we substantiate our theoretical considerations by numerically analyzing three exemplary models: an Ising model (Sec. III A), a hard-core boson model (Sec. III B) and an integrable Heisenberg model (Sec. III C). A concluding discussion follows in Sec. IV. We give technical details of our derivations in App. A and B and make a case for the ubiquitous existence of stiffness in App. C. Definitions of numerical quantities as well as additional numerical results can be found in App. D, E, F and G.

II. INTEGRAL FLUCTUATION THEOREMS FROM STIFFNESS AND SMOOTHNESS

The eventual aim of this full section is to establish the validity of the microscopic IFT for pure initial energy eigenstates of the bath under some assumptions. To this end, we introduce, as an intermediate step, a coarse-grained IFT (Sec. II A) and show that it holds under the assumption of stiffness (Sec. II B). In a second step, this result is processed to show that under the additional assumption of smoothness not only the coarse-grained IFT but also the microscopic IFT holds (Sec. II C).

A. Microscopic and coarse-grained integral fluctuation theorem

We consider a system-bath setup with total time-independent Hamiltonian

$$H = H_0 + H_{\mathrm{int}} = H_{\mathrm{sys}} + H_{\mathrm{bath}} + H_{\mathrm{int}}\,, \tag{2}$$

where H_{sys} is the system Hamiltonian and H_{bath} is the bath Hamiltonian. System and bath are allowed to interact via an interaction term H_{int}. The eigenstates of the system (bath) are denoted by $|k\rangle$ ($|b\rangle$). The composite system is initialized in a product state

$$\rho(0) = \sum_{k,b} P^k_{\mathrm{ini}} W^b_{\mathrm{ini}} |k,b\rangle\langle k,b|\,, \tag{3}$$

where $|k,b\rangle = |k\rangle \otimes |b\rangle$. Here, the initial system (bath) state is diagonal in the eigenbasis of the system (bath) Hamiltonian. The quantity P^k_{ini} (W^b_{ini}) is the initial weight distribution over the energy eigenstates of the system (bath). System and bath are initially uncorrelated and then brought into contact at $t = 0$ via H_{int}. The composite system evolves unitarily in time, i.e., $\rho(t) = U(t)\rho(0)U^\dagger(t)$, where $U(t) = \exp(-\mathrm{i}Ht)$ is the time evolution operator ($\hbar = 1$). A central operator of interest is the entropy production operator [24, 33]

$$\sigma(t) = -\log \rho_{\mathrm{sys}}(t) + \beta(H_{\mathrm{bath}} - \mu N_{\mathrm{bath}})\,, \tag{4}$$

where the reduced density operator of the system at time t is denoted by $\rho_{\mathrm{sys}}(t) = \mathrm{Tr}_{\mathrm{bath}}[\rho(t)]$, $\beta = 1/(k_{\mathrm{B}}T)$ is the inverse temperature of the bath and k_{B} is the Boltzmann constant. A nonzero μ has only to be taken into account if a "particle-number-like" quantity exists, which is conserved on the full system and may flow between system and bath.

The operator $\sigma(t)$ is explicitly time-dependent due to the first term. The eigenvalues of $\sigma(t)$ are given by

$$\sigma^{j,a}(t) = -\log P^j_{\mathrm{sys}}(t) + \beta\varepsilon^a_{\mathrm{bath}}\,, \tag{5}$$

where $\varepsilon^a_{\mathrm{bath}}$ is an eigenvalue of the operator in brackets $(H_{\mathrm{bath}} - \mu N_{\mathrm{bath}})$ in Eq. (4) and $P^j_{\mathrm{sys}}(t)$ are the eigenvalues of $\rho_{\mathrm{sys}}(t)$. For simplicity, we will still refer to the $\varepsilon^a_{\mathrm{bath}}$ as energy eigenvalues. The eigenstates are denoted by $|\sigma^{j,a}(t)\rangle$. We consider an ensemble average of differences in projective measurement outcomes at the initial time $t = 0$ and some final time t [19] (denoted by

double brackets $\langle\!\langle \bullet \rangle\!\rangle$). Given some arbitrary but nicely behaved function f, the ensemble average of $f(\sigma(t))$ is defined by

$$\langle\!\langle f(\Delta\sigma)\rangle\!\rangle = \sum_{j,k,a,b} f(\sigma^{j,a}(t) - \sigma^{k,b}(0)) \times P^k_{\text{ini}} W^b_{\text{ini}} R(jk,ab)\,, \tag{6}$$

where

$$R(jk,ab) = |\langle \sigma^{j,a}(t)|U(t)|\sigma^{k,b}(0)\rangle|^2 \tag{7}$$

is the probability to transition from an initial state $|\sigma^{k,b}(0)\rangle$ to a final state $|\sigma^{j,a}(t)\rangle$. For brevity, we drop the explicit time dependence of the quantity in double brackets and in the argument of the transition probabilities. For $f(x) = x$, Eq. (6) yields the average entropy production $\langle\!\langle \Delta\sigma \rangle\!\rangle$, which may be written as a standard quantum mechanical expectation value (denoted by $\langle\bullet\rangle$)

$$\begin{aligned}\langle\!\langle \Delta\sigma \rangle\!\rangle &= \langle \sigma(t) - \sigma(0)\rangle \\ &= \Delta S_{\text{sys}} + \beta \Delta U_{\text{bath}} - \beta\mu \Delta N_{\text{bath}}\,.\end{aligned} \tag{8}$$

The first term is the change in von Neumann entropy of the system, the other terms account for entropy change in the bath due to heat and particle transfer, respectively. Another important quantity is $\langle\!\langle e^{-\Delta\sigma}\rangle\!\rangle$, which is defined by Eq. (6) by setting $f(x) = \exp(-x)$. This quantity (hereafter referred to as the microscopic IFT quantity) appears in the frequently considered integral fluctuation theorem (hereafter referred to as the microscopic IFT) which reads

$$\langle\!\langle e^{-\Delta\sigma}\rangle\!\rangle = 1\,. \tag{9}$$

This microscopic IFT is known to hold exactly if the initial energy distribution of the bath is (grand-)canonical [19, 24]. It is also well-known that the microscopic IFT implies the second law of thermodynamics in the sense that the average entropy production (between some initial and some final point in time) is positive. This can be obtained by plugging Eq. (9) into the Jensen inequality $e^{\langle\!\langle x\rangle\!\rangle} \leq \langle\!\langle e^x\rangle\!\rangle$ yielding $\langle\!\langle \Delta\sigma\rangle\!\rangle \geq 0$, which is tantamount to the generalized inequality of Clausius [Eq. (1)].
An explicit expression for the microscopic IFT quantity is given by

$$\langle\!\langle e^{-\Delta\sigma}\rangle\!\rangle = \sum_{j,k,a,b} P^j_{\text{fin}} W^b_{\text{ini}}\, e^{-\beta(\varepsilon^a_{\text{bath}} - \varepsilon^b_{\text{bath}})} R(jk,ab)\,, \tag{10}$$

where $P^j_{\text{fin}} = P^j_{\text{sys}}(t)$. Importantly, even though P^k_{ini} does not appear anymore, the sum over k must still be kept (otherwise the IFT does not even hold for canonical initial states). For system-bath setups treatable with exact diagonalization techniques, Eq. (10) constitutes a convenient formula to check whether the IFT holds.

Continuing, we construct a coarse-grained version of the IFT quantity [Eq. (17)] and discuss/proof a corresponding coarse-grained fluctuation theorem [Eq. (21)]. The starting point is the conceptual restriction to finite energy resolutions. We think of the system only comprising a few energy levels, e.g., a single spin. Hence, we will resort to dividing just the energy scale of the bath into bins of finite size δ, see Fig. 1. As of yet, individual eigenvalues were denoted by an "ε". Now, energy intervals are denoted by an "E" and enumerated by capitalized indices. The bin size δ should be small compared to the energy scale of the bath, but large compared to its level spacing, or, to be more precise, δ should be chosen as small as possible subject to the condition that the number of bath eigenvalues $\varepsilon^b_{\text{bath}}$ in an interval centered around $B\delta$ [defined as Ω_B below Eq. (12)] is still a smooth function of B.
The probability $R(jk,Ab)$ to transition from an initial eigenstate $|k,b\rangle$ to any state $|j,a\rangle$ with $\varepsilon^a_{\text{bath}} \in E^A_{\text{bath}}$, i.e., to a range of bath eigenstates, is obtained by

$$R(jk,Ab) = \sum_{a\in A} R(jk,ab)\,. \tag{11}$$

To clarify the notation, "$a \in A$" is short for "sum over all a such that $\varepsilon^a_{\text{bath}} \in E^A_{\text{bath}}$". Here, a comment on the case in which the system has an additional "good quantum number" [as discussed below Eq. (4)] is in order. In this instance, the set of "target" states of the transition probability defined in Eq. (11) should not only be specified by the respective energy interval, but also by a specific value for the above quantum number. Thus, the set should technically be labeled as, e.g., A_Z to indicate all eigenstates of the bath with eigenvalues in the energy interval E^A_{bath} featuring the quantum number Z (where Z is an eigenvalue of N_{bath}).
In order to avoid clutter, we suppress the quantum number in the explicit notation whenever it is dispensable, which is the remainder of this section. However, the quantum number will be explicitly displayed in Apps. D, F, G. The suppression of the quantum number is also applied in the usage of the letter B introduced next.

Figure 1. Energy scale of the bath divided into intervals according to $E^B_{\text{bath}} = [(B-1/2)\delta, (B+1/2)\delta]$, where $B = ..., -2, -1, 0, 1, 2, ...$. The interval E^B_{bath} is of width δ and is centered around the midpoint $B\delta$.

We define the *average* probability to transition from an initial state $|k,b\rangle$ with $\varepsilon^b_{\rm bath} \in E^B_{\rm bath}$ to a final energy interval $E^A_{\rm bath}$ by

$$\overline{R}(jk,AB) = \frac{1}{\Omega_B}\sum_{b\in B} R(jk,Ab)\,, \tag{12}$$

where Ω_B is the number of bath energy eigenvalues $\varepsilon^b_{\rm bath}$ within the energy interval $E^B_{\rm bath}$ (up to a bin size-dependent prefactor, Ω_B is essentially the density of states (DOS) of the operator $H_{\rm bath} - \mu N_{\rm bath}$).
To continue, we introduce auxiliary processes in which a states evolve under $U^\dagger$. Corresponding transition probabilities are defined by

$$\widetilde{R}(jk,ab) := |\langle \sigma^{j,a}(0)|U^\dagger(t)|\sigma^{k,b}(t)\rangle|^2 \tag{13}$$

[this is to be compared to Eq. (7)]. We also define auxiliary average transition probabilities $\widetilde{R}(jk,AB)$, completely analogous to $\overline{R}(jk,AB)$, cf. Eq. (7), Eq. (11) and Eq. (12), except for a replacement of $R(jk,ab)$ by $\widetilde{R}(jk,ab)$ in Eq. (7).
Next, we compute the ratio between a given average transition probability and the corresponding auxiliary quantity, i.e.,

$$\frac{\overline{R}(jk,AB)}{\widetilde{R}(kj,BA)} = \frac{\Omega_A}{\Omega_B}\,. \tag{14}$$

Note that this relation does not rely on the concept of microreversibility. In the following, we assume an exponential DOS, i.e.,

$$\Omega_B \propto e^{\beta\delta B}\,. \tag{15}$$

Of course, we do not assume Eq. (15) to hold globally, but only for states that actually participate in the dynamics resulting from some initial state. (Strong) restrictions to this set of states may arise from conservation of energy and, possibly, additional conserved quantities like particle number. Strictly speaking Eq. (15) is an assumption just like the (yet to be) introduced concepts of stiffness and smoothness. However, Eq. (15) is a "traditional" assumption for short-range interacting systems (without additional conserved quantities) that at least goes back to Landau and Lifshitz [34]. Thus, there will be less focus on it than on stiffness and smoothness.
By algebraic manipulation of Eq. (14), multiplying with $P^j_{\rm fin}W^B_{\rm ini}$ (where $W^B_{\rm ini} := \sum_{b\in B} W^b_{\rm ini}$) and summing over j,k,A,B we get that

$$\begin{aligned}\sum_{j,k,A,B} P^j_{\rm fin}W^B_{\rm ini}e^{-\beta\delta(A-B)}\overline{R}(jk,AB) \\ = \sum_{j,k,A,B} P^j_{\rm fin}W^B_{\rm ini}\widetilde{R}(kj,BA)\,.\end{aligned} \tag{16}$$

The l.h.s. of Eq. (16) looks similar to the r.h.s. of Eq. (10), such that we define the coarse-grained ("c.g.") IFT quantity as

$$\langle\!\langle e^{-\Delta\sigma}\rangle\!\rangle_{\rm c.g.} = \sum_{j,k,A,B} P^j_{\rm fin}W^B_{\rm ini}e^{-\beta\delta(A-B)}\overline{R}(jk,AB)\,. \tag{17}$$

Indeed, Eq. (17) may be interpreted as a "coarse-grained" version of $\langle\!\langle e^{-\Delta\sigma}\rangle\!\rangle$ in the sense that:
i. energy changes in the bath are now counted on the level of energy intervals rather than individual energy eigenvalues,
ii. the transition probabilities now apply to transitions from microcanonical initial states (restricted to the initial interval $E^B_{\rm bath}$) to the final energy interval $E^A_{\rm bath}$ rather than to transitions between individual energy eigenstates and
iii. the initial probabilities for the bath are now probabilities to find the bath in the respective energy interval rather than in the corresponding eigenstate.
One may be inclined to think that Eq. (17) in general becomes Eq. (10) in the limit of small energy intervals. But this sentiment is flawed, since Eq. (15) and thus Eq. (17) rely on notions that ultimately break down in the limit of small energy intervals. This is the case, if δ is too small to render Ω_B a smooth function of B and thus Eq. (15) cannot apply.
It is important to note that for a microcanonical initial bath state the microscopic IFT quantity [Eq. (10)] becomes equal to the coarse-grained IFT quantity [Eq. (17)] for temperatures that are not too low, i.e, for $\beta\delta \ll 1$. Thus, establishing the coarse-grained IFT [$\langle\!\langle e^{-\Delta\sigma}\rangle\!\rangle_{\rm c.g.} = 1$] would already be sufficient to also establish the microscopic IFT [$\langle\!\langle e^{-\Delta\sigma}\rangle\!\rangle = 1$] for microcanonical initial bath states, if the above conditions apply. However, a single initial energy eigenstate of the bath certainly violates these conditions and will be separately addressed in Sec. II C.

B. Validity of the coarse-grained integral fluctuation theorem via stiffness

Now we are set to define the crucial property of stiffness, which will be utilized to show that the coarse-grained IFT [$\langle\!\langle e^{-\Delta\sigma}\rangle\!\rangle_{\rm c.g.} = 1$] holds for all possible initial distributions $W^B_{\rm ini}$ including microcanonical conditions.

A transition probability to go from some initial energy interval E^B_{bath} to a final energy interval E^A_{bath} is called *stiff* (for given j,k), if we have that

$$\overline{R}(jk,AB) = \overline{R}(jk,A-B)\,, \tag{18}$$

i.e., the probability to transition from the initial energy interval E^B_{bath} to a state within the final energy interval E^A_{bath} is only a function of the difference in energies.
As will become clear in the remainder, the assumption of stiffness is a central ingredient that allows to establish the validity of the coarse-grained and microscopic IFT in parameter regimes of the respective systems that are not covered by the approaches in Refs. [24, 28, 29], see also explanations in and around Fig. 7. While stiffness itself is an assumption, in App. C we present a consideration indicating that stiffness may in general be the rule rather than the exception. It may further be worth noting that some authors consider the existence of stiffness at large energies as so obvious that they rely on it without any further justification [27]. In Sec. III, we provide numerical evidence for stiffness for all considered models.
Stiffness as defined in Eq. (18) implies a useful relation for the time-reversed transition probabilities, i.e.,

$$\sum_A \widetilde{R}(kj,BA) = \sum_B \widetilde{R}(kj,BA)\,, \tag{19}$$

which is based on Eq. (14) and Eq. (15). For the concise derivation see App. A. From the double stochasticity of the regular $R(jk,ab)$ we can deduce that

$$\sum_{k,B} \widetilde{R}(kj,BA) = 1\,. \tag{20}$$

For the derivation of the coarse-grained IFT we start from the r.h.s. of Eq. (16). We consider a microcanonical bath state with occupation probability $W^B_{\text{ini}} = \delta_{B,B_0}$, where δ_{B,B_0} denotes the Kronecker delta and W^B_{ini} thus completely "fills" one energy interval B_0. Plugging W^B_{ini} into Eq. (16) yields

$$\begin{aligned}\langle\!\langle e^{-\Delta\sigma}\rangle\!\rangle_{\text{c.g.}} &= \sum_{j,k,A,B} P^j_{\text{fin}}\delta_{B,B_0}\widetilde{R}(kj,BA) \\ &= \sum_{j,k,A} P^j_{\text{fin}}\widetilde{R}(kj,B_0A) \\ &= \sum_{j,k,B_0} P^j_{\text{fin}}\widetilde{R}(kj,B_0A) = 1\,.\end{aligned} \tag{21}$$

Firstly, the sum over B was carried out. Then Eq. (19) was employed to replace the summation over A with a summation over B_0. Lastly, the sums factorize and yield unity by means of Eq. (20). Thus, the validity of the coarse-grained IFT is shown for microcanonical initial states under the assumption of stiffness. This is the first main result of our paper.
This result naturally entails the follow-up question, whether or not stiffness is to be expected for a wide range of systems. A full-fledged answer is certainly beyond the scope of this work and possibly subject of future research.

C. Validity of the microscopic integral fluctuation theorem via stiffness and smoothness

In this subsection, we will define the property of smoothness of transition probabilities and show that under the assumption of smoothness the coarse-grained IFT quantity [Eq. (17)] actually becomes an arbitrarily good approximation of the microscopic IFT quantity [Eq. (10)]. This holds even if the bath initially only occupies an individual energy eigenstate. In general, the probability to transition from some initial energy eigenstate to some final energy interval differs from the average transition probability to go from the initial energy interval to the final energy interval. We denote the difference of these two quantities by r according to

$$R(jk,Ab) = \overline{R}(jk,AB) + r(jk,Ab)\,. \tag{22}$$

We call a set of transition probabilities $R(jk,Ab)$ from an initial state $|k,b\rangle$ to a final energy interval E^A_{bath} *smooth* (for given j,k), if we have that

$$r(jk,Ab) \approx 0 \tag{23}$$

for all $b \in B$, i.e., all transition probabilities to go from a state with initial energy $\varepsilon^b_{\text{bath}}$ within the initial interval E^B_{bath} to the final energy interval E^A_{bath} are close to the average value of transition probabilities within that initial energy interval. In App. B it is shown in detail that

$$\langle\!\langle e^{-\Delta\sigma}\rangle\!\rangle \overset{r\to 0}{\longrightarrow} \langle\!\langle e^{-\Delta\sigma}\rangle\!\rangle_{\text{c.g.}}\,, \tag{24}$$

i.e., the two versions of the IFT indeed coincide if the transition probabilities are sufficiently smooth.
A well-controlled approximation of the exponential factor enters this derivation as well, for details see App. B. Hence, the validity of the microscopic IFT, even and especially for initial eigenstates, may be inferred from the validity of the coarse-grained IFT, if Eq. (23) applies. This is the second main result of our paper.
In general, the validity of Eq. (23) cannot be directly inferred form the validity the eigenstate thermalization hypothesis [5], however there is a strong connection: An approximation (whose quality depends on the details) to the $R(jk,Ab)$ may be computed in first-

order time-dependent perturbation theory. Within this framework, it may be shown that Eq. (23) applies if the eigenstate thermalization hypothesis applies to H_{int} when displayed in the eigenbasis of H_0, see App. C.

III. NUMERICAL ANALYSIS

In this section, we present a numerical analysis on three systems, a transverse Ising model with defects, a hard-core boson model and an integrable Heisenberg chain, all of which consist of a considered system, a bath and an interaction. For each model we investigate various interaction strengths and present a finite-size scaling concerning the bath size. Our primary goal is to check whether the coarse-grained and/or the microscopic IFT hold for microcanonical and pure initial states, respectively. We also analyze to what extent stiffness and smoothness are fulfilled/violated in each case. We also, though less thoroughly, address whether or not the DOS of the bath is indeed exponential, cf. Eq. (15).

For conciseness, we present more data for the Ising model in the main text than for the two other models. However, the corresponding numerical results for the latter can be found in App. E, F and G.

We employ exact diagonalization to calculate energy eigenvalues and eigenstates and use a Chebyshev iterator to evolve states in time.

Through the operator σ [cf. Eq. (4)], the microscopic as well as the coarse-grained IFT quantities [cf. Eq. (10) and Eq. (17)] involve the parameters β and (in specific cases) μ. Optimal values for these parameters correspond to energy and, possibly, particle number of the initial bath state for a given system. The computation of this correspondence is rather technical and may be somewhat involved, therefore, we describe the employed method in detail in App. D.

Furthermore, checking stiffness and smoothness requires adequately defined quantifiers that capture how well Eq. (18) and Eq. (23) are fulfilled, respectively. Both quantifiers defined below tend to zero if the respective assumptions (stiffness and smoothness) indeed apply.

We introduce a stiffness quantifier $\overline{\chi}$ that is defined by

$$\overline{\chi} = \frac{1}{4N_B} \sum_{j,k,B:|B-B_0|\leq C\Xi(\lambda)/\delta} \sum_{W} \left|\overline{R}(jk;W+B,B) - \overline{R}(jk;W+B_0,B_0)\right|, \tag{25}$$

where N_B is the number of terms in the sum over B. We choose the parameter $C = 3$, however, $\overline{\chi}$ is not very sensitive to this specific choice (this quantifier basically measures the deviation from the "diagonal structure", which is visible in Fig. 4.)

The quantity $\Xi(\lambda)$ that determines the limit in the first summation in Eq. (25) is the average standard deviation of the transition probability distributions over final energy intervals.

$$\Xi(\lambda) = \frac{1}{n_b} \sum_b \sqrt{\langle\psi_t^{k,b}|H_0^2|\psi_t^{k,b}\rangle - \langle\psi_t^{k,b}|H_0|\psi_t^{k,b}\rangle^2} \tag{26}$$

The states $|\psi_t^{k,b}\rangle = \exp(-\mathrm{i}H(\lambda)t)|k,b\rangle$ are states of the composite system at the final time t, the index b is restricted to a small energy regime of unit width around $\mathcal{E}_0$ and n_b is the respective number of the b's taken into account. While the construction of $\overline{\chi}$ is quite involved, the meaning is simple: a value of $\overline{\chi}$ that is small compared to unity signals that Eq. (18) holds to good accuracy.

For smoothness we define a quantifier by

$$\overline{\varphi} = \frac{1}{4\Omega_{B_0}} \sum_{j,k,A,b\in B_0} \left|R(jk,Ab) - \overline{R}(jk,AB_0)\right|, \tag{27}$$

where the sum runs over all final energy intervals E_{bath}^A and energy eigenvalues $\varepsilon_{\mathrm{bath}}^b$ in the energy interval $E_{\mathrm{bath}}^{B_0}$. This quantifier measures the deviation of the transition probabilities $R(jk,Ab)$ from the average transition probability, cf. Eq. (22). A small value of $\overline{\varphi}$ compared to unity indicates that smoothness is fulfilled to a good extent.

In the following, in order to ease the numerics, we replace the eigenstates of $\sigma(t)$ by the eigenstates of H_0, i.e., $|\sigma^{k,b}(t)\rangle \to |k,b\rangle$. While this would, in principle, not be necessary, it greatly reduces numerical effort. Both sets of eigenstates are product states with coinciding bath states. The system states differ to the extend to which $\rho_{\mathrm{sys}}(t)$ develops nonzero off-diagonal elements (in the basis in which it was initially diagonal). We argue and numerically confirm that these off-diagonal elements remain exactly zero for the hard-core boson and the Heisenberg model, and negligible for the Ising model, even for strong interactions, cf. App. E.

A. Transverse Ising model

The first setup under consideration is a transverse Ising model with defects. The system (blue) consists of a single spin and the bath (orange) is a ring of length L, yielding a total of $L+1$ spins, see Fig. 2. The system, bath and interaction Hamiltonians are given by

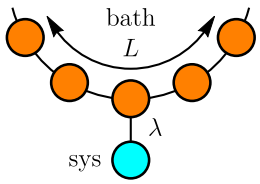

Figure 2. Sketch of the transverse Ising model.

$$H_{\text{sys}} = \sigma_0^x\,, \qquad H_{\text{int}} = \lambda\,\sigma_0^z\sigma_1^z\,, \tag{28}$$
$$H_{\text{bath}} = \sum_{i=1}^{L}\sigma_i^z\sigma_{i+1}^z + \sum_{i=1}^{L}\sigma_i^x + h_3\sigma_3^z + h_6\sigma_6^z\,,$$

where $\sigma_i^{x,y,z}$ denote Pauli matrices on site i and we set $L+1\equiv 1$. The local magnetic fields are chosen as $h_3 = 0.55$ and $h_6 = 0.81$, while the interaction strength λ is varied. This choice of parameters ensures that the bath exhibits chaotic behavior [35]. We fix the inverse temperature to $\beta = 0.1$, which for $L = 18$ corresponds to $\mathcal{E}_0 = -4.01$. This yields an acceptable validity of Eq. (15) within the relevant energy regime (cf. App. E). The bin size is adequately chosen as $\delta = 0.03$.

Firstly, we will investigate the coarse-grained IFT. The composite system is initialized in a product state of a spin-up system state and a microcanonical bath state

$$\rho(0) = \frac{\pi_\uparrow \otimes \pi_{\mathcal{E}_0,\delta}}{\text{Tr}[\pi_\uparrow \otimes \pi_{\mathcal{E}_0,\delta}]}\,, \tag{29}$$

where $\pi_{\mathcal{E}_0,\delta}$ denotes a projector onto an energy shell of width δ centered around the energy $\mathcal{E}_0$.

For a first overview, the temporal behavior of the deviation from unity of the coarse-grained IFT quantity [Eq. (17)] is depicted in Fig. 3 for various interaction strengths. Note that a value of zero indicates the perfect validity of the coarse-grained IFT. For all considered interactions strengths λ, the coarse-grained IFT is fulfilled to very good accuracy, even for the moderate bath size $L = 18$. This is our first main numerical result.

Since stiffness necessarily renders the coarse-grained IFT valid [see Sec. II B], we now examine stiffness in the transverse Ising model in more detail. To get a better intuition for the property of stiffness, a colormap of the average transition probability as a function of the initial and final energy is shown in Fig. 4 for $(j,k) = (\downarrow,\uparrow)$. The translational invariance along the diagonal clearly indicates the presence of stiffness. For a more quantitative analysis, the stiffness quantifier $\overline{\chi}$ is plotted over inverse bath size in Fig. 5. There is a clear decrease of the stiffness quantifier with bath size for all interaction strengths. Moreover, the figure suggests that stiffness becomes perfectly fulfilled and thus the coarse-grained IFT exactly valid in the thermodynamic limit. This is our second main numerical result.

Before we present microscopic IFT data for pure initial states below, we display data for our second quantifier. The smoothness quantifier is logarithmically plotted in Fig. 6 as a function of bath size L. It appears to decrease exponentially with L for all interaction strengths. Thus, perfect smoothness in the sense of Eq. (23) may be expected in the thermodynamic limit. This is our third main numerical result (in accordance with the ETH).

Next, we turn our attention to the microscopic IFT for pure states. The initial states are now product states of a spin-up system state and pertinent energy eigenstates of the bath, i.e.,

$$\rho(0) = |\uparrow, b_0\rangle\langle\uparrow, b_0|\,. \tag{30}$$

To keep the display of numerical results as concise and transparent as possible, we no longer show data for independently varied interaction strengths and system sizes as done in, e.g., Fig. 5 and Fig. 6. Rather, we focus on

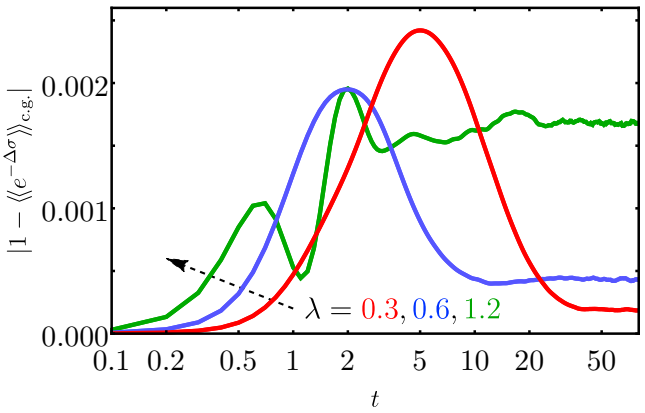

Figure 3. "Violations" of the coarse-grained IFT [Eq. (21)] plotted over time t for the Ising model ($L = 18$) for various interaction strengths. Even the maxima of the deviations are very small, i.e., the coarse-grained IFT is well fulfilled for all interaction strengths λ.

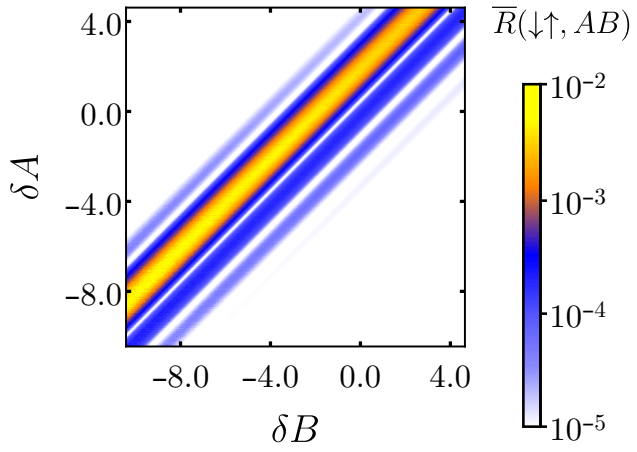

Figure 4. Average probabilities to transition from a mean bath energy δB to δA [Eq. (12)] while the system spin transitions from $|\uparrow\rangle$ to $|\downarrow\rangle$. The translational invariance along the diagonal indicates the existence of stiffness [Eq. (18)]. The transition probabilities are calculated for the Ising model with $\lambda = 0.3$ for $L = 15$ at $t = 4$, the bin size is chosen as $\delta = 0.03$.

parameter sets that are of particular interest, since a justification of the microscopic IFT for these sets is so far lacking in the literature. A short explanation of this absence is in order. Recent results establish the validity of the microscopic IFT at times shorter than the so-called Lieb-Robinson time and/or longer than the relaxation time [24, 28, 29]. As the Lieb-Robinson time τ_{LR} increases with L and the relaxation time τ_{rel} decreases with λ, there are combinations of (small) bath sizes and (weak) interactions for which there is a gap between the Lieb-Robinson time and the relaxation time [note that the relaxation time τ_{rel} quickly becomes independent of L as the bath size grows, see also Fig. 13 in App. E]. Within this gap, the reasoning in Refs. [24, 28, 29] cannot establish the validity of the microscopic IFT. In the following, we focus on this "gapped" region in parameter space. Since the Lieb Robinson-time increases at most linearly with system size and the relaxation time scales inversely with the square of the interaction strength [see Fig. 13 in App. E], the temporal gap remains open for combinations of λ, L fulfilling

$$\lambda \leq K/\sqrt{L}\,, \tag{31}$$

where K is some suitable constant. We choose to check the situations at the "edge" of this parameter region, i.e., for the equality sign in Eq. (31) with $K = 0.3\sqrt{18}$. This value of K turns out to be appropriate to produce a substantial temporal gap between the respective Lieb-Robinson times and relaxation times as indicated in Fig. 7 by the dashed vertical lines (the Lieb-Robinson time is taken to be $\tau_{\mathrm{LR}} = 0.05L$ in accord with Ref. [28], the relaxation times are to be inferred from Fig. 13).

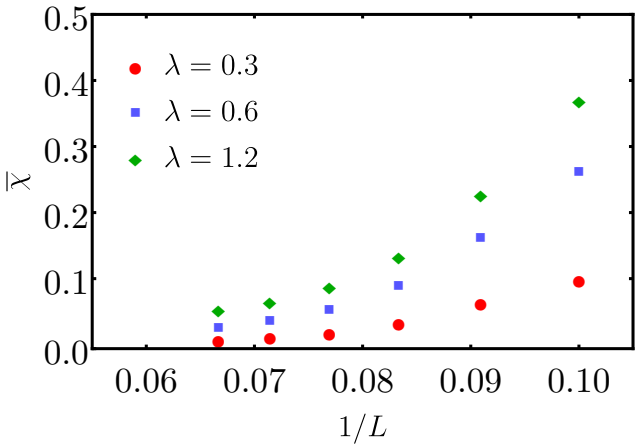

Figure 5. Bath-size dependence of the stiffness quantifier $\overline{\chi}$ for the Ising model at $t = 4$ for various interaction strengths. For all interaction strengths λ the quantifier decreases with increasing bath size, indicating perfect stiffness in the limit of infinitely large baths, i.e., $L \to \infty$.

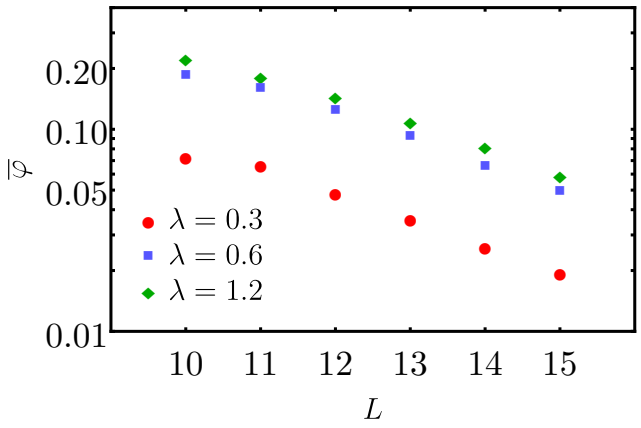

Figure 6. Bath-size dependence of the smoothness quantifier $\overline{\varphi}$ for the Ising model for various interaction strengths λ at $t = 4$. For all interaction strengths λ the quantifier decreases (approximately exponentially) with increasing bath size, indicating perfect smoothness in the limit of infinitely large baths, i.e., $L \to \infty$.

Since the quantity displayed in Fig. 7 is somewhat involved, we explain it in detail. Each pure initial state yields a time-dependent microscopic IFT quantity, which more or less deviates from unity at different times t. For conciseness, we plot the average (denoted by "$\overline{\ldots}$") over the absolute value of said deviations for 100 individual pure states. These initial states are energy eigenstates of the bath from a range around the initial energy $\mathcal{E}_0$ [36]. A small average of the absolute deviations signals a good agreement with the microscopic IFT for the majority of the individual initial states. (Note that this could not be inferred from a small average of the deviations themselves, since the latter are not non-negative). Further note, that even though there is an averaging involved, Fig. 7 serves as a check of the microscopic IFT [Eq. (9)] rather than a check of the coarse-grained IFT [Eq. (21)].

Next, we interpret the actual data displayed in Fig. 7. For each system size, the deviations exhibit a clear maximum at times, which fall into the gap between Lieb-Robinson and relaxation time. These maxima may be related to the build-up and drop-off of correlations between system and bath [37, 38]. However, already for relatively small system sizes, the maximum deviation is rather small, e.g., approximately one percent for $L = 12$. But more importantly, the maximum of the deviations decreases exponentially with increasing bath size along the scaling set by Eq. (31), as especially the inset of Fig. 7 shows. Recall that, even though the bath size (and thus the Lieb-Robinson time) increases, due to the scaling implemented by Eq. 31, the gap between between Lieb-Robinson and relaxation does not shrink, it

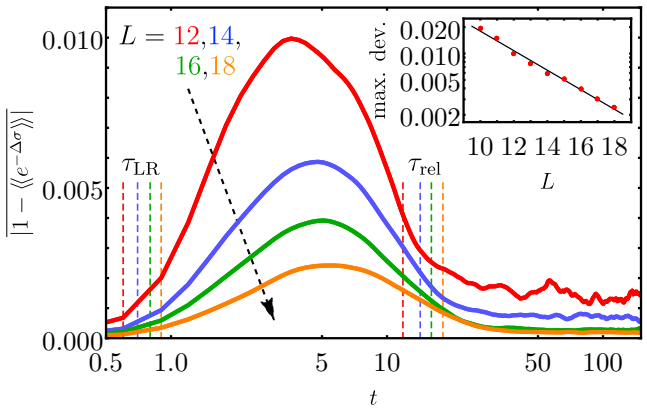

Figure 7. Average "violations" of the microscopic IFT [Eq. (9)] plotted over time t for the Ising model for a simultaneous scaling of interaction strength λ and bath size L. This scaling is chosen to keep open a gap between the Lieb-Robinson time $\tau_{\rm LR}$ (dashed vertical lines) and the relaxation time $\tau_{\rm rel}$ (dashed vertical lines), even in the limit of large baths, cf. Eq. (31). Inset: Maximum average violation of the microscopic IFT logarithmically plotted over bath size (curves for odd L and $L < 12$ are not depicted in the large figure for clarity of presentation). The average violation decreases exponentially with bath size L, indicating the increasing validity of the microscopic IFT even within the temporal gap. Note that this finding goes beyond the results of Refs. [24, 28, 29].

rather even grows, see Fig. 7. Thus, we find the microscopic IFT for pure states to be fulfilled to very good accuracy already for mesoscopic sized baths at all times, regardless of whether or not the Lieb-Robinson time and the relaxation time overlap. This finding is our fourth main numerical result. As explained above, it goes conceptually beyond the findings of Refs. [24, 28, 29]. It furthermore confirms the expectations induced by Fig. 5 and Fig. 6.

B. Hard-core boson model

The second setup of interest is a hard-core boson model, which was also the subject in Ref. [24]. The system (blue) consists of a single site and the bath (orange) is a rectangularly $(3 \times L)$ shaped lattice, yielding a total of $3L + 1$ sizes, see Fig. 8. The system interacts with one corner of the bath.

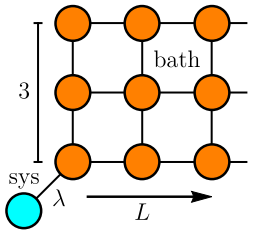

Figure 8. Sketch of the hard-core boson model.

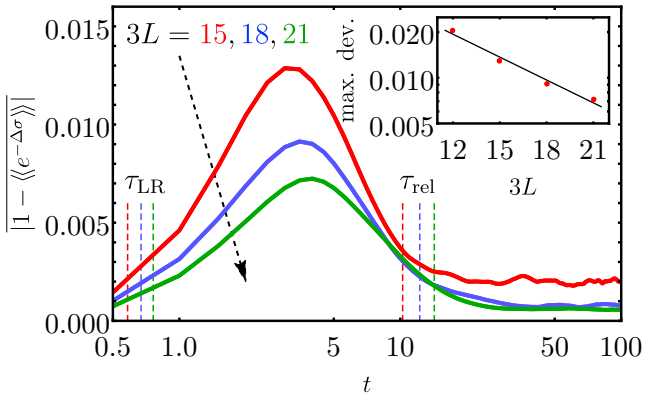

Figure 9. Data on "violations" of the microscopic IFT, displayed as in Fig. 7, but for the hard-core boson model. Also in this case, the violations vanish with increasing bath size, even though the gap between Lieb-Robinson time $\tau_{\rm LR}$ and the relaxation time $\tau_{\rm rel}$ does not.

The relevant Hamiltonians read

$$H_{\rm sys} = n_0\,, \qquad H_{\rm int} = -\lambda(c_0^\dagger c_1 + c_1^\dagger c_0)\,, \tag{32}$$

$$H_{\rm bath} = \sum_i n_i - \sum_{\langle i,j\rangle}(c_i^\dagger c_j + c_j^\dagger c_i) + \gamma \sum_{\langle i,j\rangle} n_i n_j\,,$$

where c_j ($c_j^\dagger$) are annihilation (creation) operators of a boson on site j and $n_j = c_j^\dagger c_j$ is the occupation number on site j. The double sums $\langle i,j\rangle$ run over horizontally and vertically neighboring sites. Following Ref. [24], we initialize the full system with bath states $|b_0\rangle$ from the third-filling sector, i.e., $\sum_i \langle b_0|n_i|b_0\rangle = L$, where the sum runs over all bath sites. We consider $\gamma = 0.1$ and again choose the bin size as $\delta = 0.03$. For $3L = 21$ an inverse temperature of $\beta = 0.1$ corresponds to a bath energy $\mathcal{E}_0 = 5.80$. The pure initial states are chosen as formulated in Eq. (30). Since the total Hamiltonian conserves particle number and system and bath can exchange particles due to the interaction term, we have to determine a pertinent μ as mentioned in Sec. III [and detailed in App. D]. For $3L = 21$ we find $\mu = -5.20$ [the accuracy to which this μ renders Eq. (15) valid may be inferred from Fig. 15 in App. G].

For this model (as well as for the Heisenberg model in the next section) we resort to just showing the most important data for the microscopic IFT in the same way as done in Fig. 7. This data is displayed in Fig. 9. (Figures depicting the coarse-grained IFT as well as stiffness and smoothness quantifiers can be found in App. F.) Again, we choose a scaling of the interaction strength with bath size as $\lambda(L) = 0.3\sqrt{21/L}$. Similarly as for the Ising model, Fig. 9 shows that the maximum deviation from the microscopic IFT decreases exponentially with bath size. Just like in the case of the Ising model, this

indicates that the the microscopic IFT for pure states is fulfilled to very good accuracy already for mesoscopic sized baths at all times, regardless of whether or not the Lieb-Robinson time and the relaxation time overlap.

C. Heisenberg model

As a third numerical example we consider an integrable (in the sense of the Bethe-Ansatz) system, the Heisenberg model. The system (blue) consists of a single spin and the bath (orange) is an open chain of length L, see Fig. 10. The Hamiltonians are given by

$$H_{\mathrm{sys}} = S_0^z\,, \quad H_{\mathrm{int}} = \lambda(S_0^x S_1^x + S_0^y S_1^y + \Delta S_0^z S_1^z) \quad (33)$$
$$H_{\mathrm{bath}} = \sum_{i=1}^{L-1} (S_i^x S_{i+1}^x + S_i^y S_{i+1}^y + \Delta S_i^z S_{i+1}^z + S_i^z)\,,$$

where $S_i^{x,y,z}$ denote spin operators on site i. The anisotropy is chosen as $\Delta = 1.4$ such that the bath exhibits diffusive transport behavior [39]. Just as for the hard-core boson model, we initialize the system as in Eq. (30) with a bath state from the third-filling sector, which here means $\sum_i \langle b_0|S_i^z|b_0\rangle = L/3$. For $L = 21$ the bath energy corresponding to $\beta = 0.1$ is given by $\mathcal{E}_0 = -3.33$, the bin size is chosen as $\delta = 0.015$. Since the total Hamiltonian conserves magnetization and system and bath are able to exchange magnetization, we must again take a chemical potential into account (which here plays the role of a global magnetic field). A value of $\mu = -5.68$ renders Eq. (15) sufficiently applicable, cf. App. G.

Similarly as for the hard-core boson model, we only show the figure for the average deviation of the microscopic IFT quantity for pure states in Fig. 11, again in the same display style as Fig. 7. The scaling of the λ with the bath size is given by $\lambda(L) = 0.3\sqrt{21/L}$. Further numerical data is shown in App. G.

For this model we find a qualitatively different behavior than for the nonintegrable models. First of all, the absolute magnitude of the deviations is quite larger than for the Ising model and hard-core boson model, namely on the order of ten percent even for longer times. Furthermore, the maximum deviation does not seem to decrease at all while enlarging the bath (see inset of Fig. 11). Consequently, an eventual fulfillment of the microscopic IFT for pure states is not expected, not even for larger

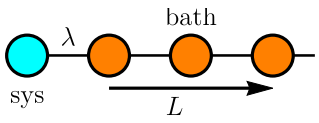

Figure 10. Sketch of the Heisenberg model.

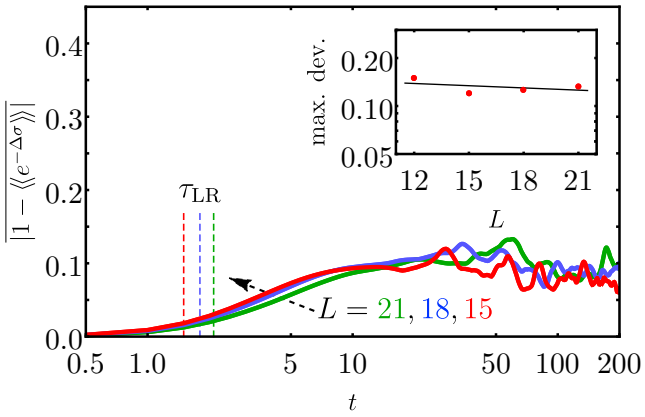

Figure 11. Data on "violations" of the microscopic IFT, displayed as in Fig. 7, but for the Heisenberg model. Violations are larger than for the Ising and the hard-core boson model, moreover, they are almost independent of bath size, inside as well as outside the gap between Lieb-Robinson time τ_{LR} and the relaxation time τ_{rel} (which is not visible on this scale). This failure of the microscopic IFT even for large systems is traced back to the lack of smoothness, which in turn is traced back to integrability, see text.

baths. This finding is interpreted as follows: Smoothness is closely related to the applicability of the eigenstate thermalization hypothesis, cf. Sec. II C. However, to this integrable Heisenberg model, the eigenstate thermalization hypothesis does not apply. Thus, it is natural to assume that the breakdown of the microscopic IFT roots in the breakdown of smoothness. Further numerical analysis supports this assumption, since transition probabilities do not become smoother with increasing bath size as displayed in Fig. 22 in App. G.

IV. DISCUSSION AND CONCLUSION

In this article, we presented justifications for a well-known microscopic IFT for entropy production, as well as for a coarse-grained version of the latter. The coarse-grained IFT was analytically shown to hold under the assumption that the relevant transition probabilities are sufficiently stiff. Moreover, the validity of the microscopic IFT for pure states follows if said transition probabilities are additionally sufficiently smooth. We defined and explained the concepts of stiffness and smoothness in detail. The validity of both versions of the IFT has been checked for three exemplary setups including integrable and nonintegrable ones.

For both nonintegrable models the main takeaway is the same. Both IFT's are fulfilled to very good accuracy already at moderate bath sizes. This accuracy increases as baths grow. Correspondingly, we find stiffness as well as smoothness to apply to very good accuracy already at

moderate bath sizes. Further, this accuracy increases as baths grow. These findings apply to setups that are not covered by comparable but conceptually different investigations in Refs. [24, 28]. The integrable Heisenberg model shows a qualitatively different behavior. The average deviation for the pure state IFT is much larger than in the nonintegrable case. Moreover, a decrease of the maximum deviation cannot be observed.

ACKNOWLEDGMENTS

We thank T. Sagawa and E. Iyoda for extensive and fruitful discussions. This work was supported by the Deutsche Forschungsgemeinschaft (DFG) within the Research Unit FOR 2692 under Grant No. 397107022 (GE 1657/3-2) and No. 397067869 (STE 2243/3-2).

Appendix A: Derivation of Eq. (19)

Throughout this derivation we consider j, k to be arbitrary but fixed, such that we refrain from explicitly writing them in each step. We start from the r.h.s. of Eq. (19) and plug in the definition of $\widetilde{R}(BA)$. Then we use $\widetilde{R}(ba) = R(ab)$, insert a one in the form of Ω_B/Ω_B and use the definition of $\overline{R}(AB)$. Next, we employ Eq. (15) and Eq. (18). Now the resulting expression only depends on the difference $A - B$ and it is possible to replace the sum over A by a sum over B. Finally, we perform all steps that lead to this point backwards to arrive at the r.h.s. of Eq. (19).

$$\begin{aligned}\sum_A \widetilde{R}(BA) &= \sum_A \sum_{a\in A, b\in B} \frac{1}{\Omega_A}\widetilde{R}(ba) \qquad \text{(A1)}\\ &= \sum_A \frac{\Omega_B}{\Omega_A}\overline{R}(AB) = \sum_A e^{\beta\delta(B-A)}\overline{R}(A-B)\\ &= \sum_B e^{\beta\delta(B-A)}\overline{R}(A-B) = \sum_B \widetilde{R}(BA)\end{aligned}$$

Appendix B: Derivation of Eq. (24)

Here, we show that the coarse-grained and the microscopic IFT coincide under the assumption of smoothness [Eq. (23)]. To start, one more ingredient is needed. We will make use of a well-controlled approximation of the exponential factor, i.e.,

$$e^{-\beta(\varepsilon^a_{\text{bath}} - \varepsilon^b_{\text{bath}})} \approx e^{-\beta\delta(A-B)}\,. \qquad \text{(B1)}$$

Before embarking on the derivation below, we will show that this approximation is practically always justified for small bin sizes. Since $e^{-\beta x}$ is a monotonically decreasing function of x and $\varepsilon^{a,b}_{\text{bath}} \in E^{A,B}_{\text{bath}}$, we have the inequality chain

$$\begin{aligned}& e^{-\beta\delta(A-B)}e^{-\beta\delta} \qquad \text{(B2)}\\ &= e^{-\beta((A\delta+\delta/2)-(B\delta-\delta/2))}\\ &\le e^{-\beta(\varepsilon^a_{\text{bath}} - \varepsilon^b_{\text{bath}})} \qquad \text{(B3)}\\ &\le e^{-\beta((A\delta-\delta/2)-(B\delta+\delta/2))}\\ &= e^{-\beta\delta(A-B)}e^{\beta\delta}\,. \qquad \text{(B4)}\end{aligned}$$

In the limit of small bin sizes δ (while keeping $A\delta$ and $B\delta$ constant) the relevant expression in Eq. (B3) is pinned between the expressions in Eq. (B2) and Eq. (B4). Thus, the approximation in Eq. (B1) is satisfied to very good accuracy for larger systems for which the bin size can be chosen small.

The starting point of the derivation below is the r.h.s. of Eq. (10). Firstly, the sums over a and b are split according to the belonging of $\varepsilon^a_{\text{bath}}$ and $\varepsilon^b_{\text{bath}}$ to their respective energy intervals E^A_{bath} and E^B_{bath}. Then, Eq. (B1) is employed such that the exponential factor can be pulled to the front. Next, we recognize the sum over a from Eq. (11). To go to the next line, we plug in Eq. (22) and abbreviate all terms linear in r as $\mathcal{O}(r)$. Then, we made use of the definition $W^B_{\text{ini}} = \sum_{b\in B} W^b_{\text{ini}}$ introduced above Eq. (16).Finally, we employ the assumption of smoothness [Eq. (23)], which allows to neglect terms linear in r. The result is the r.h.s. of Eq. (17).

$$
\begin{aligned}
\langle\!\langle e^{-\Delta\sigma}\rangle\!\rangle &= \sum_{j,k,a,b} P^j_{\rm fin} W^b_{\rm ini}\, e^{-\beta(\varepsilon^a_{\rm bath}-\varepsilon^b_{\rm bath})} R(jk,ab) \qquad \text{(B5)}\\
&\approx \sum_{j,k,A,B} P^j_{\rm fin} e^{-\beta\delta(A-B)} \sum_{b\in B} W^b_{\rm ini} \sum_{a\in A} R(jk,ab)\\
&= \sum_{j,k,A,B} P^j_{\rm fin} e^{-\beta\delta(A-B)} \sum_{b\in B} W^b_{\rm ini}\, R(jk,Ab)\\
&= \mathcal{O}(r) + \sum_{j,k,A,B} P^j_{\rm fin} e^{-\beta\delta(A-B)} \sum_{b\in B} W^b_{\rm ini}\, \overline{R}(jk,AB)\\
&= \mathcal{O}(r) + \sum_{j,k,A,B} P^j_{\rm fin} W^B_{\rm ini} e^{-\beta\delta(A-B)} \overline{R}(jk,AB) \overset{r\to 0}{\longrightarrow} \langle\!\langle e^{-\Delta\sigma}\rangle\!\rangle_{\rm c.g.}
\end{aligned}
$$

Appendix C: Stiffness, riggedness and the ubiquity of the latter

Here, we present a consideration leading to the overall expectation that stiffness is the the norm rather than the exception. In a first step, we show that a specific feature in the ETH ansatz for $H_{\rm int}$ yields stiffness at least in first order perturbation theory. This feature is called "riggedness". Beyond first order perturbation theory, it is difficult to make rigorous statements on the relation between stiffness and riggedness. In a second step, the existence of riggedness is linked to the insensitivity of autocorrelation functions of respective observables and other dynamics to extremely small changes in temperature. This insensitivity is ubiquitous to the extend that is hardly ever specifically mentioned.

i. First step: While we intend to argue that there is a close relation between stiffness and the ETH, it is important to note that the validity of the ETH ansatz for $H_{\rm int}$ as such does *not* imply stiffness. However, a slightly "strengthened" version of the ETH ansatz called the "rigged" ETH [40] entails stiffness in leading-order perturbation theory, as will be substantiated in the following. The standard ETH ansatz [41] for the interaction Hamiltonian reads

$$
(H_{\rm int})_{fi} = \mathcal{F}_{\rm d}(\epsilon)\delta_{fi} + \eta(\epsilon)^{-1/2}\mathcal{F}_{\rm od}(\epsilon,\omega)\mathfrak{r}_{fi}\,. \qquad \text{(C1)}
$$

Here, $\mathcal{F}_{\rm d}$ and $\mathcal{F}_{\rm od}$ are real and smooth functions of their arguments, $\epsilon = (\epsilon_f+\epsilon_i)/2$ and $\omega = \epsilon_f - \epsilon_i$. The quantity $\eta(\epsilon)$ is the density of states, which will below be assumed to be exponential. The $\mathfrak{r}_{fi}$ are (pseudo-)random numbers (with the constraint $\mathfrak{r}_{fi} = \mathfrak{r}^*_{fi}$) drawn from a Gaussian distribution with zero mean and unit variance. In this general notation the subscripts i and f encode states of the uncoupled Hamiltonian, i.e., with respect to the scenario at hand, $i = (k,b)$ and $f = (j,a)$. Without loss of generality, we can set $\mathcal{F}_{\rm d}(\epsilon) \approx 0$ for a moderately sized energy interval. The modification that implements the rigged ETH consists of the additional assumption that $\mathcal{F}_{\rm od}$ is (approximately) independent of the mean energy ϵ, at least within the above energy interval, i.e.,

$$
\mathcal{F}_{\rm od}(\epsilon,\omega) \approx \mathcal{F}_{\rm od}(\omega)\,. \qquad \text{(C2)}
$$

The (approximate) independence of $\mathcal{F}_{\rm od}(\epsilon,\omega)$ from ϵ has already been numerically demonstrated for physical observables [31, 40].

Next we show how stiffness follows from riggedness in leading-order perturbation theory. The probability to transition from some initial state $|i\rangle$ to some final state $|f\rangle$ in first-order time-dependent perturbation theory is given by

$$
R(fi) \propto |(H_{\rm int})_{fi}|^2 g(\omega,t)\,, \qquad \text{(C3)}
$$

where $g(\omega,t) = \sin^2(\omega t/2)/\omega^2$. The average probability to transition from some initial state $|i\rangle$ with $\epsilon_i \in E_I$ to some final energy interval E_F [Eq. (12)] in first-order time-dependent perturbation theory then reads

$$
\begin{aligned}
\overline{R}(FI) &\propto \frac{1}{\Omega_I} \sum_{i\in I, f\in F} |(H_{\rm int})_{fi}|^2 g(\omega,t) \qquad \text{(C4)}\\
&= \frac{1}{\Omega_I} \sum_{i\in I, f\in F} \frac{\mathcal{F}^2_{\rm od}(\omega)|\mathfrak{r}_{fi}|^2 g(\omega,t)}{\eta(\epsilon)}\,,
\end{aligned}
$$

where Ω_X (with $X = I, F$) is the number of terms in the respective sum. If the bin sizes are adequately chosen (as described in Sec. II A), the only quantities that vary non-negligibly in the above sums are the $|\mathfrak{r}_{fi}|^2$. To an accuracy set by the law of large numbers, their summation can be approximated as $\sum_{i\in I, f\in F}|\mathfrak{r}_{fi}|^2 \approx \Omega_I\Omega_F$.

All other quantities may be "pulled out of the sum":

$$\overline{R}(FI) \approx \frac{\mathcal{F}^2_{\mathrm{od}}(\delta(F-I))g(\delta(F-I),t)}{\Omega_I \eta(\delta(F+I)/2)}\Omega_I\Omega_F\,. \quad \text{(C5)}$$

To proceed, we detail the assumption that $\eta(\epsilon)$ is exponential, i.e.,

$$\eta(\epsilon) = e^{\beta\epsilon} \quad \Rightarrow \quad \Omega_X \approx \delta e^{\beta\delta X}\,. \quad \text{(C6)}$$

Inserting Eq. (C6) into Eq. (C5) and simplifying yields

$$\overline{R}(FI) = \delta\mathcal{F}^2_{\mathrm{od}}(\delta(F-I))g(\delta(F-I),t)e^{\beta\delta(F-I)/2}\,, \quad \text{(C7)}$$

which is clearly a function of $F-I$ only, thus the corresponding $\overline{R}(FI)$ are indeed stiff. The only assumption used in this derivation are the rigged ETH [Eq. (C2)] and an exponential density of states [Eq. (C6)]. While the latter is a generally well-known feature of short-range interacting systems, the former has not yet been exhaustively scrutinized in the literature. However, some numerical evidence already exists [31] and further was presented in Sec. III. An even more encompassing consideration in support of the wide occurrence of stiffness will be put forth next.

ii. Second step: This goes to establish the ubiquity of riggedness. We start with a standard textbook result on the canonical ensemble, which links the variance s_E^2 of the energy distribution to the heat capacity C_V (at constant volume V) via

$$s_E^2 = k_{\mathrm{B}}T^2C_V\,. \quad \text{(C8)}$$

Furthermore, the difference of two mean energies at temperature T and $T+\Delta T$, respectively, is given by

$$\Delta\overline{E} = \overline{E}(T+\Delta T) - \overline{E}(T) = C_V\Delta T\,. \quad \text{(C9)}$$

As we think of ΔT being small, this is basically the definition of the heat capacity. For later reference we link the total heat capacity to the specific heat capacity per particle c_V as $C_V = c_V N$ where N is the number of particles. The crucial point now is the following: the calculation of autocorrelation functions and other physical quantities at a given temperature only concerns a certain sector of the respective operator when displayed in the energy eigenbasis. This means, only the matrix elements within a certain "energy window" contribute substantially to the autocorrelation function. This window has the width s_E and is centered at $\overline{E}$. The centers of two windows at different temperatures are separated by $\Delta\overline{E}$. Now clearly, if $\Delta\overline{E}$ exceeds s_E, the calculation of the two autocorrelation functions concerns two disjoined sectors of the respective operator. So if the rigged ETH in the sense of Eq. (C2) would not apply, the two autocorrelation functions would be entirely different, since $\mathcal{F}^2_{\mathrm{od}}(\epsilon,\omega)$ is essentially the Fourier transform (with respect to ω) of the autocorrelation function at energy $\epsilon \mathrel{\widehat{=}} \overline{E}$. This leads to the question at what temperature difference ΔT_{sep} this separation of the energy windows actually occurs. To answer this question consider the ratio

$$\frac{\Delta\overline{E}}{s_E} = \frac{\Delta T}{T}\sqrt{\frac{c_V N}{k_{\mathrm{B}}}}\,. \quad \text{(C10)}$$

Defining ΔT_{sep} as the temperature difference at which $\Delta\overline{E} = s_E$, Eq. (C10) yields

$$\Delta T_{\mathrm{sep}} = T\sqrt{\frac{k_{\mathrm{B}}}{c_V N}}\,. \quad \text{(C11)}$$

From the scaling as $\propto 1/\sqrt{N}$ on the r.h.s. of Eq. (C11), it may already be inferred that ΔT_{sep} will be very small, even for mesoscopic systems, since already in this case N will be very large.

As an example, consider one gram of iron with a heat capacity of $C_V \approx 0.5$ J/K. Plugging Boltzmann's constant $k_{\mathrm{B}} \approx 10^{-23}$ J/K and room temperature $T \approx$ 300K into Eq. (C11) yields a temperature difference of $\Delta T_{\mathrm{sep}} \approx 10^{-9}$ K, i.e., one nanokelvin. Since we do not observe that measurements of dynamical physical quantities like autocorrelation functions, etc. vary on this scale, it may be inferred that the rigged ETH [Eq. (C2)] applies in a plethora of cases. This, in turn, renders stiffness a very likely property for a wide range of setups, as explained in the beginning of the present section.

Appendix D: Definitions of parameters and quantifiers

In the following, we define the numerical procedures according to which temperature and chemical potential, which first appear in Eq. (4), are calculated. The rationale behind the definitions of temperature and chemical potential is the desired validity of Eq. (15).

Temperature: Temperature corresponds to the growth of a pertinent DOS at a certain energy $\mathcal{E}_0$. Thus, in order to render Eq. (15) as good an approximation as possible to the actual DOS, the inverse temperature β is determined by an exponential fit to $\Omega_{B=E/\delta}|_{\mu=0}$ in the direct vicinity of $\mathcal{E}_0$. Here, $\ldots|_{\mu=0}$ indicates that the respective DOS corresponds to H_{bath} only (rather than $(H_{\mathrm{bath}} - \mu N_{\mathrm{bath}})$). Practically, we choose an inverse temperature $\beta = 0.1$ for all examples and determine the corresponding $\mathcal{E}_0$'s, cf. Fig. 14. In case that the particle number (magnetization) is a conserved quantity (such as for the models in Secs. III B, III C), this is done for $\Omega_{B_N=E/\delta}|_{\mu=0} := \Omega_N(E)$, where N is the number of particles in the initial bath state.

Chemical potential: The determination of a pertinent (nonzero) μ as appearing in Eq. (4) is only

necessary if the full model conserves particle number (magnetization, etc.). In this case we proceed as follows, we consider the relevant DOS's $\Omega_X(E)$ of the X-particle subspaces of the bath, where $X = N-1, N, N+1$. Then, we choose the three points $(\mathcal{E}_0 - \omega - \mu(N-1), \Omega_{N-1}(\mathcal{E}_0 - \omega))$, $(\mathcal{E}_0 - \mu N, \Omega_N(\mathcal{E}_0))$ and $(\mathcal{E}_0 + \omega - \mu(N+1), \Omega_{N+1}(\mathcal{E}_0 + \omega))$, where ω is the level spacing of the considered system only (in the examples in Secs. III B, III C we have $\omega = 1$) and take a function of the form $K\exp(\beta E)$, featuring the already set inverse temperature β.
The parameters μ and K are adjusted such that the three points are as close as possible to the given function. This fitting procedure determines μ. For an illustration see, e.g., Fig. 15 in App. F.

Appendix E: Additional numerics on the transverse Ising model

As mentioned in Sec. III, for the numerics we assumed that eigenstates $|\sigma^{j,a}\rangle$ of the entropy production operator equal the eigenstates $|j,a\rangle$ of the uncoupled Hamiltonian H_0 such that Eq. (7) concerns transition probabilities between energy eigenstates of H_0. This assumption is only strictly true if the reduced density operator of the system remains diagonal in the energy eigenbasis of the system for all times, which may indeed be the case if the setup possesses certain symmetries. Such a symmetry is present in the hard-core boson model as well as in the Heisenberg model. However, since this symmetry is absent in the transverse Ising model, the off-diagonal elements of the system's reduced density operator will differ from zero. In this case, even in the absence of symmetry, the off-diagonal elements are expected to be sufficiently small. This expectation is based on typicality, i.e., the mathematical finding that the overwhelming majority of all pure states on the full system (with respect to the unitary Haar-measure) yields local density matrices with exponentially small off-diagonal elements [1, 42]. Note that typicality arguments apply irrespective of the interaction strength. We also directly check this assumption numerically in the following. In Fig. 12 the average absolute value of the off-diagonal element $\overline{|\rho^{12}_{\mathrm{sys}}(t)|}$ is plotted over t for $\lambda(L) = 0.3\sqrt{18/L}$. Even for the most unfavorable case of $\overline{|\rho^{12}_{\mathrm{sys}}(t)|} \approx 0.01$, the average overlap between the uncoupled eigenstates and the respective eigenstates of the entropy production operator is still > 0.995. Further, the maximum deviation decreases exponentially with increasing bath size, as can be seen in the figures inset. Hence, we view our assumption as justified.
The temporal behavior of the averaged first diagonal element is depicted in Fig. 13 for various bath sizes L. Shown is the deviation from the equilibrium value $(\rho^{\mathrm{can}}_{\mathrm{sys}})_{11} = 0.45$ as predicted by a Gibbs ensemble. The relaxation time τ_{rel} is determined by the dashed line, which lies at one tenth of the initial value.

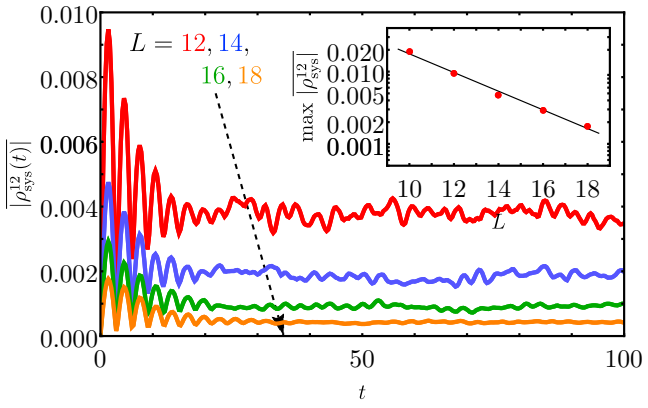

Figure 12. Average off-diagonal element of the system's reduced density matrix of the Ising model plotted over time for $\lambda(L)$.
Inset: Maximum value logarithmically plotted over bath size (curve for $L = 10$ is not depicted in the large figure).
The maximum value decreases exponentially with bath size L, indicating that the assumption of small off-diagonal elements made in Sec. II A is justified.

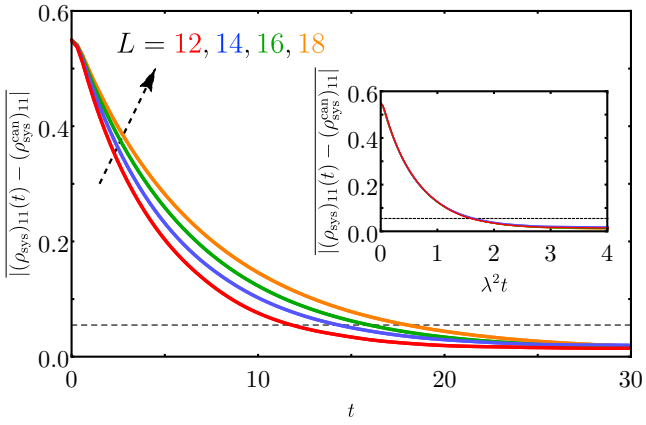

Figure 13. Temporal behavior of the first diagonal element of the system's reduced density operator for the Ising model for $\lambda(L) = 0.3\sqrt{18/L}$. Depicted is the average deviation from the thermal value of $(\rho^{\mathrm{can}}_{\mathrm{sys}})_{11} = 0.45$. The relaxation time τ_{rel} is defined as the point in time at which the curve has decayed to one tenth of its initial value (dashed line). Inset: time axis scaled with λ^2, the collapse of all curves is evident signaling the independence of τ_{rel} and L.

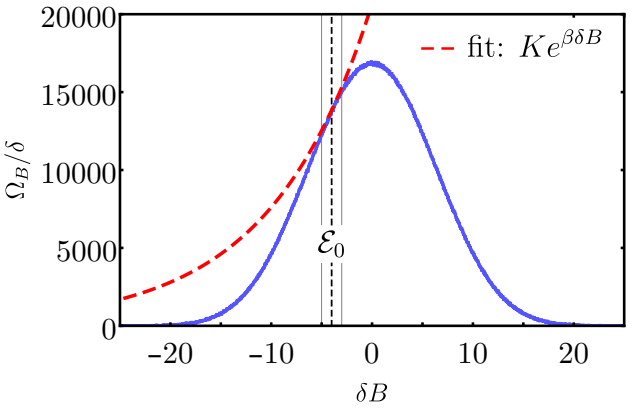

Figure 14. Density of states Ω_B/δ plotted as a function of (mean) energy δB. The bath size is $L = 18$ and the bin size is $\delta = 0.03$. The dashed line indicates the initial energy $\mathcal{E}_0 = -4.01$ and the faint gray solid lines mark the region $\mathcal{E}_0 \pm 1$ in which the exponential fit approximates the DOS, thus rendering Eq. (15) applicable.

The DOS of the bath is depicted in Fig. 14. In the vicinity of $\mathcal{E}_0 = -4.01$ the DOS can indeed be well approximated by a single exponential function with exponent $\beta = 0.1$ and some fit parameter K. This renders our assumption of a local exponential DOS applicable [Eq. (15)].

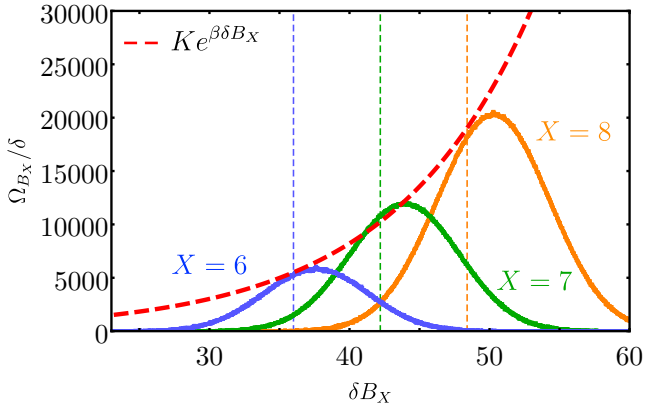

Figure 15. Densities of states Ω_{B_X}/δ plotted as functions of the (mean) energies δB_X for the hard-core boson model. Depicted are the three relevant subsectors with $X = 6, 7, 8$. The chemical potential takes the value $\mu = -5.20$ such that all relevant parts of the spectra can be described by a single exponential function.

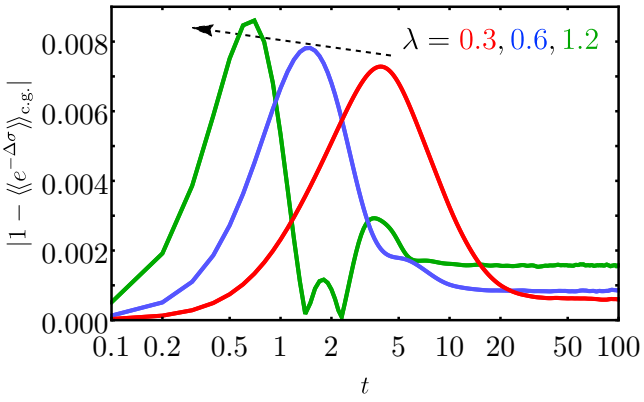

Figure 16. "Violations" of the coarse-grained IFT plotted as a function of time for the hard-core boson model ($L = 21$) for various interaction strengths. The coarse-grained IFT is well fulfilled for all λ.

Appendix F: Additional numerics on the hard-core boson model

This section presents additional numerics for the hard-core boson model. The DOSs partaking in the dynamics can be seen in Fig. 15. The chemical potential is adjusted to $\mu = -5.20$ such that all energetically relevant parts of the spectra are described by a single exponential. The coarse-grained IFT quantity as a function of time is depicted in Fig. 16. The stiffness quantifier is depicted in Fig. 17 as a function of inverse bath size and the smoothness quantifier in Fig. 18 as a function of L. The interaction strength takes on the same values as for the Ising model, namely $\lambda = 0.3, 0.6, 1.2$.

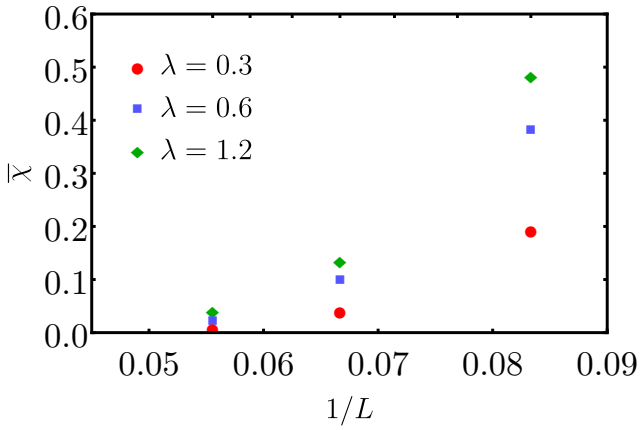

Figure 17. Bath-size dependence of the stiffness quantifier $\overline{\chi}$ for the hard-core boson model. For all interaction strengths the quantifier decreases with increasing bath size, indicating that stiffness (and therefore the coarse-grained IFT) is better and better fulfilled.

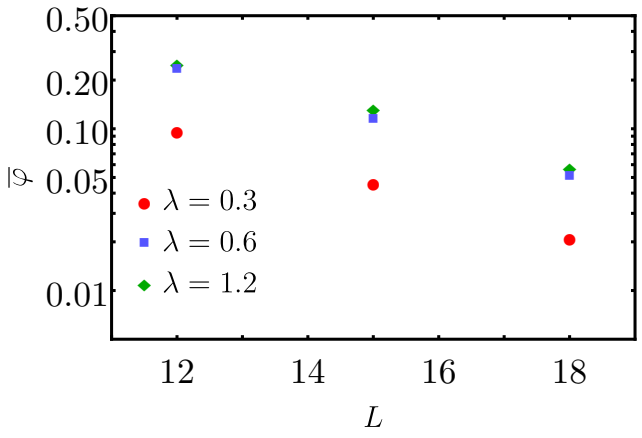

Figure 18. Smoothness quantifier $\overline{\varphi}$ for the hard-core boson model logarithmically plotted over bath size L. The exponential decrease with bath size is evident for all interaction strengths, indicating that smoothness is better and better fulfilled the larger the bath becomes.

All three figures are generally quite similar to the respective figures for the Ising model. Firstly, the coarse-grained IFT is fulfilled to a good extent with long-time values depending on the interaction strength.
The stiffness quantifier again decreases with increasing bath size. Thus, the validity of the coarse-grained IFT is expected for large baths.
Furthermore, the smoothness quantifier shows an exponential decay with bath size for all interaction strengths. This is in line with the findings displayed in Fig. 9 in the main text.

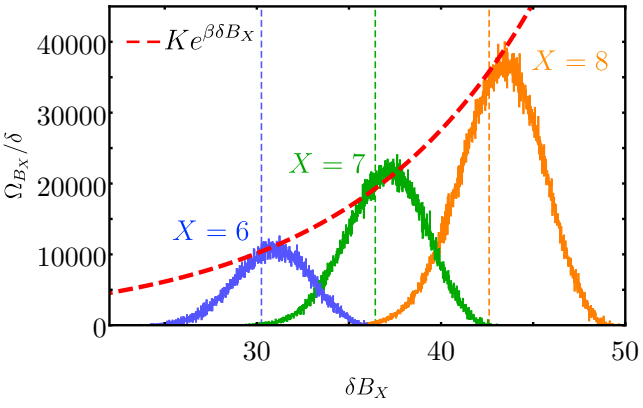

Figure 19. Densities of states Ω_{B_X}/δ plotted as functions of the (mean) energies δB_X for the Heisenberg model. Depicted are the three relevant subsectors with $X = 6, 7, 8$. The chemical potential takes the value $\mu = -5.68$ such that all relevant parts of the spectra can be described by a single exponential. The bath size is $L = 21$ and the bin size is $\delta = 0.015$.

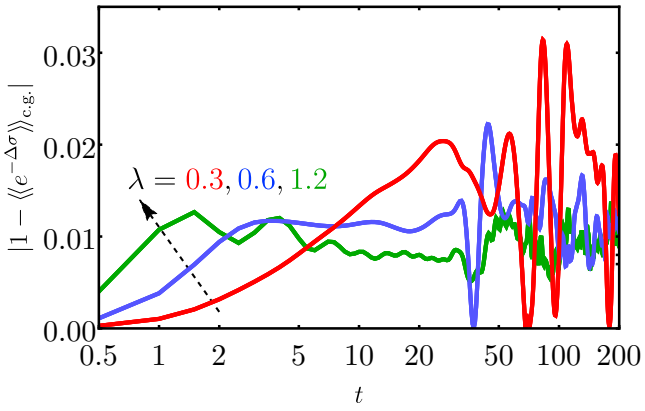

Figure 20. "Violations" of the coarse-grained IFT plotted as a function of time for the Heisenberg model ($L = 21$) for various interaction strengths. The coarse-grained IFT is more or less fulfilled for all λ, even though the magnitude of the deviation is larger than in the nonintegrable models.

Appendix G: Additional numerics on the Heisenberg model

In this section, we present additional numerics for the Heisenberg model. The densities of states of the relevant subsectors can be viewed in Fig. 19. The chemical potential is adjusted to $\mu = -5.68$ such that the energetically relevant parts of the DOS in Fig. 19 are indeed well described by a single exponential, which renders Eq. (15) (approximately) valid. The coarse-grained IFT quantity as a function of time is depicted in Fig. 20. Stiffness and smoothness quantifiers are shown in Fig. 21 and Fig. 22 as functions of (inverse) bath size.
The deviations from unity of the coarse-grained IFT quantity in Fig. 20 are larger compared to the nonintegrable models. Evidently, the larger the interaction strength λ is, the smaller the deviations are. Similarly as in the other models, the stiffness quantifier in Fig. 21 decreases with increasing bath size.
However, the smoothness quantifier in Fig. 22 does not show the exponential decay behavior observed in the nonintegrable cases. This confirms the observation from Fig. 11 in the main text, where it was found that the microscopic IFT does not become more and more fulfilled by enlarging the bath (although for slightly different λ). This finding suggest that for the integrable model it is indeed the violation of smoothness (and not stiffness) that causes the violation of the microscopic IFT.

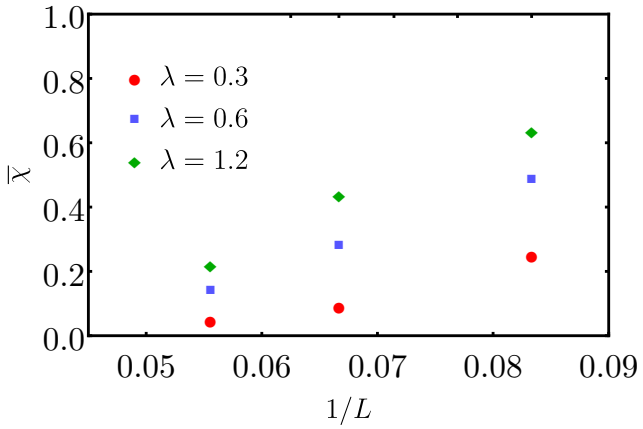

Figure 21. Bath-size dependence of the stiffness quantifier $\overline{\chi}$ for the Heisenberg model. For all interaction strengths the quantifier decreases with increasing bath size, indicating that stiffness (and therefore the coarse-grained IFT) is better and better fulfilled.

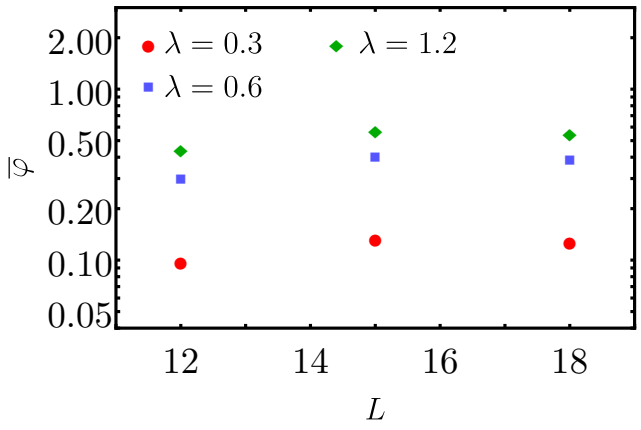

Figure 22. Smoothness quantifier $\overline{\varphi}$ for the Heisenberg model logarithmically plotted over bath size L. An exponential decrease with bath size as in the nonintegrable models cannot be observed, indicating that smoothness is violated to some extent.

[1] C. Gogolin and J. Eisert, Rep. Prog. Phys. **79**, 056001 (2016).
[2] J. M. Deutsch, Phys. Rev. A **43**, 2046 (1991).
[3] M. Srednicki, Phys. Rev. E **50**, 888 (1994).
[4] M. Rigol, V. Dunjko, and M. Olshanii, Nature **452**, 854 (2008).
[5] L. D'Alessio, Y. Kafri, A. Polkovnikov, and M. Rigol, Adv. Phys. **65**, 239 (2016).
[6] J. Richter, A. Dymarsky, R. Steinigeweg, and J. Gemmer, Phys. Rev. E **102**, 042127 (2020).
[7] S. Goldstein, J. L. Lebowitz, R. Tumulka, and N. Zanghì, Phys. Rev. Lett. **96**, 050403 (2006).
[8] S. Lloyd, arXiv:1307.0378 (2013).
[9] P. Reimann, Phys. Rev. Lett. **99**, 160404 (2007).
[10] S. Trotzky, Y.-A. Chen, A. Flesch, I. P. McCulloch, U. Schollwöck, J. Eisert, and I. Bloch, Nat. Phys. **8**, 325 (2012).
[11] A. M. Kaufman, M. E. Tai, A. Lukin, M. Rispoli, R. Schittko, P. M. Preiss, and M. Greiner, Science **353**, 794 (2016).
[12] C. Gross and I. Bloch, Science **357**, 995 (2017).
[13] M. F. Parsons, F. Huber, A. Mazurenko, C. S. Chiu, W. Setiawan, K. Wooley-Brown, S. Blatt, and M. Greiner, Phys. Rev. Lett. **114**, 213002 (2015).
[14] D. Ohl de Mello, D. Schäffner, J. Werkmann, T. Preuschoff, L. Kohfahl, M. Schlosser, and G. Birkl, Phys. Rev. Lett. **122**, 203601 (2019).
[15] C. Jarzynski, Annu. Rev. Condens. Matter Phys. **2**, 329 (2011).
[16] C. Jarzynski, Phys. Rev. Lett. **78**, 2690 (1997).
[17] C. Jarzynski, J. Stat. Phys. **98**, 77 (2000).
[18] G. E. Crooks, Phys. Rev. E **60**, 2721 (1999).
[19] M. Esposito, U. Harbola, and S. Mukamel, Rev. Mod. Phys. **81**, 1665 (2009).
[20] M. Campisi, P. Hänggi, and P. Talkner, Rev. Mod. Phys. **83**, 771 (2011).
[21] S. An, J.-N. Zhang, M. Um, D. Lv, Y. Lu, J. Zhang, Z.-Q. Yin, H. T. Quan, and K. Kim, Nat. Phys. **11**, 193 (2015).
[22] T. P. Xiong, L. L. Yan, F. Zhou, K. Rehan, D. F. Liang, L. Chen, W. L. Yang, Z. H. Ma, M. Feng, and V. Vedral, Phys. Rev. Lett. **120**, 010601 (2018).
[23] R. Clausius, *The Mechanical Theory of Heat,* (London: Taylor and Francis, 1867).
[24] E. Iyoda, K. Kaneko, and T. Sagawa, Phys. Rev. Lett. **119**, 100601 (2017).
[25] P. Talkner, P. Hänggi, and M. Morillo, Phys. Rev. E **77**, 051131 (2008).
[26] P. Talkner, M. Morillo, J. Yi, and P. Hänggi, New Journal of Physics **15**, 095001 (2013).
[27] B. Cleuren, C. Van den Broeck, and R. Kawai, Phys. Rev. Lett. **96**, 050601 (2006).
[28] E. Iyoda, K. Kaneko, and T. Sagawa, Phys. Rev. E **105**, 044106 (2022).
[29] K. Kaneko, E. Iyoda, and T. Sagawa, Phys. Rev. E **96**, 062148 (2017).
[30] J. Gemmer, L. Knipschild, and R. Steinigeweg, arXiv:1712.02128 (2017).
[31] D. Schmidtke, L. Knipschild, M. Campisi, R. Steinigeweg, and J. Gemmer, Phys. Rev. E **98**, 012123 (2018).
[32] L. Knipschild, A. Engel, and J. Gemmer, Phys. Rev. E **103**, 062139 (2021).

[33] M. Esposito, K. Lindenberg, and C. V. den Broeck, New Journal of Physics **12**, 013013 (2010).
[34] L. D. Landau and E. M. Lifshitz, *Statistical Physics,* (Butterworth-Heinemann Ltd, 1980).
[35] J. Wang and W.-g. Wang, Phys. Rev. E **97**, 062219 (2018).
[36] For each individual eigenstate (with an energy close to $\mathcal{E}_0$) we calculate the corresponding β as described in App. D. Similarly, if necessary, we also calculate μ for each individual eigenstate.
[37] S. Cusumano, V. Cavina, M. Keck, A. De Pasquale, and V. Giovannetti, Phys. Rev. A **98**, 032119 (2018).
[38] K. Ptaszyński and M. Esposito, Phys. Rev. Lett. **122**, 150603 (2019).
[39] B. Bertini, F. Heidrich-Meisner, C. Karrasch, T. Prosen, R. Steinigeweg, and M. Žnidarič, Rev. Mod. Phys. **93**, 025003 (2021).
[40] J. Richter, J. Gemmer, and R. Steinigeweg, Phys. Rev. E **99**, 050104 (2019).
[41] M. Srednicki, J. Phys. A: Math. Gen. **32**, 1163 (1999).
[42] S. Popescu, A. Short, and A. Winter, Nat. Phys. **2**, 754 (2006).

Preprint of Publication [P5]

Robin Heveling, Jiaozi Wang, and Jochen Gemmer
"Numerically probing the universal operator growth hypothesis"
Physical Review E **106**, 014152 (2022)
DOI: 10.1103/PhysRevE.106.014152

Numerically Probing the Universal Operator Growth Hypothesis

Robin Heveling,* Jiaozi Wang,† and Jochen Gemmer‡
Department of Physics, University of Osnabrück, D-49076 Osnabrück, Germany

Recently, a hypothesis on the complexity growth of unitarily evolving operators was presented. This hypothesis states that in generic, non-integrable many-body systems the so-called Lanczos coefficients associated with an autocorrelation function grow asymptotically linear, with a logarithmic correction in one-dimensional systems. In contrast, the growth is expected to be slower in integrable or free models. In the paper at hand, we numerically test this hypothesis for a variety of exemplary systems, including 1d and 2d Ising models as well as 1d Heisenberg models. While we find the hypothesis to be practically fulfilled for all considered Ising models, the onset of the hypothesized universal behavior could not be observed in the attainable numerical data for the Heisenberg model. The proposed linear bound on operator growth eventually stems from geometric arguments involving the locality of the Hamiltonian as well as the lattice configuration. We investigate such a geometric bound and find that it is not sharply achieved for any considered model.

I. INTRODUCTION

The issue of the emergence of irreversible behavior from the unitary time evolution of quantum mechanics has yet to be answered in a satisfying manner [1]. In this context, concepts like the "eigenstate thermalization hypothesis" [2–4] and "quantum typicality" [5–7] have been introduced as possible fundamental mechanism behind an eventual equilibration of isolated quantum systems. The idea of typicality is that an overwhelming majority of pure states (at some energy) give rise to corresponding thermal expectation values. Thus, it is quite likely that over the course of time a pure state eventually ends up in the giant "bubble" of typical states, signaling an apparent equilibration of the system. In the Heisenberg picture formulation of quantum mechanics, not the states are time-dependent, but the observables themselves. Hence, it may be somewhat expected to find a similar notion of typicality for observables, going from initially simple, few-particle operators to more complex, generic ones. Recent works have studied this notion of operator growth from various angles [8–13].

In this paper, we refer to the particular work presented in Ref. [14], in which a hypothesis on the universality of operator growth is brought forth. Said hypothesis is formulated in the framework of the *recursion method* [15, 16] and makes a statement about the growth of the so-called Lanczos coefficients, real numbers that characterize the complexity growth of operators over the course of time. In the following, we numerically test this operator growth hypothesis for various models and observables. Similar numerical investigations haven been conducted [17, 18]. Further, we attempt to put the informal version of the hypothesis into a more quantitative context with regard to the functional form of the hypothesized universal growth pattern.

The paper at hand is organized as follows: we briefly restate the universal operator growth hypothesis and introduce related quantities in Sec. II. Following, in Sec. III, we derive an upper bound on the complexity growth of operators based on geometric arguments. We present our numerical results and relate them to the operator growth hypothesis in Sec. IV. We summarize our main results and conclude in Sec. V.

II. OPERATOR GROWTH HYPOTHESIS

For self-containedness, in this section, we restate the operator growth hypothesis brought forward in Ref. [14]. To start, the main quantities that eventually play a role in the hypothesis are introduced. We consider a system in the thermodynamic limit described by a local Hamiltonian $\mathcal{H}$ [here, local means short-range, few-body interactions]. An observable of interest represented by a Hermitian operator $\mathcal{O}$ gives rise to a corresponding autocorrelation function

$$C(t) = \mathrm{Tr}[\mathcal{O}(t)\mathcal{O}]\,, \tag{1}$$

where $\mathcal{O}(t) = e^{\mathrm{i}\mathcal{H}t}\mathcal{O}e^{-\mathrm{i}\mathcal{H}t}$ is the time-dependent operator in the Heisenberg picture ($\hbar = 1$). In the following, it is convenient to work directly in the Hilbert space of operators and denote its elements $\mathcal{O}$ as states $|\mathcal{O})$. This Hilbert space of operators is equipped with an inner product $(\mathcal{O}_1|\mathcal{O}_2) = \mathrm{Tr}[\mathcal{O}_1^\dagger\mathcal{O}_2]$, which induces a norm via $||\mathcal{O}|| = \sqrt{(\mathcal{O}|\mathcal{O})}$. The Liouvillian superoperator is defined by $\mathcal{L}|\mathcal{O}) = [\mathcal{H}, \mathcal{O}]$ and propagates a state $|\mathcal{O})$ in time such that the autocorrelation function may be written as $C(t) = (\mathcal{O}|e^{\mathrm{i}\mathcal{L}t}|\mathcal{O})$.

The *Lanczos algorithm* can be employed to calculate a tridiagonal representation of the Liouvillian $\mathcal{L}$ in a (finite) subspace determined by some "seed" observable

* rheveling@uos.de
† jiaowang@uos.de
‡ jgemmer@uos.de

$\mathcal{O}$. To start the iterative scheme detailed below, we take the normalized initial state $|\mathcal{O}_0) = |\mathcal{O})$, i.e., $(\mathcal{O}|\mathcal{O}) = 1$, and set $b_1 = ||\mathcal{L}\mathcal{O}_0||$ as well as $|\mathcal{O}_1) = \mathcal{L}|\mathcal{O}_0)/b_1$. Then we iteratively compute

$$\begin{aligned} |\mathcal{Q}_n) &= \mathcal{L}|\mathcal{O}_{n-1}) - b_{n-1}|\mathcal{O}_{n-2})\,, \\ b_n &= ||\mathcal{Q}_n||\,, \\ |\mathcal{O}_n) &= |\mathcal{Q}_n)/b_n\,. \end{aligned} \tag{2}$$

The tridiagonal representation of the Liouvillian in the *Krylov basis* $\{|\mathcal{O}_n)\}$ is then given by

$$L_{mn} = (\mathcal{O}_m|\mathcal{L}|\mathcal{O}_n) = \begin{pmatrix} 0 & b_1 & 0 & \dots \\ b_1 & 0 & b_2 & \\ 0 & b_2 & 0 & \ddots \\ \vdots & & \ddots & \ddots \end{pmatrix}_{mn}\,, \tag{3}$$

where the *Lanczos coefficients* b_n are real, positive numbers output by the algorithm. They can be interpreted as hopping amplitudes in a tight-binding model and their iterative computation is an elementary part of the recursion method [15, 16].

Before the hypothesis itself is stated, we will briefly present the relation between the Lanczos coefficients b_n and the autocorrelation function $C(t)$ or, respectively, its Fourier transform, the spectral function

$$\Phi(\omega) = \int_{-\infty}^{\infty} e^{-\mathrm{i}\omega t}\, C(t)\, \mathrm{d}t\,. \tag{4}$$

There exists a (non-linear) one-to-one map between the Lanczos coefficients b_n and the spectral function $\Phi(\omega)$, thus, a set of b_n's uniquely determines $\Phi(\omega)$ and vice versa. It can be shown that the Lanczos coefficients b_n appear in the continued fraction expansion of $\Phi(\omega)$, i.e.,

$$\Phi(\omega) = \mathrm{Re}\,\cfrac{2}{\mathrm{i}\omega + \cfrac{b_1^2}{\mathrm{i}\omega + \cfrac{b_2^2}{\mathrm{i}\omega + \dots}}}\,. \tag{5}$$

The universal operator growth hypothesis brought forward in Ref. [14] concerns the asymptotic behavior of the Lanczos coefficients b_n. The hypothesis can informally be stated as follows: The Lanczos coefficients b_n should "grow as fast as possible" in generic, non-integrable systems. It turns out that [as detailed below] the fastest possible growth rate is (asymptotically) linear, i.e.,

$$b_n \sim \alpha n + \gamma + o(1) \tag{6}$$

for some real constants $\alpha > 0$ and γ. In the special case of a one-dimensional system, the fastest possible growth is sub-linear due to an additional logarithmic correction, i.e.,

$$b_n \sim A\,\frac{n}{\ln n} + o(n/\ln n)\,, \tag{7}$$

where $A > 0$ is a real constant and $o(g_n)$ denotes some real sequence f_n with $\lim_{n\to\infty} |f_n/g_n| = 0$.

These bounds on fastest possible (asymptotic) growth eventually originate from a powerful statement on the behavior of the spectral function $\Phi(\omega)$ for large ω. The spectral function usually features non-vanishing high-frequency tails for generic many-body systems. By means of geometric arguments these tails can be rigorously bounded by an exponential function such that

$$\Phi(\omega) \leq K e^{-\kappa|\omega|}\,, \tag{8}$$

for some adequately chosen constant $K > 0$ and decay constant $\kappa > 0$, which is related to the geometry of the system [19]. It can be shown that spectral functions actually featuring exponentially decaying tails give rise to asymptotically linear growth in the Lanczos coefficients [20, 21]. Therefore, the operator growth hypothesis is equivalent to an exponentially decaying spectral function and basically states that the Lanczos coefficients should grow as fast as "permitted by the geometry". There are a few examples for which linear growth is analytically known to be achieved [14, 22].

III. BOUND ON GROWTH VIA MOMENTS

The asymptotically linear bound on the growth of the b_n or, respectively, the exponential bound on the decay of the spectral function $\Phi(\omega)$ are ultimately a consequence of geometric arguments concerning the locality of the Hamiltonian and the observable as well as the specific lattice geometry of the system [19]. A straightforward way to apply these arguments is by considering the moments μ_{2n} of the autocorrelation function and determining an upper bound on these moments by taking the respective geometry of the system into account. The moments of the autocorrelation function $C(t)$ are defined by

$$\mu_{2n} = \frac{\mathrm{d}^{2n}}{\mathrm{d}t^{2n}} C(t)\big|_{t=0} \tag{9}$$

or, respectively, in terms of the spectral function

$$\mu_{2n} = \int \omega^{2n}\, \Phi(\omega)\, \mathrm{d}\omega\,. \tag{10}$$

Since $C(t)$ is an even function, all odd moments necessarily vanish. The information contained in the mo-

ments μ_{2n} is identical to the information conveyed by the Lanczos coefficients b_n. It is detailed in App. A how to translate between the two quantities.

Employing the Heisenberg equation of motion for time-dependent operators, Eq. (9) can be written as

$$\mu_{2n} = ||\mathcal{L}^n\mathcal{O}||^2 \,. \tag{11}$$

This quantity will be bounded from above in the following. We again consider a local operator $\mathcal{O}$ with $||\mathcal{O}|| = 1$ and a local Hamiltonian $\mathcal{H} = \sum_\ell h_\ell$ with local terms h_ℓ or, respectively, a local Liouvillian $\mathcal{L} = \sum_k \ell_k$ with local terms $\ell_k = [h_k, \cdot\,]$.

The norm of a local Liouvillian ℓ [we assume periodicity such that all ℓ_k are of the same type] applied to some operator $\mathcal{A}$ can be bounded by

$$||\ell\mathcal{A}|| \leq \mathcal{E}\,||\mathcal{A}||\,, \tag{12}$$

where $\mathcal{E} = E_{\max} - E_{\min}$ denotes the maximum eigenvalue of ℓ and $E_{\max}$ ($E_{\min}$) is the maximum (minimum) eigenvalue of the local Hamiltonian h. Equality holds if the operator $\mathcal{A}$ is an eigenoperator of the local Liouvillian with the largest eigenvalue. Utilizing the triangle inequality and iteratively applying Eq. (12) yields

$$\begin{aligned} ||\mathcal{L}^n\mathcal{O}|| &= ||\sum_{k_1,\ldots,k_n} \ell_{k_n}\ldots\ell_{k_1}\mathcal{O}|| \\ &\leq \sum_{k_1,\ldots,k_n} ||\ell_{k_n}\ldots\ell_{k_1}\mathcal{O}|| \\ &\leq \sum_{k_1,\ldots,k_n} \mathcal{E}^n = \mathcal{E}^n N_{\text{sum}}(n)\,, \end{aligned} \tag{13}$$

where N_{sum} denotes the number of terms in the sum [it is specified below which terms are actually counted]. This number typically grows quite fast with n and can be exactly determined for simple geometries, as is presented at the end of this section. Consequently, the moments can be bounded as

$$\mu_{2n} = ||\mathcal{L}^n\mathcal{O}||^2 \leq \mathcal{E}^{2n} N_{\text{sum}}^2(n)\,. \tag{14}$$

This bound on the moments is sharp, meaning first, no sequence of moments μ_{2n} calculated via Eq. (9) can possibly grow faster and, importantly, second, that this bound can *in principle* be actually achieved with an equality sign. This is the case if and only if two conditions are met. Firstly, to get an equality in the triangle inequality, all operators occurring in the sum must be collinear. Secondly, the largest eigenvalue $\mathcal{E}$ must be realized at each application of a local Liouvillian. Indeed, it would be quite surprising if this bound were to be achieved tightly for physical systems. On the other hand, it may not be as far off as one might initially guess, since multiple applications of the same operator [here $\mathcal{L}$] to a state increase the overlap of the resulting state with the states at the edges of the spectrum [given that the initial state has some overlap with eigenstates corresponding to extremal eigenvalues].

The fastest possible growing moments, i.e., moments equal to the r.h.s. of Eq. (14), can be translated to corresponding Lanczos coefficients as described in App. A. For later reference, we denote the coefficients obtained this way by $\mathcal{B}_n$. They depend on the energy scale $\mathcal{E}$ as well as on the lattice geometry expressed through N_{sum}, both quantities are exactly known for the models studied below. Even though Eq. (14) gives a rigorous upper bound on the moments, the $\mathcal{B}_n$ obtained from this bound do not necessarily constitute a pointwise upper bound on the b_n. In Sec. IV A we give more details on the interpretation of the coefficients $\mathcal{B}_n$.

To end this section, we exemplarily determine the number N_{sum} for the simple case of a one-dimensional chain with nearest-neighbor interactions, i.e., $\mathcal{H} = \sum_\ell h_{\ell,\ell+1}$. We start with a local operator $\mathcal{O}$ whose support is only on site zero [the support of an operator contains all sites on which the operator is not equal to the identity, e.g., here $\mathcal{O} = \ldots \otimes I \otimes \mathcal{O}_0 \otimes I \otimes \ldots$, where I denotes the identity on a given site]. The operator $\mathcal{L}\mathcal{O}$ consists of operators $\ell_{-1,0}\mathcal{O}_0$ with support on sites $(-1,0)$ as well as $\ell_{0,1}\mathcal{O}_0$ with support on sites $(0,1)$. Next, $\mathcal{L}^2\mathcal{O}$ contains six operators with support on sites $(-2,-1,0)$, $(-1,0)$, $(-1,0,1)$, $(-1,0,1)$, $(0,1)$, $(0,1,2)$, respectively. In these lists we include [and count] trivially non-vanishing operators, i.e., operators that vanish due to a lack of overlap between respective supports are not counted [for example the operator $\ell_{8,9}\mathcal{O}_0$ trivially vanishes], however, operators with respective overlap between supports [like $\ell_{0,1}\mathcal{O}_0$] are always counted, even though the operator may vanish due to the specific choice of the local Hamiltonian and initial observable. In this manner, we iteratively apply the Liouvillian to the initial operator, grow the supports accordingly and keep track of the number of potentially non-vanishing operators. For the case at hand, the above procedure gives rise to a sequence of numbers $N_{\text{sum}}(n) = 1, 2, 6, 22, 94, 454, 2430, 14214, \ldots$ of terms in the sum in Eq. (14). As rigorously shown in Ref. [23], there exists a closed mathematical expression for this sequence, i.e., $N_{\text{sum}}(n) = B_n(2)$, where B_n denote the Bell polynomials.

The above strategy of counting terms [which is presented in Ref. [23] in a more rigorous way] in principle also works for more complicated geometries, e.g., higher-dimensional or with long-range interactions. However, it can be quite involved to keep track of all contributions and closed expressions like the one above are generally difficult to come by. Thus, for the lattice geometries investigated below, i.e., with next-nearest-neighbor interactions and two-dimensional, respectively, we compute the sequences iteratively up to some n.

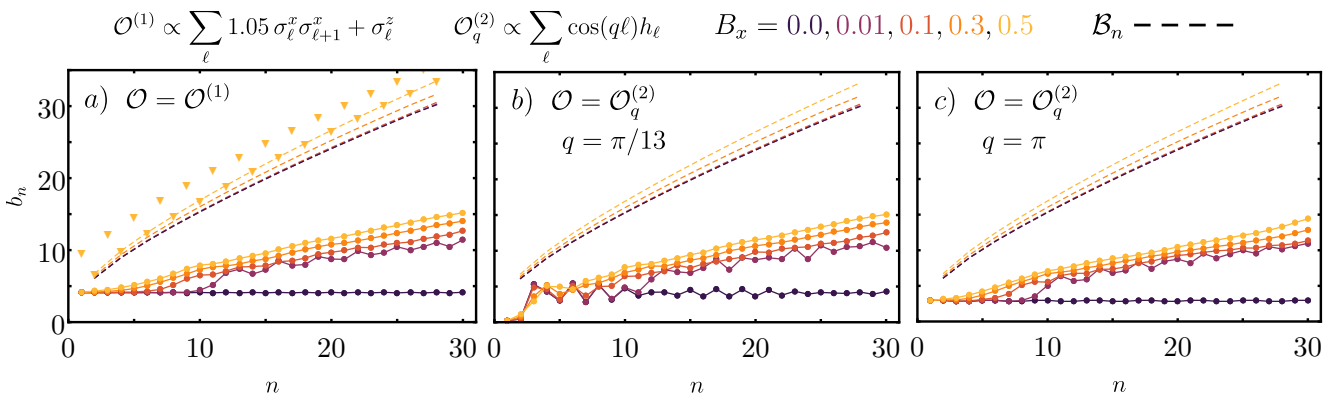

FIG. 1. Lanczos coefficients b_n of the transverse Ising model for the 2-local observables *a)* $\mathcal{O}^{(1)}$, *b)* slow mode of $\mathcal{O}_q^{(2)}$ with $q = \pi/13$, and *c)* fast mode of $\mathcal{O}_q^{(2)}$ with $q = \pi$. The integrability-breaking magnetic field attains values from $B_x = 0.0$ to $B_x = 0.5$. For all observables, the transition from a free model to a non-integrable model is evident. The coefficients $\mathcal{B}_n$ are explicitly depicted in *a)* for the case $B_x = 0.5$ as yellow dots. Dashed lines indicate the "lower branches" of the corresponding $\mathcal{B}_n$. To avoid clutter, only the dashed lines are depicted as a guide to the eye for other values of B_x and in all following figures. The coefficients $\mathcal{B}_n$ are larger than the physical b_n by a factor of about two for all observables.

IV. NUMERICAL ANALYSIS

In this section, we numerically check the proposed operator growth hypothesis by explicitly calculating the Lanczos coefficients b_n for various exemplary setups. These setups include one-dimensional and two-dimensional Ising models as well as one-dimensional Heisenberg models, all paired with a variety of different observables. We compare the calculated b_n with the coefficients $\mathcal{B}_n$ [obtained from the r.h.s. of Eq. (14)] by explicitly calculating $\mathcal{E}$ and N_{sum} for each model.

In practice, it is only possible [for the considered systems at least] to obtain a finite number N of Lanczos coefficients b_n, since the dimension of the operator space grows exponentially. The achievable number of coefficients N is around 30 for the 1d Ising model and around 15 for the Heisenberg model. The difference in obtainable b_n is due to the fact that the operator space grows much faster for the Heisenberg model than for the Ising model. For all considered systems the Hamiltonian $\mathcal{H}$ consist of two terms, an integrable part $\mathcal{H}_0$ and an integrability-breaking part $\mathcal{V}$, i.e.,

$$\mathcal{H} = \mathcal{H}_0 + \lambda\mathcal{V} \tag{15}$$

[except for the 2d Ising model, where $\mathcal{H}_0$ is already non-integrable]. The parameter λ tunes the non-integrability of the model. We suppose that the total Hamiltonian $\mathcal{H}$ (as well as $\mathcal{H}_0$ and $\mathcal{V}$ individually) can be written in terms of local Hamiltonians, i.e., $\mathcal{H} = \sum_\ell h_\ell$. Again, the local terms usually describe short-range, few-body interactions. For each model, we consider a number of observables $\mathcal{O}$. Importantly, all observables should have zero overlap with any conserved quantity [24], for example $(\mathcal{O}|\mathcal{H}) = 0$.

A. Transverse Ising model

The first model under consideration is a transverse Ising model with a tilted field. Respective unperturbed and total Hamiltonians are given by

$$\mathcal{H}_0 = \sum_\ell J_{xx}\sigma_\ell^x\sigma_{\ell+1}^x + B_z\sigma_\ell^z \tag{16}$$
$$\mathcal{H} = \mathcal{H}_0 + B_x\sum_\ell \sigma_\ell^x\,,$$

where $\sigma_\ell^{x,y,z}$ denote Pauli operators on site ℓ. The magnetic field B_x in x-direction plays the role of the integrability-breaking parameter λ in Eq. (15), i.e., the system is non-integrable for $B_x \neq 0$ and integrable for $B_x = 0$. We set $J_{xx} = 1.0$ and $B_z = -1.05$ and calculate the Lanczos coefficients for various observables as detailed in Sec. II. In practice, it is convenient to adopt the set of Pauli strings as a working basis of the Hilbert space of operators [14, 25].

The behavior of the Lanczos coefficients during a transition from an integrable to a non-integrable 1d Ising model has been systematically probed in Ref. [17] for local observables supported on one or two sites. Thus, here, we primarily focus on observables with support throughout the whole system. As a first example, we consider the 2-local observable

$$\mathcal{O}^{(1)} \propto \sum_\ell 1.05\,\sigma_\ell^x\sigma_{\ell+1}^x + \sigma_\ell^z\,, \tag{17}$$

where 2-local means that the local terms are supported on two sites respectively. The choice of the parameter 1.05 in front of the xx-coupling term ensures that $(\mathcal{O}^{(1)}|\mathcal{H}) = 0$.

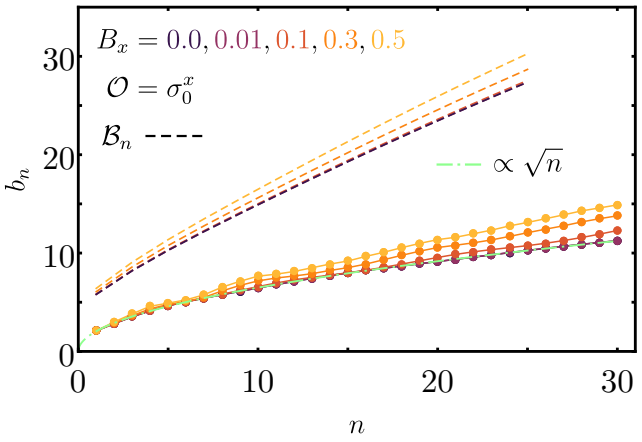

Figure 2. Lanczos coefficients b_n of the transverse Ising model for a local observable $\mathcal{O}^{(3)} = \sigma_0^x$ for various integrability-breaking parameters B_x. The distinction between the free and non-nonintegrable curves is not as striking a before. Green dash-dotted line indicates a fit $\propto \sqrt{n}$ to the data of the integrable model. Dashed lines serve as a guide to the eye for the coefficients $\mathcal{B}_n$, which are larger by a factor of about two.

This exact setup was also studied in Ref. [14]. The corresponding Lanczos coefficients are depicted in Fig. 1a for various values of the integrability-breaking parameter B_x.

The Hamiltonian of the bare transverse Ising model [with $B_x = 0$] can be mapped onto free fermions via a Jordan-Wigner transformation. Further, the observable in Eq. (17) is local in the fermionic picture. In this non-interacting case, the Lanczos coefficients seem to be more or less constant. As soon as a small perturbation that breaks the integrability is introduced, e.g., $B_x = 0.01$, the Lanczos coefficients begin to grow. The distinction between the free case and non-integrable cases is clearly visible in Fig. 1a. The growth of the Lanczos coefficients for larger values of B_x already looks quite linear. A possible logarithmic correction due to the system's one-dimensionality is not directly noticeable in the data, although it has been observed in this model [17].

Before we continue, we want to make some remarks on the interpretation of the coefficients $\mathcal{B}_n$. As mentioned, the $\mathcal{B}_n$ are computed by assuming that the moments grow as fast as possible, i.e., an equality sign in Eq. (14), and translating these maximum moments to Lanczos coefficients as detailed in App. A. However, even though Eq. (14) gives a rigorous upper bound on the moments, the resulting $\mathcal{B}_n$ do not necessarily constitute a strict pointwise upper bound on the b_n [this is simply due to the way the Lanczos coefficients are calculated from the moments]. Thus, the $\mathcal{B}_n$ should not be thought of as such. Rather, the $\mathcal{B}_n$ represent a sort of "global uniform" upper bound, meaning that it is impossible to further increase the value of one specific coefficient "by hand", without simultaneously decreasing the value of another one [or several other ones]. In this sense the $\mathcal{B}_n$ are the "maximum" coefficients. If the "physical" coefficients b_n would follow the $\mathcal{B}_n$ tightly, then one could indeed conclude that the upper bound in Eq. (14) was sharply achieved and that the Lanczos coefficients would indeed grow "as fast as possible", given the constraints in Eqs. (12), (13).

The values of the $\mathcal{B}_n$ are explicitly depicted in Fig. 1a for $B_x = 0.5$. The coefficients clearly exhibit some even-odd effects. These even-odd effects also occur for all other considered parameters and models. To avoid clutter, we only show the "lower branches" of the $\mathcal{B}_n$ as dashed lines for smaller values of B_x. Therefore, the dashed lines in Fig. 1a [and all following figures] serve as a guide to the eye for the "maximal possible" coefficients $\mathcal{B}_n$. The energy scale is $\mathcal{E} = 3.2$ [for $B_x = 0.5$] and N_{sum} is obtained as detailed at the end of Sec. III, with the important difference that the initial operator is now supported on two sites. In Fig. 1a, it is evident that the coefficients $\mathcal{B}_n$ are larger than the physical coefficients b_n by about a factor of 2. Thus, the upper bound on the moments is not achieved, i.e., Eq. (14) is an overestimate [26]. This general behavior of the b_n as well as the $\mathcal{B}_n$ is reproduced for the next observable, which constitutes an energy density wave with momentum q, i.e.,

$$\mathcal{O}_q^{(2)} \propto \sum_\ell \cos(q\ell) h_\ell \,. \tag{18}$$

We study a relatively slow dynamic with $q = \pi/13$ and a relatively fast dynamic with $q = \pi$. Both observables are local in the fermionic picture. The Lanczos coefficients b_n and coefficients $\mathcal{B}_n$ are depicted in Fig. 1b for $q = \pi/13$ and in Fig. 1c for $q = \pi$. In both cases, the qualitative behavior is quite similar to the first observable. Again, the Lanczos coefficients of the free model with $B_x = 0$ seem to be more or less constant. Once the additional magnetic field is added, the model becomes non-integrable and at some point, the b_n grow approximately linearly. Just as for the first observable, the derived bounds are not tight and the $\mathcal{B}_n$ are larger by a factor of about two.

The final considered observable for the one-dimensional Ising model is a local operator whose support only contains a single site, i.e.,

$$\mathcal{O}^{(3)} = \sigma_0^x \,. \tag{19}$$

The corresponding Lanczos coefficients are depicted in Fig. 2. There is a clear qualitative difference compared to the observables investigated thus far. For the free case with $B_x = 0$ the Lanczos coefficients seem to no longer be bounded by a constant.

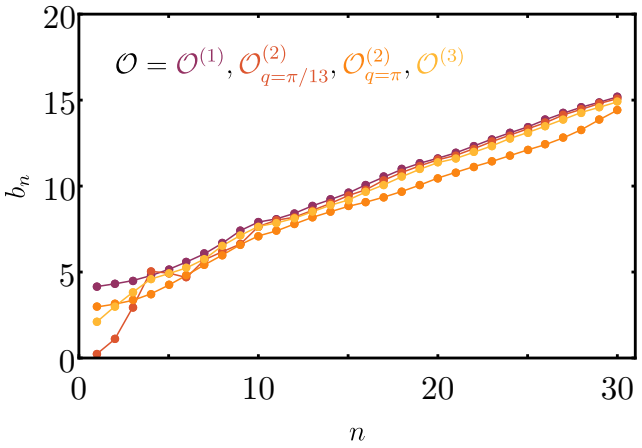

Figure 3. Comparison between Lanczos coefficients for the Ising model with $B_x = 0.5$ for all four observables considered thus far. The growth is quite similar for larger n hinting at a universality of operator growth.

Rather, the growth is quite accurately described by a square-root $\propto \sqrt{n}$ [see fit]. For this particular model and observable the square-root-like growth can be understood analytically [22]. Further, this kind of growth has been observed for a variety of other integrable models [14, 16, 27]. We suspect that this qualitatively different behavior compared to the previous cases is due to the specific choice of the observable, which is, in contrast to all previously considered observables, non-local in the fermionic picture. Consequently, one could be inclined to formulate two sufficient conditions, which both have to be met in order for the b_n to be bounded by a constant. First, the Hamiltonian has to describe a free model and, second, the observable has to be local. For the observable at hand, which is non-local in the fermionic picture, the second condition is violated. Therefore, the Lanczos coefficients are not bounded by a constant, rather they grow as a square-root.

As the Hamiltonian departs from the integrable/free point once $B_x \neq 0$, the b_n grow faster [which is not too surprising, since there are simply more terms in the Hamiltonian]. From the computed data it is not immediately obvious whether the growth becomes linear (with a logarithmic correction) or remains more or less square-root-like. Possibly, the data for larger B_x in Fig. 2 hints at an onset of linear growth for larger n. However, the distinction is certainly not as clear as for the local observables. Without previous knowledge of which coefficients belong to which B_x, it would be quite difficult to say if a set of b_n belongs to an integrable/free or non-integrable model [barring the absolute values]. Therefore, calculating the b_n as a potential method to determine or define (non-)integrability does not seem feasible, since the number at which universal behavior sets in may be larger than the practically computable number of Lanczos coefficients. Again, the $\mathcal{B}_n$ are off by a factor of about 2.

It is interesting to note that in the non-integrable models all considered observables seem to more or less lead to similar growth patterns and attain similar values for larger n. For comparison, Fig. 3 depicts the Lanczos coefficients for all four observables considered thus far for $B_x = 0.5$. This figure certainly supports the hypothesis of a universality of operator growth brought forth in Ref. [14]. Particularly striking is the relation between the observable $\mathcal{O}^{(1)}$ and the slow Fourier mode $\mathcal{O}^{(2)}_{q=\pi/13}$, since for $n \gtrsim 10$ the coefficients practically coincide. Before leaving the Ising model and continuing with the Heisenberg model, we want to briefly present data on the 2d Ising model. As the 2d Ising model is non-integrable, the hypothesis predicts a strict asymptotically linear growth [without logarithmic correction] of the Lanczos coefficients b_n. Respective Hamiltonians of the two-dimensional Ising model are given by

$$\mathcal{H}_0 = \sum_{\ell,\ell'} J_{xx}\sigma^x_{\ell,\ell'}\sigma^x_{\ell+1,\ell'} + J'_{xx}\sigma^x_{\ell,\ell'}\sigma^x_{\ell,\ell'+1} + B_z\sigma^z_{\ell,\ell'}$$
$$\mathcal{H} = \mathcal{H}_0 + B_x \sum_{\ell,\ell'} \sigma^x_{\ell,\ell'}\,, \tag{20}$$

where primed indices number the vertical direction and unprimed indices the horizontal direction. As in the 1d case, we set $J_{xx} = 1.0$, $B_z = -1.05$ and vary B_x. The coupling strength in vertical direction is set to $J'_{xx} = 0.5$. This model in non-integrable for all values of B_x. The energy scale is given by $\mathcal{E} = 3.9$ [for $B_x = 0.5$].

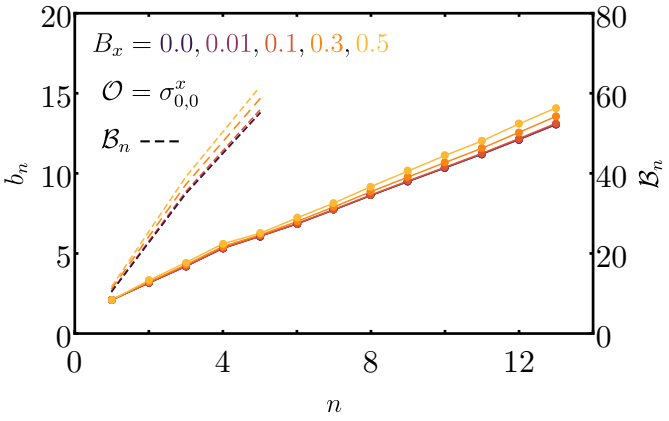

Figure 4. Lanczos coefficients b_n of the two-dimensional transverse Ising model for an observable $\mathcal{O} = \sigma^x_{0,0}$ for various B_x. For all values of B_x the growth is nicely linear. Dashed lines serve as a guide to eye for the coefficients $\mathcal{B}_n$, which are much larger (note the additional vertical axis on the right).

We again consider a local observable whose support is only on one site, i.e.,

$$\mathcal{O} = \sigma^x_{0,0}\,. \tag{21}$$

The calculated Lanczos coefficients b_n are depicted in Fig. 4. Since the space of operators grows extremely fast, it is only practically possible to calculate about 13 coefficients. These coefficients grow in a nicely linear fashion for all values of B_x, which is in accord with the operator growth hypothesis. The coefficients $\mathcal{B}_n$ from the derived upper bound on the moments are very far off. So far off, in fact, that there is an additional vertical axis for the coefficients $\mathcal{B}_n$ on the right side in Fig. 4, which includes a factor of four. As mentioned, the number N_{sum} is computed iteratively. For the two-dimensional Ising model the operator space grows so fast that the $\mathcal{B}_n$ are only attainable up to $n = 5$.
Summarizing the results from this section, the operator growth hypothesis is supported by [most of] the numerical data. The Lanczos coefficients of the one-dimensional non-integrable Ising models seem to eventually attain approximate linear growth for observables that are local in the fermionic picture. In these cases, the transition from free to non-integrable is clearly visible. A possible logarithmic correction is not directly noticeable in the presented data. However, it is possible to reveal the predicted correction by rescaling the axes appropriately [17]. Further, the data for the two-dimensional Ising model supports the hypothesis for all considered values of B_x. Only the data for the third observable $\mathcal{O}^{(3)} = \sigma^x_0$ remains somewhat inconclusive.
The transition is not as distinct as for the other observables, however, the onset of the hypothesized universal behavior may be suspected for larger n. All these numerical results support the in Ref. [14] proposed operator growth hypothesis in the sense that the b_n grow asymptotically linear. This is the first main result of the paper at hand.
In Ref. [14], the operator growth hypothesis is several times informally stated as: the Lanczos coefficients should "grow as fast as possible" and therefore eventually attain said linear growth. In fact, the data presented in this section corroborates the notion of asymptotically linear growth. However, the Lanczos coefficients could, in principle, grow much faster, as indicated by the coefficients $\mathcal{B}_n$, which are not tightly achieved in any of the considered models. Thus, we want to clarify the "fastest possible growth" is not to be understood with respect to the absolute numerical values of the coefficients, but rather in regard to the functional form of their growth. Indeed, the coefficients b_n seem to grow with quite a similar functional form as the [much to large] coefficients $\mathcal{B}_n$, also cf. V. This is the second main result of the paper at hand.

B. Heisenberg model

The second model of interest is a Heisenberg model with an additional next-nearest-neighbor interaction. Respective Hamiltonians are given by

$$\mathcal{H}_0 = \sum_\ell \sigma^x_\ell \sigma^x_{\ell+1} + \sigma^y_\ell \sigma^y_{\ell+1} + \Delta \sigma^z_\ell \sigma^z_{\ell+1} \tag{22}$$
$$\mathcal{H} = \mathcal{H}_0 + \Delta' \sum_{\ell,\ell'} \sigma^z_\ell \sigma^z_{\ell+2}\,.$$

The anisotropy of the nearest-neighbor interaction is denoted by Δ and the integrability-breaking next-nearest-neighbor interaction is tuned by the parameter Δ' [which plays the role of λ in Eq. (15)]. The bare Heisenberg chain [with $\Delta' = 0$] is integrable for any Δ.
The model is gapless and exhibits ballistic transport behavior [of spin and energy] for $|\Delta| < 1$, whereas for $|\Delta| > 1$ the transport of spin is diffusive, while energy transport is still ballistic [28]. In the following numerics we cover both cases by choosing values $\Delta = 0.5, 1.5$. The parameter Δ' that breaks the integrability is varied in the same fashion as B_x in the Ising model.
Note that the full Hamiltonian in Eq. (22) conserves the total magnetization in z-direction. Therefore, it is natural to consider a spin density wave with momentum q, i.e.,

$$\mathcal{O}_q \propto \sum_\ell \cos(q\ell)\sigma^z_\ell\,. \tag{23}$$

Similar as for the energy density wave in the Ising model, we study a relatively slow dynamic with $q = \pi/13$ [depicted in Figs. 5a, 5c for $\Delta = 0.5, 1.5$ respectively] and a relatively fast dynamic with $q = \pi$ [depicted in Figs. 5b, 5d for $\Delta = 0.5, 1.5$ respectively].
Since the Heisenberg Hamiltonian contains more coupling terms than the Ising Hamiltonian, the dimension of the operator space [with respect to the Pauli basis] grows faster and we are restricted to a smaller number of coefficients, only about 15.
Comparing the variance (relative deviations) of the Lanczos coefficients for $\Delta = 0.5$ and $\Delta = 1.5$, it is striking that the coefficients for $\Delta = 1.5$ vary much less for different values of Δ'. This is most likely due to the relative strength of the perturbation. Let $||\mathcal{H}_0^\Delta||$ denote the norm of the unperturbed Hamiltonian with anisotropy Δ and $||\lambda\mathcal{V}||$ the strength of the perturbation [where λ conforms to Δ']. Then, for example $||0.5\mathcal{V}||/||\mathcal{H}_0^{1.5}|| = 0.34$, but $||0.5\mathcal{V}||/||\mathcal{H}_0^{0.5}|| = 0.47$ [for comparison, in the one-dimensional Ising model $||0.5\mathcal{V}||/||\mathcal{H}_0|| = 0.28$].

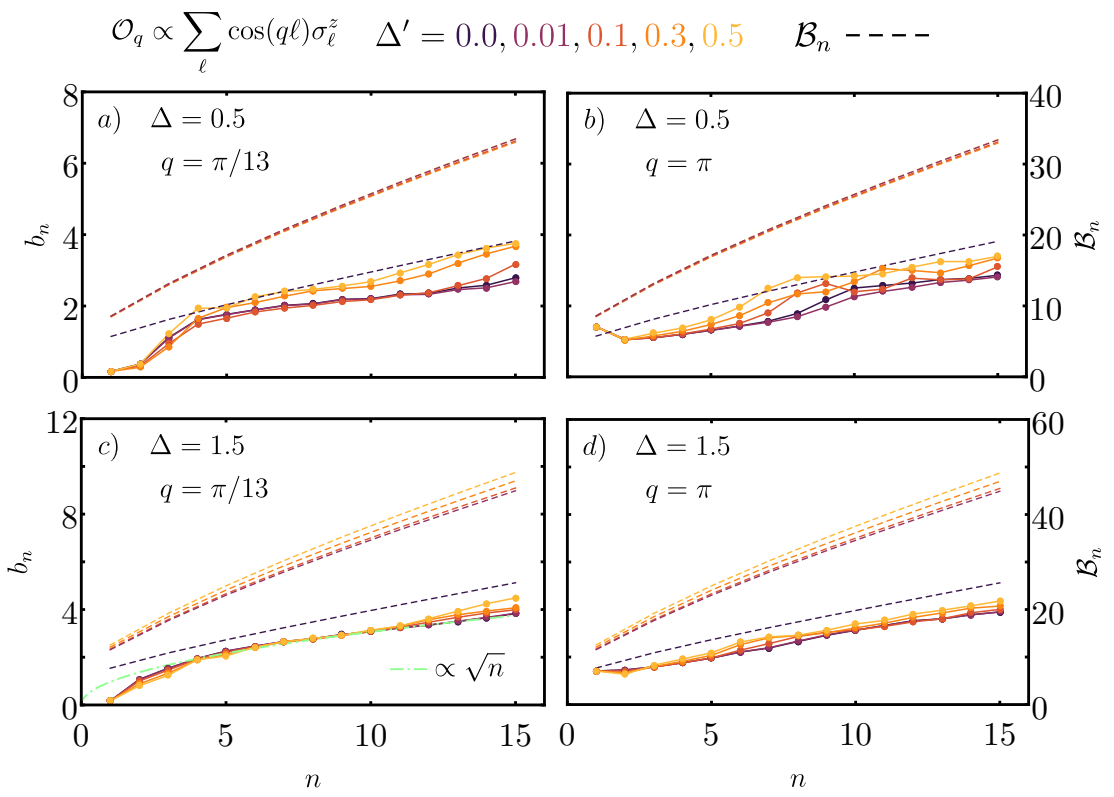

FIG. 5. Lanczos coefficients b_n of the Heisenberg model for spin density waves. Depicted are various combinations of anisotropies and momenta: *a*) $\Delta = 0.5$, $q = \pi/13$; *b*) $\Delta = 0.5$, $q = \pi$; *c*) $\Delta = 1.5$, $q = \pi/13$; *d*) $\Delta = 1.5$, $q = \pi$. The integrability-breaking parameter Δ' attains values from 0.0 to 0.5. Dashed lines serve as a guide to the eye for the coefficients $\mathcal{B}_n$, which are much larger (note the additional vertical axes on the right).

Again, the stronger the perturbation, the faster the coefficients grow, which is simply due to additional terms in the Hamiltonian [in order to not obscure the main points, we refrain from rescaling the Hamiltonian accordingly]. Other than that, the growth is more irregular than in the Ising model, at least in the regime where data is available. For both values of Δ the transition occurs between an integrable [$\Delta' = 0$] and non-integrable [$\Delta' \neq 0$] model. However, for $\Delta = 0.5$ there is neither square-root-like growth in the integrable case nor linear growth in the non-integrable case visible [for both modes with $q = \pi/13$ in Fig. 5a and $q = \pi$ in Fig. 5b]. For $\Delta = 1.5$, $\Delta' = 0.0$ and $q = \pi/13$ the growth of the coefficients is more similar to a square-root [see fit] and only visibly deviates for $n \gtrsim 12$, see Fig. 5c. For the faster mode with $q = \pi$ the growth seems more linear with relatively small deviations, see Fig. 5d.

The coefficients $\mathcal{B}_n$ are much larger than any of the b_n such that the additional vertical axes contain a factor of five in all cases. The number of terms in the sum N_{sum} grows quite a lot faster than in the Ising model due to the next-nearest-neighbor interaction. These terms must in principle be included as soon as Δ' attains an arbitrarily small value strictly greater than zero. This leads to a somewhat gross overestimation, since the energy scale $\mathcal{E}$ remains basically unaltered for small Δ'. This is visible in all figures for the Heisenberg model, where the coefficients $\mathcal{B}_n$ for $\Delta' = 0$ are calculated with the smaller numbers N_{sum} of nearest-neighbor interaction. In principle, one could improve the upper bound on the moments by introducing a second energy scale $\mathcal{E}_{\text{nnn}}$ of the next-nearest-neighbor interaction and count terms according to the appearance of nearest-neighbor terms $\ell_{k,k+1}$ and next-nearest-neighbor terms $\ell_{k,k+2}$. This is, however, more complicated and not in the spirit of the derivations presented in Refs. [14, 19].

Summarizing, the numerical data for all considered values of Δ and q can neither really reject nor support the operator growth hypothesis [not least because data for larger n is not available]. The transitions between integrable and non-integrable models are certainly less striking than for the Ising model. Again, only looking at the b_n it would be impossible to say which coefficients belong to an integrable or non-integrable model.

This possibly raises the question whether the distinction between integrability and non-integrability regarding the growth of the b_n is an adequate distinction to make. As mentioned in Sec. II, the Lanczos coefficients are uniquely determined by the autocorrelation function $C(t)$. The Heisenberg model for $\Delta = 1.5$ and $\Delta' = 0$ is integrable and exhibits diffusive transport behavior [28], which is usually attributed to chaotic, non-integrable systems. In view of this, it may be not too surprising that the operator growth hypothesis is not supported by the [limited] numerical data presented in this section. This is the third main result of the paper at hand.

V. CONCLUSION

The first main message of the paper at hand concerns the explicitly calculated data on the Lanczos coefficients. We numerically probed the operator growth hypothesis proposed in Ref. [14], which states that in generic, non-integrable systems the Lanczos coefficients grow asymptotically linear [with a logarithmic correction in 1d]. We explicitly calculated Lanczos coefficients b_n for various combinations of models [including 1d and 2d Ising models as well as ballistic and diffusive Heisenberg models] and observables [including energy and spin density waves as well as local ones].

We found that the Ising model data generally supports the operator growth hypothesis. In particular, as soon as an integrability-breaking perturbation is added to the Hamiltonian, the coefficients eventually attain a linear growth [this transition is more pronounced in the case of a free Hamiltonian with a local observable (in the fermionic picture) than in the case of a free Hamiltonian with a non-local observable (in the fermionic picture)]. Further, the 2d Ising model exhibits clear linear growth. Inconclusive, however, remains the data for the Heisenberg model. For none of the combinations of considered parameters there is a clear distinction between the integrable and non-integrable cases. Of course, it may be possible that the hypothesized universal behavior only sets in at some larger n, which is not accessible by our numerical tools.

The second main message of the paper at hand concerns the coefficients $\mathcal{B}_n$, which are obtained by considering the fastest growing moments and converting them into Lanczos coefficients. The informal version of the operator growth hypothesis is stated several times in Ref. [14], namely that "the Lanczos coefficients should grow as fast as possible" and a corresponding bound on the moments leading to linear growth [with a logarithmic correction in one dimension] is given [26]. As seen in the available numerical data, even the "optimized" bound in Eq. (14) is not remotely tight and the "physical" Lanczos coefficients b_n increase much slower than the "fastest possible growing" coefficients $\mathcal{B}_n$ in all considered models. Therefore, technically, the Lanczos coefficients do not grow as fast as possible. Nevertheless, the physical Lanczos coefficients b_n seem to grow in a manner that is compatible with the "functional form" of the maximal growth, i.e., we observe more or less linear growth for the Ising models, only with a flatter slope than would be induced by the bound on the moments. Along this line of thinking, there are arguments which suggest that the coefficients $\mathcal{B}_n$ capture the correct asymptotic behavior, only with a rescaled "effective" energy scale $\tilde{\mathcal{E}}$ that is generally different from $\mathcal{E}$ [23]. Thus, treating $\mathcal{E}$ in Eq. 12 as a fitting parameter may give reasonable results. This is, however, beyond the scope of this work and a possible prospect for future research.

ACKNOWLEDGMENTS

We thank D. Parker for interesting discussion on this topic and for a comment on an earlier version of this paper. We are also grateful to A. Dymarsky and J.D. Noh for some helpful remarks and for bringing our attention to related work. This work was supported by the Deutsche Forschungsgemeinschaft (DFG) within the Research Unit FOR 2692 under Grant No. 397107022 (GE 1657/3-2).

Appendix A: Translating between b_n and μ_{2n}

For completeness, we briefly present the relation between the coefficients b_n and the moments μ_{2n} [29].

i. From moments to Lanczos coefficients:

To calculate the Lanczos coefficients b_n from a given set of moments μ_{2n} we proceed as follows: we define $c_n = \mu_{2n}/\mu_0$ and compute determinants of certain matrices constructed from the normalized moments c_n, i.e.,

$$B_n = \det(c_{i+j})_{0\leq i,j\leq n-1} \tag{A1}$$

where $n \geq 2$ and $B_0 = B_1 = 1$ as well as

$$C_n = \det(c_{i+j+1})_{0\leq i,j\leq n-1} \tag{A2}$$

where $n \geq 1$ and $C_0 = 1$. Then the Lanczos coefficients are obtained as fractions of determinants via

$$b_{2n}^2 = \frac{B_{n+1}C_{n-1}}{B_nC_n}\,, \quad b_{2n-1}^2 = \frac{B_{n-1}C_n}{B_nC_{n-1}}\,. \tag{A3}$$

ii. From Lanczos coefficients to moments:

We take the representation L of the Liouvillian $\mathcal{L}$ in the Krylov subspace spanned by the vectors generated by the Lanczos algorithm, cf. Eq. (3). The moments μ_{2n} can be easily read off as the upper-left element of even powers $2n$ of the matrix L, i.e., $\mu_{2n} = (L^{2n})_{00}$.

[1] C. Gogolin and J. Eisert, Reports on Progress in Physics **79**, 056001 (2016).
[2] J. M. Deutsch, Phys. Rev. A **43**, 2046 (1991).
[3] M. Srednicki, Phys. Rev. E **50**, 888 (1994).
[4] L. D'Alessio, Y. Kafri, A. Polkovnikov, and M. Rigol, Advances in Physics **65**, 239 (2016).
[5] S. Lloyd, "Pure state quantum statistical mechanics and black holes," (2013), arXiv:1307.0378.
[6] S. Goldstein, J. L. Lebowitz, R. Tumulka, and N. Zanghì, Phys. Rev. Lett. **96**, 050403 (2006).
[7] P. Reimann, Phys. Rev. Lett. **99**, 160404 (2007).
[8] C. W. von Keyserlingk, T. Rakovszky, F. Pollmann, and S. L. Sondhi, Phys. Rev. X **8**, 021013 (2018).
[9] A. Nahum, S. Vijay, and J. Haah, Phys. Rev. X **8**, 021014 (2018).
[10] T. Rakovszky, F. Pollmann, and C. W. von Keyserlingk, Phys. Rev. X **8**, 031058 (2018).
[11] V. Khemani, A. Vishwanath, and D. A. Huse, Phys. Rev. X **8**, 031057 (2018).
[12] S. Gopalakrishnan, D. A. Huse, V. Khemani, and R. Vasseur, Phys. Rev. B **98**, 220303 (2018).
[13] A. Chan, A. De Luca, and J. T. Chalker, Phys. Rev. X **8**, 041019 (2018).
[14] D. E. Parker, X. Cao, A. Avdoshkin, T. Scaffidi, and E. Altman, Phys. Rev. X **9**, 041017 (2019).
[15] D. C. Mattis, in *Physics in One Dimension* (Springer Berlin Heidelberg, 1981) pp. 3–10.
[16] V. S. Viswanath and G. Müller, *The Recursion Method: Applications to Many-Body Dynamics* (Springer, New York, 2008).
[17] J. D. Noh, Phys. Rev. E **104**, 034112 (2021).
[18] A. Dymarsky and M. Smolkin, Phys. Rev. D **104**, L081702 (2021).
[19] D. A. Abanin, W. De Roeck, and F. Huveneers, Phys. Rev. Lett. **115**, 256803 (2015).
[20] D. S. Lubinsky, Acta Applicandae Mathematica **33**, 121 (1993).
[21] A. Magnus, in *The Recursion Method and Its Applications* (Springer Berlin Heidelberg, 1987) pp. 22–45.
[22] X. Cao, Journal of Physics A: Mathematical and Theoretical **54**, 144001 (2021).
[23] A. Avdoshkin and A. Dymarsky, Phys. Rev. Research **2**, 043234 (2020).
[24] P. Mazur, Physica **43**, 533 (1969).
[25] J. Dehaene and B. De Moor, Phys. Rev. A **68**, 042318 (2003).
[26] In Ref. [14], App. F a different upper bound on the moments [similar to the bound in Eq. (14)] is derived, i.e., $\mu_{2n} \leq P_n^2 (2\mathcal{E}')^{2n}$, where $P_n \leq n4^n \max_{\ell\in[0,n]} \ell^{n-\ell}$ and $\mathcal{E}' = ||h||$. It is shown that this bound corresponds to asymptotically linear growth with a logarithmic correction. Since the spectral function $\Phi(\omega)$ attains negative values for moments equal to the r.h.s. of the above bound, it is not possible to obtain corresponding $\mathcal{B}_n$. However, the numbers P_n grow rapidly, much quicker than the sequence of numbers found at the end of Sec. III, further, $2\mathcal{E}'$ is larger than $\mathcal{E}$. Thus, the above bound on the moments is looser than the derived bound in Eq. (14).
[27] M. H. Lee, Phys. Rev. Lett. **87**, 250601 (2001).
[28] B. Bertini, F. Heidrich-Meisner, C. Karrasch, T. Prosen, R. Steinigeweg, and M. Žnidarič, Rev. Mod. Phys. **93**, 025003 (2021).
[29] C. G. Joslin and C. G. Gray, Molecular Physics **66**, 757 (1989).

Preprint of Publication [P6]

Robin Heveling, Jiaozi Wang, Christian Bartsch, and Jochen Gemmer
"Stability of exponentially damped oscillations under perturbations of the Mori-Chain"
Journal of Physics Communications **6**, 085009 (2022)
DOI: 10.1088/2399-6528/ac863b

Stability of Exponentially Damped Oscillations under Perturbations of the Mori-Chain

Robin Heveling,* Jiaozi Wang,† Christian Bartsch,‡ and Jochen Gemmer§
Department of Physics, University of Osnabrück, D-49076 Osnabrück, Germany

There is an abundance of evidence that some relaxation dynamics, e.g., exponential decays, are much more common in nature than others. Recently, there have been attempts to trace this dominance back to a certain stability of the prevalent dynamics versus generic Hamiltonian perturbations. In the paper at hand, we tackle this stability issue from yet another angle, namely in the framework of the recursion method. We investigate the behavior of various relaxation dynamics with respect to alterations of the so-called Lanczos coefficients. All considered scenarios are set up in order to comply with the "universal operator growth hypothesis". Our numerical experiments suggest the existence of stability in a larger class of relaxation dynamics consisting of exponentially damped oscillations. Further, we propose a criterion to identify "pathological" perturbations that lead to uncommon dynamics.

I. INTRODUCTION

The apparent emergence of irreversibility from the underlying reversible theory of quantum mechanics is a long-standing puzzle that lacks an entirely satisfying answer to this day [1]. Over the course of the last decades, fundamental concepts like the "eigenstate thermalization hypothesis" [2–4] and "quantum typicality" [5–7] have crystallized, which give conditions under which isolated quantum systems eventually reach an equilibrium state. However, while these mechanisms ensure eventual equilibration, they make no statement in which manner the equilibrium state is actually reached, i.e., they do not narrow down the eligible routes to equilibrium. In contrast, it is evidently true that some relaxation dynamics, e.g., exponential decays, are much more common in nature than others, e.g., recurrence dynamics.

There are recent attempts to explain this prevalence with the idea that some dynamics are stable versus perturbations of the Hamiltonian. These attempts include, for example, investigations based on Hamiltonian perturbations on the level of random matrices [8]. Further, there exist advances that consider an entire ensemble of permissible perturbations [9–11]. It is then analytically shown that weak "typical" perturbations lead to an exponential damping of the original dynamics [9]. This renders exponential decays stable since only the decay constant changes, whereas recurrence dynamics are exponentially suppressed.

With the paper at hand, we address the issue of stability of certain [classes of] relaxation dynamics in the framework of the *recursion method* [12, 13]. Central quantities that appear within this framework are the so-called Lanczos coefficients, real numbers that characterize the complexity growth of operators over the course of time. As will be presented in Sec. II, the Lanczos coefficients can be interpreted as hopping amplitudes in a tight-binding model. In this manner, many physical problems, like calculating correlation functions, can practically be reduced to a one-dimensional [finite or semi-infinite] chain, which we refer to as the "Mori-chain" in the title of this paper. In the following, we consider perturbations on the level of Lanczos coefficients and examine the resulting effect on various kinds of relaxation dynamics.

The particular advantage of our approach within the recursion method framework is that all considered scenarios can be set up to directly comply with the universal operator growth hypothesis [14], which previous approaches have been lacking [8]. Said hypothesis concerns the asymptotic growth of the Lanczos coefficients and it basically states that the coefficients should eventually attain linear growth [with a logarithmic correction in one dimension]. The hypothesis is backed up by analytical as well as numerical evidence [14–16].

The paper at hand is structured as follows: Sec. II constitutes a preliminary section on the recursion method and the operator growth hypothesis. Afterwards, in Sec. III, the concrete strategy to study the stability of certain classes of dynamics is explained in detail. In Sec. IV we present and discuss our numerical results. We conclude in Sec. V.

II. PRELIMINARIES: RECURSION METHOD AND OPERATOR GROWTH HYPOTHESIS

In this section, we briefly recall the basics of the recursion method [12, 13] as well as the universal operator growth hypothesis [14]. We consider a system described

* rheveling@uos.de
† jiaowang@uos.de
‡ cbartsch@uos.de
§ jgemmer@uos.de

by some Hamiltonian $\mathcal{H}$. An observable of interest represented by a Hermitian operator $\mathcal{O}$ gives rise to a corresponding autocorrelation function

$$C(t) = \mathrm{Tr}[\mathcal{O}(t)\mathcal{O}]\,, \tag{1}$$

where $\mathcal{O}(t) = e^{\mathrm{i}\mathcal{H}t}\mathcal{O}e^{-\mathrm{i}\mathcal{H}t}$ is the time-dependent operator in the Heisenberg picture ($\hbar = 1$). In the following, it is convenient to work directly in Liouville space, i.e., the Hilbert space of operators, and denote its elements $\mathcal{O}$ as states $|\mathcal{O})$. Elements of the Liouville space evolve under the Liouvillian $\mathcal{L} = [\mathcal{H}, \cdot\,]$, i.e., $|\mathcal{O}(t)) = e^{\mathrm{i}\mathcal{L}t}|\mathcal{O})$, similar to wave functions that evolve under the Hamiltonian $\mathcal{H}$. Using the Liouvillian superoperator, the autocorrelation function may be written as $C(t) = (\mathcal{O}|e^{\mathrm{i}\mathcal{L}t}|\mathcal{O})$. The Liouville space is equipped with an infinite-temperature inner product $(\mathcal{O}_1|\mathcal{O}_2) = \mathrm{Tr}[\mathcal{O}_1^\dagger\mathcal{O}_2]$, which induces a norm via $||\mathcal{O}|| = \sqrt{(\mathcal{O}|\mathcal{O})}$.

In the following, the central object of interest is the Liouvillian $\mathcal{L}$ represented in a particular basis $\{|\mathcal{O}_n)\}$, the so-called *Krylov basis*. The Krylov basis is routinely constructed as part of the *Lanczos algorithm*. In this basis, which is determined by some "seed" observable $\mathcal{O}$, the representation of the Liouvillian is tridiagonal. To initialize the algorithm, we take the normalized state $|\mathcal{O}_0) = |\mathcal{O})$, i.e., $(\mathcal{O}|\mathcal{O}) = 1$, and set $b_1 = ||\mathcal{L}\mathcal{O}_0||$ as well as $|\mathcal{O}_1) = \mathcal{L}|\mathcal{O}_0)/b_1$. Then we iteratively compute

$$\begin{aligned} |\mathcal{Q}_n) &= \mathcal{L}|\mathcal{O}_{n-1}) - b_{n-1}|\mathcal{O}_{n-2})\,, \\ b_n &= ||\mathcal{Q}_n||\,, \\ |\mathcal{O}_n) &= |\mathcal{Q}_n)/b_n\,. \end{aligned} \tag{2}$$

The tridiagonal representation of the Liouvillian in the *Krylov basis* $\{|\mathcal{O}_n)\}$ is then given by

$$L_{mn} = (\mathcal{O}_m|\mathcal{L}|\mathcal{O}_n) = \begin{pmatrix} 0 & b_1 & 0 & \dots \\ b_1 & 0 & b_2 & \\ 0 & b_2 & 0 & \ddots \\ \vdots & & \ddots & \ddots \end{pmatrix}_{mn}\,, \tag{3}$$

where the *Lanczos coefficients* b_n are real, positive numbers output by the algorithm. For our purposes, it is sufficient to assume a finite-dimensional space. Then, the algorithm halts at step $n = d + 1$, where d is the dimension of the Liouville space, and L is a $d \times d$-matrix. Rewriting the Heisenberg equation of motion in the Krylov basis yields

$$\partial_t\varphi_n = -b_{n+1}\varphi_{n+1} + b_n\varphi_{n-1}\,, \tag{4}$$

where we defined $\varphi_n := \mathrm{i}^{-n}(\mathcal{O}_n|\mathcal{O}(t))$. The initial condition is given by $\varphi_n(0) = \delta_{n0}$ and both φ_n and b_n are set to zero by convention when n is "out of bounds". The above Eq. (4) takes the form of a discrete Schrödinger equation and can be numerically solved by familiar means of, e.g., exact diagonalization or iterative schemes like Runge-Kutta and Chebyshev polynomials. As mentioned, the Lanczos coefficients b_n can be interpreted as hopping amplitudes in a tight-binding model. Then, the correlation function coincides with the amplitude of the first site, i.e., $C(t) = \varphi_0(t)$.

For later reference, we introduce the spectral function $\Phi(\omega)$ as the Fourier transform of the correlation function, i.e.,

$$\Phi(\omega) = \int_{-\infty}^{\infty} e^{-\mathrm{i}\omega t}\, C(t)\,\mathrm{d}t\,. \tag{5}$$

It can be shown that the Lanczos coefficients b_n appear in the continued fraction expansion of $\Phi(\omega)$.

$$\Phi(\omega) = \mathrm{Re}\;\cfrac{2}{\mathrm{i}\omega + \cfrac{b_1^2}{\mathrm{i}\omega + \cfrac{b_2^2}{\mathrm{i}\omega + \dots}}} \tag{6}$$

Consequently, there exists a (non-linear) one-to-one map between the Lanczos coefficients b_n and the autocorrelation function $C(t)$. Thus, a set of b_n's uniquely determines $C(t)$ and vice versa.

Lastly, we present the universal operator growth hypothesis as brought forth in Ref. [14]. The hypothesis concerns the asymptotic behavior of the Lanczos coefficients b_n and basically states that in generic, non-integrable systems the Lanczos coefficients of local, few-body observables grow asymptotically linear, i.e., above some n the growth is given by

$$b_n \sim \alpha n + \gamma + o(1)\,, \tag{7}$$

where $\alpha > 0$ and γ are real constants and $o(g_n)$ denotes some real sequence f_n with $\lim_{n\to\infty}|f_n/g_n| = 0$. In the special case of a one-dimensional system, the asymptotic growth is sub-linear due to an additional logarithmic correction [14].

III. PROBING FOR STABILITY

In this section, we devise our strategy to probe the stability of classes of dynamics with respect to certain types of perturbations. This section consists of the following parts: We present ways to find Lanczos coefficients corresponding to a chosen [class of] correlation functions [Sec. III A]. Next, we present four physically motivated requirements that the Lanczos coefficients should fulfill [Sec. III B]. Then, we discuss the particular type of perturbations we consider [Sec. III C]. Finally, we introduce quantifiers that allow to evaluate the stability of the respective dynamics [Sec. III D].

A. Dynamics and Lanczos coefficients

The preliminary section already touched on the relation between a correlation function $C(t)$ and the corresponding Lanczos coefficients b_n. As mentioned, this correspondence is one-to-one, thus, a set of b_n's uniquely determines $C(t)$ and vice versa. However, the convergence can be quite subtle, i.e., there may be fairly similar dynamics with vastly different Lanczos coefficients. On the other side, similar Lanczos coefficients may lead to quite different dynamics.

In the numerical experiments below, we proceed as follows. First, we choose a correlation function $C'(t)$ whose stability we want to probe. We may specify $C'(t)$ as a concrete analytical function, or as a member of a class of functions, e.g., exponential decays. The exact Lanczos coefficients corresponding to $C'(t)$ are denoted by b'_n. These coefficients are, in general, unknown and obtaining them is quite a difficult task. Our objective is to find Lanczos coefficients b_n corresponding to a correlation function $C(t)$ that should be practically indistinguishable from $C'(t)$ for all intents and purposes [$C(t) \simeq C'(t)$]. These "approximate" coefficients b_n may be obtained in three different ways:

i. The exact coefficients b'_n may be analytically known. In this case $b_n = b'_n$ as well as $C(t) = C'(t)$.

ii. The coefficients may be obtained via an educated guess. In this case, the b_n may be quite different from b'_n while still $C(t) \simeq C'(t)$.

iii. The coefficients may be "reverse-engineered" from the correlation function $C'(t)$. For details see App. A.

In the following, we will omit the technical distinction between $C(t)$ and $C'(t)$, since we assume that Lanczos coefficients can be found for which the two correlation functions are practically indistinguishable.

B. Design of the Lanczos coefficients

In the following, we compare dynamics of correlation functions $C_A(t)$ and $C_B(t)$ with respect to their stability under a certain class of perturbations. Corresponding sets of Lanczos coefficients b_n^A and b_n^B may be obtained by one of the three methods mentioned in the last section. We demand that these Lanczos coefficients satisfy the following [partly physically motivated] requirements sufficiently well:

i. The Lanczos coefficients b_n^X should reproduce the respective correlation function $C_X(t)$ to an acceptable accuracy, where $X = A, B$ (this is sort of obvious and has already been addressed above).

ii. The Lanczos coefficients b_n^X should comply with the universal operator growth hypothesis, i.e., they should eventually attain linear growth.

iii. The resulting correlation functions $C_A(t)$ and $C_B(t)$ should decay on more or less the same time scale. This is to ensure a fair comparison between the two, since faster dynamics are typically less affected by perturbations than slower ones.

iv. The Lanczos coefficients b_n^A and b_n^B should be similar in magnitude. In particular, we demand that the quantity $\sum_n (b_n^X)^2$ is comparable for $X = A, B$. We show in App. B that this sum is related to the spectral variance of the Hamiltonian. Hence, this condition fosters the notion that the two correlation functions $C_A(t)$ and $C_B(t)$ originate from different observables while the underlying Hamiltonians are quite similar. In practice, a value of

$$q(b_n^{\mathrm{A}}, b_n^{\mathrm{B}}) = \frac{\sum_n (b_n^{\mathrm{A}})^2}{\sum_n (b_n^{\mathrm{B}})^2} \tag{8}$$

close to unity is desirable.

C. Design of the perturbations

The considered perturbations are designed on the level of Lanczos coefficients. The coefficients b_n corresponding to some correlation function $C(t)$ will be slightly altered according to

$$\tilde{b}_n = b_n + \lambda v_n \,, \tag{9}$$

where the perturbed coefficients are denoted by $\tilde{b}_n$. Here, λ is the perturbation strength and v_n is specified below. We show in App. C that this particular form of the perturbation yields a sensible scaling of the perturbed Hamiltonian with λ.

In general, it is an intricate problem to determine how a perturbation in the form of v_n corresponds to a perturbation $\mathcal{V}$ on the level of Hermitian matrices. This is

an issue that we do not attempt to tackle in this paper. Here, we try to make as few assumptions as possible and model the perturbation v_n as random numbers [with the only restriction of a minimal correlation length, see below]. Concretely, we set

$$v_n = \sum_{k=1}^{N_\mathrm{f}} x_k \cos(2\pi nk/d) + y_k \sin(2\pi nk/d)\,, \qquad (10)$$

where the x_k, y_k are real, random numbers from a Gaussian distribution with zero mean and unit variance. They are normalized as $\sum_k x_k^2 + y_k^2 = 1$.
The sum in Eq. (10) is capped at a number N_f. This corresponds to excluding shorter wavelength or higher frequencies, which induces a minimal correlation length in the coefficients $\tilde{b}_n$ [reddish noise]. No truncation at all, i.e., $N_\mathrm{f} = d$, would be equivalent to adding uncorrelated random numbers [white noise] to the coefficients b_n. This choice can be justified by invoking the tight-binding model interpretation in which the Lanczos coefficients represent hopping amplitudes between neighboring sites. Simply altering the hopping amplitudes in a random, uncorrelated manner leads to localization effects similar to Anderson localization [17]. Through unsystematic varying of N_f, we find that the transition from delocalized to localized behavior is quite sharp. Since the aim is to study the stability of certain relaxation dynamics, we choose N_f as large as possible, but small enough to avoid said localization effects. In practice, this amounts to $N_\mathrm{f} \approx d/3$. In Sec. IV C, we ease this restriction to identify "pathological" perturbations.

D. Assessing stability

Once the perturbation has acted on the coefficients b_n and yielded the perturbed coefficients $\tilde{b}_n$, we can calculate the corresponding perturbed dynamics $\tilde{C}(t)$ as laid out in Sec. II. Now, some tools are needed in order to judge how strongly the dynamics were altered by the perturbation. In particular, it is important to assess to what extent the perturbed dynamics still falls into the original class of functions to which the unperturbed dynamics belonged. For example, we may ask if $\tilde{C}(t)$ is still exponential, given that the original dynamics $C(t)$ was exponential [the decay constants may differ]. To this end, we attempt to fit the perturbed dynamics with a function that also described the unperturbed dynamics, e.g., we may try to fit $\tilde{C}(t)$ with $f(t) = Ae^{-\mu t}$. In practice, the fit is obtained via a standard fitting routine.
Before we introduce quantifiers that measure the effect of the perturbation, some remarks on the fitting ansatz are in order. Correlation functions are symmetric in time, thus, all odd moments necessarily vanish. In particular, correlation functions have zero slope at $t = 0$. Further, we normalize the correlation function to unity at $t = 0$. However, for fitting we choose functions that lack these features, i.e., the above exponential ansatz may yield an A that slightly differs from unity. Further, the slope of an exponential at $t = 0$ is never zero. This "negligence" is due to the fact that we are more interested in an overall description of relaxation dynamics, rather than in the details of the short-time behavior.
We assess the quality of a fit $f(t)$ by calculating "how far off" it is from the given perturbed dynamics. Concretely, we define a measure of the "error" or "deviation" ϵ by the expression

$$\epsilon = \sqrt{\frac{1}{N_\mathrm{eq}} \sum_{n=0}^{N_\mathrm{eq}} (\tilde{C}(t_n) - f(t_n))^2}\,. \qquad (11)$$

Here, the respective functions are evaluated at available points in time $t_n = n\delta t$, where δt is the time step used to solve the equation of motion. The upper bound N_eq corresponds to a time at which the dynamics in question has seemingly equilibrated [18].
To get a feeling of which numerical value of ϵ constitutes a good or bad fit, we refer to the exemplary numerical data displayed in Figs. 3, 4, 8 and 9.
We introduce a second quantifier σ that measures how strongly the unperturbed dynamics are altered due to the perturbation in the first place.

$$\sigma = \sqrt{\frac{1}{N_\mathrm{eq}} \sum_{n=0}^{N_\mathrm{eq}} (\tilde{C}(t_n) - C(t_n))^2}\,. \qquad (12)$$

The construction of this quantity is similar to the construction of the quantity ϵ that measures the fit quality.

IV. NUMERICAL ANALYSIS

In this section, we apply the presented strategy to certain relaxation dynamics. In particular, we investigate and compare the stability of two classes of dynamics. The first class in question is the class of damped oscillations, whose damping is due to an ordinary exponential factor. This class also includes simple exponential decays, which can be viewed as damped oscillations with zero frequency. These dynamics are ubiquitous in nature. For example, slow exponential dynamics may commonly arise whenever a system interacts weakly with an environment or whenever long-wavelength Fourier components of spatial densities of conserved quantities are considered. Further, expo-

nentially damped oscillations are routinely observed as short-wavelength components.

The possible choices for the second class of dynamics are of course manifold. Since an exhaustive analysis is impossible, we decide on a "Gaussianized" version of the first class. This is supposed to mean that the class includes Gaussian decays as well as oscillations damped by Gaussian factors.

The restriction of the second class of course stifles any aspiration of generality. Thus, the following results should be viewed as mere numerical experiments that corroborate the existence of stability in the first class.

Concretely, in Sec. IV A, we compare exponential and Gaussian decay. In Sec. IV B, the comparison is between two damped oscillations, one with an exponential damping factor and the other with a Gaussian damping factor. Lastly, in Sec. IV C, we identify "pathological" perturbations that destroy the considered dynamics.

Throughout the next sections, we set the dimension of the Liouville space to $d = 10000$ and the frequency cut-off to $N_\mathrm{f} = 3333 \approx d/3$. We repeat the strategy $N = 1000$ times by drawing random numbers x_k, y_k and present statistics for the quantifiers ϵ and σ.

A. Exponential vs. Gaussian decay

In the first round of our stability investigation, an exponential decay competes against a Gaussian decay. Following the strategy laid out in the previous sections, the first step is to find suitable Lanczos coefficients that comply with the four conditions presented in Sec. III B. We begin with the Gaussian decay. The Lanczos coefficients that exactly correspond to Gaussian decay of the form $C(t) = e^{-t^2/2}$ are analytically known [method one in Sec. III A)], i.e., $b_n = \sqrt{n}$ [19]. Nevertheless, the second condition, the compliance with the operator growth hypothesis, needs to be satisfied. To this end, we choose a cutoff-point $n^\star$ at which the coefficients are continued in a linear fashion. This yields the following Lanczos coefficients ["g" = "Gaussian"]

$$b_n^\mathrm{g} = \begin{cases} \sqrt{n}\,, & n \leq n^\star \\ \alpha n + \gamma\,, & n > n^\star\,. \end{cases} \tag{13}$$

The parameters α and γ are determined by the requirement of a smooth transition from square-root growth to linear growth, i.e., $\alpha = 1/(2\sqrt{n^\star})$ and $\gamma = \sqrt{n^\star}/2$. The change from square-root to linear growth for $n > n^\star$ does not strongly affect the "Gaussianity" of the correlation dynamics [compare Fig. 2] such that condition one remains fulfilled.

Next, coefficients for an (approximate) exponential decay need to be found. As mentioned, a correlation function can never be truly exponential, since it necessarily features zero slope at $t = 0$. Thus, we only require the exponential decay to be present after a short Zeno-time, which is usually exceedingly short compared to the relaxation time [20, 21]. We achieve an approximate exponential decay via an educated guess [method two in Sec. III A]. Slow dynamics are characterized by a relatively small first coefficient b_1, followed by a jump to a larger remainder of coefficients $b_{n\geq 2}$. Thus, we make the following ansatz for the coefficients ["e" = "exponential"]

$$b_n^\mathrm{e} = \begin{cases} a\,, & n = 1 \\ \alpha n + \gamma\,, & n \geq 2\,. \end{cases} \tag{14}$$

The parameter a is set to 1.2, a similar magnitude as the first Gaussian coefficient b_1^g. The other parameters α and γ are the same as in the Gaussian case. Thus, condition two, i.e., compliance with the universal operator growth hypothesis, is fulfilled. The Lanczos coefficients as defined in Eq. (13) and Eq. (14) are depicted in Fig. 1. Since both sets of coefficients coincide for $n > n^\star$, condition four is satisfied as the quantity $q(b_n^\mathrm{g}, b_n^\mathrm{e}) = 0.999993$ is sufficiently close to unity. The corresponding dynamics are depicted in Fig. 2. The ansatz for the coefficients b_n^e in Eq. (14) indeed yields a nice exponential decay. A fit of the form $Ae^{-\lambda t}$ with $A = 1.02$ and $\lambda = 0.24$ captures the dynamics quite well. Thus, condition one is sufficiently fulfilled for the exponential decay as well.

Further, we can extract from Fig. 2 that both dynamics decay on more or less the same time scale. Therefore, we also view condition three as satisfied. If any, the Gaussian dynamics is faster and thus less prone to perturbations.

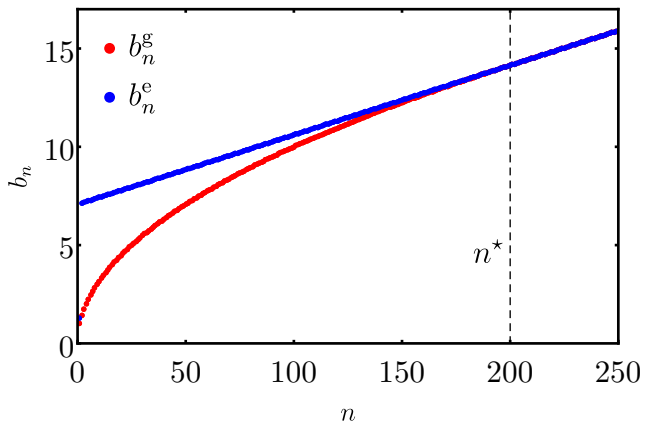

Figure 1. Lanczos coefficients corresponding to Gaussian decay (red) and exponential decay (blue). The square-root growth transitions to linear growth at $n = n^\star$.

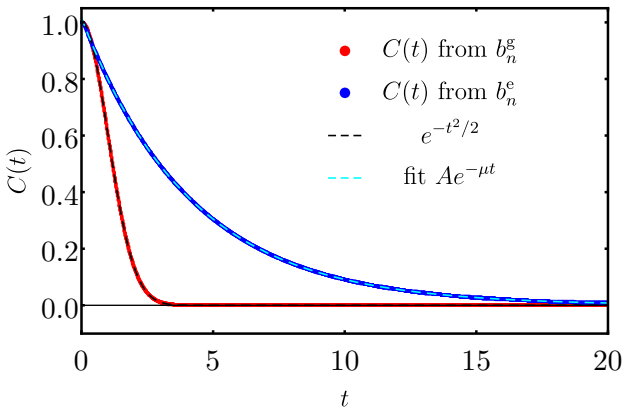

Figure 2. Unperturbed correlation functions $C(t)$ calculated from the respective Lanczos coefficients. Dashed curves indicate an exponential fit (cyan) and an exact Gaussian $e^{-t^2/2}$ (black).

Now that we have checked all four conditions presented in Sec. III B, we are ready to apply the perturbation as laid out in Sec. III C. We set $\lambda = 0.5$. Three exemplary perturbed dynamics with respective fits for the exponential case are depicted in Fig. 3.
It is evident that the perturbed dynamics are still nicely described by an exponential, only the decay constant changes. For the Gaussian decay, three exemplary perturbed dynamics with respective fits are depicted in Fig. 4. Two displayed perturbed Gaussian curves feature oscillations, which can not possibly be captured by a Gaussian fit ansatz. The three depicted fits are much worse than in the exponential case.

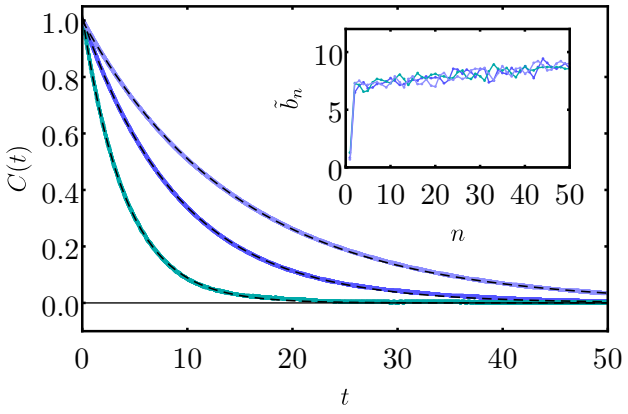

Figure 3. Three exemplary correlation functions originating from the perturbed exponential Lanczos coefficients $\tilde{b}_n^{\mathrm{e}}$. Dashed, black lines indicate exponential fits. The quantifier ϵ of all three dynamics is relatively close to the mean value, see Fig. 5. Inset: corresponding perturbed Lanczos coefficients.

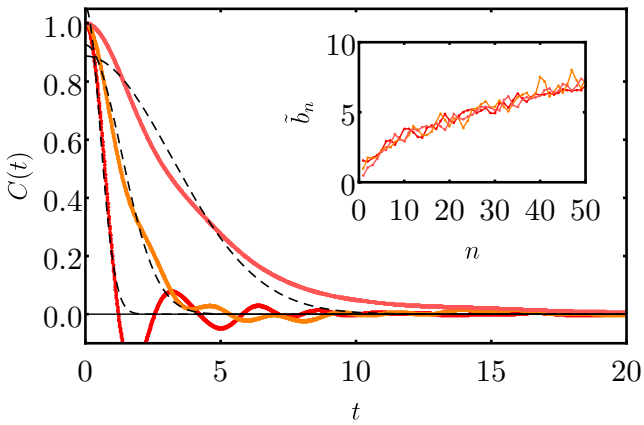

Figure 4. Three exemplary correlation functions originating from the perturbed Gaussian Lanczos coefficients $\tilde{b}_n^{\mathrm{g}}$. Dashed, black lines indicate Gaussian fits. The quantifier ϵ of all three dynamics is relatively close to the mean value, see Fig. 5. Inset: corresponding perturbed Lanczos coefficients.

The impression from these six exemplary curves is confirmed in Fig. 5, which shows histograms of deviations ϵ of the fits from the respective perturbed dynamics. The symbol Ω denotes the number of values ϵ within a bin of size $5 \cdot 10^{-4}$. There is a clear division between the exponential cases (blue) and the Gaussian cases (red). The deviations ϵ of the exponential decays are much smaller than those of the Gaussian decays. In particular, the mean value $\bar{\epsilon}_{\mathrm{e}} = 0.002$ (indicated by a blue, dashed line) in the exponential case is about twenty times smaller than in the Gaussian case $\bar{\epsilon}_{\mathrm{g}} = 0.042$. For a visualization of this comparison see Fig. 3 and Fig. 4, whose exemplary curves feature values of ϵ close to the respective mean values.
We have to be aware that this apparent stability of the exponential may be due to the possibility that exponential decays are generally less affected by our constructed perturbation than the Gaussian decays. To check this possibility and to show that this is not the case, we consider the quantifier σ, which measures the difference between the perturbed and the unperturbed dynamics. The inset of Fig. 5 depicts a scatter plot of all 1000 pairs (σ_i, ϵ_i). If one decay would be consistently less affected than the other, a cluster of points to the left [small values of σ] would emerge. This is evidently not the case, as the distribution along the horizontal axis is relatively similar for both decays. The existence of the diagonal edge is expected, since there can be no fit that is "farther away" from the perturbed dynamics than the unperturbed dynamics itself, which is, of course, also an eligible candidate for fitting.

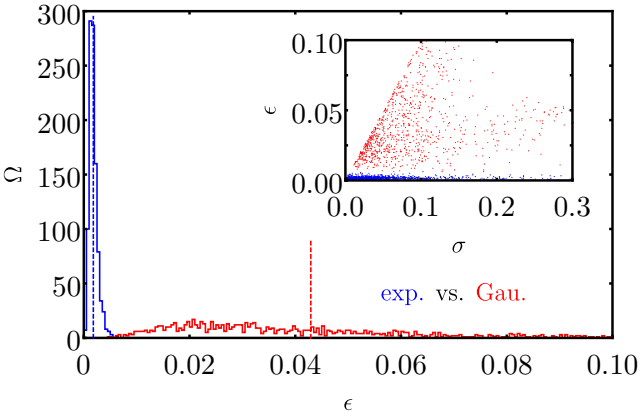

Figure 5. Histogram of the fit quality measure ϵ with a bin size of $5 \cdot 10^{-4}$. Dashed lines indicate respective mean values. The stability of the exponential decay is evident. In contrast, the Gaussian decay does not seem to be stable, as the deviations ϵ become quite large. Inset: scatter plot of all points (σ_i, ϵ_i). Both dynamics are equally affected by the perturbation.

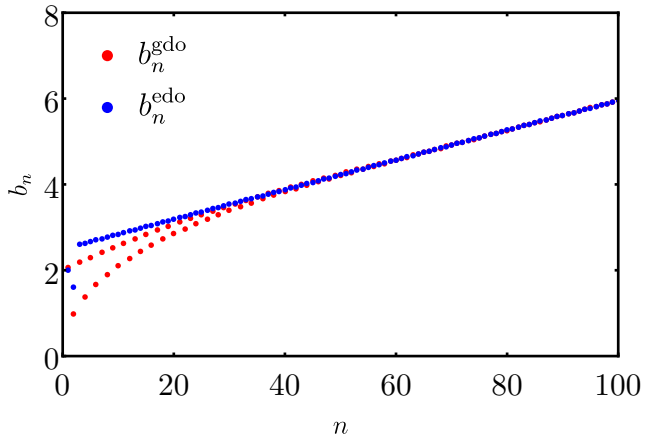

Figure 6. Lanczos coefficients corresponding to an oscillation damped by a Gaussian (red) and an oscillation damped by an exponential (blue).

Thus, we conclude that exponential decays is indeed stable with respect to perturbations [as in Eq. (10)]. In contrast, Gaussian decays seem to be quite unstable. This is the first main result of the paper at hand.

B. Damped oscillations: exponential vs. Gaussian

In the second round, we investigate and compare two types of damped oscillations, one with an exponential damping factor, the other with a Gaussian damping factor. As in the last section, first, two sets of Lanczos coefficients need to be found that satisfy all four conditions imposed in Sec. III B.

We again begin with the Gaussian case. The coefficients b_n^{gdo} ["gdo" = "Gaussian damped oscillation"] that correspond to an oscillation damped by a Gaussian factor a neither analytically known, nor can we make an educated guess. This only leaves the third method, in which we "reverse-engineer" the coefficients from the dynamics itself. To this end, we choose a particular correlation function $C(t) = e^{-t^2/8}\cos(2t)$ and proceed as detailed in App. A. This procedure allows us to obtain about 50 Lanczos coefficients. After that, the coefficients are continued "by hand" in a manner that first, respects the pattern exhibited by the coefficients so far, and second, eventually becomes linear.

For the exponentially damped oscillation we can again make an educated guess [method two] for the coefficients b_n^{edo} ["edo" = "exponentially damped oscillation"].

We set the first two coefficients b_1, b_2 to some values ($b_1 = 2.0$, $b_2 = 1.6$), followed by a jump to larger coefficients $b_{n\geq 3}$, which then grow in a linear fashion. The slope is determined by and coincides with the slope in the Gaussian case.

The unperturbed Lanczos coefficients and corresponding correlation functions are depicted in Fig. 6 and Fig. 7, respectively. The "reverse-engineered and continued by hand" coefficients b_n^{gdo} indeed reproduce the given correlation function $C(t) = e^{-t^2/8}\cos(2t)$. Further, the guess for b_n^{edo} yields a nice exponentially damped curve, i.e., the fit ansatz with $[A = 1.04, \mu = 0.57, \omega = 2.19, \phi = -0.32]$ nicely captures the dynamics. Therefore, condition one is satisfied for both cases. The two sets of coefficients were designed to eventually attain linear growth, thus condition two is

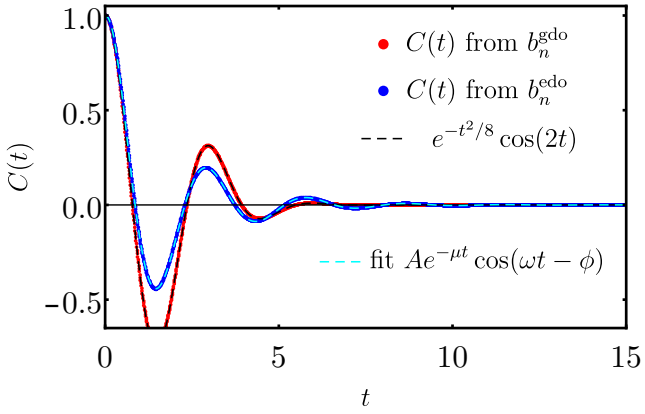

Figure 7. Unperturbed correlation functions $C(t)$ calculated from the respective Lanczos coefficients. Dashed curves indicate a fit of an exponentially damped oscillation (cyan) and the oscillation damped by a Gaussian $e^{-t^2/8}\cos(2t)$ (black).

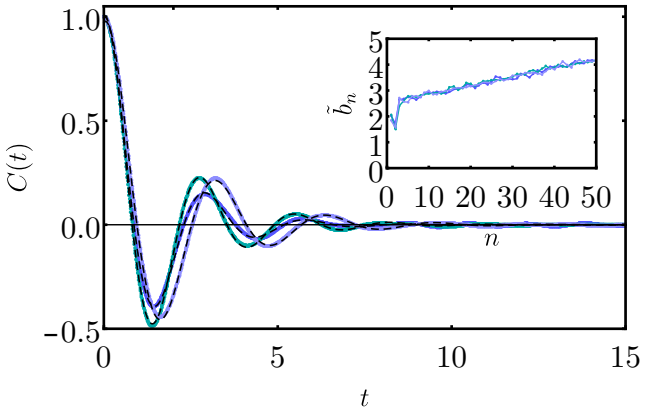

Figure 8. Three exemplary correlation functions originating from the perturbed Lanczos coefficients $\tilde{b}_n^{\mathrm{edo}}$. Dashed, black lines indicate 4-parametric fits of exponentially damped oscillations. The quantifier ϵ of all three dynamics is relatively close to the mean value, see Fig. 10. The perturbation not only changes the decay constant, but also the frequency. Inset: corresponding perturbed Lanczos coefficients.

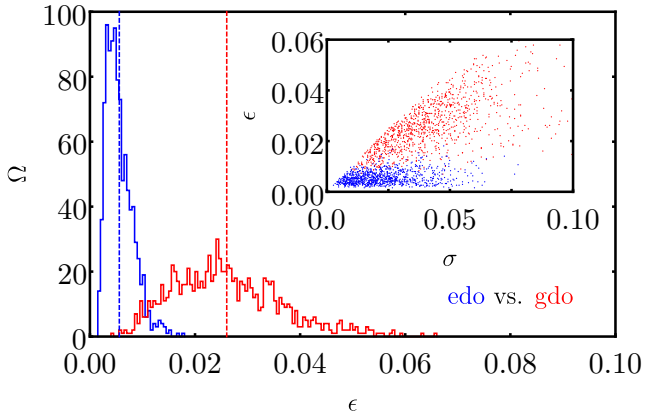

Figure 10. Histogram of the fit quality measure ϵ with a bin size of $5 \cdot 10^{-4}$. Dashed lines indicate respective mean values. The stability of the exponentially damped oscillations is evident. In contrast, the Gaussian counterpart does not seem to be stable, as the deviations ϵ become quite large. Inset: scatter plot of all points (σ_i, ϵ_i). Both dynamics are more or less equally affected by the perturbation.

fulfilled. It is evident from Fig. 7 that both dynamics decay on similar time scales, rendering condition three satisfied. Lastly, the quantity $q(b_n^{\mathrm{gdo}}, b_n^{\mathrm{edo}})$ practically equals unity. Thus, all four conditions are met.
Next, we switch on the perturbation and set $\lambda = 0.1$. Exemplary perturbed dynamics are displayed in Fig. 8 and Fig. 9, respectively. The perturbed dynamics are fitted with the 4-parametric ansatz $C(t) = Ae^{-\mu t}\cos(\omega t - \phi)$ in the exponential and $C(t) = Ae^{-\mu t^2}\cos(\omega t - \phi)$ in the Gaussian case.

While the perturbed coefficients in the exponential case still lead to correlation functions that are within the class of exponentially damped oscillations [with different decay constants μ and frequencies ω], the same can not be said for the Gaussian case, where the perturbed dynamics decay too slowly and can not by captured by the fit ansatz above.

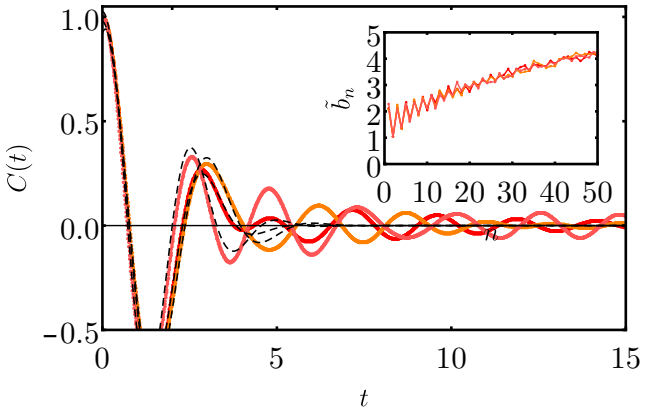

Figure 9. Three exemplary correlation functions originating from the perturbed Lanczos coefficients $\tilde{b}_n^{\mathrm{gdo}}$. Dashed, black lines indicate 4-parametric fits of oscillations damped by a Gaussian. The quantifier ϵ of all three dynamics is relatively close to the mean value, see Fig. 10. Inset: corresponding perturbed Lanczos coefficients.

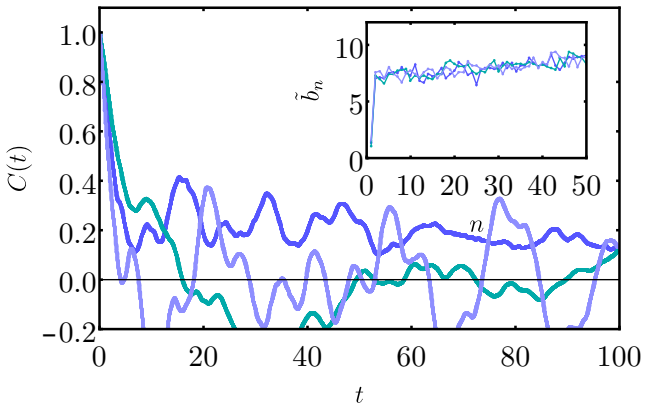

Figure 11. Three exemplary dynamics originating from perturbed Lanczos coefficients $\tilde{b}_n^{\mathrm{e}}$. The perturbation consists of uncorrelated random numbers, i.e., $N_{\mathrm{f}} = d$ in Eq. (10). The exponential decay is completely destroyed and the correlation function does not seem to equilibrate at all. Inset: corresponding perturbed Lanczos coefficients.

The impression from the six exemplary curves is confirmed in Fig. 10, which displays histograms of the quantifier ϵ. Again, the division into two distinct peaks is evident. The respective mean values $\bar{\epsilon}_{\mathrm{gdo}} = 0.026$ and $\bar{\epsilon}_{\mathrm{edo}} = 0.006$ are indicated as dashed, vertical lines and differ by a factor of about five. For a visualization of what these values mean for the fit quality, see Fig. 8 and Fig. 9, whose curves feature values of ϵ close to the respective mean values. Thus, we conclude that the exponentially damped dynamics are quite stable and, in particular, more stable than the oscillations damped by a Gaussian. The disparity between the two is not as strong as for the decays in the previous section [however, different values of λ may not be directly comparable.]
The inset of Fig. 10 again shows a scatter plot of all points (σ_i, ϵ_i). The blue cluster of dots is a little more concentrated to small values of σ, indicating that the exponentially damped oscillations are a little less altered by the perturbation than their Gaussian counterpart. However, the marginal distribution over σ is still less partitioned into two peaks than the one over ϵ [which is the data in the histogram itself]. Hence, the stability of exponentially damped oscillations is still due to the nature of the dynamics and not due to a smaller effect of the perturbation on the dynamics.
We conclude that exponentially damped oscillations are stable with respect to perturbations [as in Eq. (10)]. In contrast, oscillations damped by a Gaussian seem to be quite unstable. This is the second main result of the paper at hand.

C. Pathological perturbations

In this section, we lift the restriction imposed on the v_n earlier, which was that frequencies were cut at $N_{\mathrm{f}} \approx d/3$. Instead, we include all frequencies in the construction of the perturbation, which amounts to setting $N_{\mathrm{f}} = d$. This case simply corresponds to adding uncorrelated random numbers to the unperturbed coefficients b_n. Otherwise, the strategy is pursued in the same manner as above.
Three exemplary dynamics for exponential decays are depicted in Fig. 11 [for conciseness, we refrain from showing more exemplary data for the other cases]. As is evident, the exponential decay is completely absent and replaced by quite irregular dynamics, which do not seem to reach an equilibrium [N_{eq} is set as large as possible [18] in these cases]. These curves hint at the presence of localization effects, which prevent the "particle" [in the tight-binding picture] to leave the first site.
A histogram of the Gaussian vs. exponential data can be viewed in Fig. 12. The mean values read $\bar{\epsilon}_{\mathrm{g}} = 0.15$ in the Gaussian case and $\bar{\epsilon}_{\mathrm{e}} = 0.12$ in the exponential case, which is some orders of magnitude larger than before when shorter wavelengths were excluded. Further, the accumulation of points along the diagonal in the inset suggests that the curves no longer resemble their original form, which is expected judging from Fig. 11.
The histogram for the oscillating cases is displayed in Fig. 13. The mean deviations read $\bar{\epsilon}_{\mathrm{gdo}} = 0.035$ and $\bar{\epsilon}_{\mathrm{edo}} = 0.025$. These values are comparable to the Gaus-

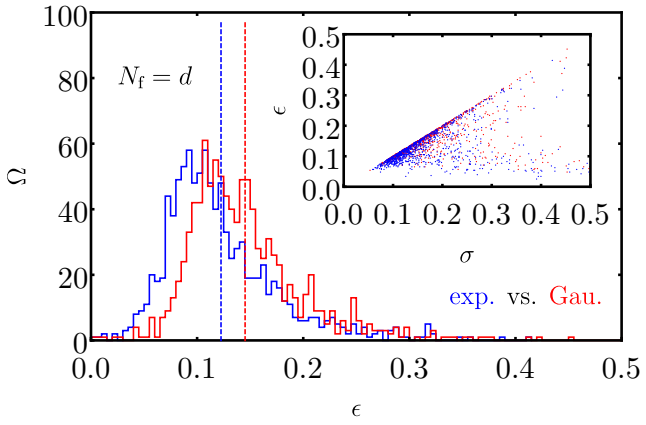

Figure 12. Histogram of the fit quality measure ϵ with a bin size of $5 \cdot 10^{-3}$. Dashed lines indicate respective mean values. For both oscillating cases the deviations ϵ are quite large. Thus, both relaxation dynamics are unstable with respect to the perturbation including all wave lengths. Inset: scatter plot of all points (σ_i, ϵ_i). Points accumulate along the diagonal edge indicating that the respective dynamics are heavily altered due to the perturbation.

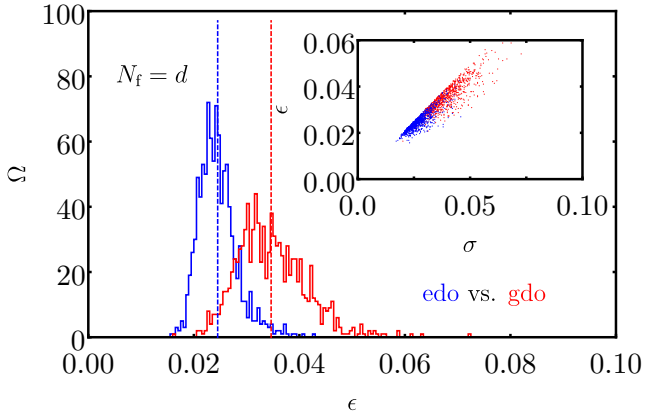

Figure 13. Histogram of the fit quality measure ϵ with a bin size of $5 \cdot 10^{-4}$. Dashed lines indicate respective mean values. For both the exponential and the Gaussian case the deviations ϵ are extremely large. Thus, both relaxation dynamics are unstable with respect to the perturbation including all wave lengths. Inset: scatter plot of all points (σ_i, ϵ_i). Points accumulate along the diagonal edge indicating that the respective dynamics are heavily altered due to the perturbation.

sian case in Fig. 10. However, since the quantifier ϵ measures more or less the deviation "per time step", the comparison of values $\bar{\epsilon}$ between dynamics that do and do not equilibrate can be void of meaning. In practice, judging from all figures displaying exemplary curves, a value ϵ of about one percent corresponds to fits that "look good to the eye".

Based on these observations, we specify a property of perturbations that lead to non-generic or pathological dynamics. Namely, a perturbation is "untypical", if it gives rise to Lanczos coefficients that vary non-smoothly, i.e., there is no minimal correlation length within the coefficients. Again, what this means on the level of Hermitian matrices is difficult to assess and beyond the scope of this work. This is the third main result of the paper at hand.

V. CONCLUSION

In this paper, we performed numerical experiments to probe the stability of two classes of relaxation dynamics. The first class consisted of exponentially damped oscillations, which also includes exponential decays. The second class was chosen as a Gaussian counterpart to the first class, i.e., including Gaussian decays and oscillations damped by a Gaussian.

The whole strategy was formulated in the framework of the recursion method, in particular, the perturbations were constructed as an alteration of the Lanczos coefficients. Unperturbed coefficients b_n and perturbation v_n were chosen to satisfy certain physically motivated conditions.

The first main message of the paper at hand is that the exponential class of dynamics is relatively stable under the considered perturbations. In contrast, the Gaussian counterpart is found to be quite unstable. These findings confirm and extent upon previous results based on random matrices [8], which did not comply with the operator growth hypothesis.

We want to emphasize that within this work the main focus should be put on the stability of the former class of relaxation dynamics, as these are ubiquitous in nature, examples are given at the beginning of Sec. IV. The investigation of the latter class should just be taken as an exemplary comparison. In fact, the choice of a Gaussian counterpart to the first class is quite arbitrary. Any number of relaxation dynamics could have been investigated instead.

The second main message of the paper at hand concerns the nature of the perturbations themselves. Not only, but also in the context of the works on "typicality of perturbations" [9–11], it could be interesting to find properties of perturbations that lead to non-generic, "pathological" dynamics. Here, we identified such a criterion, namely that the perturbation should yield Lanczos coefficients whose minimal correlation length is still above some threshold value.

As is evident from Fig. 11, including short correlations seems to lead to unorthodox dynamics. The displayed curves do not seem to reach an equilibrium, at least on the available time scale. Rather, localization-like effects are introduced, which cause some part of the wave function to remain on the first site. On the other hand, sufficiently smooth coefficients alter the relaxation dynamics in a "controlled yet non-trivial" manner.

Perturbations in various numerical investigations based in random matrices [8, 9] as well as spin lattice models [22, 23] seem to naturally possess the above specified property. Hence, a more systematic investigation on the existence of a minimal correlation length in the coefficients for realistic setups could be a possible prospect for future research.

ACKNOWLEDGMENTS

This work was supported by the Deutsche Forschungsgemeinschaft (DFG) within the Research Unit FOR 2692 under Grant No. 397107022 (GE 1657/3-2) and No. 397067869 (STE 2243/3-2).

Appendix A: Reverse-engineering b_n from $C(t)$

In this section, we present the procedure to reverse-engineer the Lanczos coefficients b_n from a given correlation function $C(t)$. The idea is to employ the Lanczos algorithm from Sec. II, but on the level of spectral functions $\Phi(\omega)$ rather than on the level of observables $|\mathcal{O})$. The inner product of operators turns into an inner product of functions, i.e.,

$$(\Phi_1|\Phi_2) = \int \Phi_1^\star(\omega)\Phi_2(\omega)\,\mathrm{d}\omega\,. \tag{A1}$$

Further, the application of the Liouvillian $\mathcal{L}$ to an operator $\mathcal{O}$ corresponds to a multiplication of the respective function in Fourier space with $-\omega$ [since the commutator with $\mathcal{H}$ corresponds to a time derivative, which is equivalent to a multiplication with $\mathrm{i}\omega$ in Fourier space],

$$\mathcal{L}|\mathcal{O}) \to -\omega\Phi(\omega)\,. \tag{A2}$$

In practice, we choose a specific correlation function $C(t)$ and calculate its Fourier transform $\Phi(\omega)$. The initial "seed" function is set to the (normalized) $\sqrt{\Phi(\omega)}$. Then, the Lanczos algorithm operates as laid out in Sec. II. In this manner, about 50 coefficients can be obtained before numerical instabilities become too pronounced.

Appendix B: Link to spectral width

The eigenvalue equation for the Hamiltonian reads $\mathcal{H}|E_i\rangle = E_i|E_i\rangle$, where E_i and $|E_i\rangle$ denote eigenvalues and eigenstates, respectively. The corresponding eigenvalue equation for the Liouvillian superoperator is given by $\mathcal{L}\mathcal{M}_\beta = \mathcal{E}_\beta\mathcal{M}_\beta$ with eigenvalues $\mathcal{E}_{\beta(i,j)} = E_i - E_j$ and eigenoperators $\mathcal{M}_{\beta(i,j)} = |E_i\rangle\langle E_j|$. Without loss of generality, we can set $\mathrm{Tr}[\mathcal{H}] = \sum_i E_i = 0$. Further, we denote the dimension of the Hilbert space by $d_\mathcal{H}$, i.e., $d_\mathcal{H}^2 = d$. Then we have

$$\begin{aligned}\sum_n b_n^2 &= \frac{1}{2}\mathrm{Tr}[\mathcal{L}^2] = \frac{1}{2}\sum_{i,j}(E_i - E_j)^2 \\ &= \frac{1}{2}\sum_{i,j}(E_i^2 - 2E_iE_j + E_j^2) \\ &= \frac{d_\mathcal{H}}{2}\Big(\sum_i E_i^2 + \sum_j E_j^2\Big) \\ &= d_\mathcal{H}\mathrm{Tr}[\mathcal{H}^2]\end{aligned} \tag{B1}$$

Thus, we see that the quantity in question is indeed linked to the spectral width of the Hamiltonian.

Appendix C: Scaling with perturbation strength

Consider a Hamiltonian $\mathcal{H} = \mathcal{H}_0 + \lambda\mathcal{V}$ consisting of an unperturbed part $\mathcal{H}_0$ and a perturbation $\lambda\mathcal{V}$ with $\mathrm{Tr}[\mathcal{H}_0\mathcal{V}] = 0$. For the spectral variance of $\mathcal{H}$ it holds true that

$$\mathrm{Tr}[\mathcal{H}^2] = \mathrm{Tr}[\mathcal{H}_0^2] + \lambda^2\mathrm{Tr}[\mathcal{V}^2]\,. \tag{C1}$$

On the other hand, with the particular choice of perturbation in Eq. (9), we get that

$$\begin{aligned}\sum_n \tilde{b}_n^2 &= \sum_n (b_n + \lambda v_n)^2 \\ &= \sum_n (b_n^2 + 2\lambda b_n v_n + \lambda^2 v_n^2) \\ &\approx \sum_n b_n^2 + \lambda^2 \sum_n v_n^2\,.\end{aligned} \tag{C2}$$

The term $2\lambda b_n v_n$ is negligible due to the specific choice of v_n. Recalling the relation in Eq. (B1), we see from Eq. (C2) that the scaling in Eq. (9) reproduces the scaling in Eq. (C1) and is therefore appropriate.

[1] C. Gogolin and J. Eisert, Reports on Progress in Physics **79**, 056001 (2016).
[2] M. Srednicki, Phys. Rev. E **50**, 888 (1994).
[3] J. Deutsch, Phys. Rev. A **43**, 2046 (1991).
[4] L. D'Alessio, Y. Kafri, A. Polkovnikov, and M. Rigol, Advances in Physics **65**, 239 (2016).
[5] S. Lloyd, "Pure state quantum statistical mechanics and black holes," (2013), arXiv:1307.0378.
[6] S. Goldstein, J. Lebowitz, R. Tumulka, and N. Zanghì, Phys. Rev. Lett. **96**, 050403 (2006).
[7] P. Reimann, Phys. Rev. Lett. **99**, 160404 (2007).
[8] L. Knipschild and J. Gemmer, Phys. Rev. E **98**, 062103 (2018).
[9] L. Dabelow and P. Reimann, Phys. Rev. Lett. **124**, 120602 (2020).
[10] L. Dabelow, P. Vorndamme, and P. Reimann, Phys. Rev. Research **2**, 033210 (2020).
[11] L. Dabelow and P. Reimann, Journal of Statistical Mechanics: Theory and Experiment **2021**, 013106 (2021).
[12] V. Viswanath and G. Müller, *The Recursion Method: Applications to Many-Body Dynamics* (Springer, New York, 2008).
[13] D. Mattis, in *Physics in One Dimension* (Springer Berlin Heidelberg, 1981) pp. 3–10.
[14] D. Parker, X. Cao, A. Avdoshkin, T. Scaffidi, and E. Altman, Phys. Rev. X **9**, 041017 (2019).
[15] J. Noh, Phys. Rev. E **104**, 034112 (2021).
[16] R. Heveling, J. Wang, and J. Gemmer, "Numerically probing the universal operator growth hypothesis," (2022), arXiv:2203.00533.
[17] P. Anderson, Phys. Rev. **109**, 1492 (1958).
[18] In practice, we define the equilibration time as follows. We choose a threshold value of 0.005. If the absolute value of $C(t)$ is smaller than the threshold value over the course a certain time interval [we choose three time units], the end-time corresponds to the upper bound in Eq. (11) and Eq. (12). The time step is $\delta t = 0.01$. If the correlation function does not equilibrate at all, N_eq is set to the maximal time before an echo due to the finiteness of the system occurs.
[19] C. Joslin and C. Gray, Molecular Physics **58**, 789 (1986).
[20] H.-P. Breuer and F. Petruccione, *The Theory of Open Quantum Systems* (Oxford University Press, 2006).
[21] E. Joos, H. Zee, C. Kiefer, D. Giulini, J. Kupsch, and I.-O. Stamatescu, *Decoherence and the Appeareance of a Classical World from Quantum Theory* (Springer, 2003).
[22] R. Heveling, L. Knipschild, and J. Gemmer, Zeitschrift für Naturforschung A **75**, 475 (2020).
[23] J. Richter, F. Jin, L. Knipschild, H. De Raedt, K. Michielsen, J. Gemmer, and R. Steinigeweg, Phys. Rev. E **101**, 062133 (2020).

Erklärung über die Eigenständigkeit der erbrachten wissenschaftlichen Leistung

Ich erkläre hiermit, dass ich die vorliegende Arbeit ohne unzulässige Hilfe Dritter und ohne Benutzung anderer als der angegebenen Hilfsmittel angefertigt habe. Die aus anderen Quellen direkt oder indirekt übernommenen Daten und Konzepte sind unter Angabe der Quelle gekennzeichnet.

Bei der Auswahl und Auswertung folgenden Materials haben mir die nachstehend aufgeführten Personen in der jeweils beschriebenen Weise entgeltlich/unentgeltlich geholfen.

1. .....
2. .....
3. .....

Weitere Personen waren an der inhaltlichen materiellen Erstellung der vorliegenden Arbeit nicht beteiligt. Insbesondere habe ich hierfür nicht die entgeltliche Hilfe von Vermittlungs- bzw. Beratungsdiensten (Promotionsberater oder andere Personen) in Anspruch genommen. Niemand hat von mir unmittelbar oder mittelbar geldwerte Leistungen für Arbeiten erhalten, die im Zusammenhang mit dem Inhalt der vorgelegten Dissertation stehen.

Die Arbeit wurde bisher weder im In- noch im Ausland in gleicher oder ähnlicher Form einer anderen Prüfungsbehörde vorgelegt.

....
Ort, Datum Unterschrift